

THE CRYOGENIC DARK MATTER SEARCH (CDMS)

a Ph. D. Thesis

by

Peter David Barnes, Jr.

1996



THE UNIVERSITY OF CALIFORNIA at BERKELEY

The Cryogenic Dark Matter Search (CDMS).

by

Peter David Barnes, Jr.

B. S. (Yale University) 1987

M. A. (University of California, Berkeley) 1990

A dissertation submitted in partial satisfaction of the

requirements for the degree of

Doctor of Philosophy

in

Physics

in the

GRADUATE DIVISION

of the

UNIVERSITY of CALIFORNIA, BERKELEY

Committee in charge:

Professor Bernard Sadoulet, Chair

Professor Lawrence Hall

Professor William J. Welch

1996

The Cryogenic Dark Matter Search (CDMS)

Copyright 1996

by

Peter David Barnes, Jr.

Errata

The following corrections have been made since this thesis was submitted to the University of California, Berkeley Library:

On page xi "Joe Weber" should read "George Weber."

The sentences immediately preceding Eq. (3.7) should read:

"Since the widths are equal, the optimum value for the cut, y_c , is just the average of the means, $y_c = (\bar{y}_e + \bar{y}_n)/2 = 0.20/\text{eV}$, where we have taken $\bar{y}_e = 0.33/\text{eV}$ and $\bar{y}_n = 0.08/\text{eV}$. Then we can compute $Q(E)$ from " (followed by Eq. (3.7))

On page 55, the list of contributors to the shield design and construction should include "Blas Cabrera, Brian Dougherty, and Mike Hennessy."

Abstract

The Cryogenic Dark Matter Search (CDMS)

by

Peter David Barnes, Jr.

Doctor of Philosophy in Physics

University of California, Berkeley

Professor Bernard Sadoulet, Chair

A substantial body of observational evidence indicates that the universe contains much more material than we observe directly via photons of any wavelength. The existence of this "missing" mass or "dark" matter is inferred by its gravitational effects on the luminous material. Accepting the existence of dark matter has profoundly shaken our understanding in most areas of cosmology. If it exists at the lowest densities measured it is hard to understand in detail the creation of the elements in the early universe. If moderate density values are correct, then we have trouble understanding how the universe came to have so much structure on large scales. If the largest densities are correct, then dark matter is not ordinary matter, but must be something exotic like a new fundamental particle.

We would like to measure the properties of the dark matter directly.

Supposing that the dark matter consists of a new fundamental particle, a

WIMP, that was in thermal equilibrium in the early universe, we have built an experiment to detect dark matter directly by elastic scattering with germanium or silicon nuclei. Our detectors are large (~ 200 g) calorimeters that can discriminate between interactions with the electrons, due to background photons and beta particles, and interactions with the nuclei, due to WIMPs and background neutrons. The detectors operate at low temperatures (~ 20 mK) in a specially constructed cryostat. To reduce the rate of background events to a manageable level, the detectors and cryostat have been constructed out of selected materials and properly shielded. This dissertation discusses the properties of the hypothetical WIMPs, the detectors, cryostat, and shielding system, and finally, the analysis methods.

To my partner, best friend, and wife

Heather Lynne Weidemann

Contents

Contents	iv
List of Figures and Tables	viii
Acknowledgements	x
1. Introduction	1
2. Dark Matter	5
2.1 Observational Evidence for Dark Matter	7
2.1.1 Determination of Ω_{Lum}	8
2.1.2 Rotation Curves of Galaxies	8
2.1.3 The Baryonic Dark Matter Problem	11
2.1.4 Determinations on Larger Scales	11
2.2 Theoretical Prejudice	13
2.3 Possible Solutions	14
2.3.1 Baryonic Dark Matter: MACHOs	15
2.3.2 Hot Dark Matter: light neutrinos	16
2.3.3 Cold Dark Matter: Axions	17
2.3.4 Cold Dark Matter: WIMPs	17
2.4 First Generation Experiments	21
3. CDMS Detectors	25
3.1 Why cryogenic?	26
3.2 Berkeley: NTD Germanium Thermistors on Germanium	27
3.2.1 Phonon Measurement	29
3.2.2 Ionization Measurement	34
3.2.3 Coupling Between the Phonon and Ionization Channels	36
3.3 Stanford: Tungsten Transition Edge Sensors	36
3.4 Electron / Nuclear Recoil Discrimination	40
3.4.1 Analysis of the Background Rejection Quality Factor	44
3.4.2 Calibration Methods	49
3.5 Large Mass Detectors	53
4. Backgrounds and Shielding	55
4.1 General Discussion	55
4.2 Cosmic Rays	57
4.2.1 Hadronic Component	57
4.2.2 Muons	59
4.3 Radioactive Contamination	62
4.3.1 Sources	62
4.3.2 Cosmogenics	64
4.3.3 Shielding	65

4.3.4	Cleanliness	66
4.4	Shield Design and Performance	67
4.5	Diagnosing the Measured Electron Recoil Background	71
5.	Cryostat	73
5.1	Major Design Issues	74
5.2	Overall Layout	78
5.3	Thermal Model	80
5.3.1	Thermal Conductivity: Microscopic Physics	81
5.3.2	Metals and the Wiedemann-Franz Law	82
5.3.3	Thermal Power Conduction: Macroscopic Modeling	85
5.3.4	Example: Cylinder with Distributed Power Input	86
5.3.5	Joints	87
5.3.6	Blackbody Radiation	88
5.3.7	Modeling Strategy for the Icebox	90
5.3.8	Results of the Model	93
5.4	Novel Non-Detector Features	95
5.4.1	Engineered Cryogenic Thermal Joints	96
5.4.2	Hinged Tails and Cold Finger Flex Section	99
5.4.3	Kevlar Loops and Spider Supports	103
5.4.4	Thermal Links in The Fridge and High Conductivity Copper Wire	109
5.4.5	Foil Seal Flanges	111
5.4.6	Future Improvements	112
5.5	Detector Towers	113
5.5.1	Tower Mechanical Design	114
5.5.2	Thermal Model for Wiring	118
5.5.3	Application to the Towers: Wiring Heat Loads	120
5.5.4	Heat sinking	121
5.5.5	Stripline	123
5.6	Monitoring System	129
5.6.1	Sensors	130
5.6.2	Wiring and Heat sinking	136
5.6.3	Future Hardware Improvements	137
5.6.4	Multiplexer	139
5.6.5	Software	143
5.7	Icebox Performance	147
6.	Analysis Methods	152
6.1	Analyzing Data with a Cut	154
6.1.1	Background Limited Experiments	156
6.1.2	Statistical Errors	157
6.1.3	Signal Model	158
6.1.4	Systematic Errors	159

6.2	Data Collection and Event Processing	161
6.3	Catalog of (Possibly) Useful Filters	164
6.3.1	Electron/Nuclear Recoil Discrimination	164
6.3.2	Multiple Scattering	165
6.3.3	Muon Veto Activity	166
6.3.4	Neutrons Unrelated to Muons	167
6.3.5	Cascade Decays	167
6.4	Energy Calibration and Detector Response	167
6.5	Theoretical Cross Sections	169
6.5.1	Axial Vector (Spin) Interactions	170
6.5.2	Scalar Interactions	171
6.5.3	Predictions of Minimal Supersymmetry	173
6.6	Expected WIMP Spectrum	175
6.7	Determining Sensitivity Limits	178
6.7.1	Including the Detector Response	178
6.7.2	Statistical Tests	179
6.7.3	Subtracting Measured Backgrounds	183
6.8	Expected Sensitivity of CDMS at Stanford	185
6.8.1	Rough Sensitivity Estimate for $m = 20 \text{ GeV}/c^2$	185
6.8.2	Detailed Sensitivity Estimate	186
6.9	The Future	188
Appendix A. Thermal Conductivity Functions		190
Appendix B. Where to Find Further Information about the Monitoring System		193
B.1	Icebox Procedures and General Information	193
B.1.1	Procedures	193
B.1.2	Data Forms	194
B.1.3	General Calibrations	194
B.2	Monitoring System	196
B.2.1	General	196
B.3	Cryogenic Wiring	197
B.3.1	Wiring to MUX	197
B.3.2	MUX I/O Panels	197
B.3.3	MUX	198
B.4	Schematics	198
B.4.1	Miscellaneous Schematics	198
B.4.2	Fridge Control	199
B.4.3	MUX Interface	199
B.4.4	MUX IV Boxes	199
B.4.5	Cables	200
B.4.6	LN Autofill	200

B.5	Sensor Information	200
B.5.1	Devices: Miscellaneous	200
B.5.2	RuO ₂ Sensors	201
B.5.3	Diode Sensors	201
B.5.4	Position Sensor Calibrations	201
References	202	

List of Figures and Tables

Figure 2.1.	Rotation Curve of the Milky Way.....	10
Figure 2.2.	Determinations of Ω vs. Length Scale.	14
Figure 2.3.	Current WIMP Event Rate Limits.	22
Figure 2.4.	Low Energy Spectrum from the Oroville Experiment.	23
Figure 3.1.	Schematic of the 60 g Berkeley Prototype Detector E5.....	28
Figure 3.2.	Phonon Spectrum in the Berkeley 60 g Detectors.	33
Figure 3.3.	Ionization Spectrum in the Berkeley 60 g Detectors.	35
Figure 3.4.	W/AI QET Sensor.	38
Figure 3.5.	Four channel W/AI QET detector.	39
Figure 3.6.	Response of the Berkeley 60 g Prototype to ^{241}Am	41
Figure 3.7.	Response of the Berkeley 60 g Prototype to ^{252}Cf and ^{241}Am	41
Figure 3.8.	Ionization Energy vs. Recoil Energy.	43
Figure 3.9.	Ionization Yield Distributions for $10\text{ keV} < E < 30\text{ keV}$	44
Figure 3.10.	Electron Recoil and Nuclear Recoil Response Functions.	46
Figure 3.11.	Signal and Background Acceptances.	47
Figure 3.12.	Background Rejection Quality Factor, Q	48
Figure 4.1.	Cross Section of the Stanford Underground Facility.	59
Figure 4.3.	Shield Design.	68
Figure 4.2.	Simulated Nuclear Recoil Spectrum in the Shield.	69
Figure 4.4.	Photon Spectrum Inside the Shield.	70
Figure 5.1.	Icebox Layout.	76
Figure 5.2.	Schematic of the Cryostat Motions During Cooldown.	79
Table 5.3.	Measured Values for h_{it}	90
Table 5.4.	Predictions of the Thermal Model.	94
Figure 5.5.	Sketch of Fiducial Locations in the Thermal Model.	94
Figure 5.6.	Vertical Cold Finger L-joint.	97
Figure 5.7.	Long Bolt Joint at the End of the Horizontal Cold Finger.	98
Figure 5.8.	Liquid Helium Tail Welded Bellows.	100
Figure 5.9.	Machined Tail Bellows.	100
Figure 5.10.	Horizontal Cold Finger Flex Section.	103
Table 5.11.	Maximum Mass Supported at Each Stage in the Cans.	104
Table 5.12.	Mechanical Properties of Various Hanger Materials.	106
Table 5.13.	Quality factor for Various Hanger Materials.	107
Figure 5.14.	E-stem Spider Supports.	108
Figure 5.15.	Detail of All Copper Foil Seal Flange.	111
Figure 5.16.	Schematic of the Detector Tower.	115
Table 5.17.	Heat Load Estimates for Seven Detector Towers.	120
Table 5.18.	Model Tower Heat Loads.	121
Table 5.19.	(PR) Values for Copper and Gold from 300 K to 9 K.	124
Table 5.20.	Stripline Heat Load Coefficients.	126

Figure 5.21.	Stripline Plan View.	127
Figure 5.22.	Stripline Section View.	127
Table 5.23.	Monitoring Sensors By Location and Type.	130
Figure 5.24.	Typical 4-Wire Resistance Measurement.	132
Table 5.25.	Thermometer Locations and Calibration Ranges.....	133
Figure 5.26.	Linear Potentiometer Measurement.	134
Figure 5.27.	Touch Sensor.....	135
Figure 5.28.	Multiplexed 4-wire Resistance Measurement.	140
Table 5.29.	Parameters for 4-Wire Resistance Measurements.	141
Table 5.30.	Logical MUX Configuration.....	142
Figure 5.31.	Physical MUX Configuration.	143
Table 5.32.	Actual Temperature Distributions in the Icebox.	148
Figure 5.32.	History of Stanford Cooldown.	151
Figure 6.1.	Event Rates for Cosmologically Interesting LSPs.	174
Figure 6.2.	Sensitivity Limits vs. WIMP mass and Energy Threshold.	188
Figure 6.3.	Current Limits, MSSM, and CDMS.	189
Table A.1.	Thermal Conductivity Values Used in the Thermal Model.	192

Acknowledgements

The physics involved in CDMS ranges from the very small (phonon and charge carrier properties in semi-conductors) to the very large (cosmology and the fate of the Universe) and it has attracted an equally broad range of talented physicists, technicians, and staff. I want to thank my many collaborators, most of whom are mentioned throughout the text, for working with me on such an exciting experiment. I am sure to have inadvertently omitted someone; I apologize in advance. I want to mention here V. Kuziminov and V. Novikov, and Mike Hennessy, who did yeoman work preparing the Stanford site for the cryostat and assisting with its installation.

I also want to thank my thesis committee, Lawrence Hall and Jack Welch, and Stuart Freedman, who participated in my Qualifying exam. Special thanks go to my advisor, Bernard Sadoulet, who has always struggled mightily to honor his students and staff despite the press of business. Bernard's vast knowledge of physics has always been available for the asking. Much of the astrophysics and critical scientific thinking I know has grown from talks with him. He is also one of the prime reasons that this group and the Center as a whole provide what Tom Shutt called "a human space for science."

One aspect of that humanity has been the staff, who are here for a million reasons, with the science down at the bottom of the list. They have graciously shared their own lives and interests with this community of "library dyslexics." I especially want to thank Rose Sergeant for her vision and organizing her professional life around relationships, not objectives; Rachel Winheld for her gentleness, determination, and quiet insight into life; Valerie MacLean for her art and too many kindnesses to mention; Mona Taylor for saving me from ignominious death by copier; Lynn Pelosi and Joseph Mattia for keeping the toys coming; and Abram Hardin for keeping a roof over our heads. The electronics shop and machine shop staffs are the most pleasant people to



work with. I especially want to thank Joe Weber for the breath of fresh air and time spent shooting the breeze. While writing this thesis I was deeply saddened by the untimely death of Andy Brocato. Andy didn't build the fridge or cryostat, but he modified both and built almost everything else that was installed in Room 87. He taught me half of what I know about design and machining. He could do things with an arc and stinger rod that mortals merely dreamed about. He always had time to talk about what he was building, his kids, his parents, politics, . . . In short, he was my friend.

My (surviving) friends have been fountains of support and love. I owe them a lifetime debt for ever broadening my horizons. At the top of the list is my wife, Heather Lynne Weidemann, to whom this thesis is dedicated. She has never wavered in her support and love, even when I was fed up with life and wanted to pump gas. My daughter Emily has completely erased any lingering doubts I might have had about life outside of physics. Tom Shutt and Krysta Wyatt are continual reminders that life can be better if it doesn't come out the way we planned. Tim Edberg is an inspiration for pursuing his dream and inspiring for sharing his photographs. Steve Weiss showed me the tools to pack in the *High Sierra* in style and by his vitality reminded me to live. Ann Parsons reminds us all of our wide-eyed fascination and enthusiasm with science. Jeff Wilkerson is never happier than sharing his amazing knowledge of the stars late at night. It is always a treat to have lunch with Paul Shestople and hear the surf report (real and virtual) from Storn White.

I also want to thank Dan Akerib for his steady encouragement, support, and leading the way; Tony Spadafora and Karl van Bibber for their encouragement as I finished this thesis; and Chris Stubbs for his mentoring and support.

It has been my privilege to know Heather Galloway. Being a very talented experimental physicist, and not to be outdone, she got so excited at seeing my newborn

daughter Emily that she went and had twins. She finally got tired of waiting for me to write and finished on her own, knowing that would spur me into action. I also want to thank Rick Haas for his quiet strength, and Austin and Haley for terrorizing Heather when I couldn't be there. When the Heathers weren't around to keep me in line, Angela Da Silva and Pat Augsburger did an admirable job. Ellen Saxe and Ronnie Karish have one of the warmest houses I know and continually express the most genuine concern for those around them and the world as a whole. Bea's excitement at seeing me and Max's lack of excitement are a nice welcome home.

Despite the help of all these friends, I certainly would have gone insane without Johnny and Rose Sergeant. Johnny's infectious energy has moved mountains of firewood, without his lifting a finger, and turns off like a light just when you are about to drop dead from exhaustion. Rose can be silly too, but when you need something else, she is there. I have never known someone to listen so carefully, and when I've had it up to as high as I can reach, there is Elk beckoning me home.

Finally, I want to thank my parents, Peter and Angela Barnes. They were my first teachers about life, love, and physics. I hope I've made you proud.

1. Introduction

The Standard Model of Cosmology is a basic picture of how our Universe has evolved since it was $\sim 10^{-2}$ seconds old.¹ Despite its simplicity, an isotropic homogeneous universe expanding from a hot big bang, it is able to explain most of what we see, from the abundances of the light elements, which were created in the first minutes, to the clustering of galaxies, which is still developing today. We have achieved this understanding in spite of our extremely poor determinations (by a physicist's standards) of most of the interesting parameters of the theory. In this business, a measurement to a factor of 2 is good work.

One of the fundamental parameters is the average energy density, which determines the overall "geometry," *i.e.* the fate of the Universe. Will it continue to expand forever? or slow nearly to a stop? or recollapse into a Big Crunch? We usually discuss the average energy density in terms of the density parameter, Ω , which we will define in Chapter 2. The dividing line between eternal expansion and eventual recollapse is stagnation, $\Omega = 1$. To determine Ω , typically people have tried to measure the mass or mass density in some volume, say a galaxy, then have extrapolated to the whole Universe assuming that they have measured a typical volume. The results have ranged from 10^{-4} –2, with the larger values coming from methods that average over a longer length scale. Even with our understanding of the past history, we can say almost nothing about the ultimate fate of the Universe.

We will discuss some of the determinations of Ω in Chapter 2. We can summarize by noting one glaring difficulty: the luminous material gives $\Omega \approx 0.002$, yet on length scales larger than about 10 kpc most of the mass is not luminous — it is not in stars, gas clouds, dust, or even black holes (which are not luminous, of course).

The gap between the density of luminous material and the density inferred on larger scales is the dark matter problem, which we can pose as two specific questions.

The determinations on galaxy scales are consistent with what we expect from the light element abundances: $\Omega_b \approx 0.03$ for the baryons alone. So the baryonic dark matter question is *where are all the baryons?*

Essentially all determinations of Ω on scales larger than a galaxy give even larger Ω values, 0.08 and up. The apparent fact that the average density on the largest scales exceeds the density of baryons is the non-baryonic dark matter problem, so the second question becomes *what is the non-baryonic dark matter?*

In Chapter 2 we will briefly discuss the possible nature of the (non-)baryonic dark matter. One possible solution to the non-baryonic dark matter problem is to hypothesize the existence a new fundamental particle which was in thermal equilibrium in the early universe and whose relic abundance today supplies the missing mass. To have these properties, such a particle would have a mass in the $\text{GeV}/c^2 - \text{TeV}/c^2$ range, and an elastic scattering cross section similar to Weak interaction cross sections, as if physics at the Weak scale was also responsible for the dark matter. Because of these two properties, this class of particles has been dubbed "WIMPs," Weakly Interacting Massive Particles.

These particles, if they exist, would fill the halo of our Galaxy with an isothermal distribution and velocities characteristic of the halo, ~ 300 km/s. The dark mass density required in the solar neighborhood is $0.3 (\text{GeV}/c^2)/\text{cm}^3$.[†] This density made of $20 \text{ GeV}/c^2$ WIMPs with a 10 pb elastic scattering cross section would have a scattering rate of order $200/A$ per day per kilogram of material with mass number A .[‡] For atoms much heavier than this $20 \text{ GeV}/c^2$ WIMP, the mean energy deposition is of order $(400/A)$ keV. It might actually be possible to detect these elastic scatters if we can

[†] For scale, the dark mass interior to Pluto's radius is $\sim 10^{-5}$ of Pluto's mass itself. This is more an indication of the size of the solar system compared to the Galaxy, than of the size of the dark matter density itself. In the sphere that extends halfway to the nearest star, the dark matter amounts to ten times the mass of Jupiter, or 0.9% of the mass of the Sun.

[‡] By contrast, a WIMP orbiting the Galaxy at our distance from the center has integrated $\sim 10^{11} \text{ pb}^{-1}$ luminosity in passing through the $0.1 M_\odot/\text{pc}^3$ of the Galactic disk in the age of the Galaxy.

construct a large mass detector, to get a sufficient number of events, with a very low energy threshold, of order 1 keV.

This dissertation will discuss the development and construction of the Cryogenic Dark Matter Search (CDMS), an experiment to detect WIMP dark matter in the Galaxy by just these elastic scatters.

A detector sensitive to such small energy depositions will typically have to have a correspondingly good energy resolution, hence one set of experimental programs has focused on semi-conductor ionization detectors, high purity germanium detectors in particular. Over the last eight years six different germanium experiments have reported no signal down to 10–20 events/(kg day) for WIMP masses from $20 \text{ GeV}/c^2$ – $5 \text{ TeV}/c^2$. These experiments have all run into seemingly irreducible backgrounds due to photons and electrons (beta decays). We will summarize the experimental situation in Chapter 2.

Note that the dominant backgrounds have been from interactions with the electrons in the detectors, whereas, for reasons we will discuss in §2.3.4, the WIMP signal is from nuclear scattering. We have developed cryogenic semi-conductor detectors that allow us to discriminate between electron and nuclear recoils, thereby rejecting the dominant background and increasing the sensitivity to WIMPs by roughly a factor of 40. The detectors measure the total energy deposition with a thermal sensor. Our collaboration has developed two kinds of thermal sensors: NTD germanium thermistors, and tungsten superconducting transition edge sensors. The phonon measurement in combination with an ionization measurement provides enough information to discriminate between electron recoils and nuclear recoils. These detectors will be the subject of Chapter 3.

To be able to measure the low count rates expected, these detectors have to be operated underground, in our case at Stanford University, in an extremely low

background environment, discussed in Chapter 4. The detectors are mounted inside a specially constructed cryostat, the subject of Chapter 5. We will finish by discussing the analysis methods and estimating the sensitivity of this experiment to WIMP dark matter.

At this writing (May 1996), the cryostat and shield have been built and tested. We have almost finished testing the first generation electronics with a 60 g prototype detector, which we expect to install in the cryostat in the coming months to take the first data. We are also designing more sophisticated electronics that will allow more automated calibration, which will be necessary to operate the six detector array, 170 g each, currently under construction. If all goes well we should be reporting a significant improvement in sensitivity in about one year's time.

An actual detection of WIMP scattering events would be a staggering achievement. It would elucidate the nature of 90% of the Universe and point to physics beyond the Standard Particle Model. It is somewhat humbling, however, to realize that any WIMP event we see will be the first (and last) non-gravitational interaction of that particle since it last scattered in the very early universe.

2. Dark Matter

The dark matter problem (two problems, actually) refers to the gap between the density of material observed in the Universe by the radiation it emits, Ω_{lum} , and the density we infer from (a) the concordance between the observed light element abundances and big bang nucleosynthesis calculations, Ω_B , and (b) dynamical determinations of the density. We will start with a very terse summary of the standard model of cosmology. Then we will discuss various ways of measuring Ω , as well as our theoretical expectations. We will see the two discrepancies between observations and theory noted above, and discuss possible solutions. Finally, focusing on one class of possible solutions, WIMPs, we will summarize the current status of WIMP search experiments and their limitations.

Our standard model in cosmology, the hot big bang model,¹ consists of an isotropic and homogeneous Universe expanding according to Einstein's theory of general relativity. The expansion is demonstrated by Hubble's law, which expresses that galaxies are observed to be receding from us, with the recession velocity proportional to the distance to the galaxy. The proportionality constant, H_0 , is somewhat uncertain, due to the difficulty in measuring distances; we parametrize our ignorance with "little h :" $H_0 = 100 \text{ (km/s)/Mpc} \times h$, with h in the range 0.5–1. The range is so broad in part because a variety of measurements tend to give values clustered near one end or the other, though there is some recent movement to accept an intermediate value, $h = 0.75$;² we will use this value throughout this dissertation. The best evidence for isotropy and homogeneity is the cosmic microwave background radiation (CMBR), which has anisotropy $< 10^{-4}$ on angular scales from 10 arc seconds to 180° . Anisotropic expansion or inhomogeneities at the last scattering surface would lead to similar sized anisotropy in the CMBR.

The isotropy and homogeneity conditions reduce the full Einstein equations to the Friedmann equation, which has two free parameters, the spatial curvature, $k = \pm 1, 0$, independent of time, and one parameter that changes as the Universe evolves with time, which can be taken as the average energy density, ρ , the scale factor, R , or, the choice we will make, the logarithmic derivative of the scale factor, which is the Hubble parameter, $H \equiv \dot{R}/R$. (Generally subscript 0 indicates the value today; the value for H_0 given above is the *current* value of H .) The spatial curvature only enters the Friedmann equation as k/R^2 , so we are free to rescale R such that k is restricted to one of the three values shown.

Given k and the value of H at a given time, the entire evolution of the Universe is determined. It evolves in one of three ways, according to the value of k : an "open" Universe, $k = -1$, expands forever ($H > 0$, $R \rightarrow \infty$ as $t \rightarrow \infty$); a "closed" Universe, $k = +1$, eventually recollapses ($H < 0$, $R \rightarrow 0$ as $t \rightarrow \infty$); a "flat" or "critical" Universe, $k = 0$, expands forever, but just barely ($H \rightarrow 0$, $R \rightarrow \infty$ as $t \rightarrow \infty$).

The Hubble parameter represents the velocity of the expansion (divided by the scale factor). The corresponding critical energy density that is just sufficient to give a critical Universe is:

$$\rho_c = \frac{3H^2}{8\pi G}, \quad (2.1)$$

where G is Newton's constant of gravitation. Given the uncertainty in H , the value of the critical density is $10.5h^2$ (keV/c²)/cm³. The ratio of the actual energy density, ρ , to the critical density is called the density parameter, Ω ; this is effectively the absolute value of the gravitational potential energy divided by the kinetic energy of the expansion. In terms of Ω , the Friedmann equation becomes

$$\frac{k}{H^2 R^2} = \Omega - 1. \quad (2.2)$$

The sign of the left-hand side is determined solely by k , so the geometry is reflected in the value of Ω : $\Omega > 1$ is closed because the gravitational energy exceeds the kinetic energy (the Universe is bound, in some sense), $\Omega = 1$ is flat because the energies are just equal (the Universe is asymptotically free), and $\Omega < 1$ is open because the kinetic energy exceeds the gravitational energy (the Universe is unbound).

In computing the fraction of critical density contributed by any species, we can remove the uncertainty due to h by expressing the result in terms of Ωh^2 . By examining the age of the Universe as a function of Ω and H , we can derive a useful constraint on this quantity: $\Omega h^2 \leq 1$, for $h \geq 0.4$ and the age of the Universe ≥ 10 Gyr.¹

2.1 Observational Evidence for Dark Matter

It is clear that Ω is an important cosmological parameter, so naturally there have been many attempts to measure it by either (a) studying the velocities of objects in galaxies, galaxy clusters, or large scale velocities or velocity flows, or (b) using other methods such as gravitational lensing, the light element abundances, or global geometry measures. One convenient metric used for the smaller objects is the mass to light ratio, Υ , usually expressed in solar units, $\Upsilon_{\odot} = 1.50 \times 10^{13}$ years ($c = 1$). This can be converted into a density by multiplying by the average luminosity density in the Universe, $\bar{\epsilon} = 1.73h \times 10^8 L_{\odot}/\text{Mpc}^3$,³⁻⁵ or directly into Ω by dividing by the critical mass to light ratio, $\Upsilon_c = 1600h \Upsilon_{\odot} \approx 1200 \Upsilon_{\odot}$.

Methods based on velocity measurements are often called dynamical methods since they use the motions of constituent objects as test particles to trace out the gravitational potential of the parent. In spiral galaxy disks, the velocities of stars perpendicular to the plane measures the surface mass density in the disk, assuming that the stars really are bound to the disk. The rotational velocity of the stars and gas indicates the total mass as a function of radius. The velocity dispersions in elliptical

galaxies or galaxy clusters similarly indicate the mass distribution. The temperature and luminosity of hot X-ray emitting gas in clusters is another dynamical tracer. These observations are interpreted by applying either some form of the virial theorem to relate the observed kinetic energy (equivalently the X-ray gas pressure) to the gravitational potential energy, or by equating the gravitational acceleration to the centripetal acceleration. We will briefly discuss these measurements and summarize our knowledge of Ω .

2.1.1 Determination of Ω_{Lum}

Given that the sun is a rather typical star, we might expect the luminous matter to give $\Upsilon \approx \Upsilon_{\odot}$ and $\Omega_{Lum} \approx 8 \times 10^{-4}$. In fact, the velocities of nearby stars indicate $\Upsilon \approx 3 \Upsilon_{\odot}$,^{6,7} hence $\Omega \approx 0.002$ in the solar neighborhood. The additional mass is made up of numerous low mass/low luminosity stars, gas, and dust, with a small contribution from the dark Galactic halo (discussed below).

From stellar modeling we can deduce the mass to light ratio for any given model star. Using the measured stellar luminosity function (the number density of stars of a given absolute luminosity in the Galactic plane), we can compute the luminosity function weighted average mass to light ratio. The luminosity function more or less flattens out for stars fainter than $M_V \approx 5$ at $\sim 10^{-2}$ stars/pc³ per unit absolute visual magnitude. Since the luminosity goes roughly as M^3 ,⁸ these are all low mass stars with very large mass to light ratios. The resulting average, dominated by stars fainter than about $M_V \approx 10$, is $\Upsilon \approx 19.3 \Upsilon_{\odot}$ and $\Omega \approx 0.016$.

2.1.2 Rotation Curves of Galaxies

Spiral galaxies observed edge on are seen to rotate about their centers. The circular speed as a function of distance from the galactic center is called the rotation

curve. Using the 21 cm line in atomic hydrogen, some rotation curves have been measured as far as 100 kpc from the galactic center, far beyond the extent of most of the luminous matter. Equating the gravitational acceleration on the H I at a radius r , caused by the (spherically distributed) mass $M(r)$ interior to r , to its centripetal acceleration, we have

$$\frac{GM(r)}{r^2} = \frac{v^2}{r}, \quad (2.3)$$

where v is the measured circular velocity. In the midst of the galaxy, we expect $M(r)$ to rise with radius as more of the galaxy is included, so we have no expectation for the trend in v . Beyond the extent of the galaxy, $M(r)$ no longer increases, so we expect the velocity to fall as $r^{-1/2}$; this has been seen in only a handful of dwarf galaxies. Essentially all rotation curves show flat or slightly increasing velocities out to the largest radii measured. This means that we have not seen the edge and don't know the total mass (from the rotation curve) for most spiral galaxies!

Figure 2.1 shows the rotation curve of the Milky Way,⁹ measured interior to the solar radius by the tangent point method^{10,11} and exterior to the solar radius by the using the angular thickness of the H I layer.⁹

From face-on spirals we know that the luminosity of the disk falls roughly exponentially with radius, with a scale length of a *few*–10 kpc. In the Milky Way, the thickness of the H I layer implies a scale length of 4 kpc.⁹ If we assume that the mass to light ratios of a few Υ_{\odot} measured in the interiors of spiral galaxies are typical for all regions of the disks (*e.g.*, light uniformly traces mass), then the exponential fall of disk luminosities with galactocentric distance implies that the rotation curve should fall with r . The fact that the rotation curves are flat means that an increasing fraction of the total galactic mass density is dark. If we try to model the rotation curve, we find that the observed stellar and gas components can not account for the rotation in both the inner

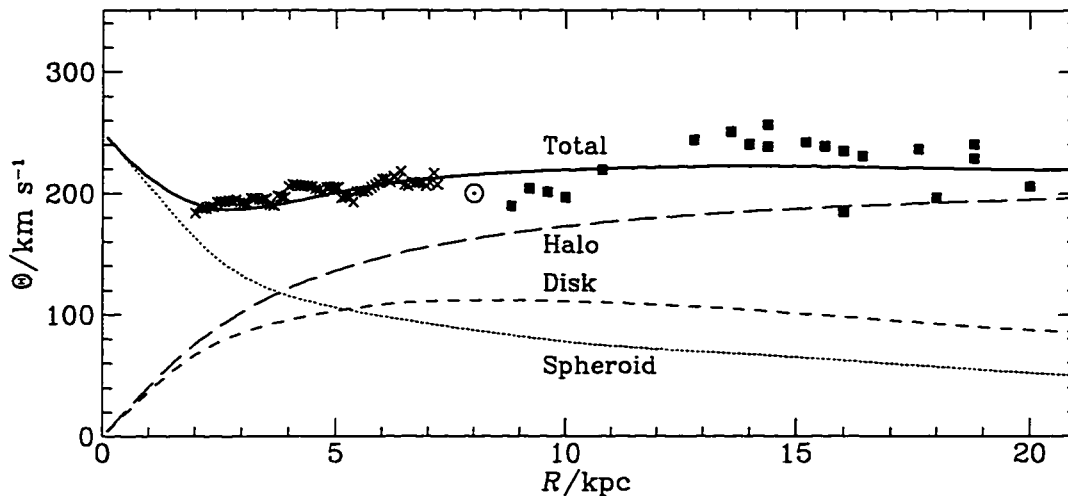


Figure 2.1. Rotation Curve of the Milky Way.

The rotation curve of the Milky Way,⁹ determined interior to the solar radius using the tangent point method (×) and exterior to the solar radius using the angular thickness of the H I layer (■). The sun is indicated by the symbol ⊙ at $R = 8$ kpc. The curves show the contributions to the total rotation velocity (heavy solid curve) due to the stellar spheroid (dotted curve), the luminous disk (short dashed curve), and the dark halo (long dashed curve).

and outer regions of the galaxy. The stellar components are modeled as an exponential disk, with a scale length \sim few–10 kpc, and a spheroidal distribution, as evidenced by the globular clusters, with a similar exponential scale length.^{10, 12} However, if we include a dark halo with a spherical distribution, we can obtain reasonable fits to the whole rotation curve.

The results of such a fit to the Milky Way rotation curve are also shown in Figure 2.1. The curves show the contribution of each component to the rotation velocity, as well as the total rotation curve from the model. (Since the additive quantity in Eq. (2.3) is the mass, the rotation velocities add in quadrature.)

By examining a variety of constraints on the Milky Way, we can infer a likely range of dark matter densities in the solar neighborhood of $\rho_{DM,\odot} \approx 0.2$ – 0.4 (GeV/ c^2)/cm³.¹³ This is the density of dark matter that we are sensitive to in CDMS.

Since the $r^{-1/2}$ fall is not seen, the rotation curves give lower limits to the total mass of galaxies. If we assume that the dark halos do not continue much past the measured rotation curves (though the relative velocities of galaxy pairs or satellite galaxies suggest that the halos extend to 100 kpc or beyond¹⁴⁻¹⁶), we infer mass to light ratios of $10\text{--}50 \Upsilon_{\odot}$ and $\Omega \approx 0.01\text{--}0.04$ for entire galaxies.

Elliptical galaxies are not supported by angular momentum, so the stars do not predominantly follow circular orbits. However, the velocity dispersion as a function of radius can be determined from a specific density model and the observed absorption-line profile.¹⁷ The gravitational potential can then be inferred using the virial theorem or equivalents.⁵ Globular cluster velocities and the temperature of X-ray emitting gas have also been used to map the potential. The resulting mass to light ratios are similar, though more uncertain, than obtained from spiral galaxies.¹⁸

2.1.3 The Baryonic Dark Matter Problem

A completely different approach is to compare the observed abundances of the light elements ($A < 8$) with the abundances expected to result from nucleosynthesis in the big bang (BBN).¹ A key parameter in the theoretical models is the baryon to photon ratio, η . There is excellent agreement between the observations and theory if $2.5 < \eta \times 10^{10} < 6$,¹⁹ which corresponds to $\Omega_{BBN} \approx 0.016\text{--}0.04$ using the photon number density determined from the CMBR. The baryon density inferred from BBN and the light element abundances also exceeds the density of luminous material. This discrepancy is called the baryonic dark matter problem.

2.1.4 Determinations on Larger Scales

Virial theorem arguments can also be applied to velocity dispersions in galaxy groups and clusters. For example, the mass to light ratio inferred from the velocity

dispersion in the Coma cluster is $300 \Upsilon_{\odot}$.⁵ If Coma is typical, then $\Omega \approx 0.25$. Coma also contains a significant quantity of hot X-ray emitting gas. Assuming that the pressure gradient is due to the increasing gravitational potential, similar values are obtained for the total cluster mass.²⁰⁻²²

We can apply a different argument within the local group (dominated by the Milky Way and Andromeda) or between the local group and the Virgo cluster: in both cases, the observed relative velocities are different than what we would expect from the Hubble flow. By equating the peculiar velocity to *acceleration* \times *time*, we can estimate the total mass responsible for the peculiar velocity. For the local group one obtains $\Omega \approx 0.08$; for the Virgo infall, $\Omega \approx 0.2$.

On scales ~ 100 Mpc, there are deviations from the Hubble flow amounting to *few* $\times 10^2$ km/s. By assuming that the fluctuations in the number density of galaxies are proportional to the fluctuations in the mass density, we can apply linear perturbation theory to work out the expected peculiar velocity flows from the observed distribution of galaxies from the IRAS survey, for example. This approach gives reasonable agreement over the 100 Mpc distance sampled by the survey.²³ With a reasonable range for the proportionality constant, this method suggests Ω in the range 0.4–1.3.

Finally, we have the "geometrical" tests. These are based on the expectation that the number density of an object per unit comoving volume should not evolve with time except by evolution of the objects themselves. Therefore, the number of objects observed per unit solid angle per unit red shift is a measure of the evolution of the comoving volume element, and hence the global geometry and Ω . This method has been attempted with radio galaxies and then optical galaxies, but by measuring the number as a function of luminosity, not red shift.²⁴ Because the luminosity of these objects evolves with time, the luminosity alone is not a good distance indicator. More recently, Loh and Spillar measured the number vs. red shift and obtained $\Omega = 0.9^{+0.7}_{-0.5}$,²⁵

but their measurements have been critiqued on numerous grounds.^{26–28} New efforts (*e.g.*, the DEEP project) are currently underway to obtain a very large number of spectroscopic red shifts for faint galaxies and thereby measure the geometry directly. Instead of counting faint galaxies, one can search for high red shift supernovae; this is being pursued as well.

2.2 Theoretical Prejudice

On the theoretical side, there is definite prejudice that $\Omega = 1$. Since the quantity $|\Omega - 1|$ grows with time, whereas $\Omega = 1$ does not evolve, it seems unlikely that we should be around just at the time when Ω first starts to differ significantly from unity (the temporal Copernican principle⁵). A second theoretical argument arises from a particular model: inflation. In the simplest picture of the expansion of the early Universe the most distant regions observable today are just coming into causal contact for the first time, yet the Universe on these scales is very homogeneous and isotropic. One way around this seeming discrepancy is to suppose that there was an early epoch when the scale factor grew exponentially, inflating a single causally connected region to a size much larger than the currently observable Universe. The inflation of the scale factor drives $\Omega \rightarrow 1$ (see Eq. (2.2)).

So what can we say about the average density in the Universe? Figure 2.2 shows the results of the various determinations of Ω , as a function of the length scale sampled by the method. First we see that the local dynamics of stars requires more mass than the stars that produce the observed luminosity. The dynamics of whole galaxies require even more mass, in accord with our expectations from big bang nucleosynthesis and the observed light element abundances. That seems not to be the whole story, however, since the dynamics on the largest scales implies values for Ω that

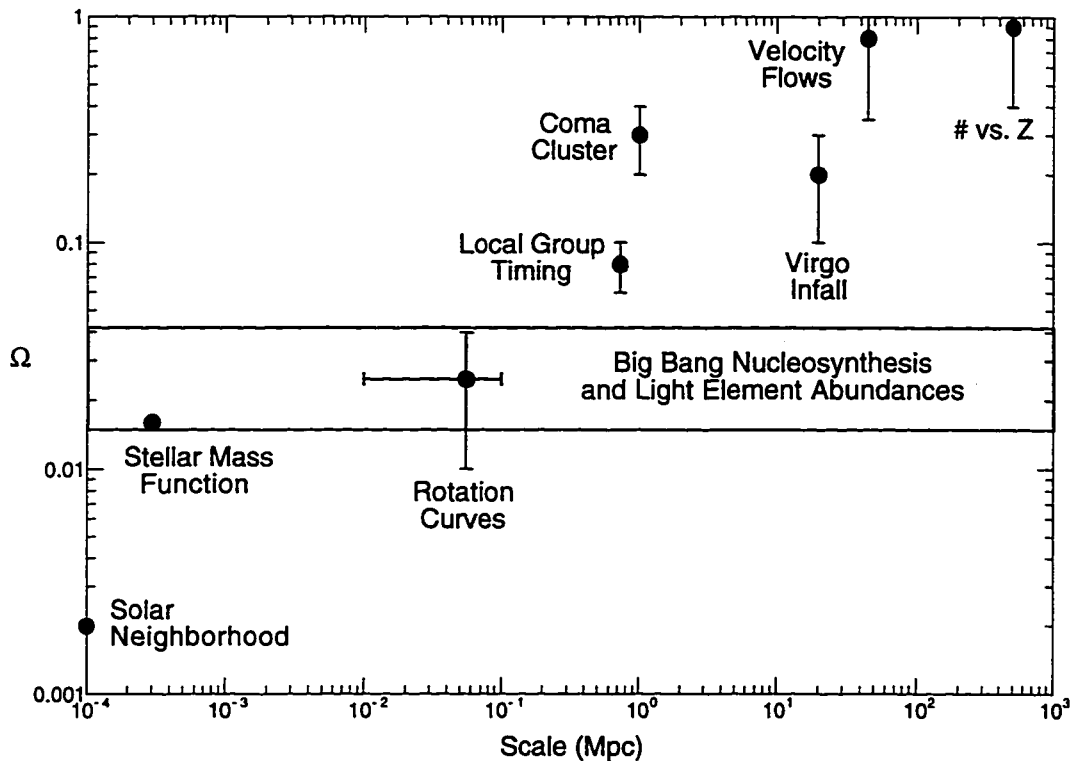


Figure 2.2. Determinations of Ω vs. Length Scale.

Results of the determinations of Ω discussed in the text as a function of the length scale sampled by the method, assuming $h = 0.75$. The light element abundance determinations come from individual stars; the resulting big bang nucleosynthesis limits use the all sky value of the cosmic background radiation temperature to measure the photon number density, hence the BBN determination has no single averaging scale.

exceed the BBN prediction, and at the largest scales we obtain values that are consistent with $\Omega = 1$.

2.3 Possible Solutions

From Figure 2.2 it is clear that we have a baryonic dark matter problem, and probably have a non-baryonic dark matter problem as well. We will discuss the most plausible explanation for the baryonic dark matter, since it has implications for this experiment, then go on to discuss the possible solutions to the non-baryonic dark matter problem.

2.3.1 Baryonic Dark Matter: MACHOs

Where are the missing baryons? The IRAS survey places strong limits on the quantity of dust in galaxies, since the dust would absorb starlight and radiate in the infrared. Cold atomic hydrogen would show up in radio maps at 21 cm, and molecular hydrogen would lead to absorption lines in quasars, both of which are constrained too low to account for the missing baryons. Clumped hot gas would emit X-rays, while diffuse hot gas would distort the CMBR spectrum due to Compton scattering. About the only viable possibility left is MACHOs, massive compact halo objects. These are either sub-stellar brown-dwarf objects, like Jupiter, that do not have enough mass ($M < 0.08 M_{\odot}$) to start hydrogen burning and become stars, or they are very old stellar remnants, white dwarves, but these would have to have lived and died without leaving any of the usual interstellar signatures (metal rich gas, supernova remnants), or they are black holes.

Following Paczynski's suggestion,²⁹ several groups have mounted observational efforts to detect MACHOs by microlensing.³⁰⁻³² The observers measure the luminosity of $\sim 10^6$ stars in the Large Magellanic Cloud each night. A MACHO passing near the line of sight causes an amplification of the apparent luminosity due to gravitational lensing. The data are examined in terms of the "spherical cow"³³ halo: an isothermal sphere distribution of identical mass MACHOs that accounts for the Galactic rotation curve. At the moment, these measurements are moderately sensitive to the mass of the MACHOs, assuming they all have the same mass. Because the distance to the lens objects is not known, however, the measurements are fairly insensitive to the fraction of the halo that is made up of MACHOs.

The interpretation depends strongly on the assumed properties of the halo between us and the LMC, *i.e.*, out of the Galactic plane at a distance of ~ 30 kpc. The halo is very poorly constrained out of the plane because of the lack of objects to trace

the gravitational potential. Because of the great uncertainties in Galactic formation and structure, it is possible to construct a wide variety of models with significantly different structure all consistent with the observations.^{34–36} At this point it seems safer to take the microlensing observations, including observations through the disk of the Galaxy to the Galactic center, as constraints on models for the Milky Way, instead of definite identification of the make up of the dark halo.

2.3.2 Hot Dark Matter: light neutrinos

Turning now to the non-baryonic dark matter, we will not discuss two dark matter "mimics":¹⁸ scale dependent constant of gravitation (non-Newtonian gravity), and a cosmological constant. We will focus on the "matter" solutions, all of which require new fundamental particles or new properties for existing particles. One way to characterize the cosmological consequences of a new particle is to ask what effects it has at the time when galaxies are starting to form. If the particle is relativistic (hot dark matter), it can free stream out of protogalaxy overdensities, thereby reducing the density contrast and delaying the onset of structure formation, which eventually starts on larger scales. Particles non-relativistic at the time of galaxy formation (cold dark matter) can start structure growth even before the baryons, leading to enhanced small scale structure.

For example, suppose that one (or more) of the known flavors of neutrinos had a small rest mass. Since their interactions are known at the energy scales where they decouple from the plasma, we can accurately compute their relic abundance today, $112 \pm 1 \text{ cm}^{-3}$. Therefore a 50 eV rest mass (or sum of rest masses) would give $\Omega = 1$.

2.3.3 Cold Dark Matter: Axions

The cold dark matter candidates are either WIMPs or axions. The axions would be the relic particles resulting from the decay of an axion field responsible for the absence of significant CP violating reactions. The axions would have a very small mass, $\sim 10^{-6}$ eV, but because they come from the decay of a zero momentum condensate, they behave like cold dark matter. (The axion is an example of a non-thermal relic: a relic particle that was never in thermal equilibrium with the rest of the Universe.)

2.3.4 Cold Dark Matter: WIMPs

The other major class of cold dark matter candidates are called WIMPs: weakly interacting massive particles, which we will denote by the symbol χ . These are hypothetical new particles that were in thermal equilibrium in the early Universe. Since they were in equilibrium, their relic abundance today is determined by the thermally averaged annihilation cross section, $\langle\sigma_A v\rangle$, at freeze out, when the WIMP number density dropped out of equilibrium with the rest of the plasma. A large cross section causes more of the WIMPs to annihilate, resulting in a smaller relic abundance. We can estimate the contribution to Ω from

$$\Omega_\chi h^2 \approx \frac{10 \text{ pb}}{\langle\sigma_A v\rangle}, \quad (2.4)$$

where we have taken $c = 1$. The cross section required to give $\Omega \sim 1$ comes from the statistics of freeze out in the standard cosmology. The fact that the cross section is of order typical Weak interaction cross sections is perhaps a hint that physics at the Weak scale is also responsible for dark matter.

In the context of a specific model, the annihilation cross section and relic abundance can be calculated. For example, a heavy Dirac neutrino with standard

electroweak coupling must have $m_\nu \geq 1.8 \text{ GeV}/c^2$ to have $\Omega h^2 \leq 1$ (the so-called Lee-Weinberg bound³⁷⁻⁴⁰).

On the one hand, a new WIMP particle should be incorporated into a more complete particle physics model without coming into conflict with the known particle physics phenomenology. On the other hand, extensions to the Standard Model of particle physics generically predict new particles to solve a number of problems with the Model (*e.g.*, the fine tuning and hierarchy problems, see Haber and Kane⁴¹ for an introduction) that crop up near the Weak scale, $\sim \text{TeV}$. Many of these new particles can have the right properties to be WIMP dark matter. Supersymmetric (SUSY) models represent the largest single class of extensions to the Standard Model. In supersymmetry each Standard Model particle is associated with superpartners with the same number of degrees of freedom (*i.e.*, a standard spin-1/2 fermion has two spin-0 superpartners). There is a new conserved discrete quantum number, R -parity, which is +1 for standard particles and -1 for superpartners. R -parity is conserved in most models, to avoid baryon and lepton violating processes at low energy. Therefore the lightest superpartner (LSP) is stable, since there is no lower energy $R = -1$ particle to decay into, making the LSP a prime WIMP candidate. The most likely LSP is generically called the neutralino, which could be a mixture of the superpartners of the photon, Z^0 , and the neutral Higgs bosons. At one time, the superpartner to the neutrinos, the sneutrino, was also a possibility, but a cosmologically viable one would have a cross section twice the Dirac neutrino cross section, and has been ruled out by the direct detection experiments described below.⁴² For a review of supersymmetric dark matter see Jungman, *et al.*⁴³

After the WIMPs freeze out, they generally cease to interact with the remainder of the particles that are in thermal equilibrium, except by gravity. (They must be neutral, or we would detect them by their interactions with photons today.) Even if the

WIMPs are responsible for only a fraction of $\Omega = 1$, they will still be accreted by galaxies and form a fraction of the dark halo. We would expect them to have velocity and space distributions characteristic of the visible objects (*i.e.*, globular clusters) in halos, namely a non-rotating isotropic Maxwellian velocity distribution with mean velocity $\bar{v} = (250 \pm 25)$ km/s and an isothermal sphere space distribution. (These are roughly steady state self-consistent distributions.¹⁰⁾

The WIMPs were once in thermal equilibrium via the reactions $\chi\bar{\chi} \leftrightarrow q\bar{q}, l\bar{l}$, where q and l are the standard quarks and leptons. By crossing the annihilation channels to the u , and d , (and s) quarks and the electrons we should expect a non-zero elastic scattering cross section with a detector. Because the WIMPs are extremely non-relativistic, the tensor and vector currents take the same form as the scalar interaction, and the axial vector interaction reduces to a coupling between the WIMP spin and the nuclear spin. If the cross section is dominated by axial vector interactions, a target with nuclear spin is required. In most SUSY models, however, the axial vector interactions are very small, so second order (scalar) interactions usually dominate.^{43,44}

Therefore we should look for elastic scattering by a number density of up to $0.3 (\text{GeV}/c^2)/\text{cm}^3 \times (m/\text{GeV}/c^2)^{-1}$ of WIMPs with mass m and velocities ~ 250 km/s in the solar neighborhood. The resulting event rate per unit detector mass is roughly

$$R_0 = \frac{\rho_{DM,\odot}}{m} \sigma \bar{v} \frac{1}{M}, \quad (2.5)$$

where $\rho_{DM,\odot} = 0.3 \text{ GeV}/\text{cm}^3$ is the local density of the dark halo, made up of particles of mass m , σ is the elastic scattering cross section per atom, \bar{v} is the relative velocity, and M is the target atom mass, sometimes written A/N_0 , where N_0 is Avogadro's number and A is the mass number of the target nucleus, which is approximately the number of grams per mole. The M^{-1} factor converts from a rate per target atom to a rate per target mass. For a 10 GeV WIMP with a 10 pb cross section scattering in germanium, we

estimate $R_0 = 5.3$ events/(kg day). To detect this small rate we need large mass detectors with very low background rates.

As we will discuss in Chapter 6, the Maxwellian velocity distribution leads to an energy deposition spectrum with the approximate form

$$\frac{dR}{dE} = \frac{R_0}{E_0} e^{-E/E_0}, \quad (2.6)$$

where E is the energy deposition and the mean energy deposition is of order

$$E_0 = \frac{\pi \mu^2}{2 M} \bar{v}^2 \quad (2.7)$$

where the reduced mass is $\mu = mM/(m + M)$. For $m \ll M$, this is approximately $1.08 \text{ keV} \times (m/(\text{GeV}/c^2))^2/A$. For $M \ll m$, E_0 becomes $A \times \text{keV}$ (though a form factor usually limits the effective energy scale E_f to the coherence energy, E_{coh} , see below). For the same WIMP mass as above scattering in germanium, $E_0 = 1.2 \text{ keV}$; the coherence energy is $E_{coh} = 50 \text{ keV}$. To be sensitive to the small energy depositions the large mass detectors must also have a very low threshold.

In the discussion above, we have focused on the properties of WIMP-nucleus scattering and neglected the electrons in the detector for two reasons. The first reason to ignore WIMP-electron scattering, which applies to all WIMP models, is the much smaller energy depositions. For $m \sim m_N \sim 1 \text{ GeV}/c^2$, (m_N is the nucleon mass), the electron recoil energy is reduced by $\sim 2000/A$ compared to the nuclear recoil energy. For $m \ll M$, the factor becomes $\sim 2000 \times A$. Second, at the low relative velocities involved, WIMPs whose cross section is dominated by scalar coupling (this includes most SUSY LSPs, but excludes models dominated by axial vector interactions) will generally scatter coherently from the nucleus as a whole, so the cross section is enhanced by a factor of A^2 (or N^2 or Z^2 , depending on the details of the model). This enhancement is reduced for large momentum transfers by a form factor, not shown above. There is no coherence for electron scattering since the electron clouds are so

large. (The coherence energy, the characteristic energy deposition where coherence loss becomes important, is reduced by $\sim 10^5$.) Therefore the rate per target mass for WIMP-nucleus scattering will be a factor of $\sim A^2/Z$ larger than for WIMP-electron scattering.

2.4 First Generation Experiments

The first generation of WIMP dark matter experiments were originally designed to search for neutrinoless double beta decay in ^{73}Ge .⁴⁵⁻⁴⁹ They consisted of kilogram scale high purity germanium (HPGe) detectors operated at 77 K. After modifications to lower the energy threshold and reduce the low energy backgrounds, they obtained the total WIMP event rate limits shown in Figure 2.3. In particular, these experiments have ruled out millicharged shadow matter,⁴⁵ cosmions,⁵⁰ massive Dirac neutrinos with standard electroweak coupling,^{45-49, 51} magninos,⁴⁵ other heavy neutrinos,⁴⁵ neutral technibaryons^{45, 46} and sneutrinos.^{42, 45, 46} In addition, the most sensitive disappearance limits on the stability of the electron are set by these experiments by looking for the K-shell X-ray when a 1s electron decays.⁴⁹

We can understand the origins of the boundaries in Figure 2.3 by looking at the low energy spectrum measured in a typical experiment. Figure 2.4 show the spectrum obtained in the Oroville experiment; the other experiments have similar performance. At low energies it is dominated by a handful of X-ray lines and tritium beta decay from cosmogenic activity in the detectors and surrounding materials. We can recast the mean energy in Eq. (2.7) for germanium targets and light WIMPs as

A new wrinkle is that nuclear recoils, from WIMP scattering, are approximately 1/3 as ionizing as electron recoils of the same total energy. The measured spectrum is usually calibrated from known X-ray or gamma ray lines. The signal is converted to

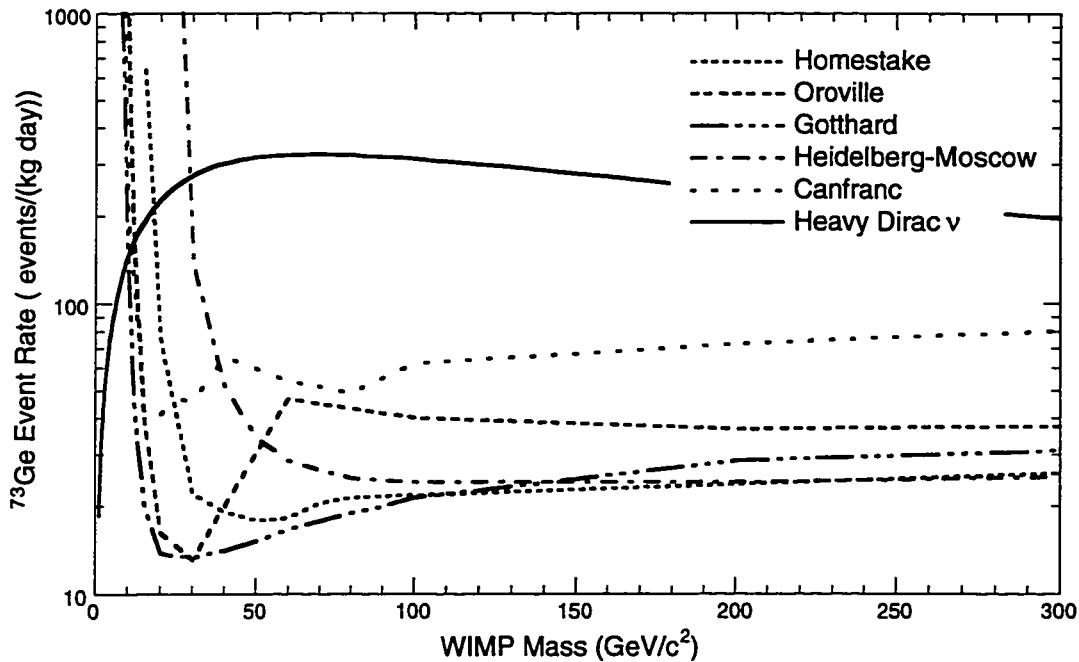


Figure 2.3. Current WIMP Event Rate Limits.

The current WIMP event rate limits achieved with large mass high purity ionization detectors: Homestake,⁴⁶ Oroville,⁴⁵ Gotthard,^{49,†} Heidelberg-Moscow,⁴⁷ and Canfranc.⁴⁸ Also shown is the event rate expected from a heavy Dirac neutrino with standard electroweak coupling. A cosmologically interesting sneutrino would have an event rate four times the Dirac neutrino, and so is also excluded.⁴²

$$E_0 \cdot \left(\frac{m}{8 \text{ GeV}/c^2} \right)^2 \times \text{keV}. \quad (m \ll M) \quad (2.8)$$

electron equivalent energy so the peaks appear at the known total energies of the photon. The result is that a nuclear recoil of total energy E_0 will appear in the spectrum at $E_0/3$. Recalling that the expected WIMP spectrum is roughly exponential, we see that the rapidly rising noise tail below 2–3 keV drastically reduces the sensitivity (increases the event rate limit) to WIMP masses below about 20–25 GeV/c^2 . Similarly, the roughly flat background underlying the peaks and tritium beta decay limits the sensitivity to higher mass WIMPs.

† There is a discrepancy between the published spectrum and the published exclusion limits for the Gotthard experiment. The published limit appears to be a factor of 3–5 lower than is consistent with the spectrum; see Gray⁵² for a discussion. Here we show the published limits.

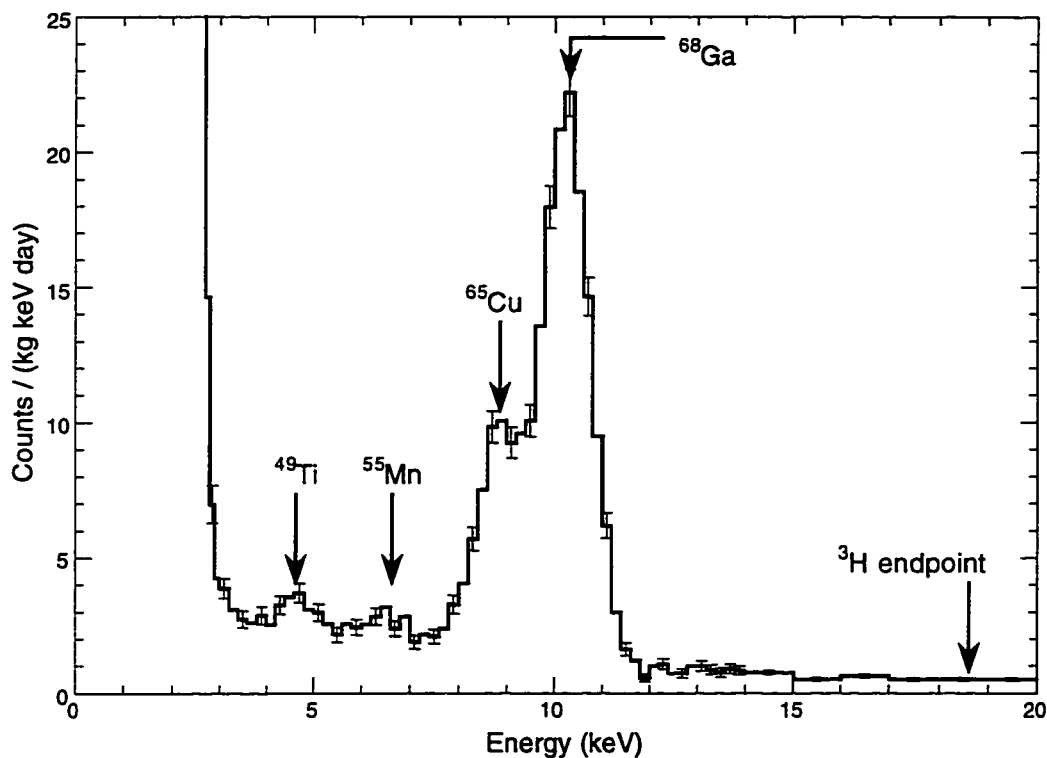


Figure 2.4. Low Energy Spectrum from the Oroville Experiment.
 Low energy spectrum from the Oroville double beta decay experiment.⁴⁵ The spectrum is dominated by electron recoils due to cosmogenic activity. (For clarity only some error bars are shown.)

Since these experiments do not have an independent measurement of the background spectrum, in the analysis they must consider the hypothetical WIMP spectrum plus an *arbitrary* non-negative background. This precludes subtracting any of the identifiable pieces, especially the featureless tritium spectrum, since they don't know how much of the observed counting rate is due to these sources and how much is caused by a "conspiracy" of WIMPs and some odd background spectrum. The experimenters have worked very hard to reduce the intrinsic background in their apparatuses by electroforming the cryostats and constructing the detectors as quickly as possible at the surface to minimize cosmic ray exposure. The level achieved seems to be the limit of what can be done with current technology. Further improvements will require some means of background rejection, since the backgrounds are already irreducible.

It is clear that the spectrum is dominated by electron recoils due to X-rays and electron interactions in the detector. However, the expected signal comes from nuclear recoils. Therefore a detector capable of distinguishing between electron recoils and nuclear recoils should be able to reject the dominant backgrounds in the current experiments and achieve significantly higher sensitivity.

3. CDMS Detectors

To increase the sensitivity of WIMP search experiments, we need to make an independent measurement of the background. Since a significant background source is radioactivity inside the detector itself, which we will discuss in Chapter 4, measurements of the background *in situ* with different detectors generally will not help. We have no way to shield against or turn off the WIMP flux, so we cannot make a source on/source off subtraction, either. The only possibility left is to make multi-parameter measurements of each event. If we can find parameters that respond differently to the signal and the dominant backgrounds we can use the difference to discriminate against the background and improve the sensitivity. One example is the dependence of the light decay time and spectrum on the recoiling particle (nucleus or electron) in NaI(Tl).⁵³

In all detectors, in addition to the ionization signal, the recoiling nucleus or electron sheds the absorbed energy by emitting phonons, which eventually show up as heat. In conventional detectors this is only significant if the flux and energy deposition are both large, for example in spacecraft radioisotope power generators or at the LAMPF, where the 1 mA beam current of 800 MeV protons deposits ~ 1 MW of power in the water target.⁵⁴ At cryogenic temperatures, however, the energy of even a single event is detectable as a measurable temperature rise. Since a recoiling nucleus is less ionizing than a recoiling electron, an ionization detector operated at low temperature with a sensitive thermometer attached should be able to distinguish between nuclear and electron recoils.

In the rest of this chapter, we will describe the two sensors we have developed to measure the phonon or thermal signal from each event. Using the Berkeley germanium detectors for illustration, we will discuss the subtleties of ionization measurement at low temperature. Then we will show how the ionization and thermal

measurements enable us to distinguish between electron and nuclear recoils, and how we can calibrate the rejection factor. Finally we will describe the large mass detectors currently under construction. The development of NTD thermistors and low voltage ionization measurements in the Berkeley group was started by Ning Wang and continued by Dan Akerib, Eric Aubourg, Alan Cummings, Rodney Diaz, Brett Ellman, John Emes, Yannick Giraud-Heraud, Rick Gaitskell, Sunil Golwala, Eugene Haller, Kohei Ito, Josef Jochum, Bill Knowlton, François Quéinnec, Bernard Sadoulet, Dennis Seitz, Tom Shutt, Walter Stockwell, Chris Stubbs, Jim Rich, Roy Therrien, Betty Young and Dominique Yvon. The Stanford detectors have been developed by Paul Brink, Blas Cabrera, Barron Chugg, Roland Clarke, Andrea Davies, Brian Dougherty, Kent Irwin, Adrian Lee, Sae Woo Nam, and Mike Penn.

3.1 Why cryogenic?

Before describing the sensors in detail, it is amusing to recall the original motivation for developing cryogenic detectors. The resolution of a detector is determined in part by the counting statistics of the number of collected quanta (*e.g.*, electron-hole pairs in an ionization detector).⁵⁵ The mean number of quanta is just the total energy deposition divided by the energetic cost of each quanta, so collecting the quanta with the smallest energetic cost will increase the number of quanta collected and improve the resolution. Even at low energy where the resolution is dominated by electronics noise, a smaller energetic cost leads to a larger signal and hence improved signal to noise.

In a high purity germanium detector (HPGe), such as used in the first generation WIMP searches, or in our ionization measurement, the cost per electron-hole pair is 3.0 eV,^{56, 57} leading to 2.0×10^4 electron-hole pairs from the 59.54 keV gamma line of ²⁴¹Am. If instead we collect the ~1 meV energy phonons in a detector at low

temperature we should in principle measure a signal of 60×10^6 phonons, with correspondingly better resolution or improved signal to noise. In principle we also have to consider the resolution limit imposed by thermal fluctuations;⁵⁸ to achieve 100 eV resolution in a 1 kg germanium detector we would need to operate around 20 mK. In practice we approach this limit on good days; but more commonly constraints on the electronics lead to noise limited resolution in excess of the thermal limits, but still considerably better than obtained in HPGe detectors.

Despite the noise limited resolution, a phonon-based sensor still has a number of advantages. Foremost, the phonon measurement in concert with an ionization measurement makes background rejection possible. With more advanced sensors than described here it might be possible to determine the nature of the recoil solely by measuring the phonon spectrum. With an array of fast sensors, it might even be possible to detect the direction of the recoiling nucleus, which would be another important handle to distinguish background from signal.⁵⁹⁻⁶¹

3.2 Berkeley: NTD Germanium Thermistors on Germanium

The Berkeley group has developed detectors using phonon sensors based on neutron transmutation doped germanium thermistors eutectically bonded to a large mass high-purity single crystal germanium target (a target for WIMP scattering).⁶²⁻⁶⁴ The last 60 g prototype is shown schematically in Figure 3.1. Simplified readout circuits are shown for one thermistor and one ionization channel; the detector has two of each. The crystal starts as a squat cylinder, ~ 4 cm $\varnothing \times \sim 1$ cm. We round the edges then implant the two faces to form resistive contacts. The contacts wrap around the edges until they almost meet, leaving a gap of ~ 1 mm. We apply ~ 0.25 V bias to the contacts creating a small drift field, ~ 0.25 V/cm, in the target to collect an ionization signal and monitor the thermistor resistance to measure the temperature of the target. The contact on the top

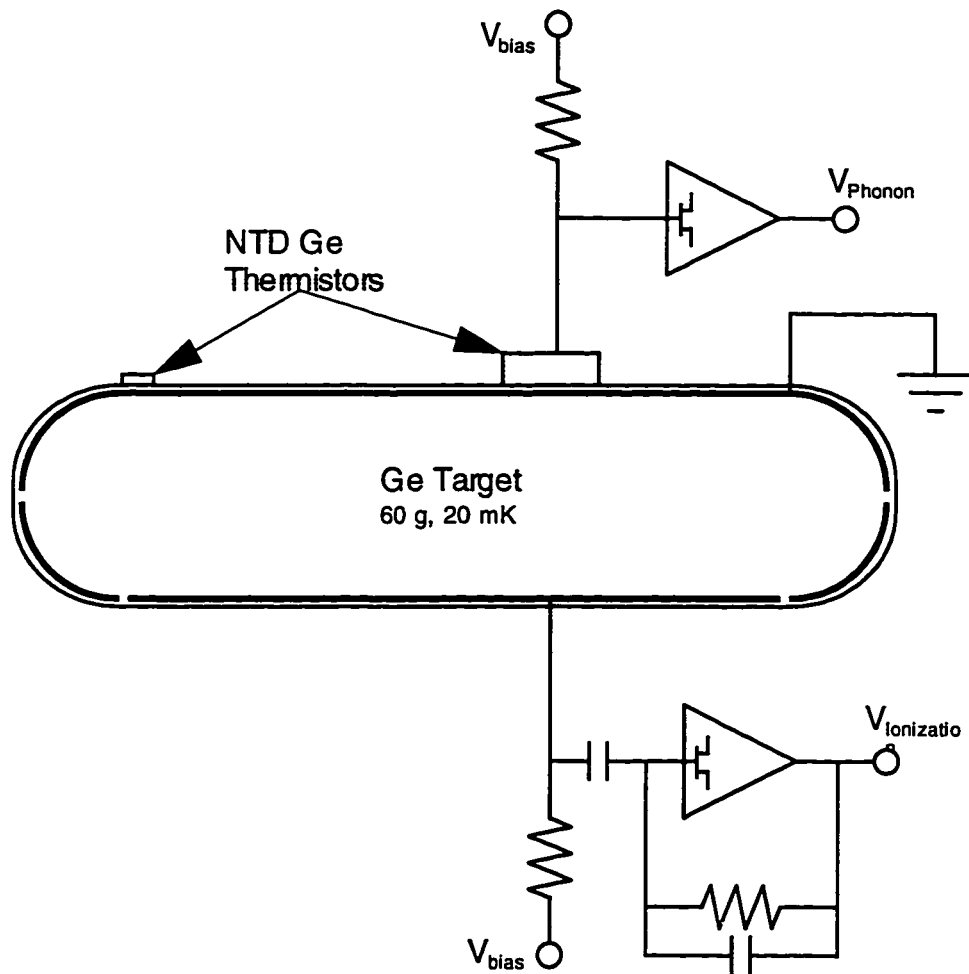


Figure 3.1. Schematic of the 60 g Berkeley Prototype Detector E5. Schematic of the last Berkeley 60 g prototype detector, named E5. The large oval is the cross section of the pure germanium target. The heavy interior lines indicate the implanted contacts (greatly exaggerated in scale), which cover each face and wrap around the sides, leaving a ~ 1 mm gap. The bottom implant is segmented to make two ionization channels. The shaded rectangles on top of the target are the NTD thermistors. Simplified readout circuits are shown for one thermistor and one ionization channel.

face is continuous and forms the ground for both the thermistor and ionization channels. The bottom contact is segmented into an inner ionization channel and an outer ionization channel of roughly equal volumes.

The energy absorbed by an electron or nuclear recoil is initially partitioned into electron-hole pairs and high energy phonons. The "ionization energy," the energetic cost per electron-hole pair, is $\epsilon_e = 3.0$ eV for electron recoils (independent of energy)

and $\epsilon_N = 9$ eV for nuclear recoils (at 60 keV and weakly energy dependent). Nuclear recoils are 1/3 as ionizing as electron recoils of the same energy. The number of electron-hole pairs created by energy deposition E is $N_{eh} = E/\epsilon$. The binding energy of each electron-hole pair is just the energy gap, $\epsilon_g = 0.746$ eV, so the amount of energy that is initially stored in the electron-hole pair binding energy is $E_b = N_{eh}\epsilon_g$. The remainder of the energy is released as phonons. In the absence of charge trapping the electrons (holes) drift under the influence of the field until they reach the contact, where they combine with holes (electrons) releasing their binding energy ϵ_g as phonons. Since the drift time is quite short compared to the thermal time constants, all the energy absorbed in the event is converted to phonons essentially instantaneously. Therefore the thermal measurement is essentially calorimetric, giving the total energy deposition. When an electron or hole becomes trapped, it releases some of the gap energy, ϵ_g , as phonons, but some of the energy gets bound up in the impurity-charge system, so charge trapping leads to a deficit in the calorimetric signal. The difference between ϵ_e and ϵ_N means that electron and nuclear recoils of the same total energy deposition give very different ionization signals. This is the basis of the electron/nuclear recoil discrimination. Now that we are oriented, we will discuss the thermistors and the ionization measurement in more detail.

3.2.1 Phonon Measurement

The NTD germanium thermistors (lot NTD #12) are fabricated from high purity germanium wafers that have been exposed in a reactor neutron beam to a total fluence of 3.7×10^{16} cm².⁶⁵ After the wafers have cooled for several months and are safe to handle, they are cut into strips by a diamond saw, lapped to remove saw damage, etched to remove polishing damage, boron implanted to form ohmic contacts, thermally annealed to remove radiation damage and activate the implant, sputtered with palladium

as a sticking layer, and finally evaporated with gold for the electrical contact pad.⁶⁴⁻⁶⁶ The thermistors are very heavily doped to the semi-conductor-metal transition. Electrical conduction proceeds by variable range thermally assisted hopping.^{66, 67} This is essentially a tunneling process in space, from one impurity site to another, so the resistivity depends exponentially on the temperature as

$$\rho = \rho_0 e^{(\Delta/T)^\alpha} \quad (3.1)$$

where ρ_0 is roughly constant, Δ depends on the doping level, and the temperature exponent $\alpha = 1/4$ ($1/2$) for systems with non-zero (zero) density of states at the Fermi energy. The absence of states at the Fermi energy arises in most heavily doped semi-conductors from Coulomb interactions between the impurities leading to a "Coulomb gap" right at the Fermi level. These systems will be insulators at zero temperature. At room temperature a typical sensor has only a few ohms resistance, and at 250 mK it is $\sim 20 \Omega$. At 50 mK it has risen to $\sim 2 \text{ k}\Omega$ and by 20 mK it is $\sim 5 \text{ M}\Omega$. Explicitly fitting our data for the exponent in Eq. (3.1), we have determined⁶⁸ that $\alpha = 0.25$ and NTD Ge does indeed have a Coulomb gap. For NTD #12, the fit value gives $\Delta \approx 5.2 \pm 0.3 \text{ K}$, where the range quoted shows the variations from sensor to sensor, probably caused by varying amounts of stress caused by the eutectic bonding method.

In addition, we have demonstrated that there is a finite thermal conductance between the electrons and phonons in the NTD, which is called the hot electron effect.⁶⁶ To measure the resistance of an NTD chip, we apply a small bias current, \sim few nA, and monitor the voltage drop, \sim few mV. The product of the current and voltage is the bias power, $\sim 10 \text{ pW}$, dissipated by the electrons in the NTD. Because of the finite conductance between the electrons and the phonons, the electrons effectively heat up above the phonon temperature. As we increase the bias power the electron temperature also increases. Since the resistivity drops with increasing temperature, the NTDs have a strongly non-linear I-V curve. Empirically we find that Eq. (3.1) accurately predicts the

resistance if we take T as the effective electron temperature, T_e , determined by the relation

$$P = g_{e\phi}(T_e^\beta - T_\phi^\beta) \quad (3.2)$$

where P is the bias power, T_ϕ is the phonon or detector temperature, ~ 20 mK, and the parameters $g_{e\phi}$ and β are measured. We find good agreement with $\beta = 6$ and $g_{e\phi} \approx 0.04$ W/K⁶.

The thermal measurement with the NTDs is essentially calorimetric: an event raises the phonon temperature of the detector by an amount equal to the energy deposition, E , divided by the heat capacity, C . The heat capacity of the target is dominated by the phonons, which obey the Debye law, giving $C \sim 0.25$ nJ/K at 20 mK. For precise work we also have to include the heat capacities of the NTD thermistors and the various metal pads and implants on the target.⁶⁴ The increase in the phonon temperature causes an increase in the electron temperature according to Eq. (3.2), which causes a change in thermistor resistance according to Eq. (3.1). Increasing the bias power increases the sensor voltage, thereby improving the signal-to-noise ratio of the thermistor resistance measurement. However, this also elevates the effective electron temperature. Because of the large exponents in Eq. (3.2), this makes the electron temperature insensitive to changes in the phonon temperature caused by the event energy. Therefore there is a balance between increasing the signal-to-noise of the thermistor measurement and decreasing the sensitivity to events; this occurs typically for $T_e - T_\phi \approx \text{few mK}$. This condition can be determined by maximizing the signal-to-noise of the phonon temperature estimate, which is the quantity of interest.^{58, 69}

The simplest way to attach the thermistors to the target is simply to use a dab of glue or epoxy; however the difference in thermal contraction between glues and the germanium of the target and NTD leads to significant stress in the NTD, which we have shown leads to large variability in performance. A more graceful bonding method takes

advantage of the existence of a Au-Ge eutectic phase. The optically polished mating surfaces are coated with a thin (200 Å) Pd sticking layer, then a modest (1000 Å) Au(1% Ga) layer. (The gallium improves the electrical contact between the NTD and the implant of the target, which is the electrical ground for the phonon circuit.) The two pieces are pressed together and heated in vacuum to 380°C (above the 356°C eutectic temperature) then slowly cooled. The result is a low stress bond that gives repeatable results when thermally cycled. In addition, the eutectic interface is transparent to the high energy athermal phonons initially emitted in an event. The athermal phonons can be measured with large sensors on small targets where the fractional target surface area covered is large. (The athermal phonons thermalize by surface and impurity scattering, therefore it is important to absorb them in the sensor before they have traveled too far in the target. This requires a large surface coverage.) The athermal phonons could be important in more advanced detectors since the phonon spectrum may contain information about the nature of the recoil (electron/nucleus) which could enable background rejection in materials that don't have ionization signals (*e.g.*, non-semiconductors). The athermal phonons might also contain information about the recoil direction, which is a very powerful background rejection handle.^{59-61, 70, 71}

Since this is a thermal measurement in a massive system, one expects fairly long time constants. The phonon pulses have rise times ~0.5 ms and fall times ~20 ms. The rise time is approximately the ratio of the NTD electronic heat capacity to the electron-phonon conductance in the NTD. The fall time is approximately the ratio of the detector heat capacity to the conductance from the detector to the refrigerator heat sink. We can control this last conductance, and therefore set the pulse decay time constant. Long decay times lead to excessive pulse pile-up, especially in our surface development laboratory, whereas short decay times reduce the pulse height by diverting the energy

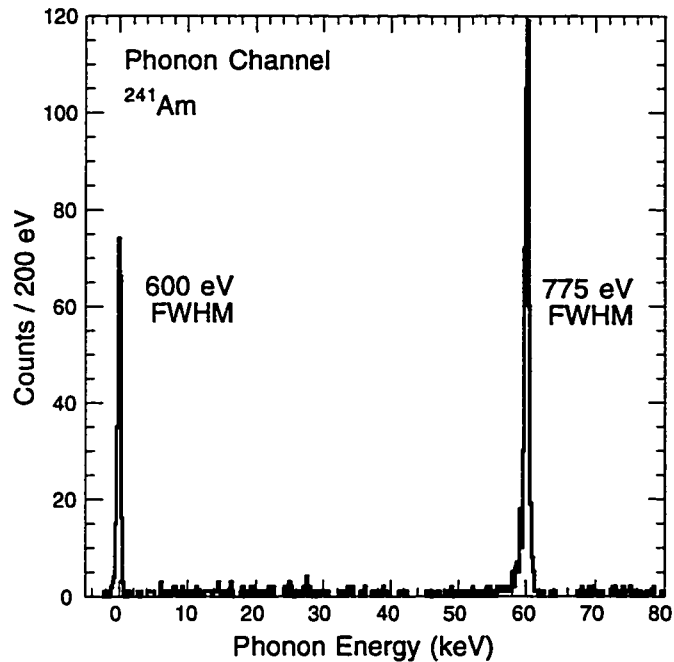


Figure 3.2. Phonon Spectrum in the Berkeley 60 g Detectors. A typical phonon spectrum from the Berkeley 60 g germanium detector prototypes exposed to the 60 keV gamma from a collimated ²⁴¹Am source and room background. The baseline electronics noise is 600 eV; the resolution at 60 keV is 775 eV (both values FWHM).

into the heat sink before it raises the NTD electron temperature, which lags the target temperature due to electron-phonon decoupling.

Because of the long time constants, the signal bandwidth is at fairly low frequency where microphonic pick-up in the electronics is a significant problem. Instead of applying a DC bias current we apply an AC bias current at ~1 kHz. The input sine-wave bias is divided by the bias resistor in series with the thermistor. The changing thermistor resistance changes the divider ratio and the amplitude of the sine-wave applied to the FET input, so the signal appears as an amplitude modulation on the sine-wave carrier. At the amplifier output we demodulate to remove the carrier, leaving us with the average carrier amplitude, which gives us the average thermistor resistance and hence electron temperature, and the modulations to that amplitude from events in the detector.

Figure 3.2 shows a typical spectrum from the thermistor signal obtained in our surface laboratory when the detector is exposed to a collimated ^{241}Am source (with the α -particles and low energy X-rays stopped by a window) and room background. The data acquisition is triggered by the ionization channel, with the threshold set just above the noise, which is at ~ 2 keV for electron recoils, corresponding to ~ 10 keV nuclear recoil threshold. The phonon channels have a baseline electronics noise FWHM of 600 eV and a FWHM resolution at 60 keV of 775 eV. The excess can be attributed to temperature drifts in the refrigerator (we do not temperature control the refrigerator), residual microphonic effects, and the larger noise in the ionization measurement, discussed below, entering via the Luke correction (also discussed below).

3.2.2 Ionization Measurement

At first glance the ionization measurement looks like a HPGe detector: we apply a drift field and measure the current pulse. It operates in a totally different mode, however. When we first cool down the detector, the charge measurement has very poor resolution due to charge trapping on impurity states (A^{\cdot}, D^{\cdot}). We ground the ionization bias to remove any drift field and flood the target with electron-hole pairs by irradiating it with a strong radioactive (or infrared) source for several hours. After this "neutralization" step essentially all impurity sites are neutralized (A^0, D^0) and no longer are trapping sites. The length of time required to neutralize the crystal is consistent with the number density of impurities and the charge trapping cross-sections. At these low temperatures there are essentially no thermally excited electrons and holes in the target, so all impurities are frozen out: even though the A^0, D^0 configuration is *extremely* out of equilibrium, it is still a steady-state. Therefore we don't need to apply a large depletion voltage as is required at 77 K. Typically we apply a field of

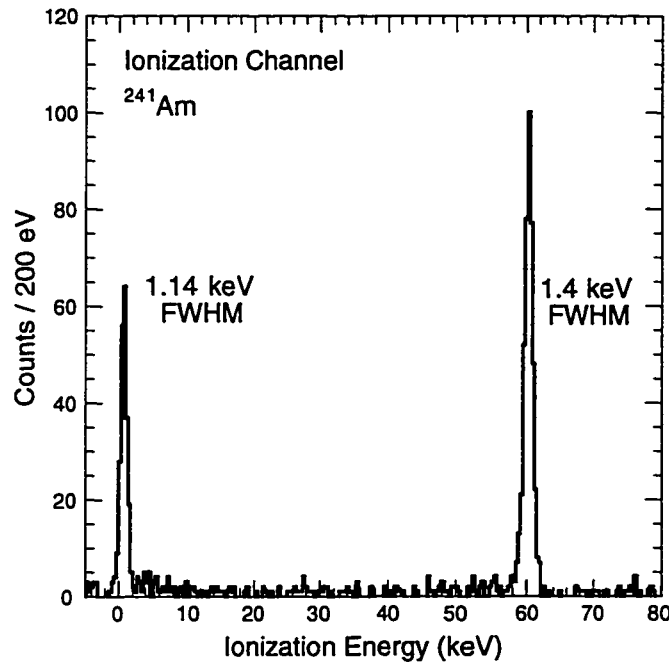


Figure 3.3. Ionization Spectrum in the Berkeley 60 g Detectors. Ionization spectrum obtained under clean conditions (target fully "neutralized") from the Berkeley 60 g germanium prototype detectors exposed to the 60 keV gamma from a collimated ^{241}Am source and room background. The electronic baseline noise is 1.14 keV; the resolution at 60 keV is 1.4 keV (both values FWHM).

~ 0.25 V/cm. This is crucial for the *phonon* measurement because of the Luke effect, discussed below.

As events occur in the target, the drifting electron-hole pairs gradually ionize some of the impurity sites (D^\pm , A^\pm) leading to space charge buildup and degradation of the resolution by random trapping. This becomes a significant effect compared to the electronics noise when $\sim 1\%$ of the impurities have become ionized. To "reset" the crystal, *i.e.*, neutralize the impurity sites again, we periodically ground the contacts to remove the drift field and illuminate the detector, with an infrared LED this time since we don't need to create as much free charge as in first neutralizing the target.

Figure 3.3 shows a typical spectrum from the ionization channel when the detector is exposed to a the same collimated ^{241}Am source as above. The ionization

channels have baseline noise FWHM of 1.14 keV and at 60 keV FWHM resolution of 1.4 keV. The excess is probably due in part to trapping and space charge.

3.2.3 Coupling Between the Phonon and Ionization Channels

A small intrinsic coupling between the ionization measurement and the thermal measurement adds to the purely calorimetric signal. As they cross the target crystal with bias voltage V_{bias} the drifting electrons and holes dissipate energy eV_{bias} per pair as phonons (e is the magnitude of the electron charge). Therefore the measured phonon signal is $E_\phi = E + N_{eh}eV_{bias}$, where E is the initial recoil energy and N_{eh} is the number of electron-hole pairs collected. This additional thermal energy is called the Luke effect.⁷² Since the drift time is much less than the thermal time constant this additional thermal energy appears as part of the phonon pulse. The actual amount of phonon energy added by the Luke effect is given exactly by the total charge collected times the ionization bias voltage, independent of the nature of the recoil (electron or nucleus) and of any charge trapping. (A charge that drifts 1/10 of the way across the crystal induces a change of $e/10$ in the image charge on the contact, so the actual charge collected already includes the effects of charge trapping.) If the bias voltage is 0.25 V and the ionization energy (energetic cost per electron-hole pair) is $\epsilon = 3$ eV (an average value), then the phonon pulse is $V_{bias}/\epsilon \simeq 4\%$ larger than the initial event energy. For the electron/nuclear recoil discrimination it is crucial that there be a small coupling between the two measurements, so that they reflect truly independent properties of the event.

3.3 Stanford: Tungsten Transition Edge Sensors

The Berkeley detectors thermalize the phonon energy in the target and NTD, losing any potential information that is contained in the initial athermal phonon pulse. For example, it might be possible to determine the nature of the recoil from the

athermal phonon spectrum, without the ionization measurement. This would allow us to use a wider variety of materials for the target, since we would not be restricted to semi-conductors. To pursue this possibility, the Stanford group is developing detectors based on tungsten/aluminum quasiparticle trap assisted electrothermal feedback transition edge sensors (W/Al QET).⁷³ Using silicon targets we have made ionization detectors very similar to the Berkeley germanium ionization measurement, and have also demonstrated electron/nuclear recoil discrimination. We are developing methods to implement the same sensor on germanium targets. Since we have already discussed ionization measurement at low temperatures, here we will focus on the Stanford phonon sensor, before turning to the electron/nuclear recoil discrimination.

When phonons from a particle interaction in the (silicon) target reach the surface, most of them will have enough energy ($E_{ph} \sim 2 \text{ meV} > 2\Delta_{Al} \sim 0.3 \text{ meV}$) to be absorbed in thin film aluminum pads (covering most of the surface) creating quasiparticles. The quasiparticles diffuse through the aluminum until they reach a tungsten transition edge sensor. The quasiparticles very quickly relax to the gap edge in the tungsten ($2\Delta_w \sim 0.024 \text{ meV}$), in the process emitting phonons which are immediately absorbed by the tungsten. The quasiparticles now do not have enough energy to diffuse back into the aluminum: they have become trapped. Eventually the quasiparticles recombine in the tungsten, releasing their binding energy as more phonons which are absorbed in part by the tungsten. The net result is that some of the athermal phonons from an event in the target have been converted to quasiparticles (in the aluminum) which eventually release their binding energy as phonons in the tungsten.

The tungsten film is voltage biased; the current is monitored by a SQUID array.⁷⁴ The phonons released in the tungsten raise the temperature of the film, increasing its resistance and reducing the current. The tungsten is stably biased by

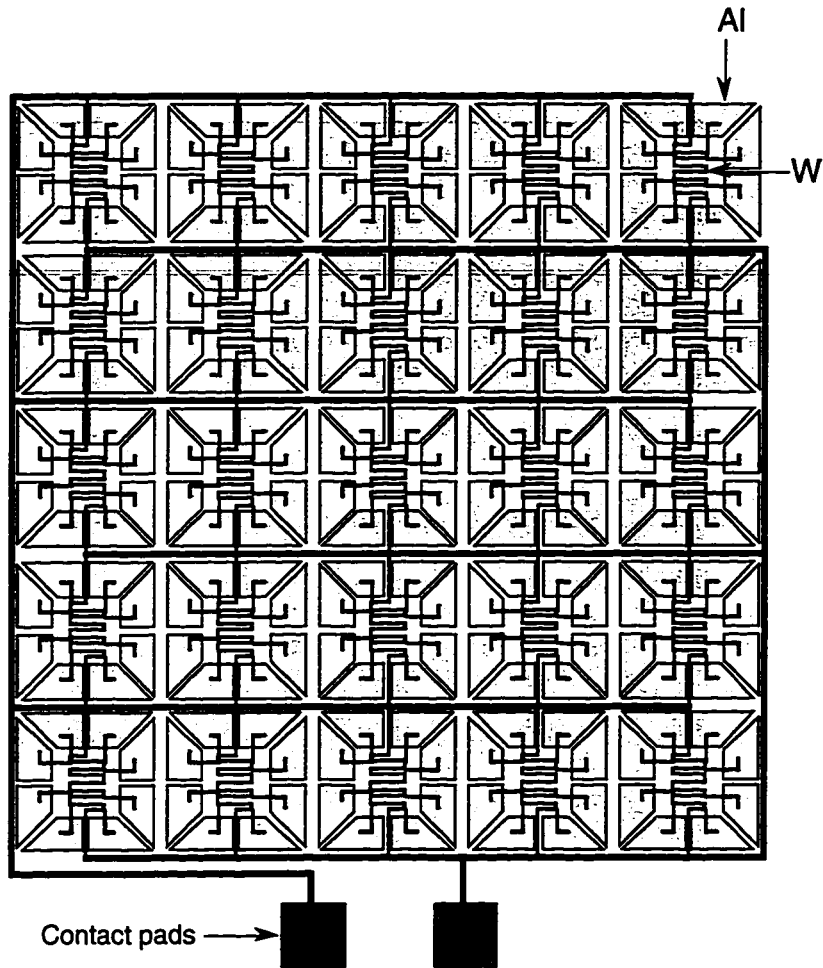


Figure 3.4. W/AI QET Sensor. Schematic of the Stanford W/AI QET sensor. Each cell contains a tungsten transition edge sensor with eight aluminum phonon collection pads attached along its length. The individual sensors are connected in parallel and voltage biased.

Joule self-heating and electrothermal feedback.⁷⁵ In the extreme feedback limit, the substrate is much colder than the transition temperature of the tungsten sensor ($T_c \sim 80$ mK). The sensor temperature is stably maintained at the center of the transition by Joule heating. (If it were hotter, the resistance would increase, decreasing the current and the Joule heating; an analogous argument applies if it were cooler.) The event energy released in the tungsten as phonons is entirely removed by the reduction in Joule heating caused by the current drop, therefore the energy absorbed by the tungsten

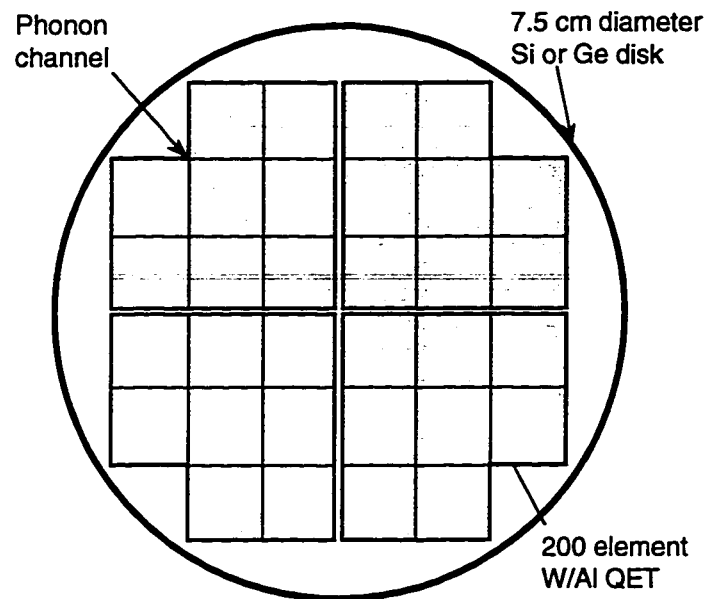


Figure 3.5. Four channel W/AI QET detector. Sketch of the Stanford four channel W/AI QET on a 7.6 cm diameter target. Each shaded square consists of one sensor pattern as shown in Figure 3.4. The eight patterns grouped together form one phonon sensor making four channels altogether. The back face of the detector has two ionization contacts forming a central fiducial volume and an outer guard ring.

is just the integral of the current drop times the bias voltage. In practice $\sim 1/12$ of the initial event energy at 6 keV appears in the tungsten film. Because only the tungsten film heats up, and the heat is removed by electrothermal feedback, the W/AI QET sensors are intrinsically very fast, with pulse fall time constants $\sim 100 \mu\text{s}$.

A schematic of a sensor is shown in Figure 3.4. Each unit cell contains a thin black tungsten meander with eight aluminum phonon collection pads attached along its length. The individual tungsten lines are connected in parallel and voltage biased. By stepping and repeating this pattern a large fraction of the surface area can be covered with aluminum collection pads. Figure 3.5 shows the layout of patterns on the large target crystals currently under development.

In a 4 g prototype with four phonon sensors, we have used the fast signals to reconstruct the X-Y event position in the plane of the target (but not the depth Z). The position is estimated from the known phonon velocity and time difference between the pulses in the two left-hand sensors vs. the pulses in the right-hand sensors, and similarly for top and bottom pairs. The detector was illuminated by an ^{55}Fe source (5.6 keV photon) through a collimator containing a grid of pin-holes. The reconstructed event distributions have widths of a few millimeters.

3.4 Electron / Nuclear Recoil Discrimination

Figures 3.2 and 3.3 show the spectra obtained by the NTD thermal sensors and the germanium ionization measurement, in each case ignoring the result of the other measurement. What happens when we make full use of the information? Figure 3.6 shows the same data as in Figures 3.2 and 3.3, but now plotting the phonon measurement vs. the ionization measurement for each event. The detector was exposed to the 60 keV gamma line from a collimated ^{241}Am source and room background (data set n_1 : ^{241}Am). We see mostly one class of events along the diagonal due to electron recoils. The ratio of the phonon energy to the charge collected (*i.e.*, the slope of the electron recoil line) gives $\varepsilon_e = 3$ eV, as expected.⁷⁶ On the 60 keV peak the tail extending to smaller ionization signals is due to increasing charge trapping and space charge buildup during the course of acquiring the data set. The slope of the tail is due to the Luke effect. The smattering of events to the left of the electron recoil line are due to incomplete charge collection at the surface contacts.

Now we bring a ^{252}Cf fission source into the room. Figure 3.7 shows the resulting 2-d plot (data set n_2 : $^{252}\text{Cf} + ^{241}\text{Am}$). A new class of less ionizing events appear due to nuclear recoils from neutron elastic scattering in the detector. The higher slope of the nuclear recoil line corresponds to $\varepsilon_n \sim 9$ eV as expected. Since we triggered on

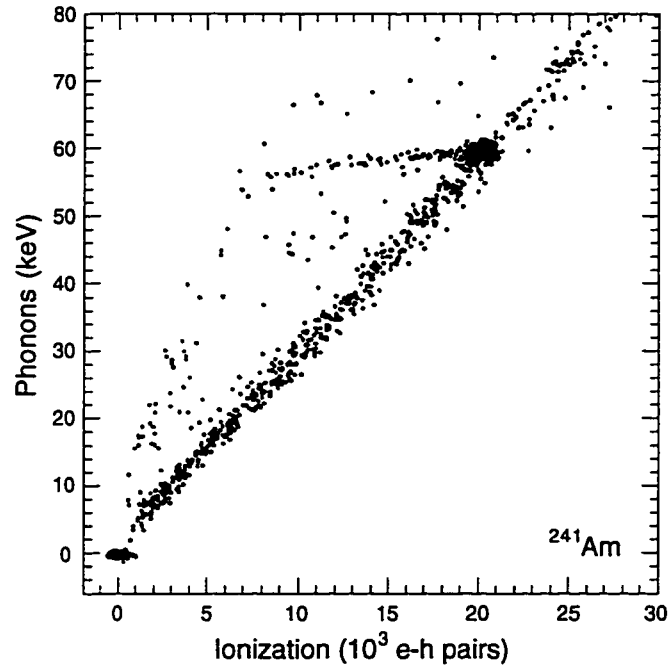


Figure 3.6. Response of the Berkeley 60 g Prototype to ^{241}Am .
 The response of the Berkeley 60 g germanium prototype detector to the 60 keV and lower energy X-rays from a collimated ^{241}Am source as well as room background.

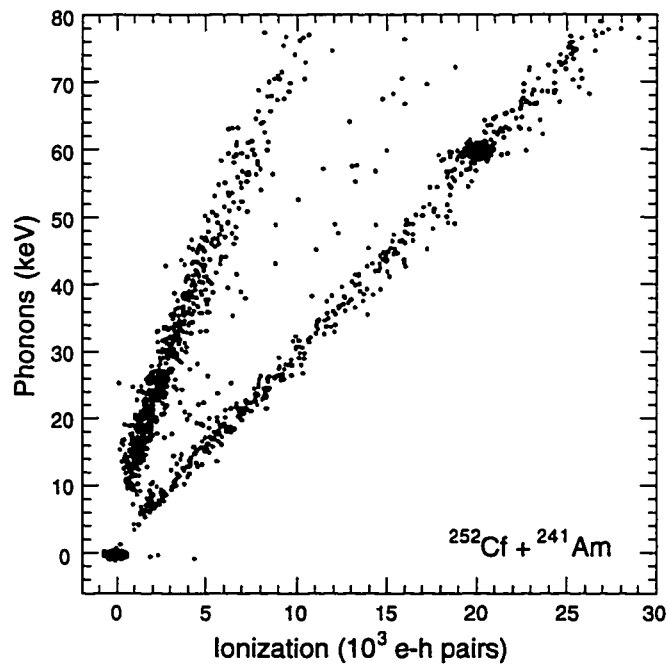


Figure 3.7. Response of the Berkeley 60 g Prototype to ^{252}Cf and ^{241}Am .
 The response of the Berkeley 60 g germanium prototype detector to the gamma and X-ray lines from a collimated ^{241}Am source, the broad spectrum photons and neutrons from a ^{252}Cf fission source, and room background.

the ionization channels near threshold, ~ 2 keV, the nuclear recoil threshold is ~ 10 keV, hence the absence of nuclear recoil events below 10 keV in the phonon channel.

Using the known ionization bias voltage we can remove the Luke effect from the phonon measurement to recover the actual recoil energy, $E = E_\phi - N_{eh}eV_{bias}$. We can also take the ratio of the ionization charge collected to the recoil energy to obtain the ionization yield, $y = \epsilon^{-1} = N_{eh}/E$, *i.e.*, the number of electron-hole pairs per eV energy deposition. This effectively removes the slope of the lines in Figures 3.6 and 3.7. Figure 3.8 shows the scatter plot of y vs. E for the two data sets. The electron recoil line at $y = 0.3$ eV is independent of recoil energy (except at low energy), as expected from semi-conductor ionization detectors.⁵⁵ (The tendency towards lower y at low energy in Figure 3.8B is evidence that the low energy photons are from sources external, not internal, to the detector. These events occur near the surface and suffer incomplete charge collection, hence the decrease in y .) The nuclear recoil line has noticeable curvature, however, demonstrating that higher energy nuclear recoils are more ionizing. The ratio, ϵ_I/ϵ_N was computed by Lindhard, *et al.*;⁷⁷ the most precise measurements of this ratio come from one of these 60 g prototype detectors.⁶³ From the widths of the 60 keV peaks in the phonon and ionization channels, we estimate the recoil energy resolution $\sigma_E = 330$ eV.

Figure 3.9 shows the distributions in Figure 3.8 projected on the y axis for $10 \text{ keV} < E < 30 \text{ keV}$. The $^{252}\text{Cf} + ^{241}\text{Am}$ data set serves to define a region of interest for nuclear recoils. The fraction of the ^{241}Am data set that lies outside the region of interest, say $0.2 \text{ eV}^{-1} < y$, is the electron recoil rejection factor, $1 - \beta$. (β is the electron recoil acceptance: the fraction of electron recoil events that fall *inside* the region of interest.) This data set gives $1 - \beta = 92\% \pm 3\%$. This value of the background rejection factor applies for the specific value chosen for the cut on y . The events in Figure 3.6 due to incomplete charge collection at the contacts show up in Figure 3.9 as the tail of

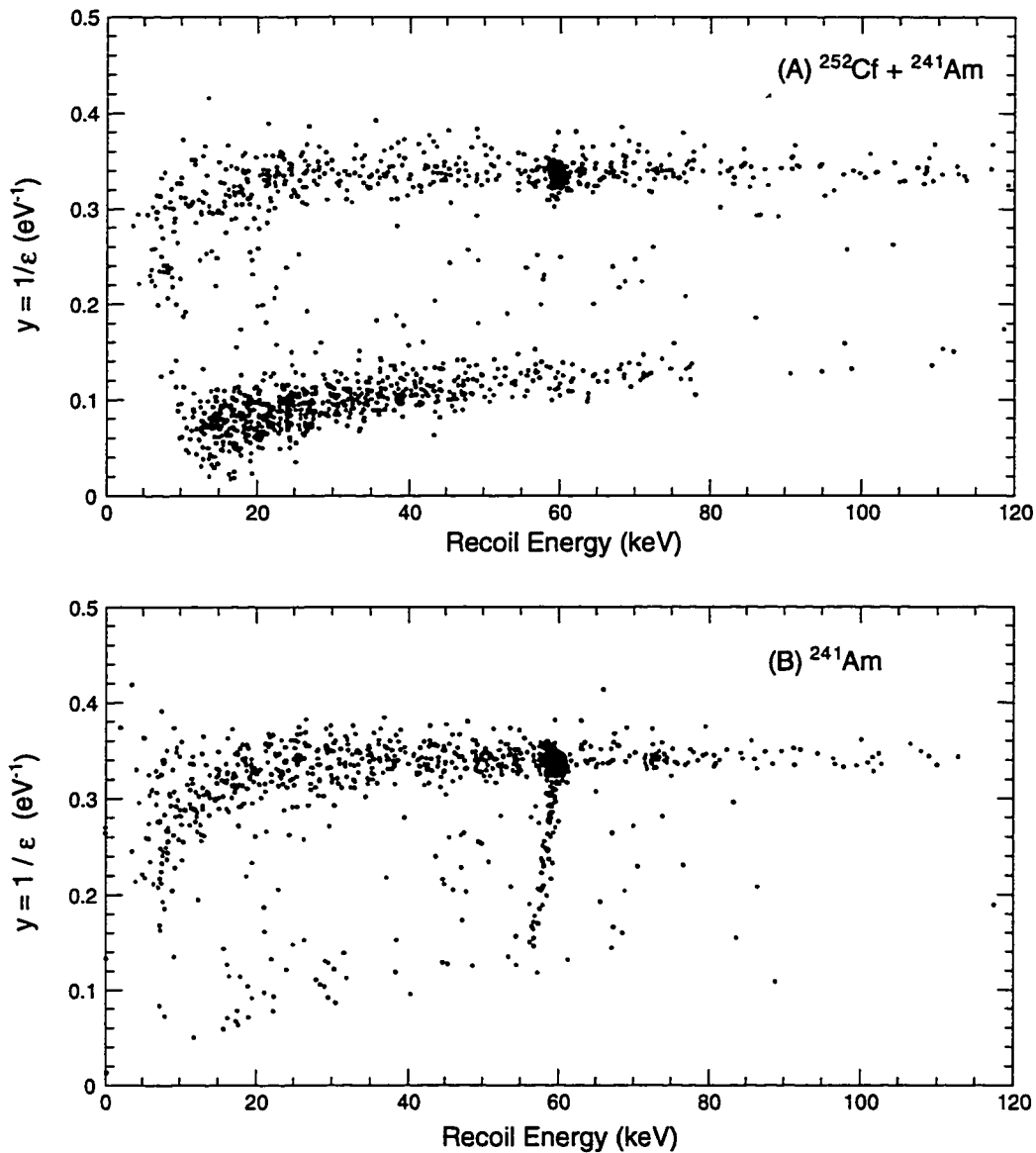


Figure 3.8. Ionization Energy vs. Recoil Energy. The ionization yield, y , vs. the recoil energy, E , for (A) the ²⁵²Cf + ²⁴¹Am data set and (B) the ²⁴¹Am data set shown in Figures 3.6 and 3.7.

the electron recoil distribution. For later reference, we note that data set 1 has a total of 241 counts, and data set 2 has 534 counts.

If we assume that the resolution in the phonon and ionization channels is dominated by Gaussian electronic noise which is independent of energy, then we expect the ionization yield distributions also to have Gaussian distributions, with width

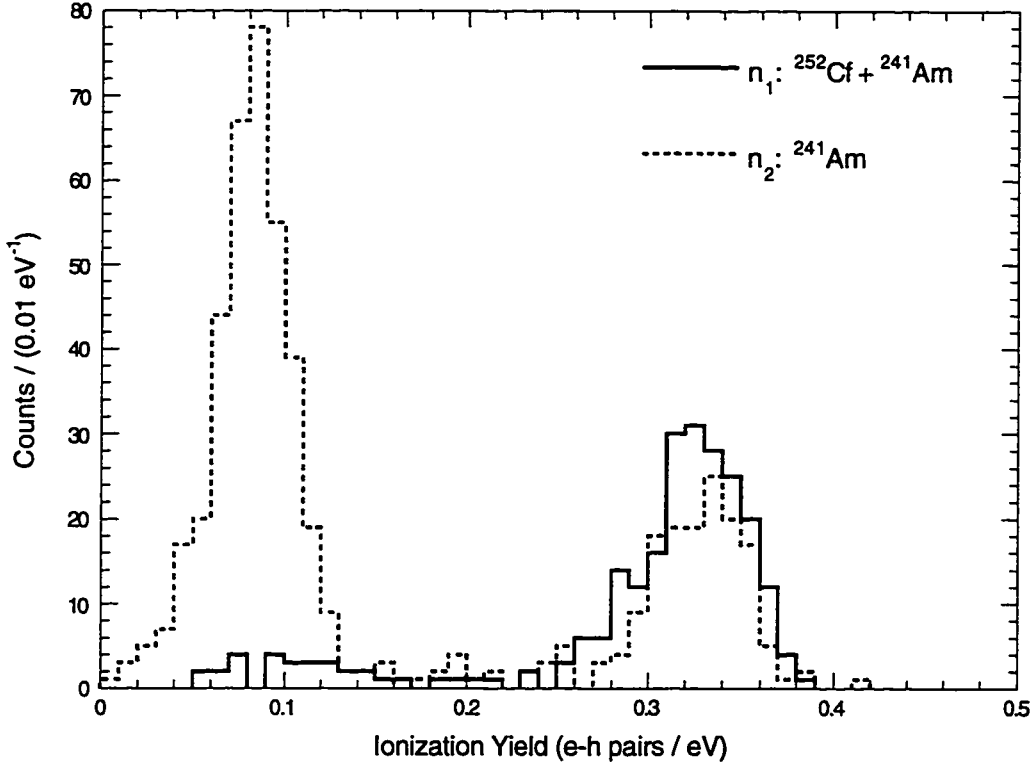


Figure 3.9. Ionization Yield Distributions for $10 \text{ keV} < E < 30 \text{ keV}$.
The distributions in Figure 3.8 projected onto the y axis, for $10 \text{ keV} < E < 30 \text{ keV}$.

$$\sigma_y(E) = \frac{\bar{y}}{E} \sqrt{\sigma_\phi^2 + \sigma_{N_{eh}}^2 (\bar{y}^{-1} + eV_{bias})^2}, \quad (3.3)$$

where \bar{y} is the mean yield for a given type of recoil at recoil energy E , σ_ϕ is the standard deviation of E_ϕ , and $\sigma_{N_{eh}}$ is the standard deviation of N_{eh} . This data has $\sigma_{y,e} = 240/E$, $\sigma_{y,N} = 200/E$, for electron and nuclear recoils respectively.

3.4.1 Analysis of the Background Rejection Quality Factor

Of course, the signal acceptance must also enter, otherwise we could make the cut at very small values of y where we have no background events and say our rejection was 100%. We will show in Chapter 6 that the sensitivity limit is given by the background rate multiplied by the rejection factor

$$Q = \frac{\beta(1-\beta)}{(\alpha-\beta)^2}, \quad (3.4)$$

where α is the signal acceptance and β is the background acceptance. Smaller values of Q are better. For the example cut above, assuming perfect signal acceptance ($\alpha = 1$), we estimate $Q = 0.09$. The rejection factor depends on the value of the cut on y ; if the cut is too low, then the background goes to zero, but the signal acceptance also goes to zero.

In order to evaluate Q as a function of the cut, we need clean samples of electron recoil and nuclear recoil events in order to know the intrinsic response of the detector to signal and background. Even with the cut $0.2 \text{ eV}^{-1} < y$, which includes all the nuclear recoil peak and excludes most of data set n_1 (^{241}Am), it is pretty clear from Figure 3.9 that there are systematic effects limiting the rejection factor. There is a hint of a nuclear recoil bump in data set n_1 , probably due to the neutron background in the laboratory. Data set n_2 ($^{252}\text{Cf} + ^{241}\text{Am}$) is very roughly equal parts nuclear recoils and electron recoils. Neither data set represents the pure response of the detector.

The problem is that each data set is a linear combination of the response functions. Data set n_1 (^{241}Am) is nearly purely electron recoil. To remove the electron recoil piece from data set n_2 , we subtract a multiple of data set n_1 :

$$n_N = n_2 - An_1 \quad (3.5)$$

For the multiple A we use the ratio of counts in the peak region since we expect these counts to be mostly due to the electron recoil response, with only a negligible contribution from the nuclear recoil response. We also implicitly assume either (a) that the electron and nuclear recoil events have the same energy distributions in the two data sets, or (b) that the response functions are independent of energy in this interval ($10 \text{ keV} < E < 30 \text{ keV}$). To obtain the nuclear recoil response we take the interval $0.29 < y \times \text{eV} < 0.37$ for the electron recoil peak and obtain $A = 0.76 \pm 0.06$. The resulting event distribution, n_N , shown as the solid histogram in Figure 3.10, reflects the

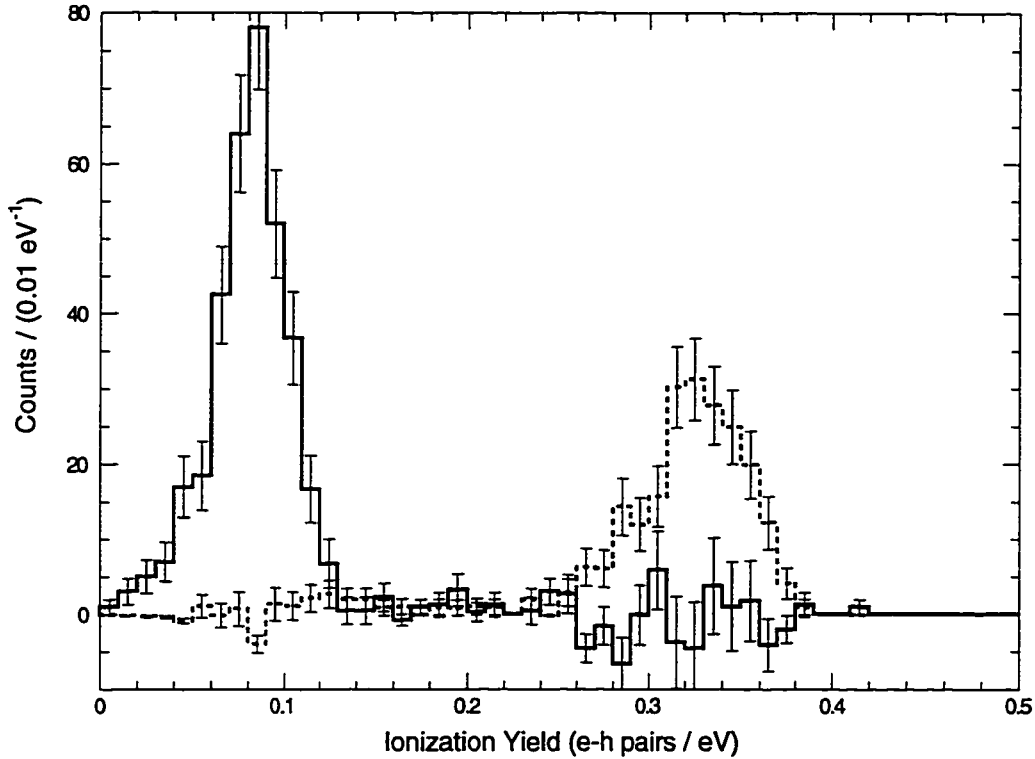


Figure 3.10. Electron Recoil and Nuclear Recoil Response Functions. Detector response to pure electron recoils and pure nuclear recoils. These distributions are derived from the data in Figure 3.9 by subtracting a multiple of one from the other so as to remove one peak from each set.

pure nuclear recoil response. In the nuclear recoil peak it has slightly fewer events than data set n_2 , since the same multiple of the nuclear recoil events of data set n_1 were also removed. We should consider the error bars in bins where the number of counts is less than a few (or negative) as suggestive not formal errors, since we have not properly taken into account the fact that the response functions are bounded from below. The total number of counts in n_N is 351 ± 16 .

Now we have to recover the pure electron recoil response from data set n_1 by a similar procedure. We consider the interval $0.05 < y \times \text{eV} < 0.11$ and find the ratio $B = 0.051 \pm 0.014$; the error is dominated by the small number of n_1 events in the interval. The electron recoil response,

$$n_e = n_1 - Bn_N, \quad (3.6)$$

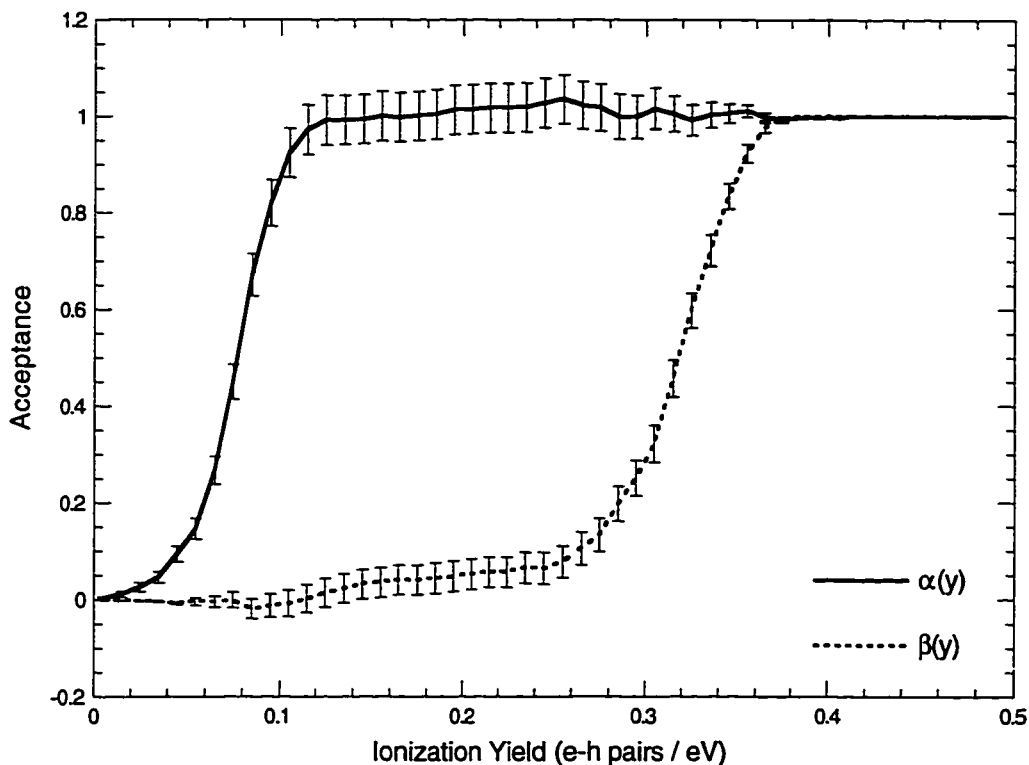


Figure 3.11. Signal and Background Acceptances. Signal and background acceptances derived from the response functions of Figure 3.10. The acceptances are the cumulative probabilities of the response functions.

is also shown in Figure 3.10 as the dotted histogram. Again, the error bars in bins with small (or negative) numbers of counts are just suggestive. The total number of counts in n_e is 223 ± 5 .

The signal and background acceptances, $\alpha(y)$ and $\beta(y)$, as functions of the cut parameter y are just the cumulative probabilities of the distributions sampled by n_N and n_e . The acceptances are shown in Figure 3.11. Again, we have not taken into account the physical bounds on the acceptances ($[0,1]$) in computing the errors. Since the response functions are well separated, the signal acceptance rises to near unity while the background acceptance is still small. This means that to zeroth order we should expect a broad minimum in the background rejection factor, Q . Figure 3.12 shows the

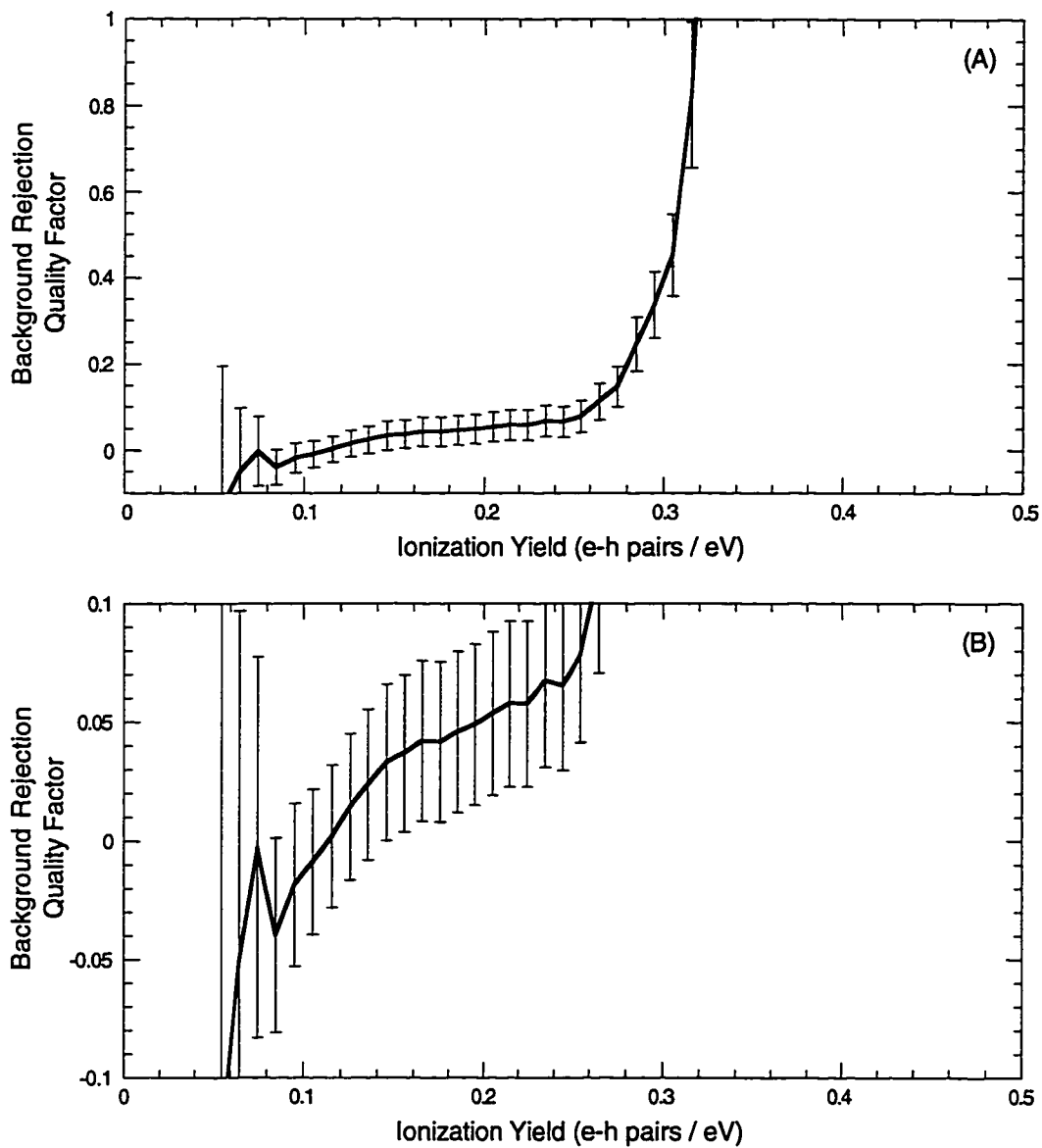


Figure 3.12. Background Rejection Quality Factor, Q .
 Background rejection factor, Q , as a function of the cut parameter, y . Smaller values are better.

resulting rejection factor, using Eq. (3.4). The physical bound on Q ($[0, \infty)$) has not been properly taken into account computing the error bars.

From Figure 3.12A we see that our general expectation from Figure 3.11 is correct: the cut parameter y can range from 0.08 eV^{-1} to 0.25 eV^{-1} and only modestly change the rejection factor. Because of the small number of events in n_1 , the subtraction

results in values of $n_e < 0$ for $y < 0.12$, so β (and hence Q) actually goes negative, though both β and Q are consistent with zero, given the errors.

Because the electronics noise dominates the noise in the phonon and ionization measurements at low energy, the distributions in y broaden, increasing the background rejection factor as we approach threshold. In order to estimate the sensitivity of the experiment in §6.8, we will need an analytic model for this behavior. Since the widths

"Since the widths are equal, the optimum value for the cut, y_c is just the average of the means, $y_c = (\bar{y}_e + \bar{y}_n)/2 = 0.20/\text{eV}$, where we have taken $\bar{y}_e = 0.33/\text{eV}$ and $\bar{y}_n = 0.08/\text{eV}$. Then we can compute $Q(E)$ from "

$$\alpha(E) = \frac{1}{2} \left(1 + \operatorname{erf} \left(\frac{y_c - y_n}{\sqrt{2}\sigma_y(E)} \right) \right)$$

$$\beta(E) = \frac{1}{2} \left(1 + \operatorname{erf} \left(\frac{y_c - y_e}{\sqrt{2}\sigma_y(E)} \right) \right)$$
(3.7)

We might want to impose the constraint $\sigma_y(E) > 0.02/\text{eV}$, corresponding to the apparent full width at half maximum of the response functions in Figure 3.10, which would take over for $E > 11.8 \text{ keV}$, but the $Q(E)$ resulting from Eq. (3.7) falls *extremely* quickly ($\sim \exp(-E/(450 \text{ eV}))$), reaching 5×10^{-10} before this constraint stops it. Instead, we will impose the constraint $Q(E) > 0.01$, not inconsistent with Figure 3.12, which takes over for $E > 4.5 \text{ keV}$.

3.4.2 Calibration Methods

It is clear from the preceding exercise that we need more data to measure the rejection factor accurately. As we will show in Chapter 6, unless they are small, the systematic uncertainties in measuring the rejection factor, especially in the determination of β , can dominate the statistical significance of the WIMP search sensitivity limit. We will show that we need of order as many calibration events as WIMP search events to avoid being limited by the systematic uncertainty in the

background acceptance, β . The relative difficulty in measuring α and β is easy to understand. Since the nuclear and electron recoils are intrinsically well separated in ionization yield, we will be operating with near unity signal acceptance. Therefore nearly all the nuclear recoils that go into a calibration are included in the running sum for the acceptance, so the statistical error is naturally small. We reject most of the background, however, so most of the electron recoils in a calibration sample are not included in the running sum in the range of interest, therefore the statistical errors are relatively large. This is the basic reason that we will need as much calibration data as search data. A further complication is the fact that the acceptances and rejection factor are energy dependent, especially near threshold. As we noted in the Introduction, the WIMP spectrum is strongly concentrated at low energy with the result that the most sensitive limits are derived from the measured spectrum at threshold, hence the focus on low energies in the discussion that follows. Because the nuclear recoil threshold in this data was 10 keV and there were so few events, we chose to consider a single large recoil energy bin, $10 \text{ keV} < E < 30 \text{ keV}$. In practice we would like to use recoil energy bins of order the detector resolution to make the most of the resolution and the WIMP search data. The key to both of these problems is to collect a large sample of known electron recoils.

The most basic approach to measuring the detector response unambiguously is to introduce a high rate source that mimics the background. This is what we did above in collecting the two data sets with an ^{241}Am source and with $^{252}\text{Cf} + ^{241}\text{Am}$ sources. By significantly increasing the event rate from a particular source, other sources of events become proportionally smaller contaminants in the sample. The main objection to this approach is that the calibration data are not taken under identical conditions to the search data: the event rate is higher, and a source is involved. It can be non-trivial to

show that the calibration data is a good mimic to the search backgrounds, and that the detector response is not affected by the high event rate.

Low Energy Sources

There is a further fundamental complication: we don't know the source of the rejection-limiting background. If it arises from a source of low energy photons external to the detector, then the electron recoil events will occur near the surface of the detector where there is incomplete charge collection, leading to a low ionization yield tail which limits the rejection. One way to reduce this background is with a simple high purity germanium or silicon wafer shielding the detector. The wafer can be made quite clean if it is placed underground immediately after crystallization from the melt, and it will completely absorb this background, significantly improving the rejection factor. In addition, the acceptance for this type of background can be measured using a set of low energy sources, or a single multi-line source. By introducing the source, we can collect a calibration data set dominated by electron recoils at low energy near the detector surface and due to the source, with a proportionately much smaller contamination of nuclear recoils than in the data presented above or obtained from the actual WIMP search. As an aside, we have made provision to install such shielding wafers in the detector towers described in Chapter 5.

Multiple Scattering

A second potential source of low energy events are Compton scatters. (Internal contamination, sources internal to the detector, will have the same event distribution as Compton scatters, so they can also be addressed by the calibration methods described below.) The fraction, $f_{low y}$, of these events that suffer charge collection losses (low measured ionization yield, y) is just the ratio of the contact thickness to the total target thickness; of course, the events with incomplete charge collection will dominate the rejection factor. A different fraction, $f_{MS} \sim 50\%$, of the Compton events have an

identifying signature: the primary photon will scatter in more than one detector (multiple scattering), leaving an unambiguous recoil at high energy that serves to tag all the coincident events as electron recoils. From all the events, the subset that contain multiple scatters serve as a calibration sample for the rejection factor. This method has a serious difficulty, however. Since only f_{MS} of the Compton events are multiply scattered, and only $f_{low,y}$ of those limit the rejection, this sample alone will not be enough events to avoid the systematic uncertainty limit. We will have to introduce a source of high energy photons that can penetrate the shielding in order to acquire enough calibration events. This will necessitate running the detector at a higher event rate, so the calibration data will not be taken under exactly the same conditions as the search data, leading to the objections noted above.

Angle Resolved Compton Scattering

A second way to obtain a clean sample of electron recoils is to use angle resolved Compton scattering.⁷⁸ In this method one irradiates the detector to be calibrated with a well collimated high energy line source. One places a second coincidence detector beyond the calibration detector at some angle to the line of sight from the source through the collimator to the calibration detector. The angle then determines the energy deposition in the calibration detector by the Compton scatter. One then acquires calibration events coincident in the two detectors with the appropriate energy in each. In effect, the calibration detector operates in a single-channel mode, not making use of its full multi-channel spectroscopy capabilities. This is the main disadvantage of the method: it takes time to scan each energy bin, *i.e.*, angle, and acquire enough events. To have sufficient angular resolution, the source and coincidence detector have to be well collimated with small acceptance angle and well shielded from each other. Further, it is hard to measure the response for small energy depositions in the calibration detector, since these are very small angle scatters and the

coincidence detector will be looking directly at the source. (This can be alleviated by working at very low rates, so that the probability of accidental coincidences is small, but this makes the calibration run even longer.)

Angle resolved Compton scattering does have one advantage over multiple scattering. With multiple scattering, we may be able to identify a pair of events unambiguously by the nature of the higher energy recoil, but we won't know that the lower energy one is due to Compton scattering (which will be uniformly distributed) and not due to photoelectric absorption (which will occur at the surface). With angle resolved Compton scattering, however, we unambiguously measure Compton events only.

3.5 Large Mass Detectors

In the Berkeley style we have several 60 g prototype germanium detectors with NTD phonon sensors and are currently constructing six 170 g detectors (BLIPs: Berkeley Large Ionization and Phonon detectors) out of natural germanium. These will be mounted in one detector tower (described in Chapter 5), for a total of 1 kg active mass.

In the Stanford style we have several small prototypes in silicon ranging from 0.25 to 4 g. We are currently constructing a 7.6 cm \varnothing \times 1 cm 100 g silicon target with four W/AI QET phonon channels and two ionization channels configured as a central fiducial volume and outer guard ring. The guard ring identifies events outside the coverage of the phonon sensors where event localization is poor. A similar sized target in germanium would weigh 250 g. A full second tower (6 detectors) of these large silicon (germanium) targets will give an active mass of 0.6 (1.5) kg.

We also have 800 g of isotopically enriched ^{73}Ge , which is interesting to search for WIMPs with only spin coupling, and 1 kg of ^{76}Ge to search for scalar coupled

WIMPS and as a control for the ^{73}Ge detector to measure the effects of isotopic enrichment on the detector performance. Detectors made from these isotopically enriched materials will be mounted in a third tower.

4. Backgrounds and Shielding

Since any background rejection technique is not perfect, an experiment looking for a small (possibly zero!) signal will most likely be limited by the background. Therefore we have made a large effort to understand what the potential backgrounds are and how to reduce their impact. We will outline the issues in §4.1, then discuss each in a little more detail. We will close with a description of the final shielding system. The background measurements, Monte Carlos, and shield design and construction were done by Dan Bauer, David Caldwell, Angela Da Silva, Mike Gray, Dave Hale, Bob Kenney, Al Lu, Boris Pritychenko, Ron Ross, Bernard Sadoulet, Al Smith, Andrew Sonnenschein, Steve Yellin, and PDB. ✓

4.1 General Discussion

There are two principle sources of background: radioactive contamination of, and cosmic ray interactions in, the detectors and surrounding materials. We have taken a number of steps to control the amount of radioactive contamination. In constructing the detector mounts and the cryostat we avoided materials that carry significant contamination. The materials we did use were screened for contamination by lot, so that we did not use supposedly clean material that was actually contaminated. We carefully prepared materials so as not to introduce contamination during processing or by dust contamination on the surface. Finally, we erected a shield to absorb the radiation from contaminated materials outside the apparatus.

The cosmic rays can be divided into two kinds, muons and hadrons. The hadrons produce radioactive contamination by disrupting stable nuclei, leaving unstable nuclei which subsequently decay. Because these radioactive decays are ultimately due to the cosmic ray flux, they are called cosmogenic activity. Though the hadrons

produce a prodigious activity at the earth's surface, they are completely absorbed by only ten meters of material, so a short distance underground the hadronic component of the cosmic rays is essentially negligible. Therefore the experiment must be performed underground, in our case at the Stanford University Low Background Facility (Stanford Underground Facility, or SUF for short). In addition, we must minimize the time the supposedly "clean" materials spend at the surface being exposed to the hadronic components of the cosmic rays.

The muon component of the cosmic rays produces radioactive contamination at a much smaller rate than the hadronic component. The muons are much more penetrating, however, so even at moderate depths they can be a problem. The unstable nuclei left in the muon wake decay by emitting α , β , and γ rays. The nuclei are usually very unstable, so the decay products are emitted nearly in coincidence with the muon passage. A plastic scintillator surrounding the shield will signal the passage of a muon, allowing us to veto any detector events nearly in coincidence. The unstable nuclei can also "evaporate" neutrons. These rattle around for a considerable time, slowly losing energy until they are captured. A neutron will scatter off the nuclei in a detector, giving a signal indistinguishable from a WIMP, so the detector background rejection techniques will not be able to reject it. This is the principle drawback in looking for WIMPs at a shallow site. With suitable moderator and by vetoing on muons, however, we can reduce the rate of neutron induced recoils to a manageable level.

Now we can see the overall shape of the experiment. It will have to be underground. The detectors, mounts, and cryostat will have to be constructed of carefully selected and treated materials, and have to be placed underground as quickly as possible. The cryostat will have to be surrounded by a neutron moderator and an absorber of α -, β -, and γ -rays that is itself clean. There will also be a muon veto. In the remainder of this chapter we will discuss these background sources and finish by

describing the final shield and its performance. A. Da Silva discusses in detail the background issues and details of our measurements and simulations.⁷⁹

4.2 Cosmic Rays

The (truly) cosmic rays hitting the top of the atmosphere are primarily protons ($\sim 10^3 / (\text{m}^2 \text{ s sr GeV})$ at $\sim 0.7 \text{ GeV}$ falling as $E^{-2.7}$), with $\sim 1/12$ as many ^4He nuclei and an approximately equal number of electrons, and smatterings of heavier nuclei up to iron (see, for example, Longair⁸⁰ or Lal and Peters⁸¹). When these particles enter the atmosphere they cause cosmic ray air showers, in the case of protons by the reactions $p(X,Y)\pi^0 \rightarrow 2\gamma \rightarrow \text{electromagnetic cascade}$ and $p(X,Y)\pi^\pm \rightarrow \nu_\mu \mu^\pm \rightarrow \nu \bar{\nu} e \rightarrow \text{electromagnetic cascade}$, where X is any nucleus present in the atmosphere. An electromagnetic cascade develops when a charged particle, π , μ , or e , in this case, emits a bremsstrahlung photon with enough energy to create charged particle pairs (e^+e^- , $\mu^+\mu^-$, $\pi^+\pi^-$) which themselves have enough energy to emit further bremsstrahlung photons. By this loop the initial energy is partitioned into equal numbers of charged particles, antiparticles, and photons, until the average particle energy drops below some critical value, $\sim 83 \text{ MeV}$ in air. If the muons from the second reaction have energies above $\sim 2 \text{ GeV}$ they will survive to the surface, giving rise to a surface muon flux. The second reaction is also responsible for the flux of atmospheric neutrinos, which can interact in the rock deep underground, leading to an isotropic flux of high energy muons (the upward-going muons measured by proton decay experiments, for example).

4.2.1 Hadronic Component

The spallation products, Y , of the reactions above include many unstable nuclei, which constitute a natural fallout, called (along with the n 's and p 's) the hadronic component of the cosmic ray flux at the surface. Two important reactions are

$^{14}\text{N}(n,p)^{14}\text{C}$ ($T_{1/2} = 5730$ years) at a rate of $2.2 /(\text{cm}^2 \text{ s})$ and $^{14}\text{N}(n,^{12}\text{C})^3\text{H}$ ($T_{1/2} = 12.3$ years) at a rate of $0.2 /(\text{cm}^2 \text{ s})$. These have a residence time in the atmosphere of order 25 years, leading to a steady natural fallout that can be incorporated in many materials during manufacturing resulting in internal contamination.

A second consequence of the spallation products is that many of them reach the surface with appreciable energies. The net flux of heavy charged particles is $\sim 10^{-4} /(\text{m}^2 \text{ s sr GeV})$ at ~ 0.7 GeV falling as $E^{-2.7}$. These scatter in materials leaving radioactive contaminants, resulting in cosmogenic activity. For example, the first generation of dark matter experiments based on HPGe ionization detectors are limited⁸² in part by internal contamination of ^3H due to exposure at the surface, as well as activity from the reaction $^{70}\text{Ge}(n,3n)^{68}\text{Ge}$ ($EC, T_{1/2} = 270.8$ d) ^{68}Ga ($\beta^+, T_{1/2} = 68.1$ m) ^{68}Zn (stable). The β^+ spectrum endpoint (including the e^+e^- annihilation energy) is 2.9211 MeV, which dominated the high energy background, including the $\beta\beta$ signal region at 2.038 MeV.⁸³ The ^3H β^- spectrum and ^{68}Ga decay, which also emits a K -shell X-ray at 10.367 keV, both affected the WIMP sensitivity.^{45,50} The internal contamination produced in the detectors would be overwhelming if we were to perform the experiment at the surface. However, most of the charged particles lose energy very quickly and are absorbed by a modest amount of material, equivalent to of order 10 m of water (m w.e.), therefore the experiment must be located at least that deep underground.

Low Background Facility

Since the detector technology is so new and significantly more complicated than the HPGe ionization detectors used in previous experiments, we decided to locate the experiment near our home institutions so we could rapidly make improvements as we learn more about how the detectors operate in extended runs. After exploring several

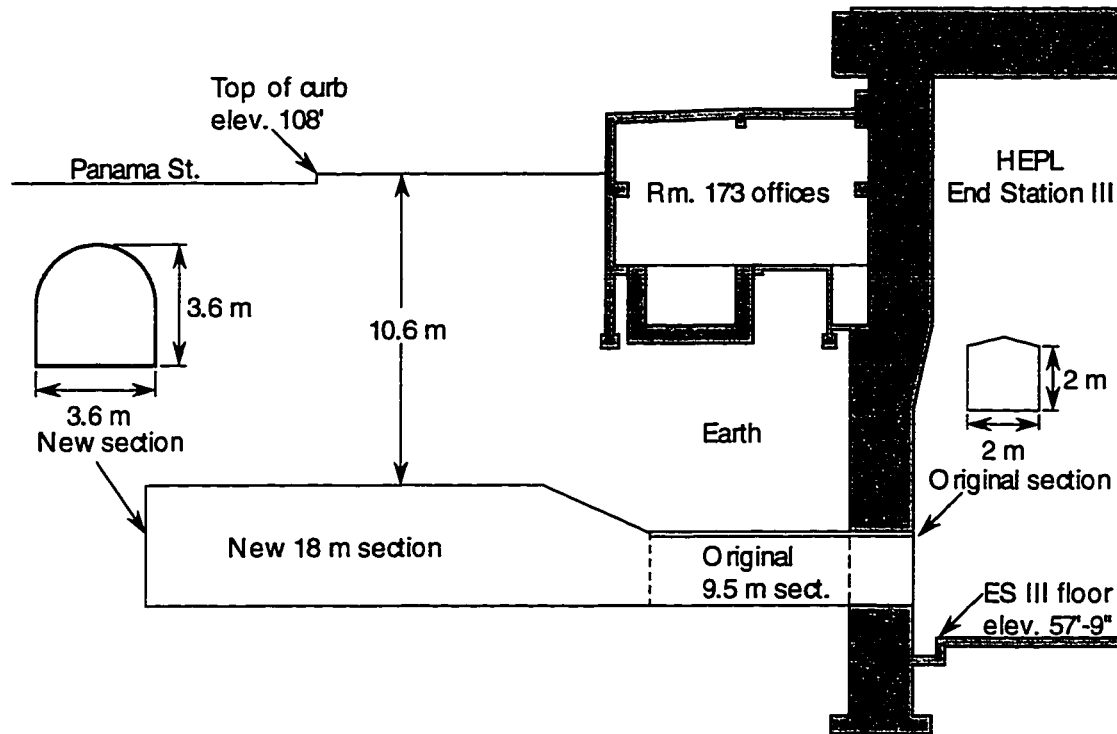


Figure 4.1. Cross Section of the Stanford Underground Facility. Cross section of the Stanford Underground Facility, or Low Background Facility, showing the access tunnel under a basement and the experimental hall extending under the adjacent road. The useful floor area is 15 m x 3 m, with a central overhead clearance of 3 m. The shielding depth is 16 m w.e.

possible sites, we elected to modify a beam dump at the Hansen Experimental Physics Laboratory on the Stanford University campus (see Figure 4.1). We extended the beam dump, which had never been used, into a small experimental hall, approximately 15 m long and $(3 \text{ m})^2$ in cross section. By locating the hall past the end of the original beam dump, we are under a road, not under the basement of the annex above, so we have $16 \pm 1 \text{ m w.e.}$ shielding in all directions overhead.⁷⁹

4.2.2 Muons

Because they only undergo ionization losses, the muons are much more penetrating than the hadronic component of the cosmic rays. At 16 m w.e. the muon flux, $29.2 \pm 0.2 /(\text{m}^2 \text{ s sr})$, is just starting to fall significantly with increasing depth. A

passing fast muon has a number of consequences. The emitted bremsstrahlung photons Compton scatter repeatedly until they are absorbed by the photoelectric effect. One of the scatters can be in the detector itself, giving an electron recoil background event. These electron recoil events are closely related in time to the muon passage, so they will be efficiently removed by a muon veto, even before using the detector discrimination. Both real and virtual photons associated with the muon can lead to neutron production by photonuclear reactions (γ, n) or photofission (γ, Xn). Finally, a slow negative muon can capture and produce neutrons by $\mu^-(p, n)\nu_\mu$. The neutrons are particularly damaging since they rattle around a long time (175 μ s in polyethylene⁷⁹), possibly scattering in the detector giving a nuclear recoil background, before becoming slow enough that the resulting nuclear recoils are below the detector threshold.

At our shallow depth, the neutrons due to muons are quite significant. The measured flux in the tunnel at Stanford is $(8.1 \pm 0.6) \times 10^{-5}$ neutrons/(cm² s) with energies above a few hundred eV.⁷⁹ This is completely dominated by neutron production in the cement and dirt from muon interactions. Inside a 20 cm thick lead shield, needed to absorb the external photon background (discussed below), the neutron flux increases by almost a factor of 22 due to muon interactions in the lead. The flux is approximately linear in the lead thickness at least up to 20 cm thickness.

Neutron Moderator

One line of defense against the muon induced neutrons is to moderate the neutrons below detector threshold before they reach the detector. Note that an 18 keV neutron has a maximum energy deposition on germanium of 1 keV. The most efficient moderator is hydrogen, or more practically, polyethylene, where the neutrons lose on average half their energy in each scatter. There is also neutron production in the polyethylene. A steady state between production and moderation is reached with ~20 cm of polyethylene, so a thicker moderator generally won't reduce the background

significantly. When the polyethylene is surrounded by a 10 cm lead shield, ~30 cm of moderator is required to have equal contributions from the polyethylene and the lead. Muon interactions in the cryostat are also a significant source of neutrons. By sacrificing some detector volume we can line the inside of the cryostat with 10 cm of moderator which will reduce the rate significantly.

Muon Veto

In addition to the moderator, a second line of defense against the neutrons (and the photons due to muon passage) is to surround the lead shield with a muon veto made of plastic scintillator. The veto has to be thick enough to separate the muon signals (minimum ionizing, $\sim 2 \text{ MeV}/(\text{g cm}^2)$) from the large flux of photons due to radioactive contamination in the laboratory, which have a maximum energy $\sim 2.5 \text{ MeV}$. In addition, for each detector event the data acquisition should record both the time since the most recent veto hit and the signal amplitude in the veto, so that in the analysis both the veto time and the sensitivity to muons can be traded against live time to obtain the best WIMP sensitivity. Since the muons come primarily from overhead (approximately $\cos^2\theta$ distribution, where θ is the zenith angle) the veto is built very hermetic at the top (and less so at the bottom where the lead shield is supported). We expect to have an efficiency for detecting muons of better than 99%.

The simplest way to apply the muon veto is just to reject any event with veto activity in the prior $\sim 200 \mu\text{s}$. Since the capture time constant is $175 \mu\text{s}$, $\sim 70\%$ of the neutrons will be captured in the veto time with a dead time of 10%. The actual neutron veto factor will be higher, since the neutrons drop below threshold before they are captured. However, the 2.2 MeV capture gamma can Compton scatter in the detector giving an event low enough in energy that the detector electron/nuclear recoil discrimination is not very effective. A more sophisticated approach would use the full time distribution between the veto signal, the first event in a detector, and a possible

second event in a detector (multiple scattering). If the Monte Carlo can accurately reproduce the distribution for modest times, we can use the simulation to estimate and statistically remove the total contribution to the event rate from muon related activity. We will return to this point in §6.3.3

The final handle on the muon induced neutron background that escapes the veto is multiple scattering. A substantial fraction of the neutrons will scatter in two detectors, unambiguously tagging the events as due to neutrons. (The WIMP scattering probability is so low that the probability of scattering twice is completely negligible.) This fraction can be simulated in a Monte Carlo that has been checked against the measured multiple scattering fraction as a function of the veto time.

4.3 Radioactive Contamination

The methods described in §4.2 deal with the backgrounds due to the cosmic rays. We also have to minimize backgrounds due to contamination of materials by naturally occurring, man-made, and cosmogenic radioactive isotopes. The significance of a given contamination depends on several factors. Clearly, the concentration of the isotope and its proximity to the detector are important. The nature and energies of the decay products are also significant. Not so obvious is the fact that only isotopes with moderate half-lives are important: for a given concentration, a very long half-life leads to a very low decay rate, hence negligible background, whereas a short half-life will decay away during the first few weeks or months of the experiment, *i.e.*, we can wait them out.

4.3.1 Sources

Of the 287 naturally occurring isotopes, only 28 are radioactive.^{84, 85} Most of these do not show up in everyday materials; only ^{238}U , ^{232}Th , and ^{40}K are important

natural sources of background in most materials. The uranium and thorium have the only naturally occurring extended decay chains, which after 14 (10) steps, respectively, stop with ^{206}Pb (^{208}Pb). ^{222}Rn in the uranium chain migrates through the ground as a gas, eventually leaking out of the ground at a rate of 6.2×10^8 atoms/(m² d).⁸⁶ The radon can be removed fairly easily by sealing up the apparatus with plastic, then flushing with old compressed air or liquid nitrogen boil-off. In addition, the concentration in the laboratory can be reduced by changing the air several times per hour with air from the surface, not from elsewhere in the building. ^{210}Pb , also in the uranium chain, is a significant contaminant in most lead, since the ore usually contains significant ^{238}U contamination. The β^- decays of ^{210}Pb and ^{234}Th in the uranium chain and ^{228}Ra and ^{212}Pb in the thorium chain lead to significant electron fluxes at low energies, while the higher energy β decays give bremsstrahlung photons. In addition, there are ~40 photon lines in each chain with absolute intensities > 1%.

^{40}K is a significant background source because potassium is ubiquitous. In particular, aluminum and glass (*i.e.*, fiberglass, including G10 and FR4 used in circuit boards) usually have significant concentrations. ^{40}K decays primarily by β^- (89.3%) and electron capture (10.3%) accompanied by a 1.46 MeV gamma ray.

Another isotope of importance is ^{115}In , which constitutes 95.7% of natural indium. Indium wire is the most commonly used cryogenic gasket material.

Because of all these activities, it is important to minimize the concentration of the uranium, thorium and potassium parents in the materials used in the experiment. The concentration is usually expressed as the number of decays per kg of material, (Bq/kg), as the mass of parent isotope per mass of material (g/g), or parts-per-million/billion (ppm/ppb = 10^{-6} / 10^{-9} g/g). The potassium concentration quoted is total potassium with the assumption that the ^{40}K fraction is 10^{-4} . Typical concentrations in the ground are ~40 Bq/kg for uranium and thorium.^{87, 88} In a clean material like electro-

refined copper, however, the concentrations are routinely below 0.86 (0.49) [8.3] mBq/kg uranium (thorium) [potassium].⁸⁹

Finally, there are a number of man-made isotopes that can lead to significant backgrounds. Since World War II, producers of steel (including stainless steel, an important cryogenic construction material) have used ⁶⁰Co pellets embedded in the walls of their furnaces to monitor the erosion of the walls. Since it was heavily recycled in the 1950's, all stainless available today contains ⁶⁰Co contamination.⁹⁰ Atmospheric nuclear weapons test and reactor accidents have added significant quantities of ³H, ¹⁴C, ⁹⁰Sr, and ¹³⁷Cs to the atmosphere. This nuclear fall-out can be incorporated in materials during manufacture or appear as surface contamination on finished parts.

For non-cosmogenic activity, there are only two ways to reduce the activity: choose intrinsically clean materials and/or store the material underground until the activity decays away. Materials are intrinsically clean either because the raw materials don't carry much contamination or because the contamination is removed by the production process, as in electro-refining copper.

4.3.2 Cosmogenics

Having selected or refined some material to remove naturally occurring or man-made activity is not enough, however. Most materials that have been at the surface for any length of time also show activity due to exposure to the cosmic rays. Again using copper as an example, one typically sees lines due to ⁵⁴Mn, ⁵⁹Fe, and ^{56,57,58,60}Co at the level of a few $\times 10^{-4}$ Bq/kg.⁹¹ This activity can be minimized by keeping the material at the surface for as little time as possible after the refining step. We stored the copper for the cryostat underground when it was not being worked on. We also store the BLIP detectors, from the raw germanium to finished state, under 4 m w.e. of shielding when they are not actually in process.

4.3.3 Shielding

The net effect of contamination by the uranium and thorium chains and potassium is typically a falling photon flux extending to the 2.614 MeV line from the ^{208}Tl in the thorium chain, which is the highest energy naturally occurring line. The spectrum is punctuated by a large number of prominent lines. As photons from a given line propagate through the material, they are repeatedly degraded by Compton scattering until eventually they are stopped by the photo-electric effect. As the photons at one energy are degraded they are "replaced" by the degradation of photons of higher energy. Therefore, for reasonably thick pieces of material the spectrum reaches a steady state consisting of lines above a smooth continuum.

Since the WIMP signal is at fairly low energy, one might guess that we could shield with only a relatively thin layer of clean material to absorb the low energy part the spectrum. This only works if the shield layer is immediately around the detector. For example, a silicon wafer immediately above and below the detector will stop the low energy flux that would have been absorbed in the surface where the detectors have inefficient charge collection. However, if there is a significant amount of intervening radio-pure material, the low energy flux will be replenished by the degradation of the high energy photons as they pass through the clean material. In addition, the high energy photons can Compton scatter in the detector resulting in low energy events. Therefore the effective attenuation of a shield, even at low energy, is governed by the total cross section at relatively high energy, around 1 MeV. It so happens that all materials have roughly the same cross section per unit mass in this region, resulting in an attenuation length (expressed as mass per unit area) of 20 g/cm^2 . Therefore, the smallest shield can be made from the most dense clean material available, which is usually lead. To bring the flux from the ppm concentrations in the laboratory walls

down to the flux from the ppb concentrations in the lead and copper, we need $-\ln(10^3) \times 20 \text{ g/cm}^2 = 140 \text{ g/cm}^2$ or 12 cm of lead.

4.3.4 Cleanliness

We have taken a number of steps to reduce or eliminate surface contamination of parts, which usually consists of contaminated dust. First, we took several steps to reduce the amount of dust in the air around the experiment. The concrete walls were sealed and painted so that they would not be sources of dust. The fresh air is filtered before entering the SUF at the experiment end. The air flow then flushes out the rest of the tunnel to the entrance, preventing air-borne contaminants in the rest of the building from reaching the experiment, as well as reducing the radon concentration. The shield and cryostat are also separated from the normal work areas by a plastic curtain to further reduce diffusion of contaminants towards the experiment. When the cryostat is open, exposing surfaces that are very near the detectors, a HEPA filter unit operates on the experiment side of the curtain and all personnel wear clean room suits, hats, boots, and gloves. At all times personnel clean their feet on clean room tacky mats before passing through the curtain. There are additional tacky mats at the entrance to the tunnel and at the entrance to the main work area where the tunnel bends and opens up (see Figure 4.1).

All equipment entering the main work area is cleaned with either distilled water or alcohol. All parts passing through the curtain are cleaned in alcohol immediately beforehand. The cryostat parts were cleaned in alcohol in a separate clean room and double bagged, with the outer bag removed in the work area, and the inner bag removed just before passing through the curtain.

4.4 Shield Design and Performance

The final shield is sketched in Figure 4.3. Inside the cryostat and surrounding the detectors is ~10 cm of polyethylene to moderate the neutrons produced in the copper. The cryostat itself is surrounded by a magnetic shield. Outside the magnetic shield is ~20–25 cm of polyethylene to moderate the neutrons produced in the ~15 cm lead shield, which is surrounded by the 4 cm thick muon veto scintillators.

Using a 3" NaI(Tl) scintillator (at room temperature), we have measured 99.5% muon detection efficiency for muons passing through the NaI counter at the center of the cryostat. With a HPGe detector located just inside the copper liner, we measured 99.8% muon detection efficiency. Because muon interactions in the cryostat itself are the dominant source of neutron background, these measurements are only an estimate of the relevant veto efficiency. It would have been better to make a box of scintillators of the same size as the cryostat and measure the muon veto efficiency before the cryostat was installed. Even so, we can say that the veto works extremely well. To estimate the sensitivity of CDMS in §6.8 we will assume a veto efficiency for muon related neutrons of 98%.

We have no direct measurements of the neutron flux or spectrum inside the shield. We have simulated the nuclear recoil spectrum in the detectors due to muon-induced neutrons in the lead and cryostat; the contribution from the polyethylene layers is negligible.⁷⁹ The simulation does not include the muon veto. The resulting spectrum is shown in Figure 4.2. A secondary result from the simulation is the distribution of neutron capture times, which is exponential with a time constant of 175 μ s. The time distribution for the neutrons to drop below threshold will have a shorter time constant than the capture time distribution.

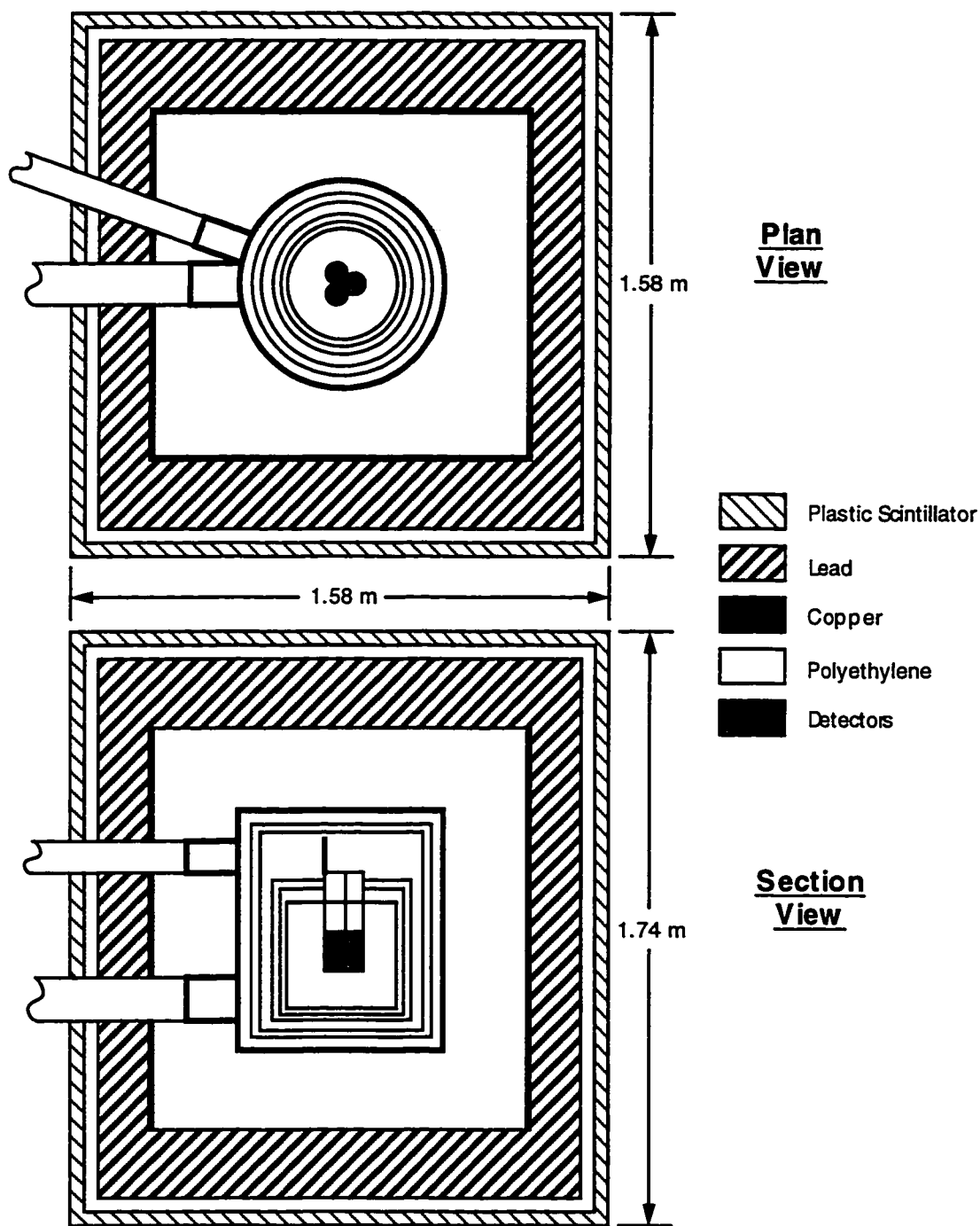


Figure 4.3. Shield Design.

Plan and section views of the shielding system surrounding the cryostat. Inside the cryostat and surrounding three detector towers is ~10 cm of polyethylene to moderate the neutrons produced in the copper. Outside the cryostat is ~20–25 cm of polyethylene to moderate the neutrons produced in the 15 cm lead shield, which is surrounded by the 4 cm thick muon veto scintillators. The thick-lined region of the cryostat is surrounded by a magnetic shield.

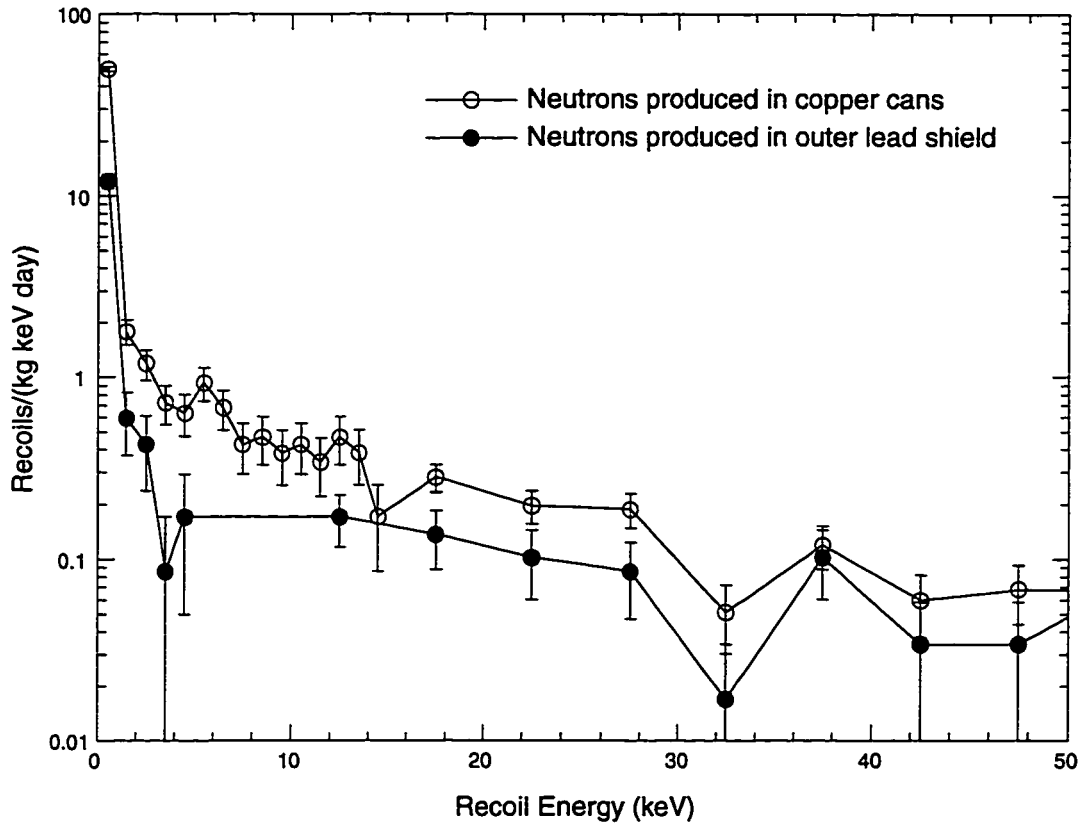


Figure 4.2. Simulated Nuclear Recoil Spectrum in the Shield. Simulated nuclear recoil spectrum in the detectors from muon-induced neutrons produced in the lead and the cryostat before applying the muon veto. The contribution from the polyethylene layers is negligible.

The predicted nuclear recoil spectrum is mostly due to muon-induced neutron production in the cryostat. Before applying the veto the predicted recoil rate at 10 keV recoil energy, ~ 0.4 events/(kg keV day), is ~ 0.15 of the rate seen in the Oroville detectors at threshold. (The Oroville threshold is ~ 3.5 keV equivalent electron energy, which corresponds to a recoil energy of 10 keV.)

In §6.8 we will need the nuclear recoil background spectrum to estimate the ultimate sensitivity of the experiment. We will use $5 \text{ counts}/(\text{kg day}) \times E^{-1}$, which is a rough fit to the neutron spectrum from the copper cans plus the outer lead shown in Figure 4.4.

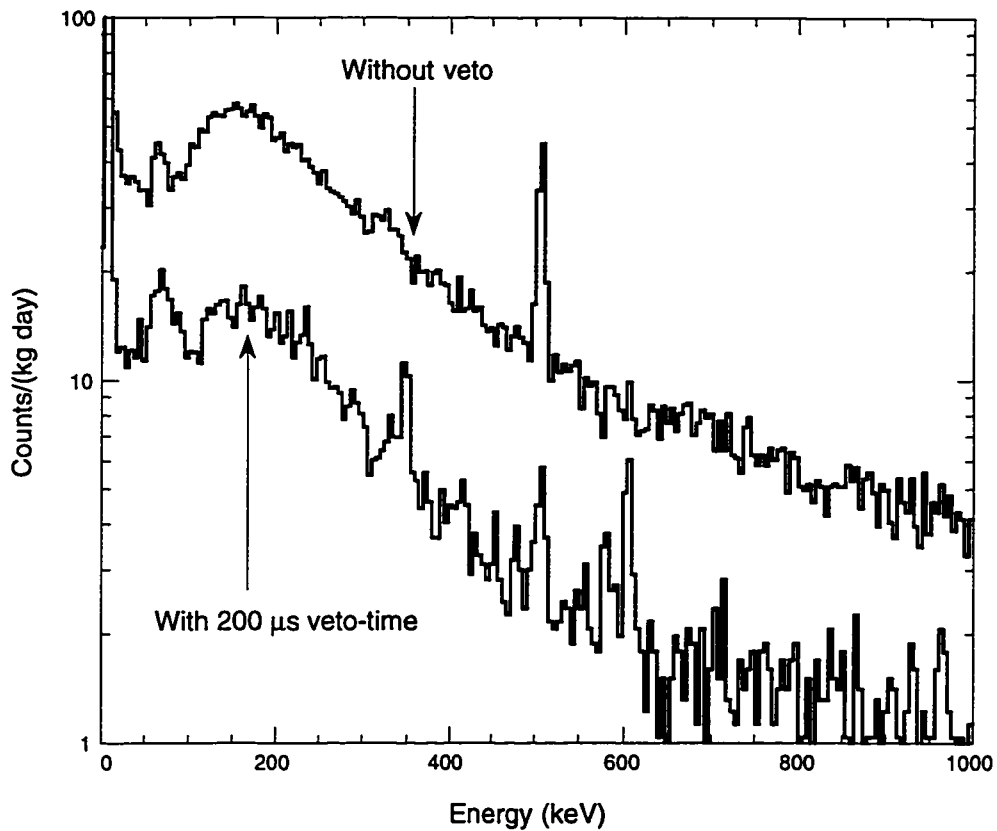


Figure 4.4. Photon Spectrum Inside the Shield.

Photon spectrum just inside the copper layer of the shield measured with a 850 g HPGe detector before the cryostat was installed. The volume to be occupied by the cryostat was filled with polyethylene.

With the same HPGe detector used above we measured the photon background just inside the copper layer before the cryostat was installed; the central volume for the cryostat was filled with polyethylene.⁷⁹ Figure 4.4 shows the raw spectrum and what is left after applying a 200 μ s veto. (Veto times longer than 200 μ s do not decrease the count rate any further.)

At low energy the mean counting rate is 12.4 counts/(kg keV day) after applying the muon veto. This residual rate is not the end of the story, however. From other measurements, we know that up to 4.7 counts/(kg keV day) is due to the HPGe detector background⁷⁹ and a significant piece of the remaining rate (7.7 counts/(kg keV day)) is

caused by ^{210}Pb contamination in the lead used for the shield. From measurements and Monte Carlo we have determined that this background is attenuated by a factor of ~ 5 by a 1 cm thick liner of cleaner (and significantly more expensive) "Nantes" lead.⁷⁹ This could be installed either around the cryostat or inside the cryostat around the internal moderator. This liner will increase the muon related neutron background because of the increased amount of material inside the first moderator layer. We will have to balance these two effects to obtain the optimum shielding configuration for our shallow site.

To estimate the sensitivity of CDMS at Stanford in §6.8 we will use 8 counts/(kg keV day) as an estimate of the low energy electron recoil background after applying the muon veto, and also assume that this rate is independent of energy. This value is consistent with either removing the detector background or installing the Nantes lead. The rate will be further reduced by the electron/nuclear recoil discrimination factor, Q .

4.5 Diagnosing the Measured Electron Recoil Background

Suppose we have accurately measured the detector response both to external low energy photon sources and to Compton scattering with small energy deposition, by the methods in §3.4.2. How can we look at the search data to disentangle the two background sources? The total Compton induced background is a lower limit to the total background. Using a Monte Carlo we can vary a source spectrum at high energy, seeking agreement with the search data on the total observed spectrum at high energy and on the distributions of multiple scattering events, both between the detectors and in energy. The low energy event rate of this model is a lower limit on the total incident background at low energy. Any excess is due to an external flux of low energy photons or to internal contamination.

Most radioactive decays that might contribute to internal activity have associated photon lines. Some of those photons will be absorbed completely, leading to lines in the search data identifiable as internal activity because the total event energy will include the nuclear recoil of the parent nucleus. The additional energy of the nuclear recoil will be absent if the line is due to external contamination. The total contribution of this internal activity will also have to be modeled by Monte Carlo, using the measured line strengths as constraints.

Any remaining background not accounted for by Compton scattering or internal contamination must be associated with a flux of low energy photons.

5. Cryostat

The cryostat poses unique challenges of cryogenic engineering. At the time we started the design, the Stanford group was developing α -phase tungsten transition edge sensors which have a critical temperature of 15 mK. We wanted the base temperature of the cryostat to have some margin below this value. At the same time it was clear that some parts of the cryostat would have to be located inside the clean lead gamma shield, so the cryostat itself would have to be radiopure. This rules out most of the standard cryogenic construction materials and techniques. We could see two basic approaches. One is to construct a dilution refrigerator out of radiopure materials, a daunting task (but attainable, see the cryostat of Fiorini's Milano group⁹²). The two main drawbacks are first that the cryostat becomes very tall, increasing the construction costs of the underground laboratory and reducing the overhead shielding at a shallow site, and second that a muon veto becomes very large, since it must surround the entire refrigerator at a shallow site (or cover the apparatus at a deep site).

The second approach is to house the detectors in a clean cryostat that penetrates the shield and is connected on the outside to a standard fridge. Here there are two variants: the clean portion can hang below the fridge and include shielding doglegs on at least some of the cold layers (see, for example, the EDELWEISS⁹³ or CRESST^{93,94} cryostats), or the cryostat can extend out sideways from the fridge, creating one dogleg, and the experimental volume can be further offset from the penetration in a second dogleg. The first variant suffers from the same height and veto problems as the clean fridge approach. One might try to neck down the thermal layers below the mixing chamber to allow a veto to enclose only the clean portion of the cryostat, but then the veto inevitably has a large hole in the top, where most of the muons come from. Since we knew the sensitivity of the experiment would ultimately be quite sensitive to the veto efficiency, we opted for the "sideways" approach.

In the rest of this chapter we outline the main design issues and the overall layout, then describe the novel solutions we developed. We also describe the monitoring system sensors and readout paths, and finally discuss operation and performance of the cryostat. For brevity, we will not discuss the design and operation of dilution refrigerators, nor the standard nomenclature for the thermal layers. These and other cryogenic techniques are well described in the standard literature.⁹⁵⁻⁹⁸ Before getting into the details any further, we should give credit to the Icebox team for the cryostat work described here: Peter Luft, Justin Orion, Paul Pipersky, Ron Ross, Bernard Sadoulet, Richard Schaefer, John Taylor, Storn White, Richard Wolgast, and PDB.

5.1 Major Design Issues

The main design issues are: (1) what standard materials are radiopure and (2) how to use them to replace the standard impure materials, (3) how much space is available for detectors, (4) how much space is available for amplifier components mounted at 4 K, (5) how much space for wiring from the components at 4 K to the detectors, (6) how the wiring from 4 K runs to room temperature, and (7) how to accommodate the thermal contractions of the layers as the system cools.

Somewhat arbitrarily, we focused on $\pi/4$ ft³ (a cylinder one foot in diameter and one foot high) as a starting point for the available detector volume, keeping an eye out for thresholds in size where the performance begins to change dramatically. Having decided on a "sideways" design, we next wrestled with the detector wiring path. In the target volume we could imagine mounting ~100 kg of 1 kg germanium detectors, with a total of ~1000 signals to room temperature. In addition to the number of signals, many of them have to be in a shielded configuration, so the wiring bundle is quite large. We could not see how to run the bundle down through the fridge, heat sinking it along the

way, to reach the horizontal "stem" section and go out to the detectors. We determined that wire access in the middle of the stem section would be extremely difficult to engineer. Ultimately, we decided to allow a second sideways penetration (the E-stem) of the shield and muon veto for the detector wiring.

With the overall shape determined (see Figure 5.1), we next looked at internal details. As already mentioned, the horizontal section connected to the fridge is called the "stem" or "cold stem" (or "C-stem," or even "F-stem"), the horizontal section for the detector wiring is the "electrical stem" or "E-stem", and the sections surrounding the detectors are the "cans." The entire cryostat except the fridge is called the "Icebox." (Icebox was the first name, but a concern that the association of "ice" and 273 K was misleading for a 10 mK beast led us to use the name "Coldbox." When we discovered that the expansion engine of our closed cycle helium liquefier had prior claim to "coldbox," we switched back to "Icebox.") We typically refer to a particular thermal layer by the name of the cooling source in the fridge, and less often by the nominal base temperature of the layer. Therefore we have the Outer Vacuum Can or Room Temperature (OVC or RT), Liquid Nitrogen (LN), Liquid Helium (LHe), Still (ST), Cold Plate (CP), and Mixing Chamber (MC) layers with nominal base temperatures of 300 K, 77 K, 4.2 K, 600 mK, 50 mK, and 5 mK, respectively. To avoid false expectations about the thermal performance, the cans are labeled by the temperature we expected to achieve there, not the base temperature of the layer back at the fridge, so we have the 300 K, 100 K, 9 K, 900 mK, 100 mK, and 10 mK cans, respectively. Of course, we are not obliged to operate the coldest can at 10 mK. In practice the fridge will operate stably up to several hundred milliKelvin.

The thermal contractions bedeviled every step of the conceptual design. To better control microphonic noise we tried to design the cold stems with expansion joints so the cans could be rigidly mounted one from the next. Our thermal modeling showed

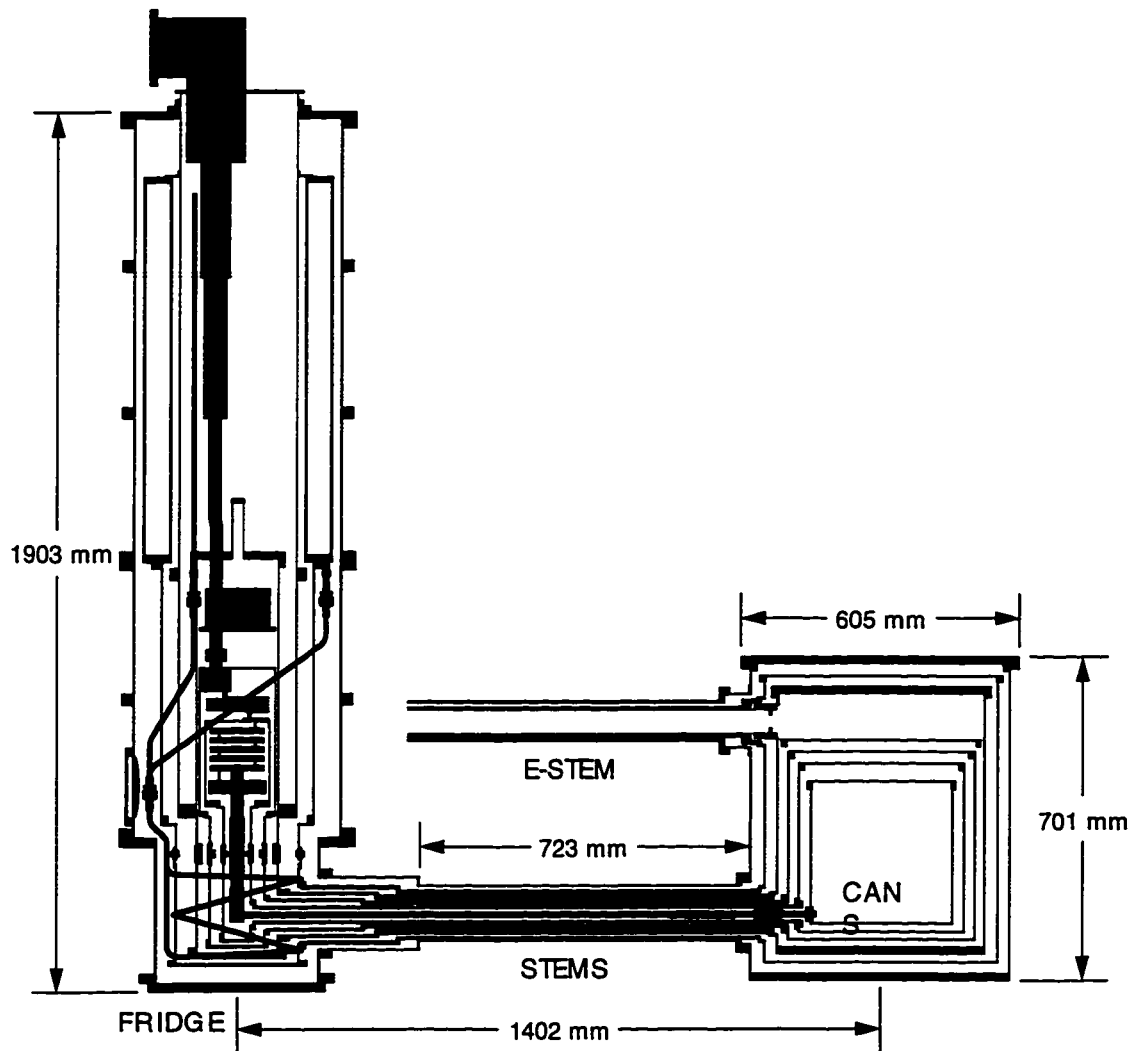


Figure 5.1. Icebox Layout.

Layout drawing of the dilution refrigerator and the Icebox cryostat. The vertical section at the left is the dilution refrigerator. The detectors sit at the center of the nested cans at the right. The cans are cooled by conduction along the stems which connect each can to the corresponding layer of the fridge. The second set of stems at the top of the three warmer cans carry the wiring for the detectors.

that the most difficult layers are the LN and LHe, since the heat flow along the layers is substantial, ~ 40 W and ~ 1 W, respectively, due to black body radiation from the next warmer walls. The thermal contraction along the length of the stem is also substantial, ~ 4 mm and ~ 6 mm, respectively, similar to the thermal contractions vertically on the same layers in the fridge. Therefore the stem has to contain a section that can extend

with a small force and it must allow the fridge end to rise without transmitting a large torque. In addition, the liquid helium cooled layer has to be helium leak tight (to a level of $10^{-(4-5)}$ atm cm³/sec) to contain the exchange gas used during the cooldown. We were unable to design a reasonably compact, high thermal conductance, low spring constant, flexible section for these layers.

A second problem in the rigid design is the low thermal conductivity legs for the cans to stand on. Because the cans are quite large and heavy, any support strong enough to carry the load in compression also has a substantial thermal conductance, which gives a large heat load on each stage. Ultimately, we settled on the "porch swing" design described below in §5.2.

As already discussed in §4.3.1, most of the standard cryogenic materials are forbidden because of radioactive contamination. Brass, used for flanges and screws, is an alloy so it is not particularly clean to begin with. It usually contains a few percent lead (essentially a lubricant) to improve its machining characteristics, leading to bremsstrahlung from the high energy beta decay of the ²¹⁰Bi daughter of ²¹⁰Pb. Stainless steel is widely used for screws and mechanical support between thermal stages because of its low thermal conductance to yield point ratio. However, most stainless contains ⁶⁰Co, which beta decays with two high energy gamma rays. Aluminum is used for vacuum and liquid vessel walls from room temperature down to LHe, but it contains potassium which contains ⁴⁰K which decays predominantly by electron capture with a high energy gamma. Silver alloys are used as brazing material to make all vacuum joints between stainless steel and copper, but silver has two long lived isotopes from cosmogenic production (¹⁰⁸Ag, ¹¹⁰Ag). Finally, the most common cryogenic vacuum seal uses indium wire for the gasket, but indium beta decays. This leaves us with copper as the only standard cryogenic material we can use.

The sideways design eliminates the need for most of the standard but radioactive materials. We can use a conventional fridge since it is outside the lead shield. To avoid all brazing material and welding stinger rods we used parent metal only full penetration electron beam welding for all joints. Instead of brass flanges, we use copper flanges with threads made by forming, not cutting, taps. We found a source of reasonably clean brass and had all the screws made from this material. In place of stainless steel rods to hang the cans from, we use Kevlar loops. The most difficult problem is working without indium. To make the seals, we developed a rounded nose sealing design using hardened copper flanges, a soft copper gasket, and brass screws.

With these solutions, we spent ~3 calendar years designing and ~2 calendar years (partially in parallel with the design time) constructing an all copper cryostat put together with electron beam welds and clean brass screws. The total cost, including the dilution fridge and support equipment, approached one million dollars. Most of the detail drawings are referenced in two assembly drawings: LBNL Mechanical Engineering Drawings 22G3626 ICE BOX PAIL ASSEMBLY and 22G3536 E-STEM ASSEMBLY.

5.2 Overall Layout

The overall Icebox layout is shown in Figure 5.1. The vertical section at the left is an Oxford 400S⁹⁹ dilution refrigerator with a liquid nitrogen bath and no liquids below the mixing chamber. It has a base temperature under 5 mK when operated by itself. All cooling power is generated in the fridge. The parts below the level of the mixing chamber where each layer makes a step to smaller diameter are the tails with their side-access ports. Each tail has a removable bottom cover to allow the bolts attaching the tail to the fridge to be tightened after all the stems have been connected to the tails. The nested horizontal tubes are the cold stems, which connect on the left to

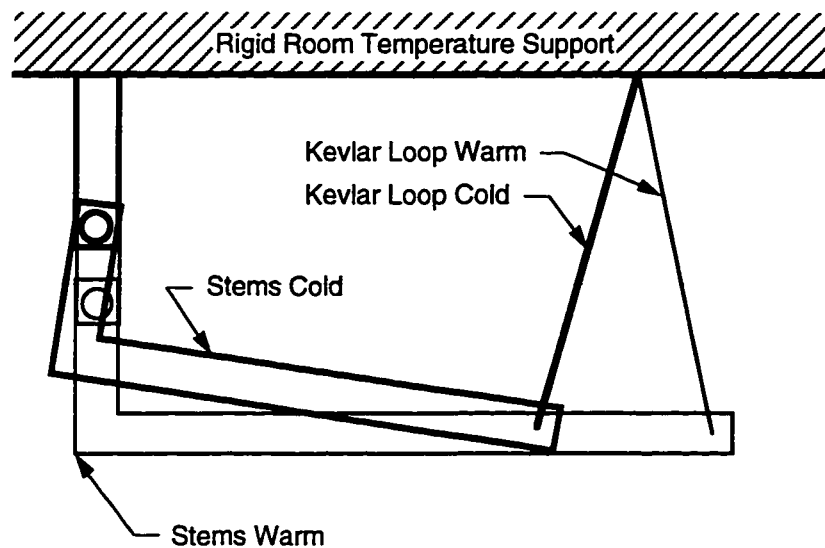


Figure 5.2. Schematic of the Cryostat Motions During Cooldown. The thin lined object is an extremely simplified model for one layer of the cryostat in the warm (300 K) condition. As a result of thermal contractions, in the cold condition the hinge axis in the tail is lifted by $-4-6$ mm, causing the stem to tilt by -4 mrad. At the same time, the contraction of the stem pulls the base of the can, supported by the Kevlar loop, to the left. The net result, exaggerated to make them visible in the figure, including contractions and motions, is represented by the thick line object.

the side-access ports of the tails and on the right to the lower flanges on the cans. Each layer of the fridge supports the weight of the corresponding tail and the left (cold) end of the corresponding stem. The other end of each stem is supported by the corresponding can, with each can hung by Kevlar loops from the next warmer can. The ultimate support is the room temperature OVC (Outer Vacuum Can) can. The top of each can is removable to allow installation and removal of the detector/amplifier packages. At the side of each of the OVC, LN, and LHe cans near the top is another port for the E-stem layers. Each of these is supported by the can at one end and the room temperature feedthrough box (not shown) at the other.

The porch swing design accommodates the thermal contractions as illustrated in Figure 5.2. At all times the tails remain centered on the vertical axis of the fridge. As already mentioned, the cans are not rigidly connected one from the next, but are hung

on a pair of Kevlar loops (described in §5.4.3 below) with the plane of the loops perpendicular to the stems. These loops act as the chains at either end of a porch swing, allowing the can to move toward the fridge as the stem contracts. As the fridge contracts during the cooldown each tail is lifted up by the fridge, while the cans move up vertically because of the contraction of the Kevlar. The tails are not rigid bodies, but are hinged, again in a plane perpendicular to the stems. This hinge allows the tail/stem/can rigid body to rotate about the tail hinge as the tail lifts up. During installation the LN and LHe stems are on the OVC stem centerline, so that when cold the LN stem is above the OVC centerline, the LHe stem is slightly above the LN centerline, and the colder stems are on the LHe centerline. We allowed enough clearance in the stems to accommodate worst case motion. Starting with all parts on centerline warm eases the assembly.

5.3 Thermal Model

We made significant use of a thermal model for the cryostat to explore the impact of alternative designs and materials. There exists a vast thermal engineering and modeling literature not referenced here. We will motivate the main results needed to do the modeling, and explain the underlying physical mechanisms. By treating the carriers of thermal energy as a gas, we can make simple models for the thermal and electrical conductivities. Then using the definition of the thermal conductivity, we can make an analogy to the electrical case, with the thermal conductivity replacing the electrical conductivity, the temperature replacing the voltage, and the heat flow (power) replacing the electric current. We can develop this into expressions relating the integral of the thermal conductivity to the power flow in a part, which leads to a scheme for modeling the entire cryostat.

5.3.1 Thermal Conductivity: Microscopic Physics

A simple model for the thermal conductivity explained in all the solid state physics textbooks is based on the kinetic theory of gases (see, for example, Kittel¹⁰⁰). The model assumes that the conduction arises from a diffusive process, hence the power is proportional to the gradient of the temperature. Thermal energy is carried by a number density, n , of particles with individual heat capacity, c . The particles move with an average velocity, v , over a mean free path, ℓ , which is limited by scattering processes to be described later. The flux of particles crossing an isotherm from the warm side is $\frac{1}{2}nv$, where $v_x^2 = \frac{1}{3}v^2$ is the average velocity in one dimension (squared). Each particle is coming from a region characterized by $T + \Delta T$, and gives up energy $c\Delta T$ when it scatters. The temperature difference is just $\Delta T = \ell \nabla T = \tau v_x \nabla T$. The flux crossing in the other direction comes from a region cooler by ΔT , so the net energy transport is

$$\mathbf{j} = -\frac{1}{2}nv, 2v_x \tau \nabla T = -\frac{1}{3}Cv\ell \nabla T, \quad (5.1)$$

where C is the bulk heat capacity. We take the coefficient, $\frac{1}{3}Cv\ell$, as the thermal conductivity, κ , which may be temperature dependent, $\kappa(T)$.

In insulators the energy carriers are phonons. At low temperatures the mean free path becomes limited by impurity scattering (or the size of the sample, if it is clean). We can use the Debye model (again see Kittel¹⁰¹) which assumes a constant phonon velocity, and gives $C \propto T^3$. This predicts a low temperature thermal conductivity proportional to T^3 . In practice, the exponent is often less than 3. At high temperatures, the phonon mean free path is limited by scattering off of other phonons. The number density of phonons grows as T , so the mean free path and the thermal conductivity are proportional to T^{-1} . Again, in practice the exponent is often less than one. Some example thermal conductivities are given in Appendix A.

5.3.2 Metals and the Wiedemann-Franz Law

In metals, the electron velocity is much larger than the phonon velocity, so the thermal conductivity is (usually) dominated by the electronic contribution. The free electron Fermi gas model predicts a specific ratio between the electronic thermal conductivity and the electrical conductivity,^{102, 103} known as the Wiedemann-Franz Law (W-F):

$$\kappa(T) = \frac{\pi^2 k_B^2}{3e^2} T \sigma(T) = \mathcal{L} T \sigma(T), \quad (5.2)$$

where the Lorenz number is

$$\mathcal{L} = \frac{\pi^2 k_B^2}{3e^2} = 24.43 \frac{\text{nW } \Omega}{\text{K}^2}, \quad (5.3)$$

and k_B is Boltzman's constant, e is the electron charge, and $\sigma(T)$ is the electrical conductivity. This law is applicable in metals at room temperature and above and at low temperature (< 10 K). We can understand it qualitatively as follows. The electrons carry a thermal "charge" $k_B T$ driven by the energy gradient field $k_B \nabla T$. They also carry an electric charge e driven by the energy gradient field eE , so we might expect the ratio of the conductivities to be proportional to $(k_B/e)^2$. The factor of $\pi^2/3$ comes from the fact that only the electrons near the Fermi energy contribute to the transport.

At low temperatures, the dominant scattering target is impurities. Since the lowest excited states in impurities are much greater in energy than $k_B T$ there are few empty electronic states low enough in energy for an electron to enter once it has excited the impurity. The impurity is never thermally excited and able to give energy to an electron. Since the electron can not change its energy, impurity scattering is called elastic. Impurity scattering can, however, change the momentum direction by a large amount, which affects the conductivities.

Electrical conductivity arises from the wholesale displacement of the Fermi sphere from zero momentum under the influence of an applied electric field. Large angle scattering limits the conductivity by tending to recenter the Fermi sphere about zero momentum. Since the impurity density is independent of the temperature, the electrical conductivity should also become independent of temperature at low temperature. This is generally observed in real materials.

Thermal conductivity comes from the distortion of the Fermi surface into a form with a "hot" temperature distribution in one momentum direction and a "cold" temperature distribution in the opposite momentum direction. This results in heat transport since electrons arriving from one direction have higher average energies than the ones arriving from the opposite direction. Large angle scattering limits the thermal conductivity by restoring a uniform temperature distribution to the Fermi surface. Since impurity scattering limits both conductivities at low temperature, W-F should hold and predicts $\kappa(T) \sim T$.

A simple way to characterize the purity is to measure the residual resistance ratio (RRR), the ratio of the resistance of a specimen at room temperature, 300 K, (some people use the resistance at 273 K), to the resistance at or below LHe, 4.2 K. The ratio of resistances for the same sample gives a result independent of all geometrical factors. In relatively pure metals the resistivity at room temperature, since it is dominated by phonon scattering, is an intrinsic property of the material independent of the purity. The resistivity at low temperature is dominated by impurity scattering, so the RRR is a direct measure of the purity of a sample: higher values indicate fewer impurities. Typical commercial coppers have RRR values around 50. RRRs over 10,000 have been obtained in polycrystalline wires, and over 60,000 in a single crystal, with the oxygen annealing treatment described in §5.4.4.¹⁰⁴

At high temperatures the conductivities are limited by electron-phonon scattering. The width of the transition region of the Fermi distribution is proportional to $k_B T$. At higher temperatures, this width greatly exceeds the phonon energy, which is limited by the Debye temperature to $k_B \Theta_D$. In this regime, inelastic scattering only slowly cools the temperature distribution. Here, W-F holds with $\sigma(T) \propto T^{-1}$ because the number density of phonons grows as T . Therefore $\kappa(T)$ should be roughly constant. Again, this behavior is usually observed in real metals.

In between the high and low temperature limits, inelastic scattering of electrons is important in limiting the thermal conductivity, but has little effect on the electrical conductivity. At intermediate temperatures scattering off phonons of mean energy $k_B T$ can cause an electron to go from just above the Fermi level to just below the Fermi level without substantially changing the momentum direction. This process "cools" the temperature distribution of the Fermi surface but does not affect the displacement of the Fermi sphere under an applied field. Therefore the process reduces the thermal conductivity without affecting the electrical conductivity, so W-F gives an upper limit on the thermal conductivity at all temperatures. There are two exceptions to this rule. The first exception is dirty metals, where the electrical conductivity is limited by impurity scattering at all temperatures. These can have such a low electrical conductivity that the phonon contribution can be important and increase the thermal conductivity above the W-F estimate. The second exception are superconductors.

For superconductors in the superconducting state, electrons in the super-fluid phase dominate the electrical conductivity, but don't contribute at all to the thermal conductivity. The normal electron contribution to κ is still limited by the scattering of electrons in the normal phase, but far below the transition temperature the normal electron density is exponentially suppressed, so even the normal electrons contribute very little to κ . The thermal conductivity is then determined by the phonon

contribution, so superconductors well below the transition temperature behave thermally like insulators.

5.3.3 Thermal Power Conduction: Macroscopic Modeling

Now that we have an idea of what determines the thermal conductivity, we need to develop some tools to model the cryostat. In practice, we can estimate the heat flow in a part just from the construction, without knowing the exact temperature of its warm end, even though the temperature difference causes the heat flow. With an estimate of the heat conducted and the cold end temperature, we can estimate the warm end temperature, then by iterating obtain a consistent temperature/power profile.

As we noted in Eq. (5.1), the local thermal energy current density, \mathbf{j} , (thermal power density) driven by a temperature gradient in a material with thermal conductivity $\kappa(T)$ is

$$\mathbf{j} = -\kappa(T)\nabla T. \quad (5.4)$$

The minus sign indicates that power flows opposite to the direction of increasing temperature. The thermal conductivity depends on the local temperature, the material, and the processing of the material (annealing, *etc.*). This is the thermal analog of Ohm's Law of electric charge conduction: flow of (thermal energy/electric charge) is proportional to the gradient of the curl-free scalar (temperature/voltage) field.

For simple geometries and steady state conditions, one can determine the isothermal surfaces from the symmetries of the system. These are surfaces perpendicular to the gradient of the temperature. Labeling these isothermal "cross-sections" by a coordinate z and integrating over the cross-sectional area $A(z)$, we obtain the total power conducted through that cross-section:

$$P(z) = \int_{A(z)} -\mathbf{j} \cdot d\mathbf{A} = \int \kappa(T)\nabla T \cdot d\mathbf{A} = \kappa(T)A(z)\frac{dT}{dz}. \quad (5.5)$$

Rearranging to get all the explicit z -dependence on one side, we define a new quantity J , the mean power density integrated over the length of the system:

$$dJ \equiv \frac{P(z)}{A(z)} dz = \kappa(T) dT, \quad (5.6)$$

$$J = \int_{z=0}^{z=L} \frac{P(z)}{A(z)} dz = \int_{T=T_1}^{T=T_2} \kappa(T) dT = K(T_2) - K(T_1), \quad (5.7)$$

$$K(T) \equiv \int_0^T \kappa(T) dT. \quad (5.8)$$

Note that J , defined as the left-hand integral in Eq. (5.7), depends only on the shape of the system and the power inputs. It turns out that the power inputs are largely determined by the construction as well, so that J can be calculated from the physical description.

Now it is clear how to proceed to construct a model. Calculate J , then raise T_2 until

$$K(T_2) = J + K(T_1). \quad (5.9)$$

For simple forms of the thermal conductivity (*e.g.*, power laws), $K(T)$ is invertible, so we can even write

$$T_2 = T(J + K(T_1)). \quad (5.10)$$

Some useful thermal conductivity functions and their integrals are given in Appendix A.

5.3.4 Example: Cylinder with Distributed Power Input

For example, consider a cylinder of constant cross-section $A = 2\pi r t(1 - t/2r)$, where r is the outside radius and t is the wall thickness. Apply a fixed power P_2 (*e.g.*, from the next warmer part) at the warm end and a distributed power \mathcal{P} (W/m) (from blackbody radiation from the surrounding warmer layer) along the entire length. The

conducted power is $P(z) = P_2 + \mathcal{P}(L - z)$, and the power coming out of the cold end is $P_1 = P_2 + \mathcal{P}L$. The average power density integrated over the length is

$$J = \int_0^L \frac{P(z)}{A} dz = \frac{1}{A} \int_0^L [P_2 + \mathcal{P}(L - z)] dz = \frac{L}{A} (P_2 + \frac{1}{2} \mathcal{P}L). \quad (5.11)$$

Note that the distributed power, $\mathcal{P}L$, only contributes half as much as P_2 to J , as if we could take the entire distributed power and replace it by a local source halfway down the part.

5.3.5 Joints

The scheme above is suitable for continuous temperature gradients. Discrete temperature jumps at joints in the system require an alternative scheme based on the Wiedemann-Franz Law and the discrete electrical resistance of the joint. As we noted above in §5.3.2, at low temperatures the electrical conductivity is limited by impurity scattering, and is independent of temperature. Then $\kappa(T) = \mathcal{L}\sigma_0 T$ and

$$K(T) = \int_0^T \mathcal{L}\sigma_0 T dT = \frac{\mathcal{L}\sigma_0}{2} T^2. \quad (5.12)$$

Now we write Eq. (5.10) explicitly as

$$T_2 = \sqrt{T_1^2 + \frac{2J}{\mathcal{L}\sigma_0}}. \quad (5.13)$$

The trick to modeling a joint is to connect the integrated power density, J , to the joint electrical resistance, $R = L/(A\sigma_0)$, where A is the contact area of the joint and L is the effective length. Formally,

$$J = \int \frac{P}{A} dz = P \frac{L}{A} = PR\sigma_0. \quad (5.14)$$

Using this result in Eq. (5.13), the solution for T_2 is

$$T_2 = \sqrt{T_1^2 + \frac{2PR}{\mathcal{L}}}. \quad (5.15)$$

That is, given the joint electrical resistance, which is relatively easy to measure, Eq. (5.14) gives J and Eq. (5.15) gives the corresponding expected temperature jump.

This expression for the temperature jump across a joint with resistance R was derived using the low temperature W-F result, but at intermediate temperatures W-F does not hold. W-F generally gives an upper limit to the thermal conductivity, so we can take Eq. (5.15) as a lower limit to the actual temperature jump. To model the impedance of a joint we assume a worst case resistance, based on tests with prototypes, then use Eq. (5.15) to compute the temperature rise when the joint conducts a power P .

5.3.6 Blackbody Radiation

The thermal power density transmitted from a warm surface at temperature T_h to a colder surface at temperature T_c is

$$\mathcal{P} = \sigma f(\epsilon)(T_h^4 - T_c^4), \quad (\text{W/m}^2) \quad (5.16)$$

where here σ is the Stefan-Boltzmann constant, $56.7 \text{ nW}/(\text{m}^2 \text{ K}^4)$, and $f(\epsilon)$ is a function of the emissivity of the surfaces and the properties of any multilayer insulating blanket. For a vacuum between two parallel plates,

$$f(\epsilon_h, \epsilon_c) = \frac{1}{\frac{1}{\epsilon_h} + \left(\frac{1}{\epsilon_c} - 1\right)}, \quad (5.17)$$

where ϵ_h and ϵ_c are the emissivities of the two surfaces. If the two emissivities are equal and much less than 1,

$$f(\epsilon) = \frac{1}{\frac{2}{\epsilon} - 1} = \frac{\epsilon}{2 - \epsilon} \cong \frac{\epsilon}{2}. \quad (5.18)$$

Tabulated emissivity values are typically 0.01–0.04 for highly reflective surfaces, such as non-oxidized gold, silver, or copper, or polished aluminum.¹⁰⁵ (The natural oxides of silver and copper greatly increase the emissivities, but aluminum oxide is transparent to

the infrared radiation of interest in cryogenic systems.¹⁰⁶) Between 300 K and 77 K, an emissivity of 1 gives an absorbed power density of 457.3 W/m², $\epsilon = 0.02$ gives 4.619 W/m². Shu *et al.*¹⁰⁷ report that for black-painted surfaces covered with 3M #425 aluminum tape, the absorbed power density is 4.8 W/m².

For a system with multilayer insulation (super-insulation, MLI), the power density transmitted between adjacent layers i and $i+1$ is¹⁰⁸

$$\mathcal{P} = \sigma f(\epsilon)(T_i^4 - T_{i+1}^4) + h(T_i - T_{i+1}). \quad (5.19)$$

Here h is the conductive heat transfer coefficient that describes the effects of thermal shorts and gas conduction between layers. Adding $N + 1$ contributions like this from the hot wall to the first layer to the second layer . . . to the N^{th} layer to the cold wall, we obtain

$$(N + 1)\mathcal{P} = \sigma f(\epsilon)(T_h^4 - T_c^4) + h(T_h - T_c). \quad (5.20)$$

We can define the inter-layer heat transfer coefficient h_{il} (W/(m² K)) as

$$h_{\text{il}} = 4\sigma \overline{T^2} \overline{T} f(\epsilon) + h, \quad (5.21)$$

where $\overline{T^2} = \frac{1}{2}(T_h^2 + T_c^2)$, $\overline{T} = \frac{1}{2}(T_h + T_c)$, and write Eq. (5.20) as

$$(N + 1)\mathcal{P} = h_{\text{il}}(T_h - T_c). \quad (5.22)$$

h_{il} has the nice property that it completely describes the fabrication of the blanket and the pressure, so that for blankets with different N but the same h_{il} between the same boundary temperatures the transmitted power really is proportional to $1/(N + 1)$. The temperature distribution inside a blanket goes like

$$\frac{T_i}{T_c} = \left[1 + \frac{i}{N + 1} \frac{T_h^4 - T_c^4}{T_c^4} \right]^{1/4}, \quad (5.23)$$

neglecting conduction and convection. Table 5.3 lists values for h_{il} from a variety of blankets and laboratories. The values range from 0.04–0.24 W/(m² K), with several values around 0.1 W/(m² K). For comparison, h_{il} for the taped surface measured above

Table 5.3. Measured Values for h_{int} .
 Measured values of the interlayer heat transfer coefficient, h_{int} , defined in Eq. (5.21). The values range from 0.04–0.24 W/(m² K), with several values around 0.1 W/(m² K).

Reference	h_{int} (W/m ² K)
Scurlock, <i>et al.</i> ¹⁰⁹	0.24
Shu, <i>et al.</i> ¹⁰⁷	0.072
Shu, <i>et al.</i> ¹¹⁰ (black)	0.089
Shu, <i>et al.</i> ¹¹⁰ (taped)	0.075
Shu, <i>et al.</i> ¹¹¹	0.086
Taneda, <i>et al.</i> ¹¹²	0.040
Burmeister, <i>et al.</i> ¹¹³ ($N = 20$)	0.042
Burmeister, <i>et al.</i> ¹¹³ ($N = 30$)	0.049
Ohmori, <i>et al.</i> ¹⁰⁸ (FGM/DAM)	0.072
Ohmori, <i>et al.</i> ¹⁰⁸ (CSN/DAM)	0.16
Ohmori, <i>et al.</i> ¹⁰⁸ (DP-DAM)	0.072
Gonczy, <i>et al.</i> ¹¹⁴ (Reemay/DAM)	0.11

is 0.022 W/(m² K). The range of values indicates that the blankets are far from perfect; a typical blanket needs $N > 5$ to give a lower heat load than low emissivity surfaces. Note from the Buermeister, *et al.*, values that in practice h_{int} is not entirely independent of N , *i.e.*, changing the number of layers invariably changes the heat load due to thermal conduction between layers, so the actual power decreases less slowly than N^{-1} .

Because the stems are macroscopic holes in the radiation shield, we wanted to minimize their diameters. Therefore we only installed $N = 20$ MLI on the LN layer in the fridge and around the LN can. For the thermal model, we adopted $h_{int} \cdot 0.1$ W/(m² K).

5.3.7 Modeling Strategy for the Icebox

Our system consists of a series of cylinders, mostly connected end-to-end. For the model, we ignore the right-angle joints at the bottoms of the fridge and coldbox and just connect all the cylinders in-line. The distributed power input comes from black-body radiation; we did not include the effects of residual gas. Localized power inputs

come from supports and from radiation on the lids at the bottom of the fridge and the top and bottom of the Icebox cans.

So, starting at the warm ("right hand") end, we calculate J for each section, using Eq. (5.11) and the P_1 of the previous section for P_2 . Then proceeding left to right (cold to warm), we first calculate T_2 using Eq. (5.10) (or, at low temperature, using Eq. (5.13) directly) to get the temperature at the right hand end of each section, then calculate the discrete temperature jump due to the finite resistance of the joint using Eq. (5.15). This procedure is then iterated, since the power from supports, an input to the computation of J , depends on the temperatures output at the end. We implemented this procedure in a spreadsheet format using Microsoft Excel.

To create the model, we have to make a number of assumptions for parameters not directly measured, such as the emissivity of the surfaces, the resistance of joints, the thermal conductivity of the materials (whether our copper is relatively high or low conductivity compared to other coppers). The primary goal of the model was to identify the assumptions that, if violated, would drastically affect the performance of the cryostat. Therefore we made pessimistic assumptions wherever possible, then iteratively adopted more favorable assumptions until the model predicted acceptable performance. This procedure identified the key assumptions that we had to satisfy in the actual cryostat. For example, the emissivity of the colder layers has essentially no effect on the base temperature, so the model uses $\varepsilon = 1$, and in the fabrication we took no special precautions in the surface treatment of these layers, other than to keep them clean once built, to minimize radioactive contamination of the surface. On the other hand, the emissivity of the LN and LHe layers drastically affect the base temperature. To obtain adequate performance, the model assumes $\varepsilon = 0.04$ (0.1) for the LN (LHe) layers, respectively, except for the cans, and $\varepsilon = 0.01$ (0.04) for the LN (LHe) cans. (The model does not directly include the multilayer insulation, except by this reduction

in ϵ corresponding to $h_{int} \equiv 0.1 \text{ W}/(\text{m}^2 \text{ K})$ and $N = 20$.) To meet these assumptions in the construction, we gold-plated the LN and LHe layers and we installed $N = 20$ super-insulation around the LN can.

In various prototypes we measured joint RRRs around 70, corresponding to a resistance at 4.2 K of 100–200 n Ω . The model assumes a joint resistance of 100 n Ω , with a number of exceptions. We measured 240 n Ω on a prototype for the long bolt joint, described in §5.4.1. From data taken with heaters on the side access ports during thermal tests of the fridge itself we measured the thermal impedance of the joints between the skirts and tails at various powers and temperatures. Assuming W-F holds, we computed the best fit electrical resistance : 350 n Ω on the CP, 930 n Ω on the ST, and 8 n Ω on the LHe. Similarly, we measured the impedance between the skirt and the cooling source and obtained 1.6 $\mu\Omega$ on the CP and 1 $\mu\Omega$ on the ST. In tests of the LN cooling loop (described in §5.4.2) we measured a conductance of 42 W/K.

We used $\text{RRR} = 33$ for the copper itself (Uniform Number System (UNS) grade C10100, also known as Oxygen Free Electronic (OFE) per ASTM B152 and ASTM F68).

The model also includes the power dissipated by the detector amplifier FETs. We included four FETs for each of 6 detectors in each of two towers, for a total heat load of 0.24 W (5 mW per FET). To operate seven towers with six detectors each we will need to implement a vacuum thermal feedthrough, sketched by Dick Wolgast, to dissipate the FET power onto the LN layer, not the LHe layer.

We also included heat loads due to the detector wiring in the E-stem: 1.8 W onto the LN heat sink, and 0.22 W onto the LHe heat sink.

Finally, the model also uses the known cooling power curve of the mixing chamber, which is proportional to $(T - T_b)^2$, where $T_b = 5 \text{ mK}$, and the cooling power is 400 μW at 100 mK.

The end result of this pessimistic approach is that we should take the model at face value where we had to make realistic assumptions, such as on the LN layer and to some extent on the LHe layer, but the model should overestimate the temperatures where we did not have to modify the initial pessimistic assumptions, as on the colder stages.

5.3.8 Results of the Model

Table 5.4 shows the predicted temperatures at various locations in the cryostat on each layer, as well as the total heat load on the fridge due to the tails and cryostat. The locations are marked on the sketch of the cryostat shown in Figure 5.5.

The total heat loads on the coldest three stages are generally negligible for the fridge. With this heat load the mixing chamber should heat up to 5.1 mK (MC Location 2). The cold plate should not be overwhelmed by the 2.5 μ W. Normally we apply 2–5 mW on the Still, so we just have to reduce the heater power and let the cryostat make up the difference.

The heat loads on the LHe and LN are significant, however. The heat load on LHe will boil off an extra 33 liters per day, assuming that only the heat of vaporization is used and the model is not overly pessimistic. The LHe bath holds 36 liters, of which about 30 are useful, and the fridge alone uses about 12 liters per day, so this suggests 16 hours between transfers. The heat load on LN will boil off an extra 20 liters per day, again using only the heat of vaporization, compared to the bath volume of 60 liters and fridge consumption of 30 liters per day, so the new hold time should be nearly 29 hours. Again, these are the results of a pessimistic model, now made doubly pessimistic by only using the heats of vaporization. For the helium, in particular, the change in enthalpy of the gas as it goes from 4.2 K to 300 K is substantial, so we might expect the boiloff rates to be lower.

Table 5.4. Predictions of the Thermal Model.

Pessimistic predictions of the thermal model for the temperatures on each layer at specific locations in the cryostat, along with the total heat load on the fridge due to the tails and cryostat. The locations are marked in Figure 5.5. Location (1) is the base temperature of the layer in the fridge. To generate the required cooling power the mixing chamber will warm up to the temperature shown at (2). The top of the LHe tail is connected directly to the LHe bath, so the temperature difference between locations (1) and (2) is very small. The entire LN tail is maintained at a nearly uniform temperature due to the cooling loop, hence (2) and (3) are the same.

Location	Temperature on Layer at Location				
	(K)			(mK)	
	LN	LHe	ST	CP	MC
1. Cooling Source	77	4.2	0.60	50	5.0
2. Top of Tail	78	4.2	0.71	53	5.1
3. Cold End of Stem	78	5.3	0.81	55	5.2
4. Cold Port of Can	88	7.8	0.86	57	6.4
5. Top of Can/ Warm Port of Can	92	8.6	0.87	57	6.4
6. Last Cold Point in E-stem	114	26			
Total Power	36 W	0.97 W	1.4 mW	2.5 μW	38 nW

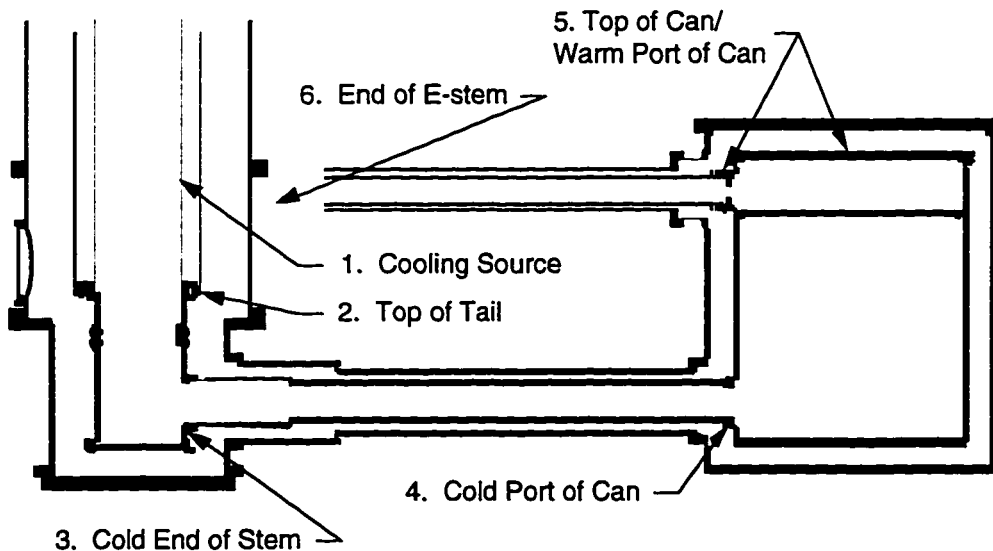


Figure 5.5. Sketch of Fiducial Locations in the Thermal Model. Simplified diagram of the Icebox showing the OVC for reference and the LHe layer as an example of the location temperatures reported in Table 5.4.

We will use the results of this model to design the detector wiring later on. As discussed above, the model generally tries to be conservative, and therefore probably overestimates the temperatures, except on the LN layer and possibly the LHe layer. To make conservative estimates of the heat load from a given wiring segment one might use the (overestimated) model temperatures for the warm end and something less than the model for the cold end. In practice, the temperature differences between stages are large enough that changing the cold end temperature from the model value to even as low as the base temperature of the stage has only a small effect on the heat load estimates. Therefore we will simply use the model estimates as is.

5.4 Novel Non-Detector Features

The limited selection of materials forced us to use non-standard construction techniques, such as the copper flanges with formed threads and electron beam welding. We also had to develop novel designs to solve some of the engineering problems, or use unusual elements in new ways. We will discuss the cold finger joints, the tail hinges and cold finger flex section, the Kevlar loops and spider supports, modifications to the fridge, and the all copper vacuum seals. We will close this section by noting some items that could stand improvement.

To avoid introducing radioactive contamination by using conventional silver alloy brazing material or welding stinger rods, we electron beam welded all joints in the stems and cans. Welding and brazing processes generally heat up the part significantly, which can lead to deformation. This problem is even more acute with electron beam welding, where the heating is *very* localized. It is very important to rough machine the parts to larger than final size before welding, then perform any finish machining to final size afterwards, particularly for flanges with mating surfaces that must be flat or with screw threads.

Instead of using ordinary cutting taps, we used forming taps for all threads. Ordinary taps cut out the material to make the thread. In the process they wear down, and sometimes chip, in both cases potentially leaving radioactive steel embedded in the part. Forming taps literally push the metal out of the way, with much less wear on the tap. This also results in a hardened screw thread, even if the base material is relatively soft to have a high thermal conductivity.

5.4.1 Engineered Cryogenic Thermal Joints

To minimize the size of the shield penetration, we strived to keep the cold stems as small in diameter as possible. For the warmer layers this did not pose an engineering problem because at the larger diameters there was adequate space to use a reasonable number of screws. The coldest layer is the most constrained. The thermal connection to the mixing chamber is made by an M20 thread with a vertical axis at the top of the vertical cold finger ("VCF"). At the centerline of the stems the cold finger has to make a right angle ("L-joint") and connect to the horizontal cold finger ("HCF") in a way that can be assembled and with very little space for a flange. The connection between the HCF and the 10 mK can ("long bolt joint") has no space for a flange.

To make reliable joints with a small number of screws, one has to consider the differential thermal contraction between dissimilar metals to ensure that the screws are fully loaded when cold, applying the maximum force on the mating surfaces. In the L-joint we used brass screws and in the long bolt joint we used a silicon bronze screw. Both joints are between copper mating parts. To achieve a stress (tensile force per cross sectional area) of 90% of the yield point, where permanent deformation of the screw starts to occur, 345 MPa in brass¹¹⁵ (silicon bronze is very similar¹¹⁶) we need a strain (fractional elongation) of 0.45%. In cooling from 293 K to 4 K copper contracts by 0.326% and brass by 0.384%,¹¹⁷ so the strain will increase by 0.06%. Therefore we

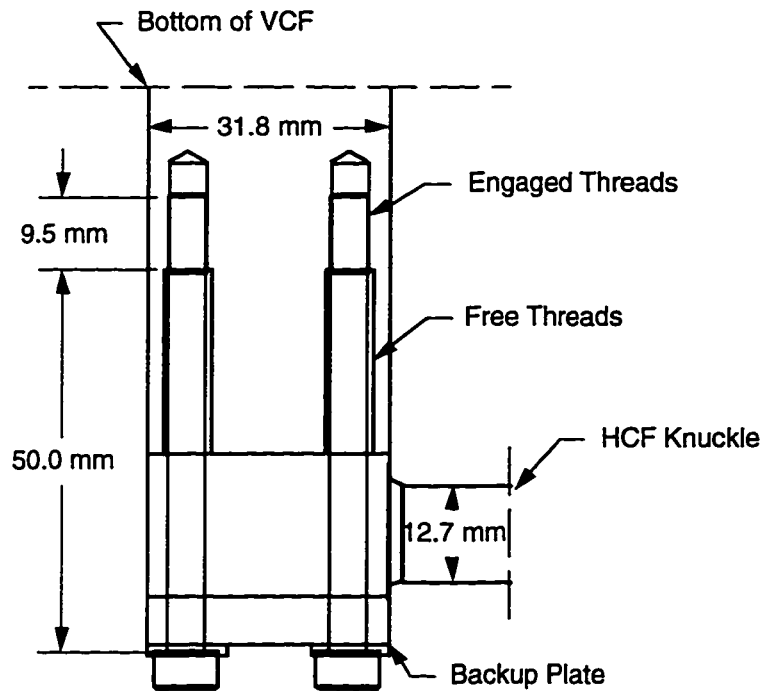


Figure 5.6. Vertical Cold Finger L-joint. Simplified drawing of the L-joint between the vertical cold finger, which is screwed into the mixing chamber of the fridge, and the horizontal cold finger which connects to the 10 mK detector can.

need to tighten the screw to a strain of 0.39% when warm. In principle, the free length of the screw (the length between the bearing surface at the screw head and the first engaged thread) does not matter, since the stress is determined by the *fractional* elongation. In practice, to have reasonable sensitivity to the changing strain or torque as the screw is tightened, one would like the screws long enough that the actual elongation amounted to a large fraction of a turn. The free length of the screw required to achieve the desired strain in one turn is $\text{Free Length} = \text{Thread Pitch} / \text{Strain}$.

For the L-joint (Figure 5.6) there was enough room to use four screws. Here there was the added complication that the azimuthal orientation of the VCF could not be determined in advance since it had to screw into the mixing chamber. The VCF was made with eight drilled and tapped holes. The HCF terminated in a knuckle with four arc slots, each arc 45° plus two screw diameters in arc length, ensuring that four holes

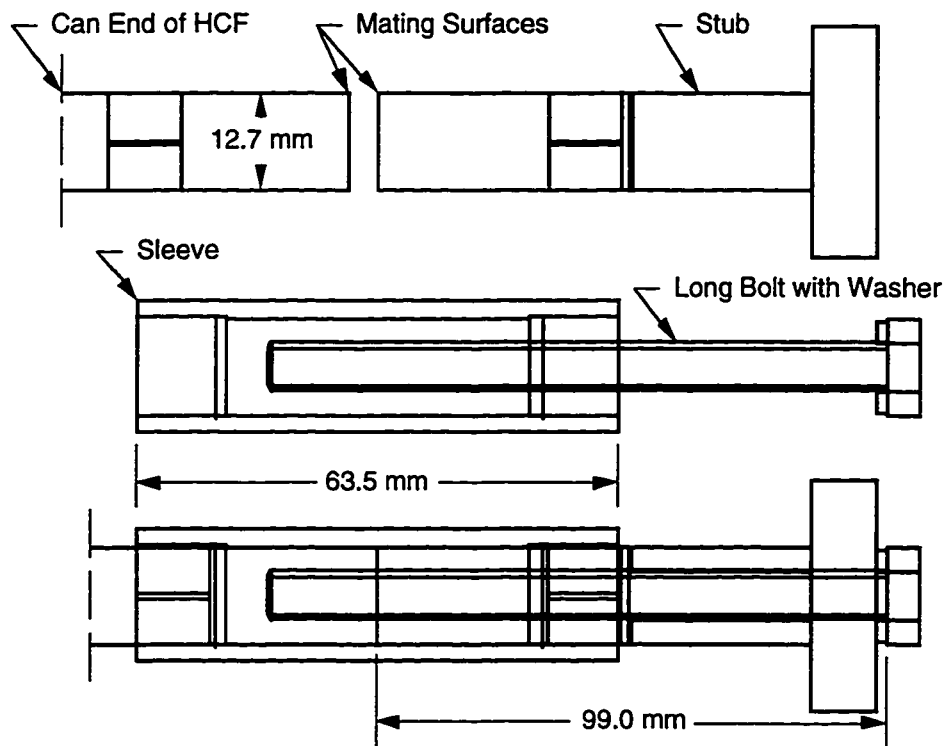


Figure 5.7. Long Bolt Joint at the End of the Horizontal Cold Finger. Exploded view of the long bolt joint between the horizontal cold finger (HCF) and the 10 mK detector can. At the top are the HCF and the stub. In the middle are the sleeve and the long bolt. The bottom view shows the final assembly. Some horizontal lengths have been shortened for illustration. The end of the HCF is extremely unconstrained since it hangs off the braid that makes the HCF flexible. Most of the complexity is because the sleeve, stub, and can must act as a wrench to hold the end of the HCF against the torque of the screw.

in the VCF would always be accessible. The screw heads bear on a backup plate with four holes, so the load is distributed over the entire face of the knuckle, instead of being confined to the area of the slot immediately around the screw. The screws used in the L-joint are $M5 \times 0.8$, *i.e.*, 0.8 mm per turn, so the free length per turn should be 205 mm. Figure 5.6 shows the free length as 50.0 mm, so the desired strain should be reached in one quarter turn past the point where the bearing surfaces come into contact.

The connection between the HCF and the 10 mK can is even more tightly constrained. There is room for only a single screw. This joint (Figure 5.7) is the last one made between the stems and the cans, so the end of the HCF is completely

inaccessible. The end of the HCF has a hexagonal cross section which slips into a sleeve with a hexagonal socket. At the other end, the sleeve holds a stub by the same hexagonal arrangement. The sleeve and stub are inserted, then the can is lowered into position. Four screws attach the stub flange to the can, so the can acts as a wrench handle for the end of the HCF through the stub and the sleeve. The single long bolt is then inserted, threaded to the HCF, and tightened. The bolt itself is an English size (the only one in the Icebox), 1/4–20, so the free length per turn should be 326 mm. Figure 5.7 shows the free length as 99 mm, so the bolt should reach 0.39% strain in about one third of a turn. In tests on a prototype we measured $RRR = 18.6 \pm 0.7$ which implies a conductance of $2 \mu\text{W/mK}$ at 5 mK.

5.4.2 Hinged Tails and Cold Finger Flex Section

To accommodate the change in angle between the vertical axis of the fridge and the centerline of the stems as the tails are lifted by thermal contraction, we designed hinges in the tails. For all but the LN tail the hinges consist of a bellows and a set of links that act as the hinge pins to define the rotation axis (see Figures 5.8 and 5.9). The hinge links are on either side of the tail perpendicular to the stem. To limit the extent of rotation and protect the bellows there are also restraining links in line with the stem. We will discuss the two bellows designs, the LN tail and its cooling loop, and finally the flex section in the horizontal cold finger.

Bellows, Hinge Links, and Restraining Links

To achieve a given rotation with a small torque requires a soft bellows, *i.e.*, a small cross sectional area/length ratio; conversely, thermal conduction requires a large area/length ratio. Since the required angular change is small (~ 1 mrad) the bellows can be relatively stiff. However, as the diameter grows the elongation (above the stem) or compression (opposite the stem) also grows, so the larger tails require a softer bellows.

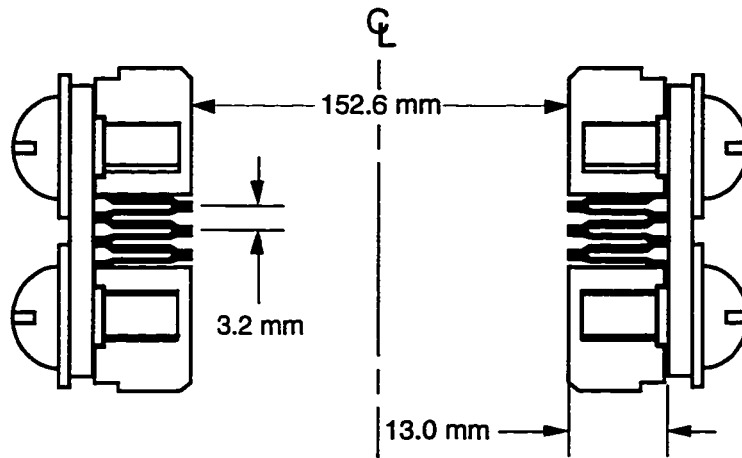


Figure 5.8. Liquid Helium Tail Welded Bellows.
 Cross section of the LHe tail bellows. The overall diameter of the tail has been greatly reduced to show details at both sides of the part. The bellows itself, shown solid black in the figure, is made by forming thin annealed copper rings in a die, then stacking the rings alternately right side up and upside down. This puts alternately the interior edges in contact then the exterior edges, which are welded together. The restraining links are the tie bars outside the bellows. The holes in the links are larger than the screws, allowing a limited range of free motion.

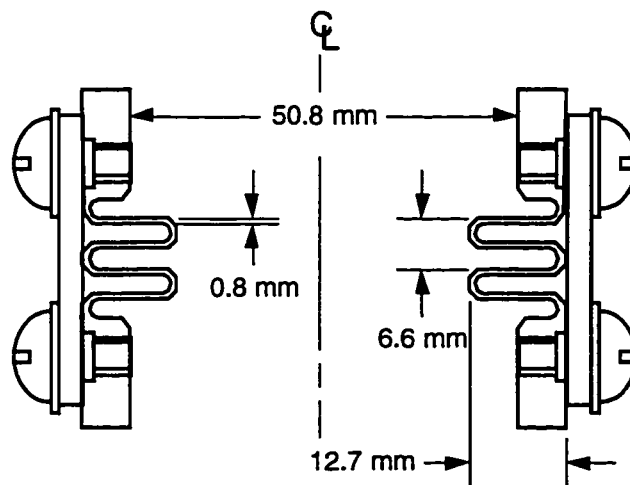


Figure 5.9. Machined Tail Bellows.
 Cross section of the 50 mK tail bellows. Unlike Figure 5.5, the overall diameter here is to scale. The bellows section is made from a solid rod of copper. The interior is drilled out, then the inside of the convolutions are made using a boring bar on a lathe. The interior is then filled with wax and the outside of the convolutions cut on a lathe. The links arrangement is the same as in Figure 5.8.

The warmer tails, which are the ones at larger radii, also require more thermal conduction since the heat loads are higher. These two factors led us to a very soft welded bellows (Figure 5.8) made out of a stack of thin formed rings for the helium leak tight LHe tail. For the inner tails we designed significantly stiffer (but much less difficult to manufacture) machined bellows, illustrated in Figure 5.9.

LN Hinge and Cooling Loop

The diameter and heat load requirements on the LN tail are large enough that even the welded bellows design is inadequate. The heat load on the LN system is nearly 40 W due to thermal radiation from the room temperature wall absorbed by the large surface area of the LN layer. Since the LN bath terminates quite high in the fridge, there is an extra part ("LN skirt") in the thermal path, as well. By bringing liquid nitrogen down to the tail itself, we can short out the impedance of the skirt and use a simple hinge without a bellows on the tail. We created two ports in the bottom of the LN bath. From one port we brought a 3/8" copper tube (the "LN cooling loop") to the bottom of the tail without contacting the LN layer. Starting at the bottom of the tail, the tube is wrapped in an ascending spiral brazed to the tail. From the top of the tail, the tube goes to the second port which leads to a standpipe that vents into the bath at the top. Topologically, the tube is a "U" shape with all the heat input on one side. This causes LN in the tube to boil. The bubbles reduce the average density compared to the bubble free leg. The different average densities in the two legs leads to a pressure gradient at the bottom of the "U" with higher pressures at the bottom of the bubble free tube. This pressure gradient drives flow through the tube.

The LN cooling loop is very efficient at carrying away the large heat input from the stems connected at the side access port. In tests using a heater mounted to a temporary side access port cover, the tail + cooling loop combination had an effective conductance to 77 K of 42 W/K.

When we transfer LHe into the fridge, the large amount of helium vapor exiting the fridge cools the neck of the LN bath enough that it stops venting. If the vent ports are not sealed, the LN bath cryopumps water vapor out of the room, potentially forming an ice plug in the vent tube, which is a very dangerous situation. Even if the formation of a plug is prevented by sealing the tube, some ice usually gets knocked into the LN bath. This ice had a tendency to get carried into the cooling loop, leading to erratic operation and eventually plugging it. Since we diagnosed this problem, we have implemented a set of one-way valves to keep the LN bath at a positive pressure of dry nitrogen, even during LHe transfers. The LN boiloff plus the dry nitrogen make-up gas supplies the nitrogen purge for the shield around the Icebox. In retrospect, a better design would have the inlet tube extend into the LN bath ~2 cm, so that any ice falling through the LN would be less likely to get carried into the cooling loop.

Horizontal Cold Finger Braid and Support Screws

For the cold finger connecting the mixing chamber to the 10 mK can that houses the detectors we didn't want to introduce the substantial thermal impedance of our machined bellows. In addition, we wanted to provide some isolation of the detectors from mechanical vibrations and sound waves (collectively called microphonics) due to the cryogens in the fridge. So, in contrast to the other tails, there is no flexibility in the vertical cold finger at the fridge. However, we still had to allow for the contraction of the fridge with two design features of the horizontal cold finger. We added a very flexible section at the can end and removed material from the top and bottom of the cold finger at the fridge end. The flex section allows for the bulk of the contraction motions and provides microphonic isolation. The long rigid section of the cold finger is now cantilevered off the mixing chamber. To provide support for the free end just before the flex section, we added four nylon shoulder screws that point inward from the 50 mK stem. Because of the net motions, this support does not lift the end of the cold

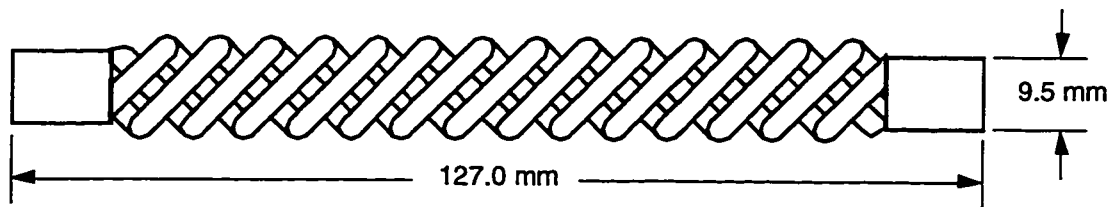


Figure 5.10. Horizontal Cold Finger Flex Section.
 Drawing of the HCF flex section before welding into the HCF, but after the ferrules have been welded on and machined into a uniform shape.

finger as much as the mixing chamber rises, but the part is now over constrained, again putting a torque on the mixing chamber. By removing material from the top and bottom of the cold finger near the fridge, we reduced the moment of inertia and hence the stiffness of the cold finger, thereby lowering the applied torque.

For the flex section (Figure 5.10) we took a short length of welding cable, which is made up of many fine strands of high quality copper wire, put the ends in ferrules and compressed them tightly around the cable. The ends of the ferrules and cable were full penetration electron beam welded to make reliable electrical contact with each strand. (Recall that the electrons are the dominant heat carriers in good metals.) The now solid ends were machined to a uniform shape, inserted into sockets on the ends of the HCF and the long bolt joint, then finally the ferrule to socket joints were full penetration electron beam welded. The finished HCF consists of the knuckle of the L-joint, the long rod with material removed at the fridge end, the flex section, and the HCF threaded end of the long bolt joint all welded into one long flexible part.

5.4.3 Kevlar Loops and Spider Supports

Because of their size and all copper construction, the cans are quite massive. The masses to be supported at each stage are shown in Table 5.11. In addition, the detectors, if they filled the 10 mK can, would have a total mass of 102 kg. If some of the 10 mK can was filled with lead for shielding there could be as much as 138 kg in

Table 5.11. Maximum Mass Supported at Each Stage in the Cans.

The masses (in kg) of the parts supported by the Kevlar loops. The only variable element is the detector mass; the value shown is the maximum. The "Added" column is the can mass plus half the mass of the cold and E-stems; the other halves are supported by the tail or the end of the E-stem, respectively. The "Total" is the total mass supported by Kevlar at this layer, equal to the previous total plus the new added mass. Finally, the OVC masses are also shown. The boldface OVC Total entry is approximately the total cryostat mass inside the shield, *excluding* the detectors.

Layer	Stems	Can	Added	Total
Detectors				102
MC	1.29	15.2	15.9	118
CP	6.34	19.8	23.0	141
ST	10.4	24.3	29.6	171
LHe	24.7	62.1	74.5	245
LN	26.0	41.5	54.5	300
OVC	17.8	117	126	324

addition (with no space left for detectors). For these loads, we wanted to be sure the support members were mechanically adequate but not excessively conductive.

The power, P , conducted from T_2 to T_1 by an object of uniform cross-sectional area A and length L is, from Eqs. (5.7) and (5.11),

$$P = \frac{A}{L} [K(T_2) - K(T_1)], \quad (5.24)$$

where we can neglect the distributed power input from blackbody radiation if the object is small. For a mass M hanging from a support, the mechanical properties of the support are summarized by two numbers, the stress and the strain. The stress is the tension, Mg , per unit cross section, A :

$$s \equiv \frac{T}{A} = \frac{Mg}{A}. \quad (\text{GPa}) \quad (5.25)$$

(Here g is the gravitational acceleration.) The resulting elongation, ΔL , of the support length, L , is given by the strain:

$$e = \frac{\Delta L}{L}. \quad (5.26)$$

The stress and the strain are related by Young's modulus: $s = Ye$. Real materials often have a reasonably constant Young's modulus out to some maximum stress, the yield point, where the material begins to adopt a permanent deformation or is otherwise near failure; this maximum stress is the yield point stress, S . There is very little low temperature data on the Young's modulus or the yield point stress, so we typically used the room temperature values. The yield point is derated by a minimum safety factor f . Combining Eq. (5.25) with $s = S/f$, we can calculate the required cross section to support a mass M :

$$A = \frac{Mgf}{S}. \quad (5.27)$$

The required area is inversely proportional to the yield point stress. Therefore, the scaling of the thermal power is

$$P = \frac{K(T_2) - K(T_1)}{S} f \cdot \frac{Mg}{L}. \quad (5.28)$$

The heat load required to support a given mass with supports of a given length is proportional to the integrated conductivity divided by the yield point stress (up to the safety factor).

For the metals we used $f = 1.43$, which is equivalent to derating the yield point stress by 70%. This is a fairly low safety factor, suitable for materials in tension. Under compression the safety factor would be much larger to prevent buckling. For Vespel and Kevlar we used $f = 3.5$ to reduce the amount of long term creep and chances of failure. Since Mg/L is fixed, we need only compute the other factors in Eq. (5.28) as our quality factor:

$$q = \frac{f}{S} [K(T_2) - K(T_1)] \quad (5.29)$$

Since the power is proportional to this quality factor, we want to choose the material with the minimum value.

Table 5.12. Mechanical Properties of Various Hanger Materials.
 Mechanical properties of the materials considered for the can hangers. Stainless steel, a standard cryogenic support material, is included for comparison only, since it is not radiopure.

Material	Yield Point Stress S (MPa)	Young's Modulus Y (GPa)	Safety Factor f	S/f (MPa)
Pure Titanium	485	116	1.43	339
Titanium Alloy	830	150	1.43	580
Vespel	86.2	3.79	3.5	24.6
Kapton	34	6	3.5	9.71
Kevlar	>724	60	3.5	>207
Stainless Steel	520	210	1.43	364

Note that nowhere has the number of supports entered. The mass requires a minimum total cross section to keep the stress low enough, which gives a minimum total heat load. We are free to divide up the cross section and the heat load into as many individual supports as we like, as long as we provide the required minimum area. The only significant choices are the material, which determines K and S , and the length, which determines the elongation and the heat load.

To support the cans we looked at Vespel, Kapton, titanium and titanium alloys, and Kevlar fishing line. The mechanical properties of grade 4 titanium,^{118, 119} stainless steel,¹²⁰ SP-1 Vespel,¹²¹ and Kapton,¹²² along with the results of our measurements on a prototype Kevlar hanger, are listed in Table 5.12. When testing the Kevlar prototype hanger we did not load it to failure, hence the S value is a lower limit. The table also shows the safety factors used and the maximum allowed stress (S/f).

The low temperature thermal conductivity of titanium,^{118, 123-127} Vespel,^{121, 128} Kevlar,¹²⁹ and stainless steel^{95, 97} can be found in the literature. Since Kapton is a polyimide like Vespel, we assumed the same thermal conductivity. Since the Kevlar is in string or braid form, we decided to pot the support straps in epoxy to make a stiff part and protect the strands. Therefore the Kevlar support will have epoxy thermal conductivity as well to contend with. To compute the quality factor in Eq. (5.29), we integrate the thermal conductivity data over the temperature ranges predicted by the

Table 5.13. Quality factor for Various Hanger Materials.
 Quality factor defined in Eq. (5.29) computed for the hanger materials listed in Table 5.12.
 Units are W/(m MPa) times the multiplier value.

Material	Temperature Ranges				
	300–88 K	92–7.8 K	8.6–0.86 K	870–57 mK	57–6.4 mK
Multiplier	1	1	10^{-3}	10^{-6}	10^{-9}
Pure Titanium	13	4.4	65	670	2800
Titanium Alloy	2.4	0.49	6.9	71	300
Vespel	3.3	0.55	3.8	24	59
Kapton	8.4	1.4	9.6	61	150
Kevlar	0.97	0.26	1.0	2.7	2.3
Stainless Steel	7.8	1.4	12	120	530

thermal model, then divide by the maximum allowed stress shown in Table 5.12. Since the hangers run from the top of the warm can to the bottom of the cold can, there is a small temperature difference between the cold end of one hanger and the warm end of the next. Table 5.13 shows the results for the quality factor. Notice that the pure titanium is quite conductive and somewhat weaker than stainless steel, so it generally has a worse quality factor. In contrast, the titanium alloy is significantly stronger than stainless steel and less conductive, so it performs better. Despite its low strength, Vespel is better than the metals, especially at low temperature, because of its low conductivity, and Kevlar is by far the best.

Kevlar is a high strength polyimide available as filament (single strands) or braid. It is occasionally used as fishing line; sporting goods stores are our usual suppliers. We take advantage of its high strength to thermal conductivity in two ways. Each can is suspended from the next warmer one by a pair of Kevlar loops. The Kevlar is 100 pound test braided Kevlar fishing line¹³⁰ with an approximately square cross section, 0.58 mm on a side. We can use Eq. (5.27) to compute the number of strands required for the largest load, which we will take to be 450 kg (if the Icebox were filled with lead). The total area required is 21.3 mm², or 63.4 strands. The load is supported by two hangers, each made of a loop, so there are a total of four support members.

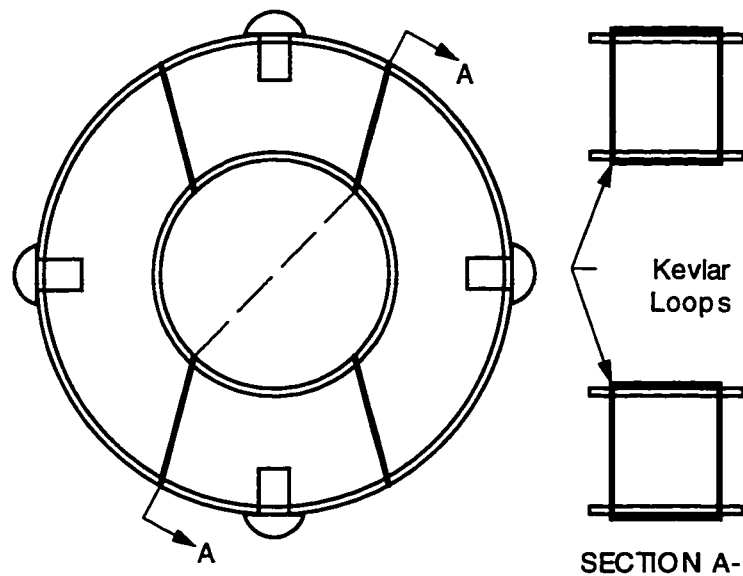


Figure 5.14. E-stem Spider Supports.
 Drawing of the spider supports used in the E-stem. The inner and outer circles are tubes held concentric by opposed Kevlar strings, drawn as heavy lines, in the manner that the spokes hold a bicycle rim and hub concentric, though the spider uses a much simpler arrangement of lines.

Therefore each loop has 16 turns. The turns are made around a spool (pulley) at each end of the loop while the spools are held in a jig. The loop assembly is then placed in a form with $\sim 1 \text{ mm}^2$ square cross section which is filled with epoxy (Epon 828 and Versamid 140, equal parts by weight). When the epoxy cures, we are left with a rigid loop with captured spools at each end. The loops inside the LHe can are 20 cm long and the loops outside are 40 cm long. The resulting heat loads are 11 mW on LN, 2.9 mW on LHe, 23 μW on the ST, 60 nW on the CP, and 50 pW on the MC can.

The second application of the Kevlar is the centering devices in the electrical stem. Because of the complicated motions, the E-stem needs some flexibility. At the warm end are a pair of thin walled stainless steel bellows. Stainless steel is allowed here in moderation because it is in the region outside the shield. In addition, the stainless sections are thermal standoffs, so the low conductivity of stainless is an advantage. The can end of the LHe E-stem uses a machined bellows, and the LN uses

an "S" shape section. Both the machined bellows and the "S" section are mechanically strong enough to hold up the can end of the E-stems. The problem is to support the warm end without putting the load on the stainless bellows, which are somewhat fragile. Again, space is an issue. For some of the earliest Icebox designs we developed a "support spider" for just this purpose — to keep nested tubes concentric without introducing a large heat load. A basic spider uses two rings of copper, one sized to just fit outside the inner nested tube, the other to just fit inside the outer tube. By using loops of string to draw the rings together, and placing the loops on opposite sides of the rings, the loops work in opposition to keep the rings concentric. The actual design used in the E-stem is illustrated in Figure 5.14. The inner sleeve rides on roundhead nylon screws as it slips over the colder E-stem. The outer sleeve also has nylon screws as bearing surfaces when the warmer stem is slid over.

5.4.4 Thermal Links in The Fridge and High Conductivity Copper Wire

One of the tests we performed with the fridge alone was to apply heat loads at the side access ports to simulate the load of the Icebox. During these tests we discovered that the thermal connections in the fridge were quite poor in some cases. In one case the screws making the first connection from the still to the still plate of the dilution unit had come loose. On both the cold plate and the still, the plates were made of brass, which has only a fair thermal conductivity. Our system is unusual in that we are applying macroscopic heat loads at the bottom of every stage, whereas the typical dilution fridge experiment has relatively small heat loads at the cold plate of most stages, due solely to the heat sinking of wires. This difference explains why the poor thermal connections due to the brass plates had not been noticed during earlier test of the fridge.

To short out the impedance of the brass, we constructed thermal links made from specially treated high purity copper wire. The links attach directly to the cooling source (the still or intermediate plate between the continuous and step heat exchangers, for the still and cold plate layers, respectively) then go directly to the flange of the corresponding skirt, which are made of copper only.

The treatment procedure, which consists of annealing in an oxygen atmosphere,¹⁰⁴ drastically increases the thermal conductivity at low temperature. The anneal is nearly hot enough to melt the wire, which speeds the diffusion of oxygen into the wire where it binds to the impurities that limit the thermal conductivity at low temperature. The slow cooldown recrystallizes the copper into large grains. In the process, the oxygen bound impurities are pushed out to the grain boundaries. The result is that the wire has the same concentration of impurities, on average, but the electron mean free path is greatly enhanced because the impurities are concentrated at the boundaries of the large grains.

We start with 1.59 mm diameter 99.95% pure copper wire, which has a RRR of 42. We clean the wire in a solution of 15% ammonium hydroxide, 15% hydrogen peroxide, and the remainder distilled water, then dry it for two hours at 150° C in vacuum (40 mT base pressure). We introduce an atmosphere of 500 mT (partial pressure) helium, 210 mT nitrogen, and 50 mT oxygen and anneal at 980° C for about 36 hours, then reduce the temperature to 700° C for another 24 hours, then turn off the oven and allow the wires to cool.[†] Finally, we remove the thick surface oxide that develops by etching the wire in 50% hydrochloric acid in water for 30 minutes, which reduces the diameter by 0.25 mm. At the end the wires are dead soft with crystal grains visible to the naked eye. With this procedure we routinely obtain RRRs of 2050 ± 100 .

[†] We are indebted to D. Osheroff of Stanford University for teaching us the procedure and allowing us to use his oxygen annealing oven.

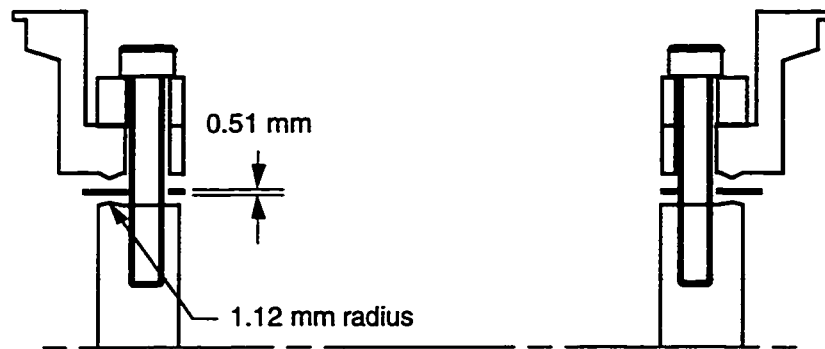


Figure 5.15. Detail of All Copper Foil Seal Flange. Cross section of the copper gasket and sealing flanges. Each flange has a half hard round nose which is pressed into a dead soft copper gasket.

5.4.5 Foil Seal Flanges

The conventional cryogenic vacuum seal gasket material is indium wire, which is radioactive. The alternatives are lead wire, which can be made from clean lead, or sometimes gold wire. Since both are considerably harder than indium, they require more pressure to get them to flow and seal. In our all copper cryostat, it is difficult to get large pressures at the seal because the threads can fail, at one end of the bolt, and the copper of the flange can flow out from under the bolt head on the other side. Instead of using lead or gold wire gaskets, we developed an all copper sealing system, shown in Figure 5.15, based on the rounded nose seals used in the Cajon VCR plumbing fittings (which are made of stainless steel). This is similar to the knife edge seals commonly used in room temperature UHV work. The flange faces are basically flat with a protruding round nose. The nose, with a 1.12 mm radius, is formed by passing a wheel with the desired cross section over the flange under pressure. If this is done after all welding on the part the nose will be hardened and not subsequently annealed. The gasket is made from copper shim stock, 0.51 mm thick, cut into large washers or flat gaskets, which are then annealed to a dead soft condition. When mated, the contrast between the hardened noses and the dead soft gasket allows the sealing pressure to push

the noses into the gasket, forming a dent. The contact length between the noses and the gasket provides the seal. Because there is not much difference in the hardness of the nose and the gasket, the nose must be rounded to start with to prevent it from wearing down, unlike the stainless knife edges pressing into copper UHV gaskets, where the knife edge lasts forever. The tolerances in machining the noses are quite small. The noses must be planar to much less than the dimple created in the gasket. They also have to be circular and, when mated, concentric (by using a set of alignment pins) to much less than the radius of the nose, again so a sufficiently deep dimple is formed to seal adequately. In tests on a prototype we measured $RRR = 24_{-16}^{+24}$ and a conductance at 4.2 K of 5 W/K.

5.4.6 Future Improvements

Given how involved the cryostat is (it took two years to design, not the two months we originally projected), we have been pleasantly surprised by how well it met our expectations during assembly and operation. Still, there are a handful of design changes we would make next time around.

The most serious problem is a nose-seal flange on the SS weldment where it connects to the LHe E-stem that has too small an aspect ratio. When we tighten the screws, the flange warps like a cup washer, so that some of the pressure is applied at the flange edge, not at the seal. This just requires using a thicker flange, keeping the weldment the same length overall.

We also struggle with inadequate tooling at three steps of the assembly. When tightening the L-joint screws, we use a "wrench" to hold the knuckle so that we don't transmit torque to the mixing chamber. The knuckle seems to have deformed slightly, so that it is very difficult to install the wrench, and we do not yet have a good system for anchoring it. Before installing the long bolt joint sleeve and stub, we have to polish

the end of the HCF flex section to remove the oxide layer that develops while we are installing the stems. This is a difficult operation since the end of the HCF is free to turn and move away from the polishing cloth, so we need a fixture like the sleeve to capture the HCF, a long bolt to keep it from sliding away, and then annular polishing disks and a tube to apply pressure and rotate the polishing disks. Finally, we would like a support fixture for the E-stem weldment to prevent it from collapsing so we can pump out and leak test the E-stem LHe seals during the assembly.

5.5 Detector Towers

Recall that the description of the Icebox said nothing about the detector mounting, cold amplifier components, or the wiring from room temperature to the amplifiers. The conventional method for installing a device into a dilution fridge is to attach the device to a sample mounting plate which is attached to the mixing chamber. Last, one makes the wiring connections between the permanently installed fridge wiring and the device leads. This is a time consuming and error-prone process. Typically, the cold components of the amplifiers are also permanently installed, so changing amplifier technology is a major effort. Finally, space limitations usually severely limit the number of low resistance, high bandwidth wires that can be installed, thus limiting the capabilities of the experiments. To circumvent these problems we have developed a modular detector and amplifier package (the tower) which connects to a modular wiring system (the stripline) to carry the signals out to room temperature. We will discuss the overall tower design, then focus on the wiring and heat sinking issues in the tower and for the stripline. The towers and striplines were designed by Dan Akerib, Bernard Sadoulet, Tom Shutt, Garth Smith, Walter Stockwell, Storn White, and PDB.

5.5.1 Tower Mechanical Design

A number of considerations determine the overall tower design. The tower should include all hardware needed (*i.e.*, supports, wiring, and heat sinking) to interface the striplines to the cold amplifier components and on down to the detectors, in a package which can be constructed on the bench, tested as an assembly, and finally installed in the Icebox. It should make the most of the available volume in the Icebox by supporting multiple detectors close together, and the overall shape of the tower should allow close packing of towers. The close packing within and between towers is to maximize the benefit of multiple scattering. It should accommodate the Stanford detectors being designed around 3" wafers. Because of the thermal motions in the cans the tower can only be mechanically supported at one temperature stage, though it can have thermal links to all stages for the heat sinking.

The final tower is illustrated in Figure 5.16. Because the detectors will dominate the mass, we decided to support the tower from the top of the MC can. This suspends the detectors below the support and holds the cold amplifier components, wiring, and heat sinking above the support. In plan view the towers are hexagonal, which allows them to be close packed in the Icebox and gives flat surfaces for the wiring and heat sinking from the LHe stage down to the detectors. The hexagon diameter (the distance between parallel sides, which is also the diameter of the largest inscribed circle) is 96 mm. This allows seven towers to be close packed in the Icebox (three at Stanford allowing ~10 cm internal moderator). Another virtue of the hexagonal shape is that the corners extend beyond the detector discs, allowing supports for lower detectors to pass around the ones above. The flat sides accommodate 16 wires, which is enough for one of the Berkeley or Stanford detectors, so each tower can support six detectors. The heart of the tower is the section from the LHe layer to the MC Layer, called the floors section. Its main function is to support the cold amplifier

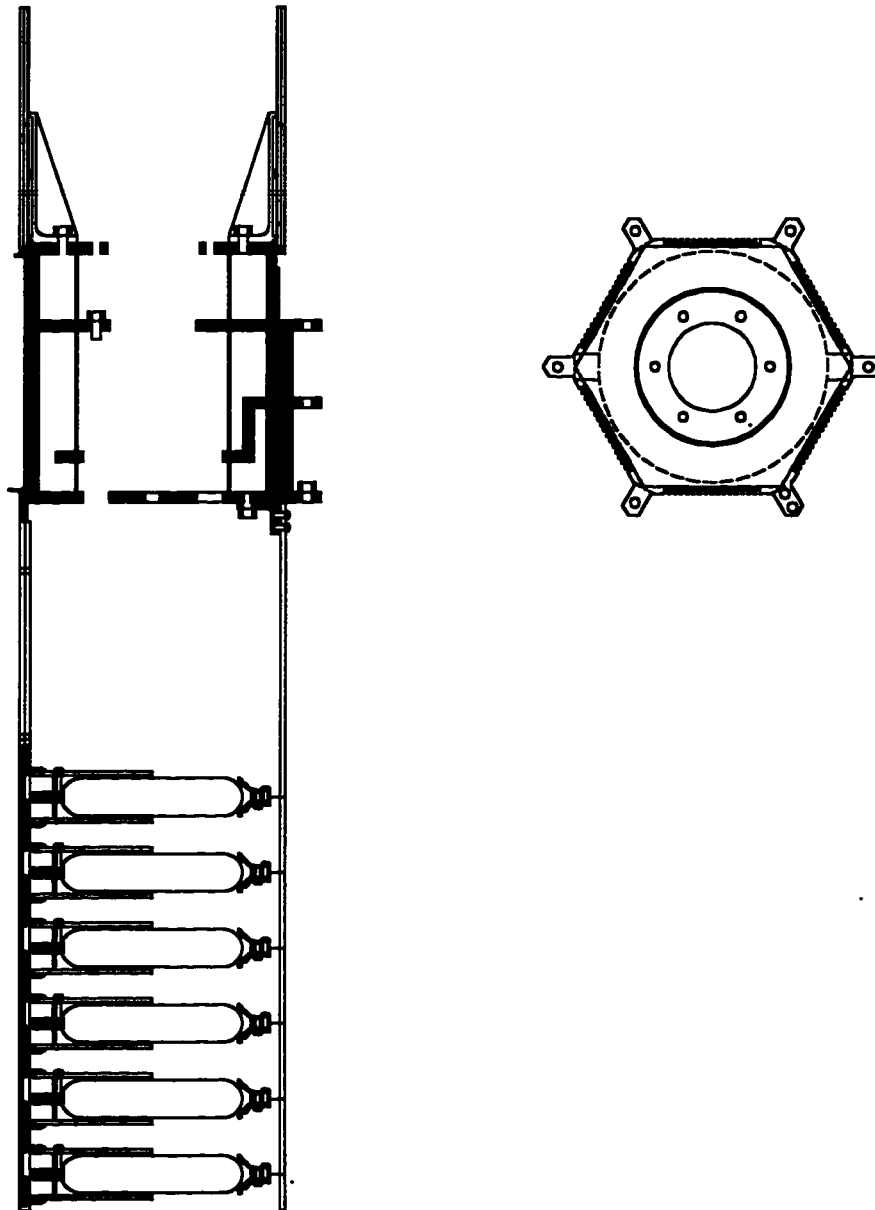


Figure 5.16. Schematic of the Detector Tower. Vertical section (left) and horizontal plan (right) views of the detector tower. The six ovals at the bottom of the section view are the detectors. Above the detectors is a gap for the internal moderator. A support member and the side coax are on the right of the detectors, only a support member is on the right. The floor sections are above the moderator space, with two FET cards shown above the LHe floor. The plan view is at the bottom of the 10 mK floor, showing the six mounting tabs and the channels for the vacuum coax wiring.

components and heat sink the wiring on its way down to 10 mK. We will discuss the wiring heat sinks in more detail below. This section is made up of copper floors at each temperature stage (LHe \sim 9 K, Still \sim 0.9 K, CP \sim 0.1 K, MC \sim 10 mK), thermally anchored by high conductivity copper wires (see §5.4.4) to the lids of the respective cans. The mechanical supports between floors are graphite tubes to minimize the conducted power. As we will see below, the wiring must be heat sunk at the LHe, Still, and MC layers. A support from the Still layer directly to the MC layer would conduct too much heat, so the tower has an extra floor at the CP layer to heat sink the support.

We have had some difficulty finding low conductivity graphite that is also radioactively clean. The material we are using now is clean but has a conductivity \sim 10 times what we have measured in other (radioactively contaminated) samples. To be able to run more than a few towers, we need to recover that factor in heat load. The design heat loads due to the graphite are shown in Table 5.18.

The FET card is mounted to the top of the LHe floor. The card is both the connector for the stripline and contains the cold components of the amplifiers, be they FETs or SQUIDs. The card is made from multilayer Kapton with copper traces. The FETs have a noise minimum around 110 K, so they are mounted on a 5 mil Kapton window, to minimize the conduction cross section. Two sides of the window are slit, further limiting the conducted power. The traces on the window are evaporated platinum to minimize the heat load from the FET conducted down the traces. At the end of the platinum a dab of conducting epoxy ensures good electrical contact between the copper and platinum traces. The window also supports a heater and thermometer, to allow us to monitor and control the FET temperature.

The wiring from LHe down to the MC floor is unconventional. Most of the signals need shielding from crosstalk. In addition, a wire moving due to mechanical vibrations in the field of static surface charges trapped on insulators will pick up a

voltage. If the wire connects to a sensitive element of the amplifier, the result is a microphonic noise spectrum falling like $1/f$ but with significant peaks out to 20 kHz. The most effective way to reduce this noise is to avoid exposing the wires to the fields from dielectrics by shielding the wires and removing the dielectrics. The scheme we have adopted is called a vacuum coax, since it uses vacuum as the dielectric in a coaxial geometry. The simplest version is to fix a wire under tension down the center of a metal tube. A small amount of insulator (epoxy) electrically isolates the wire from the tube at the ends, where the wire attaches to a connector pin. The tube acts as the shield braid on a coaxial cable, with the dielectric replaced by vacuum. In the tower design, the tube is replaced by a channel running down the side of the floor. Between floors a small gap prevents any heat flow from one floor to the next along the shield wall. At the ends and at the Still floor in the middle the wires are soldered (using low activity solder) to the heat sinks.

We have worked very hard to reduce the amount of infrared radiation that makes its way down the tower to the detectors. Both the FET card and the detector section are surrounded by nearly light tight enclosures made of copper shim stock. There are additional baffles at the wiring offsets between the FET card and the tower and the tower and the side coax. We have also installed "combs" to block the line of sight down the vacuum coax and tower channels.

The detectors are supported below the MC floor by a lightweight truss (the basement). The wiring for a given detector is brought down from the MC floor heat sink to the detector mount by a "side connector," which is a 16 wire vacuum coax assembly using continuous channels, since both ends are at the same temperature. To discuss the wires and heat sinks themselves, we will develop some more thermal modeling tools in the next section.

5.5.2 Thermal Model for Wiring

Recall that the power conducted by a wire, say, with its two ends at different temperatures is

$$P = \frac{A}{L} [K(T_2) - K(T_1)]. \quad (5.30)$$

In deriving Eq. (5.15) to compute the temperature jump across a joint of finite resistance we used the expression $R = L/(A\sigma_0)$ for the resistance, assuming that the electrical conductivity did not vary over the temperature range considered. Here we want to allow the conductivity to vary. At a given isothermal surface characterized by the temperature T , the electrical conductivity is $\sigma(T)$, and the contribution to the wire resistance of the layer with thickness dz is

$$dR = \frac{1}{\sigma(T)} \frac{dz}{A}. \quad (5.31)$$

The total resistance is found by adding up these pieces in series for each isothermal surface from T_1 to T_2 , *i.e.*,

$$R = \frac{1}{A} \int_{T_1}^{T_2} \frac{dz}{\sigma(T)}. \quad (5.32)$$

We can turn this into an integral not over z but over T using Eq. (5.5) to write

$$dz = \frac{A\kappa}{P} dT. \quad (5.33)$$

Substituting into Eq. (5.31), we have

$$PR = \int_{T_1}^{T_2} \frac{\kappa(T)}{\sigma(T)} dT = \int_{T_1}^{T_2} \kappa(T) \rho(T) dT, \quad (5.34)$$

where $\rho(T) = \sigma(T)^{-1}$ is the resistivity. Note that the product (PR) depends on the material and endpoint temperatures only; it is completely independent of the geometry that determines the actual resistance or thermal power. In essence, it quantifies the

tradeoff between conducted power and low resistance. Just for completeness, we can write the resistance as

$$R = \frac{L \int \kappa \rho dT}{A \int \kappa dT}, \quad (5.35)$$

i.e., the resistance is a weighted average of the electrical resistivity, with the weighting function being the thermal conductivity. The weighting may seem a little odd, but can be understood by noting that the thermal conductivity determines the temperature profile which determines the resistivity profile which determines the resistance.

Suppose we have N wires of the same material with the same resistance. The total heat load is just

$$NP = \frac{N}{R}(PR). \quad (5.36)$$

Then for a set of wires from T_2 to T_1 , made out of the same material, but with varying resistance, *i.e.*, varying diameter or length, the total heat load is

$$\sum_i N_i P_i = \sum_i \frac{N_i}{R_i}(PR) = (PR) \sum_i \frac{N_i}{R_i} \equiv (PR) N_{\text{Eff}}. \quad (5.37)$$

This tells us to add up the number of wires, weighted by their individual resistances, to determine the effective number of wires, N_{Eff} (wires/ Ω). Each unit of N_{Eff} contributes (PR) to the total thermal power.

Finally, using Eq. (5.2), the W-F relation between the thermal and electrical conductivity, we can perform the integral indicated in Eq. (5.34) and obtain

$$(PR) = \int_{T_1}^{T_2} \frac{\kappa}{\sigma} dT = \frac{L}{2}(T_2^2 - T_1^2). \quad (5.38)$$

This should be an accurate estimate for metals below ~ 10 K and at high temperature. Note that if W-F applies, it does not matter what metal one chooses. To obtain a given resistance implies the power given by Eq. (5.38), independent of the material.

Table 5.17. Heat Load Estimates for Seven Detector Towers.
Heat load estimates assuming W-F and $N_{Eff} = 700$ for 7 detector towers.

Temperature Range	(PR)	$N_{Eff}(PR)$
9 – 0.9 K	0.98 $\mu\text{W } \Omega$	0.69 mW
900 – 60 mK	9.8 nW Ω	6.9 μW
60 – 5 mK	44 pW Ω	31 nW

5.5.3 Application to the Towers: Wiring Heat Loads

Now let's use this formalism to examine the conventional solution for detector wiring. Each of seven towers has six faces with 16 wires, for a total of 672 wires, so even if they each have a few ohms resistance, N_{Eff} is still $\sim 10^2/\Omega$. The relevant values of (PR) and $N_{Eff}(PR)$ with $N_{Eff} = 700$ for our temperature stages assuming W-F are shown in Table 5.17:

If we want to combine ranges by skipping a heat sink, Eq. (5.34) (or Eq. (5.37)) tells us to add the values of (PR) (or $N_{Eff}(PR)$). The power estimate from 9 K is not a significant load on the Still, but is too much for the Cold Plate, so we need a heat sink at 0.9 K. From 0.9 K the heat load is significant, but manageable for the Mixing Chamber (the base temperature would rise to ~ 15 mK), so we could get by without a heat sink at 60 mK on the CP floor of the tower. However, with superconducting wire the heat loads would be reduced by a large factor (of order 10^2). Therefore, we use copper clad NbTi (0.43 mm \emptyset with cladding removed) wire. We remove the copper cladding everywhere except the places we need to solder.

The final configuration is NbTi wire going from the LHe floor to the 10 mK floor, heat sunk along the way at the ST floor. The side coax also uses NbTi wire, and the circuit board at the detector holder amounts to an additional heat sink (MCB in Table 5.18 below). The model heat loads in the tower are shown in Table 5.18. Comparing the NbTi estimates in Table 5.18 with the normal metal estimates in Table 5.17, we see that superconducting wire reduces the heat load from 1 K–5 mK by a

Table 5.18. Model Tower Heat Loads.

The heat load into each temperature stage for seven towers from the thermal model. The detector entry is the residual heat load on a single detector.

Cold End Temperature	Heat Loads		
	NbTi Wiring	Graphite Supports	Total
0.9 K	0.28 mW	0.28 mW	0.56 mW
60 mK	–	5.6 μ W	5.6 μ W
5 mK A	0.18 μ W	14 nW	18 μ W
5 mK B	80 pW	–	80 pW
Detector	6.5×10^{-18}	–	

factor of 35, even though the NbTi skips the CP layer at 60 mK. Even at 1 K the superconducting wire has cut the heat load in half.

5.5.4 Heat sinking

The goal of a heat sink is to take the power coming down an object from a higher temperature and divert it into a thermal bath at some intermediate temperature instead of permitting the power to continue down to a lower temperature. The way to achieve this diversion is with the thermal analog of an electrical resistive divider: the conductance through the heat sink should be much greater than the conductance down the part to the colder stage. The conductance is just

$$G(T_2, T_1) = \frac{P}{\Delta T} = \frac{A}{L} \frac{K(T) - K(T_1)}{\Delta T} = \frac{A}{L} \frac{1}{\Delta T} \int_{T_1}^{T_2} \kappa(T) dT. \quad (5.39)$$

$$G(T_2, T_1) \equiv \frac{A}{L} \kappa(\bar{T}). \quad (5.40)$$

In Eq. (5.40) we have replaced the average thermal conductivity by the conductivity evaluated at an average temperature. If the temperature range is truly small, as in a heat sink, it does not matter significantly whether one uses one of the endpoint temperatures or some average value. A wiring heat sink uses a dielectric to electrically isolate the wire from the fridge itself, therefore κ is typically much less for the heat sink than for

the wire. To compensate, the heat sink must have a larger area and smaller length (thickness), L .

Thermal Mismatch Resistance

At very low temperature the phonon wavelengths in the metal will be much different from the wavelengths in the dielectric. Equivalently, the sound speeds are very different. The result is a large reflection coefficient for phonons at the surface, which leads to a thermal conductance proportional to the area only. This effect is called the thermal mismatch resistance or the Kapitza resistance between the metal and the dielectric, and is in series with the bulk dielectric conductivity estimated in Eq. (5.40). Various authors estimate the mismatch conductance as

$$G_k = \frac{1}{N} \left(\frac{T}{K} \right)^3 \frac{A}{\text{cm}^2} \frac{W}{K}, \quad (5.41)$$

with the numerical factor N ranging from 7.5,⁹⁵ to 30.⁹⁸

Heat sink Design

The physical size of a heat sink is largely determined by the area required, so the space available and achieving low Kapitza resistance compete to determine the design. The bulk dielectric resistance is added in series with the Kapitza resistance. Once the bulk conductance is much larger than the Kapitza conductance, there is little further gain in overall conductance as the dielectric is made thinner, but a thinner dielectric does increase the capacitance to ground. Typically for signal wires one chooses the area to balance size and Kapitza conductivity, then chooses the dielectric thickness so the bulk conductance is approximately equal to the Kapitza conductance, to avoid excess capacitance to ground.

The design we settled on uses copper traces on Kapton. The copper traces are approximately 9.0 mm \times 1.3 mm. The Kapton consists of 7 layers 0.127 mm thick bonded together to give a total dielectric thickness of 1.2 mm. Within the uncertainty in

the Kapitza conductance the bulk Kapton and Kapitza impedances are comparable. Since the superconducting wire beyond the 100 mK heat sink is much below the transition temperature, the thermal conductivity of the wire is approximately equal to the Kapton. However, the Kapton has $A/L = 3.6$ mm, whereas the wire has $A/L = 0.5$ μm , so the heat sinks are more than adequate.

5.5.5 Stripline

A fully instrumented Icebox will have 7 towers with 6 detectors each. Each detector has four channels and needs 28 signals from room temperature. Of these, 12 require shielding against crosstalk and moderate bandwidth, either to allow AC biasing or the intrinsically high speed ionization or W/Al QET signals. In addition, the two grounds (Front End Ground and Detector Common) must be low impedance. Each detector, therefore, requires something like 14 unshielded lines, 12 lines with 12 shields, and 4 FEG and 8 Detector Common, say (using hints from the real stripline), for a total of 50 lines from room temperature. For all 42 detectors and the 96 monitoring wires (discussed in §5.6.2 below) the E-stem must carry nearly 2200 lines from room temperature to LHe, with roughly half of them in a shielding configuration. At the same time, we must control the thermal conductivity so as not to overwhelm the available cooling power, and keep the diameter of the E-stem small to minimize the shield penetration. Discrete wires or coax will not give us enough control over the dimensions to engineer the heat load and heat sinking. We decided to develop a high density multiconductor shielded flat cable (the Stripline) using flexible circuit technology. This allows us complete control over the design, so we can engineer the resistance and heat loads, and the flat geometry is ideal for mating with a heat sink.

From Eq. (5.37) and thermal considerations we can estimate the minimum trace resistance we can tolerate (in terms of heat load) and the overall length of the striplines.

Table 5.19. (*PR*) Values for Copper and Gold from 300 K to 9 K. Numerical integrations of the product of the thermal conductivity and the electrical resistivity for electrolytic tough pitch copper and commercial gold.^{131, 132}

Material	Temperature Range	
	300 K–115 K	115 K–9 K
Copper	0.838	0.157
Gold	0.918	0.138
Wiedemann-Franz	0.937	0.160

The conductivities of moderate conductivity copper and gold, the most common materials used in flexible circuits, can be found in the literature.^{131, 132} Using Eq. (5.34), we numerically compute the (*PR*) values from room temperature to the LN heat sink at 115 K and on to the LHe heat sink at 9 K and compare them to the W-F predictions in Table 5.19. Note that both materials are similar, despite the large differences between their individual $\kappa(T)$, $\rho(T)$, or even the product function $\kappa(T)\rho(T)$. This is because over both temperature ranges the integrals are dominated by the high end where the materials don't differ very much (W-F applies). Also note that the real materials are slightly less thermally conducting than the W-F estimate, since W-F overestimates the thermal conductivity when it does not apply.

Suppose we adopt as a design rule that the heat load due to detector wiring should not be more than 1/10 of the model heat loads for the cryostat itself. That is, the wiring should be a thermal perturbation not likely to make the cryostat fail. The 44 striplines contain 2200 traces; for simplicity consider all the traces to have the same geometry. Using more hints from the real striplines, let the traces themselves only contribute 2/3 of the total allowed heat load. Therefore the allowed heat load per trace is $p = \frac{1}{10} \frac{1}{2200} \frac{2}{3} = 3 \times 10^{-5}$ of the model heat load. Taking the W-F estimates of the (*PR*) product and dividing by pP_{Model} we can estimate the minimum trace resistance due to the temperature gradients: $R = 0.87$ (5.5) Ω for the sections from 300–115 (115–9) K, respectively. Of course, the total resistance is the sum of these values, plus the

resistance of the constant temperature pieces at each end. Clearly, it is hard to have low resistance wiring that doesn't have a significant effect on the cryostat performance.

The step to LHe seems to dominate the resistance, but this really just reflects the importance of black body radiation on the LN layer. The heat load on LN is 93% due to radiation, and on LHe 42% due to radiation. The total heat loads differ by 36, but the W-F (PR) values differ by only a factor of 6, leaving a factor of 6 difference that shows up in our minimum resistance estimates. To obtain sufficiently low resistance we will have to accept a wiring heat load on LHe greater than 1/10 the cryostat load.

To estimate the heat load from the dielectric, we need to estimate the cross sectional area. Let us take 8 mils of dielectric (again, hints from the stripline) on each side of the signal layer for a total insulator thickness of 0.41 mm per flex and a width of 1" = 2.54 cm. The total cross section for all 44 striplines is 4.5 cm². The Kapton thermal conductivity integrated over the appropriate temperature ranges are: $K(300\text{ K}) - K(115\text{ K}) = 3.93\text{ W/cm}$, and $K(115\text{ K}) - K(9\text{ K}) = 0.658\text{ W/cm}$. Therefore, the insulator heat load over a 1 cm length from 300 K to 115 K is 17.7 W, and between 115 K and 9 K it is 2.96 W.

We can write the total heat load analytically as

$$P = p_0 + \frac{p_1}{L}, \quad (5.42)$$

where P is the total power conducted, L is the length of stripline between the temperature stages, p_0 is the heat load due to the traces (which is independent of the length because of the fixed resistance requirement), and p_1/L is the heat load due to the dielectrics. We computed the p_1 coefficients at the end of the last paragraph. The p_0 coefficients are just 2/3 of 1/10 of the cryostat heat loads; the coefficients are shown in Table 5.20. To get the p_0 terms to double p_1/L (to meet our 2/3 assumption) we have to make the distance between the heat sinks 15 (91) cm for the interval 300–115 (115–

Table 5.20. Stripline Heat Load Coefficients.
Heat load coefficients defined in Eq. (5.42) for estimating the heat load due to 44 striplines.

Coefficient	Cold End Temperature T_1	
	115 K	9 K
p_0	2.4 W	0.065 W
p_1	17.7 W cm	2.96 W cm

9) K, respectively. The stripline must be at least 1 m long from thermal considerations alone.

Stripline Design

So what *is* the real stripline? The striplines are flexible circuits 2.9 m long and 0.92" (2.34 cm) wide over most of that length (see Figures 5.21 and 5.22). The trace layer contains 50 traces 5 mils (127 μm) wide running between pad grids for connectors at either end. The traces are patterned in 1/2 oz. per square foot copper (19 μm thick). On either side is a set of dielectric layers 6 mil (150 μm) thick consisting of 66–80 % Kapton and the remainder acrylic adhesive. Each dielectric layer has a ground plane, either 0.6 or 1.0 μm (23 or 39 microinch) thick. The difference in composition and ground plane thickness on the two sides is due to manufacturing constraints. Finally, each ground plane has a 2 mil (51 μm) thick cover layer for protection. As an indication of the high wiring densities, the final design uses 0.22 mm^2 net per signal, approximately 1/5 of the cross section of an ultra-miniature coax. The free length of the stripline from 300 K to the LN heat sink is 15 cm and from LN to LHe is 127 cm.

Heat loads

With the stripline details in hand, we can compute the actual heat loads with the standard machinery. Each stripline brings 0.226 W for a total of 9.94 W into 115 K, and 3.85 mW each for a total of 170 mW into 9 K. Of the total per stripline, 149 mW and 2.52 mW into 115 K and 9 K, respectively, or 2/3 of the total, are due to conduction by the traces.

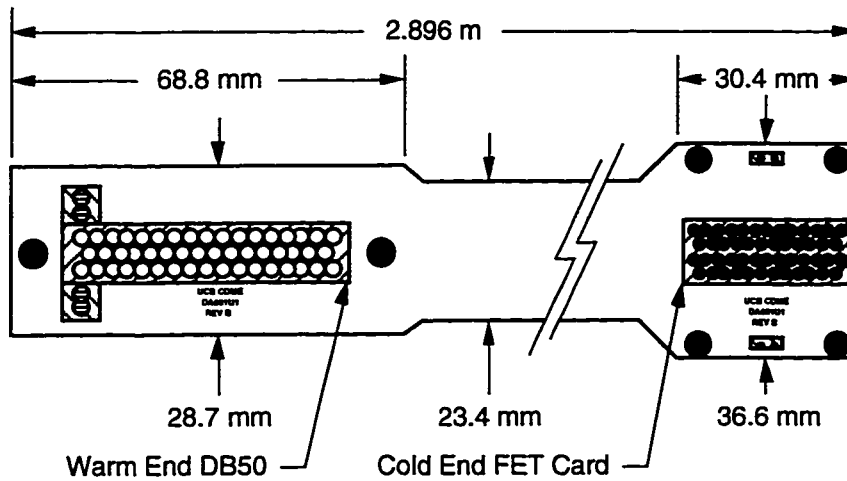


Figure 5.21. Stripline Plan View.
 Plan view of the stripline, showing the pin patterns at either end. The traces connecting the pins are 5 mil (0.127 mm) wide.

<u>FUNCTION</u>		<u>MATERIAL</u>	<u>SUPPLIER</u>
0.002" Cover	[0.001" KAPTON] LPC
1.0 μm Shield		0.001" ADHESIVE	
		1.0 μm COPPER	
0.006" Dielectric	[0.005" KAPTON] STW
		0.001" ADHESIVE	
0.0007" Traces		0.5 OZ. COPPER	LPC
	[0.001" ADHESIVE] GTS
0.006" Dielectric		0.002" KAPTON	
		0.001" ADHESIVE	LPC
		0.002" KAPTON	IBM
0.6 μm Shield		0.6 μm COPPER	
0.002" Cover		0.001" ADHESIVE	
		0.001" KAPTON] LPC

Figure 5.22. Stripline Section View.
 Section view of the stripline with the vertical scale greatly exaggerated. Metal layers are drawn in black; dielectrics are outlined. The labels on the left group functional layers. The labels on the right group the layers by the source material. The complicated bottom dielectric is necessary because it turned out to be very difficult to apply the trace layer to the STW material before patterning, otherwise we would have used the STW material for both dielectric layers.

Electrical Characteristics

Using the appropriate (PR) values for Copper from Table 5.19, we estimate the DC resistance as 0.28 and 3.1 Ω across 300–115 K and 115–9 K, respectively. With the first prototype in two configurations we measured 4.93 and 4.64 Ω average per trace. These are slightly larger than we just predicted from the heat load, but the measurement includes the length at room temperature. Though we minimized this length, it still has a substantial effect on the total resistance. In the production version we will increase the trace width at either end over the lengths past the heat sinks, which will reduce the end to end resistance. The fractional difference between the two measurements, $\pm 3\%$, is double the range of trace lengths, $\pm 1.4\%$ (due to the connector pin grids), suggesting that the trace resistances vary by somewhat more than their lengths, *i.e.*, the traces themselves are somewhat non-uniform.

We can also estimate the impedance, capacitance, and inductance of the traces. The impedance is¹³³

$$Z_0 = \frac{60 \Omega}{\sqrt{\epsilon}} \ln \left(\frac{4b}{0.67\pi w(0.8 + t/w)} \right), \quad (5.43)$$

where w is the trace width, t is the trace thickness, b is the total dielectric thickness between the ground planes, and ϵ is the dielectric constant. For the dimensions of our stripline, $Z_0 = 47.5 \Omega$, using $\epsilon = 4$.¹³⁴

We can use the parallel plate expression as an estimate of the capacitance between two thin strips with width w and separated by a distance b : $C \approx L\epsilon\epsilon_0 w/b$, where L is the length of the stripline. Consider inserting a ground plane between the thin strips. This looks like our stripline configuration, with the second strip acting as the image of the first. It has the same field configuration, hence the same capacitance, as our stripline trace to one of the ground planes. We should multiply by two to

account approximately for the second ground plane. Therefore the capacitance per unit length is approximately

$$c = \frac{C}{L} = 2\epsilon\epsilon_0 \frac{w}{b}. \quad (5.44)$$

This agrees to ~10% with the values graphed in Figure 3.10 of Blood.¹³³ The quantity $2\epsilon\epsilon_0 = 71$ pF/m using a dielectric constant of 4. For our stripline we estimate $c = 30$ pF/m.

The inductance per unit length is just

$$\ell = cZ_0^2. \quad (5.45)$$

Using the values computed above, we estimate $\ell = 68$ nH/m.

5.6 Monitoring System

Given that the Icebox is a fairly unusual design, and none of the designers had any experience building low temperature cryostats, we were quite concerned that if it did not operate as expected, we should be able to get enough information to diagnose the problem. Because we are looking for rare events, we also want to monitor the operation of the cryostat to be able to exclude events due to fluctuations in the cryostat operation. Finally, during the cooldown we want to know the cooling rates on the various layers and their current positions. We decided to place several kinds of sensors throughout the cryostat and the fridge plumbing and measure them with a computer controlled readout system. The whole shebang is called the "Icebox Monitoring System." We will describe the types of sensors used and the strategies for their placement, and the wiring and heat sinking technology. Then we will discuss the multiplexed readout, using a resistance measurement as an example. Finally, we will discuss the software organization and run management. Appendix B is an annotated bibliography of the full Monitoring System documentation. This system was designed

Table 5.23. Monitoring Sensors By Location and Type.

The distribution of sensors by type and location within the cryostat. The two kinds of thermometers are listed separately.

Sensor Type	RT	OVC	LN	LHe	ST	CP	MC	Total
Diode Thermometer		1	14	1	1	1	1	19
Ruo ₂ Thermometer				15	8	8	7	45
Oxford				1	2	1	3	7
Position			3	3	3	3	2	14
Touch			16	16	8	8	8	56
Fridge Operation	9							9
Total	9	1	33	36	22	21	21	143

by PDB and built by Dan Akerib, Pascal André, Angela Da Silva, Sunil Golwala, Kristine Ing, Susan Margulies, François Quéinnec, Guy Saidenberg, Samuel Sadoulet, Dennis Seitz, Tom Shutt, Andrew Sonnenschein, Walter Stockwell, Roy Therrien, Storn White, and PDB.

5.6.1 Sensors

The Icebox is instrumented with four types of sensors: thermometers, position sensors, touch sensors, and fridge operation sensors. Table 5.23 lists the number of each type. Since the system uses two kinds of thermometers with different readout paths, they are listed separately.

Thermometers

The thermometers answer two questions: if the cryostat is not working, why, and if it is working, how well. To answer why, we installed a thermometer at each end of each part. This allows us to measure the thermal conductance of each part, as well as the conductance of each joint. To answer how well, we calibrated each thermometer over the range of temperatures where it would be used at base. To provide accurate information during the cooldown, we installed an LN calibrated thermometer on each can. Most of the thermometers are RuO₂ chip resistors, read by a 4-wire resistance

measurement (an "I-V Board"), as shown in Figure 5.24. The current source is actually a Keithley 213,¹³⁵ a computer controlled four channel voltage source, whose outputs are filtered and buffered. The current measurement is made by amplifying the voltage drop across a resistor, typically 100 k Ω , in series with the thermometer. Both the current signal and the voltage signal are amplified by a factor of 500 by instrumentation amplifiers.¹³⁶ The amplified current and voltage signals are measured by a Keithley 2001 DMM.¹³⁵ The coldest thermometers ("Mixing Chamber Thermometers") each have a dedicated IV Board to isolate them from noise in the rest of the system. To remove the effect of voltage offsets in the system we make two measurements with the sign of the bias reversed.

The RuO₂ thermometers have a temperature dependent resistivity similar to the NTD Ge sensors used on the Berkeley detectors:

$$\rho(T) = \frac{\rho_0}{e} e^{(T_0/T)^\alpha}, \quad (5.46)$$

where ρ_0 is the resistivity at the temperature T_0 . As with the NTDs, the actual temperature exponent, α , has been found to vary somewhat, depending on the manufacturer and mounting, with most authors reporting $\alpha = 0.25$, characteristic of Anderson hopping conduction.¹³⁷⁻¹⁴⁰ One group manufactured their own films and found $\alpha = 0.345$, quite close to the value of 1/3 expected in two dimensional films.¹⁴¹

The devices we use are surface mount 1 k Ω resistors¹⁴² based on Dupont 1600 series bismuth ruthenate in silicate glass.¹⁴³ The RuO₂ are more convenient to use than the NTDs since they come already packaged with solder pads and are uniformly constructed. We fit our calibration data with $\alpha = 0.25$ over the temperature range 77 K–10 mK. The parameters for a generic calibration curve from fitting to all the data for a number of sensors are $R_0 = 415 \Omega$, $T_0 = 5.06 \text{ K}$, and $\alpha = 0.25$. This fit gives temperature errors < 10% under 100 mK, < 20% under 10 K, and < 40% under 77 K. At low temperatures the RuO₂ suffer from the usual problem — the power used to measure the

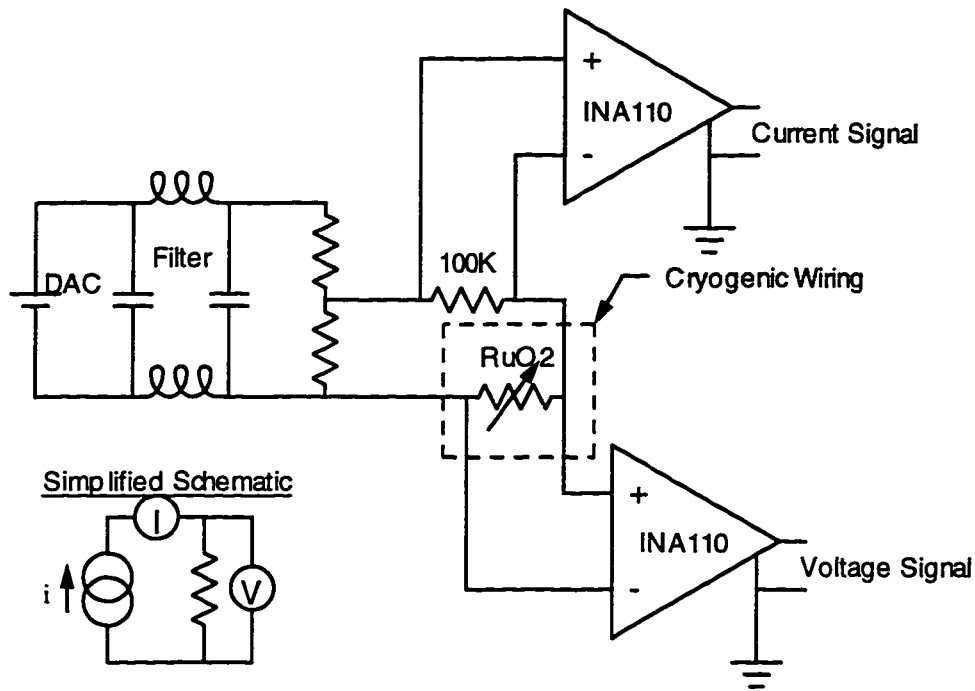


Figure 5.24. Typical 4-Wire Resistance Measurement. Schematic for the 4-wire resistance measurements. Both the current and voltage signals are measured by instrumentation amplifiers and a digital multimeter.

resistance tends to heat the resistive element above the temperature of the part it is attached to. This forces one to use ever smaller bias currents until the signals disappear into the noise. We believe that measurement errors (due to the increasing significance of the electronic noise) on sensors below 15 mK are responsible for the poor fit to the data, not an intrinsic change in the temperature dependence of the resistivity.

Since the RuO₂ thermometers have useful sensitivity only up to ~100 K, on the LN layer we use reverse biased diodes reliable from >300–10 K and measured by the circuit shown in Figure 5.23 without the current measurement. The current source is a stable 10 mA source (Lake Shore Model 102).¹⁴⁴ Naively we might expect from the I-V characteristic ($|I| \propto \exp(-e|V|/(k_B T))$) that $|V| = V_0 - V_1 T/T_1$; this is approximately correct. In practice we use the Lakeshore standard calibration curve #10 to get the right shape.¹⁴⁴

Table 5.25. Thermometer Locations and Calibration Ranges.

Cryostat Layer	Number of Thermometers	Calibration Ranges (K)		
		0.02–0.6	1.5–45	77–145
Liquid Nitrogen	14		X	X
Can Diodes	4			X
Liquid Helium	14		X	X
Pot	1	X	X	X
Still	8	X	X	
Cold Plate	8	X		
Mixing Chamber	7	X		
Oxford	7			
Total Low Level	38			
Total Mixing Chamber	7			
Total Diode	18			

For each layer of the cryostat the number of thermometers installed and their calibration ranges are listed in Table 5.25. The calibrations ranges are: 20 mK–600 mK in the 75 μ W fridge, limited by stable operation of the fridge; 1.5 K–45 K in the IR dewar with pumped helium, limited by hold time at high heating power; and 77 K–145 K in the IR dewar with nitrogen, limited by hold time at high heating power. The lower end of each range is limited by the base temperature of the cooling system. Each thermometer has been individually calibrated in the ranges indicated, and at room temperature. Over the higher temperature ranges we fit the data for all the sensors of a given type to obtain a generic calibration curve, good to a few per cent in temperature, which is used during cooldown for the devices which are only calibrated at the lower temperatures.

Position

Because of the complicated motions and contractions, during the first few cooldowns we wanted to record the positions of the various layers to alert us to impending touches and low clearance conditions. The distance between layers of the cryostat is measured using linear potentiometers.¹⁴⁵ The metal shafts pass through the

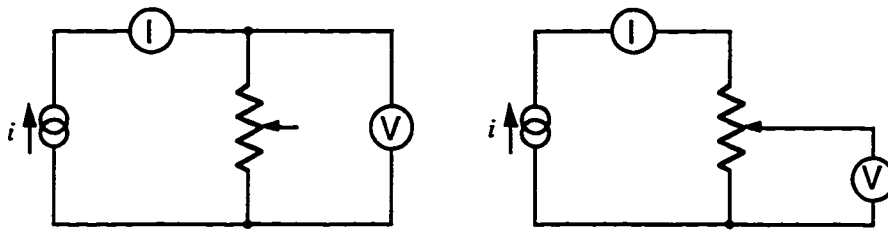


Figure 5.26. Linear Potentiometer Measurement. Schematics for reading the position sensors. The first step, shown on the left, measures the total resistance of the linear potentiometer. The second step, on the right, measures the resistance to the wiper. The ratio of these resistances is proportional to the position and independent of the temperature.

plastic wall of the sensor housing. When the sensor cools, the plastic contracts around the shaft, locking it in place. Therefore we had to turn down the shaft diameter and install the sensors compressed enough that the narrow section of the shaft was completely through the plastic. The measurement sequence is illustrated in Figure 5.26 using the simplified schematic of Figure 5.24. The potentiometer shafts have nylon extensions, so they contribute a negligible heat load.

The 14 potentiometers locate the cryostat parts at four places. (1) Four locate vertically each tail with respect to the next at the tail of the fridge. There is no sensor between the vertical cold finger and the cold plate tail because the sensors are too bulky to fit. (2) Five locate vertically each can with respect to the next at the top of the cans. (3) Five locate horizontally (along the stem axis only) each can at the E-stem entrance. The potentiometers are measured in a self-calibrating way — both the resistance to the wiper and the total resistance are measured by a 4-wire system. Note that it does not matter if the potentiometers self-heat as long as the temperature is stable during the two measurements (total and wiper resistance), so the measurement power can be much higher than is allowed for the thermometers.

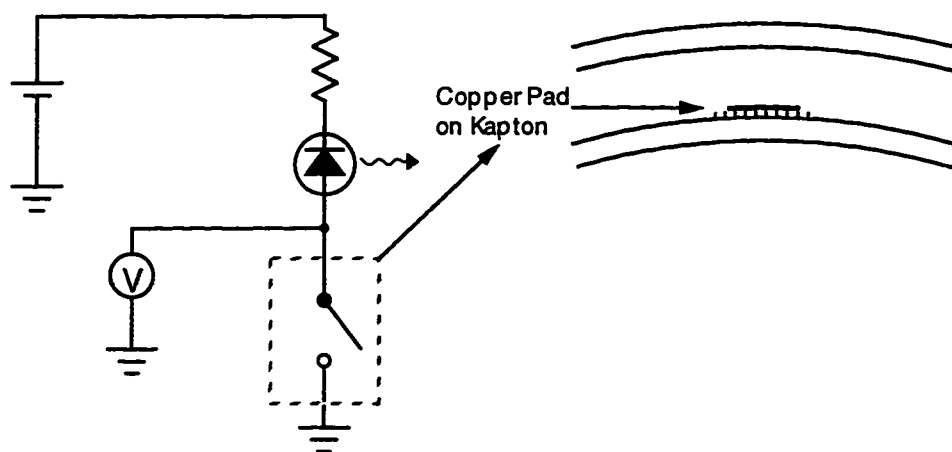


Figure 5.27. Touch Sensor.
Schematic of the touch sensor, showing its construction on the stems. The sensor itself acts as a switch. The LED is an optional visual indicator.

Touch

The touch sensor is a copper contact pad attached to the outside of a stem, as shown in Figure 5.27. The pad is insulated from its stem by a sheet of Kapton attached to the stem by epoxy. The pad is held at a non-zero potential by a power supply in series with a resistor. If the stem moves so far as to touch the adjacent stem at the pad, the pad is connected to ground by the adjacent stem, causing the voltage seen on the wire to change. Four pads nearly encircling the tube are attached at each end of the stem where the adjacent stem should hit, as well as around the E-stem entrance and the E-stem middle flange, for a total of 14 4-pad sensors.

Fridge Operation

All the fridge operation sensors are measured through a secondary MUX ("Dirty MUX") and DMM. This keeps these potentially noisy signals out of the primary MUX ("Clean MUX") system that handles all the sensors installed in the cryostat. Both liquid baths have level sensors^{99, 146} with meter indicators and strip chart recorder voltage outputs, which are fed directly to the Dirty MUX and read into the computer. The OVC vacuum is measured by one of three ion gauge tubes¹⁴⁷ located: just above the butterfly

valve on the turbo pump and at the E-stem OVC and IVC pump outs. The gauge controller¹⁴⁸ has a recorder output voltage proportional to the log of the pressure. The 1 K Pot pressure, which normally operates at a few torr, is measured by a capacitive pressure transducer.¹⁴⁹ The mixture low pressure operates from 100 mT to 1 T and is monitored in the Still line and between the circulation pumps. The sensor between the pumps allows us to calculate the actual circulation rate from the helium pressure and the pumping speed. These pressures are measured with Convectron gauge tubes.¹⁵⁰ The mixture high pressure side operates from 20–150 T or higher. It is measured before and after the nitrogen cold trap (and potentially after the helium cold trap). If the pressure at the first gauge rises while the second gauge falls, then the nitrogen trap is plugged. If the first two gauges rise and the third falls, then the helium trap is plugged, and if all three rise, then the condenser is plugged. For these gauges we use strain gauge pressure transducers.¹⁵¹ Finally, the interlock status, in particular the cooling water,¹⁵² is monitored. This is a total of 10 voltage measurements.

5.6.2 Wiring and Heat sinking

The number of sensors involved requires almost 2200 wires be brought into the vacuum spaces and heat sunk at all temperature stages along the way. On the fridge side we chose to use 36 AWG phosphor-bronze quad lead which has four color-coded wires in a flat bundle.¹⁵³ The color-coding aided construction by making it easier to trace and debug the assemblies. Phosphor-bronze has approximately twice the thermal conductivity of manganin, which is extremely low, so we only paid a small price for this choice. To bring the monitoring wires from room temperature to 4 K on the can side, we initially built a discrete wiring harness similar to the fridge side; the long range plan is to use two of the striplines for this wiring run. The heat sinks are larger versions of the tower heat sinks with a very thin dielectric layer, since capacitance is not an issue

and space is. The copper is patterned into strips, then the copper-Kapton is glued to a copper plate. The wires or connectors are soldered to the strips, then several plates are bolted to the appropriate cryostat part.

The wiring and connectors are the most labor intensive and fragile pieces of the cryostat. To make a connection between a wire and a heat sink contact pad, we have to first strip, clean, tin, and clean the wire. Then we can solder it to the heat sink pad, which has been previously cleaned, tinned, and cleaned. After a whole heat sink has been soldered, we clean, inspect, and possibly rework it, then the wiring bundle has to be strain relieved and dressed. The connectors themselves are somewhat fragile, because they have to be fine pitch and radioactively clean. On the fridge side we used a commercial fine pitch connector with a glass filled plastic housing,¹⁵⁴ but the plastic tends to loosen around the pins after soldering. Because of the glass, we could not use these in the Icebox, so we manufactured housing-less connectors using bare pins¹⁵⁵ soldered to copper-Kapton strips glued to a copper base plate. This roughly doubled the amount of assembly labor involved per heat sink. If we do this again, we should work very hard to find low activity and robust wiring and fine pitch connectors.

Once we have the signals at room temperature, they are conveyed down shielded twisted pair cables to a patch panel, where we can feed them to the appropriate multiplexer channels. The patch panel also serves to connect the temperature controller, fridge control box, multiplexed I-V box, current source, and DMM.

5.6.3 Future Hardware Improvements

There are several environmental sensors that we have not implemented, but probably should. These include motion detectors in the area around the fridge and cryostat, to monitor periods of human activity, accelerometers on the fridge or cryostat, and power line monitors.

We have not yet implemented a monitoring activity bit, set when the system commences a series of measurements, then cleared at the end. This would be acquired with the detector data, event by event, tagging periods when the monitoring system might be responsible for excess detector events.

We have not implemented temperature control of the 10 mK can. The most elegant method is to select a control thermometer, connect it to a dedicated readout, and connect the output to a temperature controller. This provides the best response, since the whole loop exists in hardware and no computer interaction is required just to maintain the temperature. It is desirable to be able to change the set point under computer control, however.

With the experience we now have, the next time around we can probably reduce the sensor count by a factor of two without compromising the diagnosis and monitoring capabilities. Since we have been successful at modeling the temperature drop along a part, we could mount only one sensor on each part, instead of the two currently, and still be able to identify low conductivity joints. We could also drastically reduce the number of touch sensors, since in practice only a few locations have ever given any indication. We could use position sensors in the fridge only for early fridge tests, and connect them through the wires used for the cold stem sensors later on.

The patch panel as currently designed involves a large amount of discrete wiring between the MUX cards, the cables, the connectors and the terminal blocks. Next time we should pay the premium for the high density cables from Keithley and design a board to break out each cable to the terminal blocks.¹⁵⁶

As we already mentioned, it would have been a lot easier to build and install the cryogenic wiring if we had found more robust low activity wiring and connectors.

Finally, we should have allowed for several more I-V channels at the mixing chamber and the top of the 10 mK can, for thermometer calibration, and at the top of the 4 K can for other expansion purposes.

5.6.4 Multiplexer

An issue with so many sensors is how to measure them all. If the readout and computer interface are cheap, as with multi-channel PC-based analog to digital converters (ADCs), each sensor can have its own readout path. Since most of our sensors need some sort of amplifier and substantial resolution in the ADC the readout is not cheap. We decided to multiplex most of the sensors into shared readout electronics, including the DMM which passes the results on to the computer. To illustrate the method, we will discuss a 4-wire resistance measurement in some detail, then we will briefly describe the logical multiplexers required for the other sensors and how to realize them with the physical multiplexer.

4-wire Resistance Measurement as an Example

The full multiplexed scheme for 4-wire resistance measurements is shown in Figure 5.28. This scheme is used to multiplex the linear potentiometers and most of the RuO₂ thermometers to a single IV Board. The coldest thermometers have a much lower noise tolerance, so they are measured using the dedicated Mixing Chamber IV Boards. In Figure 5.28 heavy lines represent differential pairs and thin lines represent single wires. Right of the dashed line, only a single sensor of each type is shown, *i.e.*, the thermometers require a single VMUX channel, but the linear potentiometers require two. The 213¹³⁵ is a computer controlled voltage source, which goes through a buffer amplifier and noise filter before entering the bias section of the I-V Board. The bias output is sent to the appropriate sensor by the BMUX logical multiplexer. The corresponding voltage sense leads are selected by the VMUX logical multiplexer, then

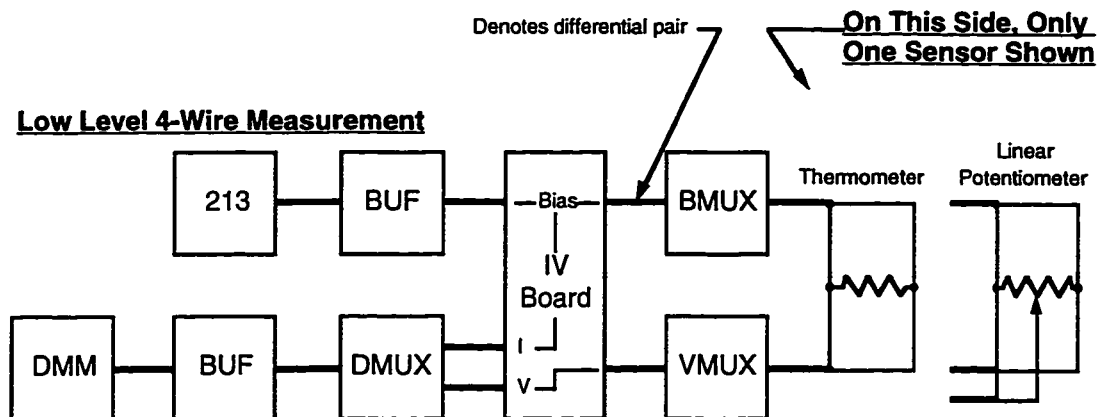


Figure 5.28. Multiplexed 4-wire Resistance Measurement. Schematic for multiplexing the 4-wire resistance measurements. Heavy lines represent twisted pairs; thin lines represent single wires. The IV Board contains a current measuring shunt resistor and two instrumentation amplifiers to measure the current and voltage. Both a thermometer and linear potentiometer are shown.

amplified on the I-V Board. The DMUX selects alternately the current then the voltage signal to be measured by the 2001 DMM.¹³⁵ The buffer between the DMUX and the DMM isolates the low level signals from DMM digital noise.

The measurement sequence is

- (1) Set the bias voltage on the 213.
- (2) Select the sensor on the BMUX and VMUX.
- (3) Select the current channel on the DMUX and measure the bias current.
- (4) Select the voltage channel on the DMUX and measure the sensor voltage.
- (5) (For potentiometers.) Select the wiper voltage channel on the VMUX and measure the full sensor voltage.

The multiplexers add one potential complication: the switch contacts develop thermal EMFs that add to the bias and sense voltages. The offsets from these thermal EMFs are canceled to first order by making the measurement through the same switch configuration with both signs of bias, then taking the difference of the measurements. This will cancel DC offsets, but not the effects of thermal gradients in the multiplexers.

Table 5.29. Parameters for 4-Wire Resistance Measurements.

Hardware Parameters	Type
213 GPIB Address	integer
213 channel	integer
Divider Ratio	real
Bias Resistance	real
Current Gain	real
Voltage Gain	integer
7002 Multiplexer GPIB Address	integer
DMUX Current Slot	integer
DMUX Current Channel	integer
DMUX Voltage Slot	integer
DMUX Voltage Channel	integer
2001 DMM GPIB Address	integer
Sensor Parameters	Type
Device Number	integer
Bias Voltage	real
BMUX Slot	integer
BMUX Channel	integer
VMUX Slot	integer
VMUX Channel	integer
Calibration Constant #1	real
Calibration Constant #2	real
Lower Limit of Calibration	real
Upper Limit of Calibration	real

In both fridges (the Icebox and the Berkeley development fridge) we see no degradation of the measurement due to the multiplexer itself.

Table 5.29 lists the hardware parameters and the sensor parameters needed to make these measurements. The thermometers also need a hard coded set of generic calibration constants to use when the measured resistance is outside the range calibrated specifically for that thermometer.

Given 38 low level thermometers (the RuO₂ thermometers not on the MC Layer and the Oxford thermometers) and 14 position sensors, the BMUX needs 60 channels and the VMUX needs 80 channels (since each position sensor needs two voltage channels). These numbers are rounded up to match the ten channel increment of the

Table 5.30. Logical MUX Configuration.

The configuration lists the number of inputs and the number of outputs, *i.e.*, the AMUX has one input (the voltage source) and 10 outputs (the MC Layer I-V Boards).

Multiplexer	Configuration
AMUX	1 x 10
BMUX	1 x 60
CMUX	1 x 10
DMUX	50 x 1
PMUX	30 x 1
VMUX	80 x 1
Dirty MUX	10 x 1

multiplexer cards. The DMUX needs two channels for the current and voltage outputs, plus more from the readouts for the other sensor types.

Logical and Physical Multiplexer Configuration

The 4-wire resistance measurements need two logical multiplexers, BMUX and VMUX. The RuO₂ thermometers on the MC Layer each have a dedicated I-V Board, so instead of multiplexing the bias after a common I-V Board, a second channel of the 213 Voltage Source is multiplexed by the AMUX into the appropriate I-V Board. The current and voltage signals from each board are multiplexed by the DMUX. The diodes are biased in series pairs (to save channels) by a common current source through the CMUX, and the voltages are multiplexed by the DMUX as well. The touch sensors are read out in pairs of pads by the PMUX, then the high and low member are selected by two DMUX channels. The net results for all the logical multiplexers are displayed in Table 5.30. The minimum number of channels have been rounded up to the nearest multiple of 10 to match the capabilities of the physical multiplexer we use.

To realize these logical multiplexers, we use a Keithley 7002 MUX Mainframe with 7011 switch cards.¹³⁵ These are relatively low cost per channel yet have very low thermal EMFs and noise. The cards have four 1 × 10 (or 10 × 1) multiplexer banks which can be used together to make larger multiplexers. In addition, the 7002

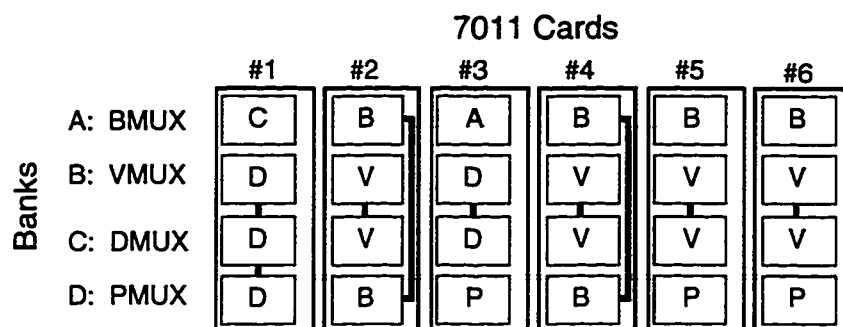


Figure 5.31. Physical MUX Configuration.
 Connection scheme for six 7011 cards to achieve the multiplexer configurations in Table 5.29. Each card is shown with its four banks vertically. Each bank is labeled by the first letter of the logical multiplexer it belongs to. The backplane signal bus ("A,B,C,D") is assigned to the logical multiplexers as indicated at the left in the figure. Connections between banks on the same card are indicated by the heavy lines.

Mainframe has four channels on the backplane that can be used to tie together multiplexers on different cards. The connection scheme used to configure the banks in the 7002 into the required logical multiplexers is shown in Figure 5.31.

The Dirty MUX is based on a single 7011 card in a 7001 MUX Mainframe.¹³⁵
 The voltage signals are measured by a Keithley 199 DMM.¹³⁵

5.6.5 Software

The monitoring hardware described is only capable of making basic physical measurements. The software organizes that into useful information. At the root level, the software manages and uses a database of sensor parameters to sequence the hardware through a measurement of a given sensor. At the next higher level, the software is responsible for scheduling the measurements. At the highest level, the software uses the cryostat state to determine the most useful information for measurement and presentation, and also provides data management at the run level. We will discuss the sensor and hardware databases, the fridge states, how measurements are scheduled, and the run management. Éric Aubourg and PDB designed the software

with many suggestions from the users. Éric Aubourg and Storn White wrote it in National Instruments LabView¹⁵⁷ on the Apple Macintosh¹⁵⁸ platform.

Sensor and Hardware Databases

The measurement algorithms use two kinds of input data. The first kind describes the configuration of the hardware: device GPIB addresses, the shared I-V Board current and voltage DMUX channels, the shared I-V Board current and voltage amplifier gains and the current sensing resistance, and the touch sensor high and low DMUX channels. The second kind of data is sensor specific. Each sensor has an ID number, cryostat location name, physical device name, a description, a measurement type that identifies the measurement algorithm, the MUX channels the sensor is wired to, and for each fridge state a set of allocation groups (defined below) the sensor belongs to and calibration functions and constants. Each measurement is converted into a useful engineering quantity ("primary quantity"), such as temperature, but all the input measurements, such as the average current and voltage and their errors and the computed resistance and measurement power, are also available for specialized analyses. Finally, the sensor database also contains the *r.m.s.* deviation in the primary quantity that should be ignored during the "excursion" monitoring described below.

Fridge States

The fridge state refers to the phase of the cooldown: room temperature, cooling and sitting at LN, cooling and sitting at LHe, cooling to base, and operating at base. For the "cooling" phases the thermometer calibrations minimize the fractional error over the whole range, while in each "sitting" phase the calibrations are optimized for the bottom of the range. Sensors that have poor calibrations in a given temperature range are flagged on the displays. The fridge state is crucial in simplifying the thermometer calibration problem and making the best use of the data available. At low temperature, too large a measurement power will heat the sensing element above the temperature of

its mount and the part it sits on. Therefore as the cryostat cools, we have to use lower and lower measurement power. However the decrease in the applied current is somewhat offset by the exponentially increasing resistance. Conversely, at higher temperatures we need to use as much power as we can, since the sensitivity ($\partial \ln R / \partial \ln T$) is small, *i.e.*, a given fractional change in temperature gives a small fractional change in resistance. Finally, the sensors do not obey the expected $R(T)$ over the whole temperature range, so we fit the calibration data to empirically determined functions over ranges appropriate to each cooldown phase.

Allocation Groups

By scheduling the measurements, instead of running through them all in turn at top speed, we can focus the measurement effort (take more samples) on the sensors of most interest, as well as have quiet periods when no measurements are taking place to be able to eliminate monitoring activity as a cause of rare detector events. Sensors belong to sets called allocation groups. The group has four properties: a name, an ON/OFF state, a sampling interval, and the timestamp when the group was last measured. When it is time to measure a group, the group timestamp is updated then each sensor in the group is measured in turn and the measurement given its own timestamp. If a sensor was measured less than 1/5 of the group sampling interval ago, it is skipped on this pass through the group list. This can happen because the groups are non-exclusive sets: a sensor can belong to more than one active group. When all the sensors in the group have been measured, the scheduler looks for the group with the oldest next time = timestamp + sampling interval. This group will be the next measured. If next time is in the future, the scheduler waits, otherwise it commences measuring the group.

Because of enforced waits in the measurements (necessary to avoid glitches of unknown origin), it takes approximately 0.8 seconds to make a 4-wire resistance

measurement with both bias directions. To go through all the sensors takes ~5 minutes. The group scheduling lets us measure some sensors only rarely, such as the liquid levels or touch sensors, freeing time to measure the position sensors and some of the thermometers fairly rapidly, and not measure some sensors at all, such as thermometers with no sensitivity at the current temperature.

We do not know the source of the glitches. They usually consist of a single measurement off by a large factor. We suspect that it is a timing problem between setting up the measurement with the multiplexer and actually recording a reading with the DMM. This ordering is currently enforced merely by the sequential nature of the code, which includes a software wait to allow for the settling time of the MUX. We now have on hand the hardware required to have the MUX trigger the DMM directly, so a few days of effort might resolve this problem and allow us to significantly decrease the measurement time.

Data and Run Management

Each measurement returns a primary value of engineering interest, as well as all the supporting data and a timestamp. The supporting data are useful to understand the reliability and accuracy of the data and the operation of the sensor and readout system. In addition, the last N measurements, where $N = 100$ typically, are available on line. This allows you to call up the recent history of any sensor for examination on the fly. The current data is displayed on a panel appropriate to the fridge state. For example, during the LN cooldown all the position sensors and the LN layer thermometers are displayed, as well as the diodes on the cans, but no other thermometers are displayed, since they have very poor sensitivity. After the LHe cooldown, the position sensors are no longer displayed, since all thermal contractions have already taken place and motion has ceased.

The data is written to disk in one of three modes. "No Logging" writes no data, "Continuous Logging" writes all data, and "Excursion Logging" writes only time periods where one of the active sensors deviated from a set point by more than n sigma, where typically $n = 5$. When an excursion occurs, all data for the preceding lookback time are written, then all data is written continuously until lookahead time after all sensors have returned within their allowed ranges. During stable running at base temperature, this drastically reduces the data size on disk to the portions where something interesting may be occurring. Essentially, this is an on-line filter of the monitoring data, removing the long stretches when the monitoring has nothing significant to explain rare events.

Finally, the software keeps track of a number of run level housekeeping details. At the start of a cryogenic run, a new disk folder (Macintosh directory tree) is created to organize the data. At the top level, a Special Events file is started with the standard start of run information. A copy of the initial sensor database is stored with the data. A number of actions cause a notation with timestamp and optional comment to be added to the Special Events file: any change to any database, a change of fridge state, a change of data logging mode, a change of data logging file, the start and end of an excursion, starting or ending a LN or LHe transfer, and a special event for those special occasions. When any database is modified, the new version is stored with the data, so that by looking in the Special Events file, one can determine the exact version of the database that was in effect at any time.

5.7 Icebox Performance

We installed the fridge in a laboratory on the Berkeley campus. It first ran to base temperature (< 5 mK) in January 1993. The non-fridge parts of the cryostat were mechanically assembled at the machine shop to work out tooling and sequencing questions prior to attaching the Icebox parts to the fridge, which started in the middle of

Table 5.32. Actual Temperature Distributions in the Icebox.

Results from the first Icebox run at Berkeley. The locations, defined in Figure 5.5, are the same as used to summarize the thermal model in Table 5.4.

Location	Temperature on Layer at Location				
	(K)			(mK)	
	LN	LHe	ST	CP	MC
1. Cooling Source	77.91		0.637	39.2	7.54
2. Top of Tail	78.59	4.07	0.641	36.6	7.54
3. Cold End of Stem	80.90	4.55	0.488	49.1	7.86
4. Cold Port of Can	88.39	5.36	0.435	40.5	10.9
5. Top of Can/ Warm Port of Can	90.50	5.3	0.497	39.5	11.0
6. Last Cold Point in E-stem	108.52	7.3			

June 1994. This first complete assembly was slowed considerably by the added work of installing the monitoring system sensors and wiring. We completed the assembly in mid August 1994 and started the cooldown procedure on 23 August 1994. The first cooldown took a total of one week. Table 5.32 shows the base temperatures at the locations marked in Figure 5.5; these should be compared to the model predictions in Table 5.4. Because the cryostat was unshielded and exposed to considerable RF power, not present underground at Stanford, and we had not completely debugged the monitoring system, there was considerable noise in the measurements, especially for the low temperature thermometers, hence the erratic readings. Since this data we have also refit the calibration data to significantly improve the accuracy at base temperature. During the course of the run we performed a series of cooling power tests by applying heat to each of the cans while monitoring the temperatures. The lowest measurement from our primary thermometer, ^{60}Co nuclear orientation with the source mounted at the top of the MC can, was 7.7 ± 0.07 mK (statistical error only).

As soon as the cryostat was back at room temperature, we started to disassemble, pack, and ship it to the tunnel at Stanford, where most of the support equipment (electricity, cooling water, plumbing) was already installed. We finished

setting up the fridge on 30 January 1995 and reached a base temperature of 5.51 ± 0.08 mK (statistics) at Stanford on 4 February 1995.

While we had the Icebox dismantled, we replaced all the sensors and connectors outside the fridge, using clean solder and the housing-less connectors, to reduce the radioactive contamination. We also cleaned each part with alcohol in a clean room and double wrapped them in plastic bags. During the assembly, the outer bag was removed just before passing through the plastic curtain defining the HEPA filtered region. The inner bag was removed inside the filtered region.

Once we completed the preparations and modifications, the actual assembly of the Icebox took three months. We started the first Icebox cooldown at Stanford, the second cooldown ever, on 10 July 1995. The cooldown proceeded slightly faster than the first time at Berkeley. Figure 5.33 shows the temperature history of the cans at the model locations 6 shown in Figure 5.5. We transferred LN for the first 13 hours, followed by 2 days topping off the baths and waiting for the can lids to cool to under 100 K. We used a total of 500 liters LN up to this point in the cooldown. The LHe slow transfer took 12 hours before collecting liquid in the bath, then another hour and a half to fill the bath. We used 300 liters LHe total to cool the cryostat and fill the 36 liter bath. We pumped the exchange gas from the IVC for 8.5 hours before performing the leak checks. The cooling rate over the next 2 hours was limited by how fast we could perform the steps of the procedure. Once the circulation was established at 6:00 PM on 15 July 1995, the MC can was under 100 mK in 1.5 hours and under 12 mK in 6 hours. In 4.25 days the MC can cooled from 300 K to < 10 mK. Because of a series of failures, starting with a computer disk, we lost essentially all data from this engineering run, so we can't present the base temperature profiles as in Table 5.32; the lower noise environment, coupled with improvements to the electronics and calibrations, resulted in considerably more consistent numbers generally in agreement with, or slightly below,

the thermal model. Over the next two weeks we optimized the circulation rate to obtain the lowest MC can temperature: 5.51 ± 0.05 mK.

The actual boiloff rates are much less than pessimistically estimated in §5.3.8. The LHe consumption averages 29 liters per day, so with the 36 liter bath we only have to transfer once a day. The LN consumption, like the LHe, is high for several days as the far ends of the cryostat gradually approach steady state temperatures. The long term average LN consumption settles down to 40 liters per day. With a 60 liter bath we have to transfer LN every 36 hours.

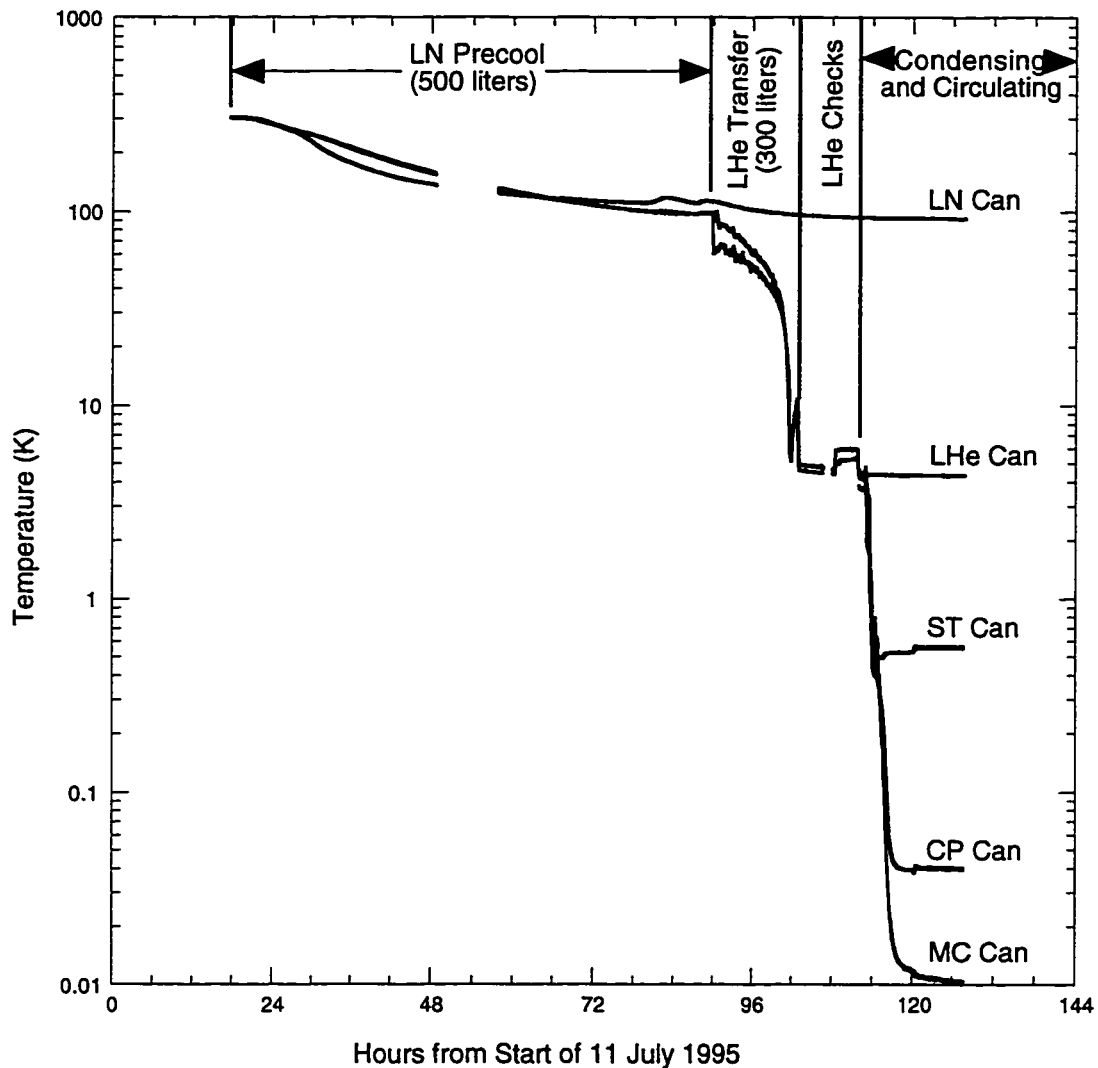


Figure 5.32. History of Stanford Cooldown.

Temperature history of the cryostat cans during the first cooldown after installation in the underground facility. The first day was spent transferring LN into the two baths, followed by two days waiting for the rest of the cryostat to cool below 100 K. The LHe slow transfer took the next twelve hours, followed by 8.5 hours pumping out the helium exchange gas. It took two hours to condense the mixture and start the circulation. After optimizing the fridge operation and performing other tests, the MC Can eventually cooled to 5.5 ± 0.05 mK.

6. Analysis Methods

Having thoroughly discussed the detectors, shielding, and cryostat, we turn to a discussion of the data analysis. Given that we have no data, this discussion will be alternately historical, describing what other experimenters have done, and hypothetical, describing how we intend to address the same problems.

The conceptual statement of the analysis problem is

$$\left. \frac{dR}{dE} \right|_{\text{Observed}} = \frac{R_0}{E_0} e^{-\frac{E}{E_0}} \times K(E) * \Sigma(E). \quad (6.1)$$

$$R_0 = \frac{1}{M} \frac{\rho_0}{m} \sigma_0 \bar{v}. \quad (6.2)$$

The event rate per atom is the WIMP flux, $(\rho_0/m)\bar{v}$ times the cross section σ_0 , where m is the WIMP mass, ρ_0 is the local WIMP energy density, and \bar{v} is a characteristic velocity. Taking this event rate per atom and dividing by the atomic mass, M , we obtain R_0 , the fiducial event rate. We will show below that the theoretical spectrum is essentially exponentially distributed with mean energy $E_0 \propto \bar{v}^2$. A number of corrections are buried in $K(E)$. The theoretical spectrum on the right hand side has to be convolved with the detector response function $\Sigma(E)$ to obtain the expected spectrum which we are to compare with the observed spectrum

The experimental effort and data filtering is on the left side of Eq. (6.1). First, the choice of detector and construction of the experiment ultimately determine the quality of the data. Having built the experiment, however, a variety of filters and statistical corrections can be applied to the raw event stream to determine the lowest counting rate that could possibly be due to the local density of dark matter.

All of the theoretical work is on the right hand side. The underlying WIMP particle theory, mixed with the structure of the proton and neutron and the spin structure of the nucleus, is buried in σ_0 . Further nuclear physics enters in the form factor, which

either rescales E_0 or is buried in $K(E)$. The astrophysics enters via the local WIMP density, ρ_0 , the average WIMP velocity in Galactic coordinates, \bar{v} , and the assumed WIMP velocity distribution that leads to the exponential energy dependence. The detector isotopic composition is a factor in $K(E)$, as well.

We have to take two steps to connect the two sides of Eq. (6.1). First, we have to include the effects of the detector response, either by convolving the theoretical WIMP spectrum on the right hand side of Eq. (6.1) with the detector response function $\Sigma(E)$ to obtain the "expected" spectrum, or by finding a "source" spectrum that, when convolved with the detector response function, accurately models the measured spectrum. Second, we have to apply some statistical test to compare the "expected" spectrum with the measured one (or the "source" spectrum with the theoretical WIMP spectrum) to make any statements about the theoretical parameters, *e.g.* R_0 , ρ_0 , σ_0 , m , *etc.* Because of the increasing specificity of the assumptions made, increasingly model dependent statements can be made as the results are expressed in terms of R_0 then σ_0 then more fundamental parameters of the theory.

We have already discussed the construction of the experiment; in §§6.1–6.4 we discuss the data processing and filtering methods. In §6.5 we summarize the structure of the cross section, and derive the theoretical WIMP spectrum in §6.6. We discuss the statistical tests that one might use to compare the measured and expected spectra in §6.7. Finally, in §6.8 we estimate the sensitivity that we will achieve at Stanford.

The various filters and cuts fall into four broad classes. The most sophisticated and desirable filters remove events one at a time, based on the value of a cut parameter constructed from the event itself, *e.g.*, the pulse shape. These are the most desirable filters since they directly reduce the measured event rate without introducing statistical errors or (usually) reducing the live time. In practice, the separation between background events and signal events is rarely perfect, so the cut is implemented as a

second class of filter, statistical subtraction: having measured the probability for a signal or background event to pass the cut (the acceptances), the number of actual events that pass is statistically corrected for the background contamination and signal rejection. Here individual events are not accepted or rejected; the correction is applied to the total number of events. This requires an independent measurement of the background, and a measurement of the fraction of background events that pass the cut, in order to do the subtraction. In this class, generally the live time is not reduced, but the statistical accuracy of the background measurement and the systematic uncertainty in the background acceptance both can affect the final result. In several very useful (and much used) filters the background is not known independently from the fraction that pass the cut. In these cases, events failing the cut are discarded, but no statistical subtraction is made for the background contamination. Finally, the data collection periods must meet some minimum conditions, *e.g.*, no recent power outages, a minimum time since the last cryogen fill, no human activity near the experiment, *etc.* This class of cut is often very costly since it can significantly reduce the live time.

6.1 Analyzing Data with a Cut

Since most of the filters and cuts are variations of statistical subtraction, we will examine this method in some detail. Consider an experiment that draws events from two (energy dependent) distributions, the signal, $s(E)$, and the background, $b(E)$. These have dimensions counts/(kg keV day). The experiment runs a detector mass M for a live time T , and classifies the observed events as either "signal" or "background" with probabilities:

$$\begin{array}{c|c}
 \begin{array}{cc}
 s(E) & \\
 \downarrow & \\
 \alpha & 1-\alpha \\
 \text{"signal"} & \text{"background"}
 \end{array} &
 \begin{array}{cc}
 b(E) & \\
 \downarrow & \\
 \beta & 1-\beta \\
 \text{"signal"} & \text{"background"}
 \end{array}
 \end{array} \tag{6.3}$$

That is, the signal acceptance is α , and the background rejection is $1 - \beta$. Good background rejection has both $1 - \alpha$ and β small. The energy distributions $s(E)$ and $b(E)$ are the counting rates as a function of energy. Each distribution also has a width in the cut parameter; α and β measure the fraction of the distribution in the cut parameter that is greater than the cut value. The distributions in the cut parameter may depend on energy, leading to energy dependence in α , β , and the cut value itself, but they do not change as the overall rate $s(E)$ and $b(E)$ vary at fixed energy. For example, the cut parameter could be the ionization yield, y , considered in Chapter 3.

If there is more than one cut to be applied, *i.e.*, two backgrounds, we are to think of applying this analysis twice. The result of the first analysis will be not an estimate of the signal but an estimate of the signal plus the second background. After the second pass, we will obtain an estimate for the signal alone. Of course, it may often be simpler with real data to apply the method of maximum likelihood. The value of this cut formalism is that it provides a simple analytic framework to model an experiment, particularly its sensitivity limits and dependence on systematic (calibration) errors.

Summing the events in bins of width δE , the number of "signal" events, N_s , and the number of "background" events, N_b , are:

$$\begin{aligned} N_s &= [\bar{\alpha}S(E, \delta E) + \bar{\beta}B(E, \delta E)]MT\delta E \\ N_b &= [(1 - \bar{\alpha})S(E, \delta E) + (1 - \bar{\beta})B(E, \delta E)]MT\delta E \end{aligned} \quad (6.4)$$

where $B(E, \delta E)$ $\{S(E, \delta E)\}$ is the average background {signal} counting rate in the bin $[E, E + \delta E]$:

$$B(E, \delta E) = \frac{1}{\delta E} \int_E^{E+\delta E} b(E) dE, \quad (6.5)$$

and similarly for $S(E, \delta E)$. The background {signal} weighted background {signal} acceptance is

$$\bar{\beta}(E, \delta E) = \frac{1}{B(E, \delta E)} \frac{1}{\delta E} \int_E^{E+\delta E} \beta(E) b(E) dE. \quad (6.6)$$

One can show¹⁵⁹ that the continuum limit ($\delta E \rightarrow 0$) is the optimum choice for a fixed bin size. In this limit, $B(E, \delta E) \rightarrow b(E)$, $\bar{\alpha} \rightarrow \alpha$, $S(E, \delta E) \rightarrow s(E)$, and $\bar{\beta} \rightarrow \beta$. For no good reason, from now on we will drop the averaging bars on α and β , but keep using the bin-averaged background and signal $B(E, \delta E)$, $S(E, \delta E)$.

What is the best estimate for S , which we will call \hat{S} ? Solving Eq. (6.4) for S , given the N :

$$\hat{S} = \frac{(1 - \beta)N_s - \beta N_b}{(\alpha - \beta)MT\delta E}. \quad (6.7)$$

This is the best estimate of the average signal counting rate in the bin $[E, E + \delta E]$. If β is known independently, then N_b can be measured along with N_s and the subtraction performed.

In some important cases, however, β can not be independently measured, so instead of using the subtraction in Eq. (6.7), the best (and conservative) estimate of S comes from the first line of Eq. (6.4):

$$\hat{S} = \frac{N_s}{\alpha MT\delta E} = S(E, \delta E) + \frac{\beta}{\alpha} B(E, \delta E). \quad (6.8)$$

This is conservative in that it overestimates S , and accurate to the extent that most of the background is rejected, *i.e.*, to the extent that β is small. The net effect is to reduce the live time, T , by the signal acceptance, α .

6.1.1 Background Limited Experiments

Suppose the experiment is background limited: $s \ll b$. (Strictly speaking, the constraints are $s/b \ll \beta/\alpha$ and $s/b \ll (1 - \beta)/(1 - \alpha)$. The lesser of these limits is less than 1 for all values of α and β . For particular extremes of α and β the ratio $s/b \ll \ll 1$,

i.e., the background may have to be *very* dominant for this limit to apply.) Then the observed numbers of events are approximately

$$\begin{aligned} N_S &\equiv \beta B(E, \delta E) M T \delta E \\ N_B &\equiv (1 - \beta) B(E, \delta E) M T \delta E \end{aligned} \quad (6.9)$$

Substituting into Eq. (6.7), the best estimate for the signal is $\hat{S} = 0$.

6.1.2 Statistical Errors

Even though we expect a background limited experiment to give zero for the estimate of the signal, because of errors in the measurement we don't conclude that there is *no* signal. That is, we measure $\hat{S} = 0$ with some finite precision. In Eq. (6.7) we have two classes of parameters, the statistical ones, N_S and N_B , and the systematic ones, α , β , M , T , and δE . Therefore, we write the variance on \hat{S} in two pieces:

$$\sigma_{\hat{S}}^2 = \sigma_{\hat{S}, \text{stat}}^2 + \sigma_{\hat{S}, \text{sys}}^2. \quad (6.10)$$

A well calibrated experiment will have the systematic variance much less than the statistical variance, *i.e.*, it will be statistics limited. Later we will derive the precision required for the systematic parameters in order to meet this condition. For now, just consider the statistical variance, which is (dropping the subscript "*stat*")

$$\sigma_{\hat{S}}^2 = \frac{(1 - \beta)^2 N_S + \beta^2 N_B}{[(\alpha - \beta) M T \delta E]^2}, \quad (6.11)$$

due to fluctuations in the numbers of events, assuming α and β (and M , T , δE) known.

Using the background limited values for the N from Eq. (6.9)

$$\sigma_{\hat{S}}^2 = \frac{\beta(1 - \beta) B(E, \delta E)}{(\alpha - \beta)^2 M T \delta E}. \quad (6.12)$$

This is the precision with which the experiment measures $\hat{S} = 0$ in the bin $[E, E + \delta E]$.

Use the first fraction in Eq. (6.12) to define the background rejection factor:

$$Q(\alpha, \beta) = \frac{\beta(1-\beta)}{(\alpha-\beta)^2}. \quad (6.13)$$

This is the rejection factor used in §3.4.1. Obviously, smaller Q 's are better. With this definition experiments with the same background and the same ratio $Q/(MT)$ will have the same sensitivity.

6.1.3 Signal Model

As we will sketch below, the WIMP spectrum we expect to observe is essentially exponential in energy:

$$s(E) = \frac{R_0}{E_0} f_\sigma e^{-E/E_F}. \quad (6.14)$$

This differs from Eq. (6.1) by a resolution correction, f_σ , and a rescaling of the energy E_0 by the form factor to give E_F ; these will be discussed in §6.6 and §6.7. R_0 is the same as in Eq. (6.2), which differs from the total measured event rate by the factor $f_\sigma E_F/E_0$. The mean energy deposition is E_F . The average differential event rate expected in the energy bin $[E, E + \delta E]$ is

$$\begin{aligned} S(E, \delta E) &= \frac{1}{\delta E} \int_E^{E+\delta E} s(E) dE \\ &= R_0 f_\sigma \frac{E_F}{E_0} \frac{1 - e^{-\delta E/E_F}}{\delta E e^{E/E_F}} \end{aligned} \quad (6.15)$$

This is the theoretical expectation for the experimental estimate in Eq. (6.7).

Conventionally, results are quoted in terms of the fiducial event rate, R_0 , so we equate \hat{S} in Eq. (6.7) with $S(E, \delta E)$ in Eq. (6.15) and solve for R_0 :

$$\hat{R}_0 = \frac{(1-\beta)N_S - \beta N_B}{(\alpha-\beta)MTf_\sigma(E_F/E_0)} \frac{e^{E/E_F}}{1 - e^{-\delta E/E_F}}. \quad (6.16)$$

This expression is relatively easy to understand. The first factor is the residual number of counts, after background subtraction, divided by the integration factor MT , to give the measured counting rate. The exponential factor scales up this counting rate at E to

the total counting rate. The last denominator corrects for finite bin width. At first glance, it looks like the last fraction blows up as δE goes to zero, however the N are proportional to δE , so there is no divergence. Again, a background limited experiment on average will estimate $\hat{R}_0 = 0$.

The statistical variance on our estimate of \hat{R}_0 is

$$\sigma_{\hat{R}_0}^2 = \sigma_S^2 \times \left[\frac{\delta E}{f_\sigma(E_F/E_0)} \frac{e^{E/E_F}}{1 - e^{-\delta E/E_F}} \right]^2. \quad (6.17)$$

6.1.4 Systematic Errors

Now let us consider the systematic errors due to uncertainties in the parameters α and β . The variance on the event rate limit due to the uncertainties in the parameters is:

$$\begin{aligned} \sigma_{\hat{R}_0, \alpha}^2 &= \left(\frac{\hat{R}_0}{\alpha - \beta} \right)^2 \sigma_\alpha^2 \\ \sigma_{\hat{R}_0, \beta}^2 &= \left(\frac{\hat{R}_0 - (N_S + N_B)F}{\alpha - \beta} \right)^2 \sigma_\beta^2 \end{aligned} \quad (6.18)$$

where the integration factor F is

$$F = \frac{1}{MTf_\sigma(E_F/E_0)} \frac{e^{E/E_F}}{1 - e^{-\delta E/E_F}}. \quad (6.19)$$

So these variances don't affect the final limit, they should be much less than the statistical variance on the estimate of \hat{R}_0 given in Eq. (6.17).

For α , since we expect $\hat{R}_0 = 0$, naively we have $\sigma_{\hat{R}_0, \alpha}^2 = 0$. A typical experiment, however, will have $\hat{R}_0 \equiv \sigma_{\hat{R}_0, stat}$, so we need

$$1 > \frac{\sigma_{\hat{R}_0, \alpha}^2}{\sigma_{\hat{R}_0, stat}^2} = \frac{\sigma_\alpha^2}{(\alpha - \beta)^2} \quad (6.20a)$$

$$\left(\frac{\sigma_\alpha}{\alpha}\right)^2 = \frac{1}{A} \frac{1+\alpha}{\alpha} \quad (6.20b)$$

We measure α by taking A known signal-like events (*e.g.*, nuclear recoils due to neutrons from a source) and asking how many of them, A_1 , pass the cut. Of course, we expect $A_1 \approx \alpha A$. From the measurement we compute $\alpha = A_1/A$ and

$$\begin{aligned} \sigma_\alpha^2 &= \alpha^2 \left(\frac{1}{A} + \frac{1}{A_1} \right) = \frac{\alpha^2}{A} \left(1 + \frac{1}{\alpha} \right) \\ \left(\frac{\sigma_\alpha}{\alpha}\right)^2 &= \frac{1}{A} \frac{1+\alpha}{\alpha} \end{aligned} \quad (6.21)$$

To meet the condition in Eq. (6.20), we need to take the minimum number of calibration events

$$A_{\min} \geq \frac{\alpha(1+\alpha)}{(\alpha-\beta)^2} \approx 2, \quad (6.22)$$

where the approximate value 2 comes by assuming good acceptance and background rejection. Therefore we need hardly any events to calibrate α .

Now consider the variance due to β expressed in the second line of Eq. (6.18).

The quantity

$$N_S + N_B \equiv BMT\delta E \equiv N_{Tot} \quad (6.23)$$

is just the total number of counts in the bin. We can rewrite Eq. (6.17) as

$$\sigma_{\hat{R}_0}^2 = \sigma_S^2 (MT\delta EF)^2, \quad (6.24)$$

and Eq. (6.12) as

$$\sigma_S^2 = \frac{QN_{Tot}}{(MT\delta E)^2}. \quad (6.25)$$

Using these last three relations and remembering that we expect $\hat{R}_0 \approx 0$, the relative sensitivity becomes

$$\frac{\sigma_{\hat{R}_0, \beta}^2}{\sigma_{\hat{R}_0, stat}^2} = \frac{\sigma_\beta^2}{(\alpha-\beta)^2} \frac{N_{Tot}}{Q}. \quad (6.26)$$

For this ratio to be much less than one, we require

$$\frac{\sigma_\beta}{\beta} < \frac{\alpha - \beta}{\beta} \sqrt{\frac{Q}{N_{Tot}}} = \sqrt{\frac{1 - \beta}{\beta N_{Tot}}}. \quad (6.27)$$

We calibrate β in the same way as α . We take B known background events (*e.g.*, electron recoils due to photons from a source) and ask how many of them, B_1 , passed the cut. We expect $B_1 \approx \beta B$; we compute $\beta = B_1/B$, and

$$\left(\frac{\sigma_\beta}{\beta}\right)^2 = \frac{1 + \beta}{B \beta}, \quad (6.28)$$

as before. To meet the condition in Eq. (6.27) we need to take the minimum number of calibration events

$$B_{\min} > \frac{1 + \beta}{1 - \beta} N_{Tot} \approx N_{Tot}. \quad (6.29)$$

For good background rejection, the coefficient in β is very close to 1. Therefore, we need to take more calibration events than the total number of data events.

Armed with this apparatus, we will first discuss two filters that have been used to reduce the effect of microphonics, then consider a variety of other filters that we might use in CDMS.

6.2 Data Collection and Event Processing

Most of the germanium double beta decay experiments, after removing radioactive contaminants from the apparatus, have discovered that their low energy spectra are dominated by microphonics.⁴⁵⁻⁵⁰ The first step they have taken to reject microphonic events is to implement some form of pulse-shape discrimination on an event by event basis. Typically the detector signal has been fed into two shaping amplifiers with different time constants, and a hardware cut implemented on the ratio of

the two output pulses. This is fairly efficient at eliminating microphonic pulses. García, *et al.*,⁴⁸ show the effect on the spectrum at low energy (their Figure 2).

In these experiments, the background acceptance β is unknown (and probably unknowable, even in principle), as is the number of background events, N_b , (since they don't acquire these events) so this event by event cut is analyzed according to Eq. (6.8), without subtracting the additional piece due to the background acceptance.

Instead of the simple hardware cut on shaping time ratios, we use a pulse shape cut on the χ^2 of a fit to the whole pulse acquired by a wave shape recorder (digital oscilloscope). Currently we hand select "clean" events which are averaged to produce a template for the pulse shape. The averaging reduces the noise in the template. A given pulse is fit to an exponential tail, to account for pulse pile up, a DC level, and a multiple of the template. The best fit multiple of the template is the amplitude estimate for the pulse. Since our signals are bandwidth limited, the noise in the time domain is correlated. To determine the error on the amplitude estimate, we need to construct a proper χ^2 . This amounts to constructing the optimal filter in the frequency domain, then using its Fourier transform as the template in the time domain. (See, Shutt⁶⁴ for further discussion.)

When implemented in hardware, a pulse shape cut has essentially no effect on the live time if real signal events always pass the cut ($\alpha = 1$). When implemented in software, the time spent reading out the events that are later discarded reduces the live time. This will be significant if the readout dead time is large and a significant fraction of the events are discarded.

The second technique used to reject microphonic events makes use of the fact that they tend to come in bursts, associated, for example, with activity at the underground laboratories, or with relief of thermal stress in the cryostat after liquid nitrogen fills.⁴⁷⁻⁴⁹ The bursts have counting rates one to two orders of magnitude larger

than quiescent periods and last from minutes to hours. To reduce the effect of mining related microphonics, Ahlen, *et al.*,⁴⁶ used data from a 14 day period of reduced mining activity at their site. The effect is demonstrated most clearly by Beck, *et al.*,⁴⁷ who show a histogram of the number of events each hour (their Figure 2). This has a clear Poisson component with mean counting rate of 0.69 counts/hour and a non-Poisson contribution extending almost to 200 counts/hour. Discarding hour long periods with 6 or more events removes <0.01 of the Poisson distributed hours, at the cost of a 32% reduction in live time. Reusser, *et al.*,⁴⁹ cut all 2-minute bins with greater than 12 counts, reducing the live time by 25%. In their case the cut also removes 5% of the Poisson distributed bins ($\alpha = 0.95$), so they reduce the remaining live time by that factor. These are examples of selecting data runs that meet specified operating conditions, in the case of Ahlen, *et al.* and Beck, *et al.* without discarding signal (except by the loss of live time), in the case of Reusser, *et al.* with a correction for the lost signal.

Statistically this case is like the one above, based on Eq. (6.8). The event is now a time bin, with the event parameter (instead of the energy) the time (or time bin index). The cut parameter is the number of events. The signal S is the counting rate due to the quiescent spectrum, independent of time, and the background $B(t)$ is the counting rate due to microphonics, which depends on time. The integration factor is the length of the time bin, δt . The bin is accepted if $N = \delta t(S + B(t)) < N_{cut}$. The probability of $\delta t S < N_{cut}$ is $\alpha(N_{cut})$, so, if $\beta B(t)$ is small the total number of counts in accepted bins will be $N_{tot} = S\alpha(N_{cut})M\delta t$, where M is the number of accepted bins. The rejected bins reduce the live time, $\alpha(N_{cut})M\delta t$, by decreasing M . In the case of Beck, *et al.*, the signal acceptance α is unity, and for Reusser, *et al.*, it is 0.95. The best estimate of the average signal counting rate is the total number of accepted counts, N_{tot} , divided by the live time, $\alpha(N_{cut})M\delta t$, giving S . Since they don't know the background acceptance (the

number of counts due to microphonics in bins that pass the cut), they do not perform the subtraction indicated in Eq. (6.7), but just consider the bins that *do* pass the cut. This is adequate if the microphonics are highly correlated in time: if there is one, there are many, so many microphonic events are removed just by removing the high count time bins, *i.e.*, βB is small.

6.3 Catalog of (Possibly) Useful Filters

In addition to the event by event cut on pulse shape and microphonic burst cut on time bins, we contemplate a number of other filters to reduce the background.

6.3.1 Electron/Nuclear Recoil Discrimination

The most powerful of these is the new feature of the cryogenic detectors, namely, electron/nuclear recoil discrimination. As we discussed in §3.4, we cut on the ionization energy, ε , or the ionization yield, $y = \varepsilon^{-1}$. Since the systematic errors on α are almost negligible, we calibrate α in a short run with a neutron source and modest rates. We calibrate β with an extended run using a photon source. The ratio of calibration run time to WIMP search live time must be greater than the ratio of the calibration counting rate to the search counting rate, *i.e.*, more calibration electron recoil events than WIMP search electron recoil events, in order not to be limited by the statistical error on β .

One subtlety that we can foresee is that the calibration spectrum may not be the same as the search spectrum, which will introduce a systematic error in the determination of β . For example, suppose β in the search data at low and moderate energies is determined by Compton scatters or cosmogenic activity internal to the detectors, both of which will be distributed uniformly throughout the detector. If the calibration spectrum is more dominated by a tail of the distribution due to incomplete charge collection for a population of events that are absorbed near the surface then we

will systematically overestimate β . One way to measure β for events uniformly distributed in the detector is through multiple scattering.

6.3.2 Multiple Scattering

By operating more than one detector at a time, we can reject coincident events, *i.e.* to obtain the singles spectrum in detector A , use the other detectors in anticoincidence.^{45,49} Here the signal acceptance is unity because the probability for a WIMP to scatter more than once is negligible (unless the WIMP cross section is very large, in which case $\alpha < 1$). Multiple scattering is sensitive to three types of background: Compton scatters, cascade decays, and neutrons. Our Monte Carlo modeling suggests that of order 50% of electron recoil events and 25% of neutron events will be part of multiple scattering events in a six detector tower.⁷⁹ The distribution of multiple events across detectors can also be used to locate the source of the activity.⁷⁹

We can apply Eq. (6.8) to simply discard the multiply scattered events. To subtract the remaining contamination, we need either a sample of tagged events, to measure the background acceptance (one minus the multiple scattering fraction), or a model for the background acceptance. Consider the low energy electron recoil background, and assume that it is dominated by Compton scatters, as we discussed above. From the low energy events we can select a tagged sample that are part of multiple scatters where the other event is at high energy and unambiguously identified as an electron recoil by the electron/nuclear recoil discrimination. The ionization yield of these tagged low energy events will give the correct β for uniformly distributed events.

In general, however, to be insensitive to the systematic error, we need more tagged events than will be available in the search data, since, by assumption, only a

fraction of the total background will be tagged. Therefore we can only perform the subtraction for backgrounds that we can increase by introducing a calibration source or that we can accurately model. For example, we can introduce a high energy source to increase the number of multiple Compton scattered events in the calibration sample. Another way to effectively increase the sample is to use all the events, before applying the muon veto cut, to measure the multiple scattering fraction.

6.3.3 Muon Veto Activity

The simplest way to use the muon veto scintillator data is as an anticoincidence shield, similar to the way the NaI veto was used by Caldwell, *et al.*¹⁶⁰ In the case of CDMS, the scintillator rejects events related to cosmic ray muons, where the NaI veto rejected Compton events and cascade decays. The basic method is to turn off the trigger for a veto time after a muon hit in the scintillator, resulting in a simple reduction in the live time. The analysis is as in Eq. (6.8). In the case of the NaI, and possibly our plastic scintillator, a further complication, as for multiple scattering, is that heavy WIMPs with large cross sections can cause a veto by depositing enough energy in the scintillator, so implementing the veto cut makes the experiment insensitive to these WIMPs.

If we want to do more than just reject muon related events and actually subtract the muon related background, we need to think carefully about how to measure β . One way is to Monte Carlo the neutron event probability as a function of time since the muon passage. The cut parameter is the time since the most recent veto activity, t . If the Monte Carlo reproduces the time distribution for $t < t_{cut}$, then we can have some confidence in the predicted $\beta(t > t_{cut})$. By varying the muon look back time we can adjust the ratio of calibration events to search events to be statistics limited, at some cost in live time.

6.3.4 Neutrons Unrelated to Muons

After discarding nuclear recoils due to neutrons related to muons and correcting for the muon related neutrons that pass the veto cut, we may still be left with nuclear recoils due to neutrons from radioactive contamination (fission and (α, n) reactions). The only handle on the neutron events uncorrelated with muons is multiple scattering. Here we are seriously hampered because we can not measure the source spectrum. If we knew the source spectrum, we could use the model validated by the muon data to calculate the multiple scattering fraction for this source spectrum, or we could just introduce a neutron source with a similar spectrum. Of the nuclear recoils remaining after the muon subtraction, the background level is measured by the multiple scattered events, and we can subtract the accepted background using the computed (or measured) multiple scattering fraction.

6.3.5 Cascade Decays

Many unstable isotopes decay in a series of steps before reaching some stable state. If the intermediate half lives are short (\leq second) and emit more than one high energy particle, the entire decay chain may be tagged by multiple scattering. Chains with longer half lives can be tagged in a position sensitive detector by looking for one step in the chain followed, after an appropriate time delay, by a subsequent step from the same volume element. This technique has been used, for example in the LSND experiment to tag the signal, not the background.^{52, 161, 162}

6.4 Energy Calibration and Detector Response

The final issues in determining the recoil spectrum are the energy calibration and detector response function. Some experiments have had the luxury (and the

nuisance) of a number of lines at relatively low energy, including K and L X-rays from Ti, Mn, Cu, Ga, Sn, and Pb, and gamma rays from ^{210}Pb , ^{57}Co , and ^{137}Cs . This set includes lines from $\sim 5\text{--}700\text{ keV}$. (If the decaying nucleus is inside the detector, then the recoil energy of the parent has to be added to the energy of the photon to determine the actual energy of the line.) In addition, several experiments have used external sources (^{60}Co : 1176 and 1333 keV, and ^{228}Th , which gives 43 strong lines from the ^{232}Th chain) and electronic pulsers for periodic calibrations. The issues are to measure any non-linearity between the measured pulse height and the deposited energy, to measure any offset, and to measure the detector response (resolution) as a function of energy. With the pulser, calibration data can be taken at a number of pulser amplitudes. The resolution is measured directly and the offset is determined by extrapolating to zero amplitude. The resulting uncertainties in energy scale have been typically $\sim 0.05\text{--}0.1\text{ keV}$ for electron recoils, compared to detector resolutions $\sim 0.4\text{--}0.8\text{ keV FWHM}$ at electron recoils of $\sim 10\text{ keV}$. To be conservative, Beck, *et al.*,⁴⁷ then shifted the energy spectrum up by the energy scale uncertainty so as to overestimate the event energy. An alternative approach is to convolve the expected signal spectrum with the resolution function of the detector, including errors and drifts in the energy scale.^{49, 52, 163} Uncertainties in the energy scale are only important for WIMPs with masses below $\sim 100\text{ GeV}$.

In CDMS we can apply the same methods. Low energy lines will calibrate the phonon channel directly. We also have the capability to inject essentially delta function thermal pulses into the detector through a heater on the implanted detector contact. Calibration of the ionization channels is important to remove the Luke gain from the phonon energy measurement and recover the initial energy deposition. We need an absolute calibration of the pulse amplitude vs. the amount of charge collected. We can use a pulser and a coupling capacitor to inject charge into the ionization circuit, but the

value of the capacitance and impedance of the line leading to the capacitor are not known under operating conditions, making the calibration very difficult. Because the Luke gain is a $\sim 10\%$ effect for our ionization bias voltages, we only need a 10% measurement of the ionization channel gain to have this error contribute only 1% to the error in the energy deposition.

6.5 Theoretical Cross Sections

We will summarize here the main results reviewed in detail by, for example, Jungman, *et al.*⁴³ The theoretical cross section will depend on the momentum transfer and the nature of the fundamental coupling between the WIMP and ordinary quarks and gluons. In general we can write the differential cross section per nucleus as

$$\frac{d\sigma}{d|\mathbf{q}|^2} = \frac{\sigma_0}{4\mu^2 v^2} F^2(|\mathbf{q}|), \quad (6.30)$$

where $q = |\mathbf{q}| = \sqrt{2ME}$ is the momentum transfer to the target nucleus, with mass M , corresponding to energy deposition E , μ is the reduced mass of the WIMP-nucleus system, and v is the relative velocity. There are two interaction types to consider in the extreme non-relativistic limit, axial vector (spin) and scalar interactions, since the vector and tensor interactions reduce to the same form as the scalar case and the pseudoscalar interaction vanishes.¹⁶⁴ The differences between axial vector and scalar are largely buried in the details of σ_0 , the fiducial cross section at zero momentum transfer, but they also affect the choice of form factor, $F(q)$. Eq. (6.30) is the only one in this section that enters the derivation of the expected WIMP spectrum, so by making a specific choice for the dominant interaction, and hence the form factor, we can go from a limit on R_0 to a limit on σ_0 .

6.5.1 Axial Vector (Spin) Interactions

At the low momentum transfers involved, Majorana WIMP-quark axial vector interactions (current-current coupling effective Lagrangian $\mathcal{L}_{\text{eff}} = d_q^{(A)} \bar{\chi} \gamma^\mu \gamma_5 \chi \bar{q} \gamma_\mu \gamma_5 q$) (arising from Z^0 or squark exchange for neutralinos) reduce to a spin coupling to the nucleon ($a_N \bar{\chi} \gamma^\mu \gamma_5 \chi \bar{n} s_\mu n$), where the nucleon coupling a_N , $N = \text{neutron or proton}$, is the sum over the light quarks of the effective axial vector quark couplings $d_q^{(A)}$ weighted by the quark spin content of the nucleon. The spin structure of the nucleon can be determined by spin polarized electron-proton scattering, though the results are not very precise and disagree with theory. The nucleon couplings are the experimentally accessible parameters of the theory. The resulting expression for σ_0 is

$$\sigma_{0,\text{spin}} = \frac{32}{\pi} G_F^2 \mu^2 \Lambda^2 J(J+1). \quad (6.31)$$

G_F is the Fermi coupling constant and

$$\Lambda^2 J(J+1) = \frac{J+1}{J} (a_p \langle S_p \rangle + a_n \langle S_n \rangle)^2, \quad (6.32)$$

where J is the spin of the nucleus and $\langle S_p \rangle$, $\langle S_n \rangle$ are the average spin content of the proton or neutron group in the nucleus. These can be determined either by detailed nuclear models or by using the measured nuclear magnetic moment and the odd group model, in which case the even group has $\langle S \rangle = 0$.

The sum and difference of a_n and a_p give the isoscalar and isovector scattering amplitudes, a_0 and a_1 , respectively, which interfere to give the form factor

$$F^2(q) S(0) = S(q) = a_0^2 S_{00}(q) + a_1^2 S_{11}(q) + a_0 a_1 S_{01}(q). \quad (6.33)$$

The $S_{ij}(q)$ have to be determined by detailed nuclear models, which have been made for only a few nuclei.^{165, 166} For these nuclei an adequate approximation to the form factor, which is probably adequate for other nuclei as well, is

$$F^2(q) = \begin{cases} j_0^2(qr_N) & qr_N < 2.55 \\ \equiv 0.047 & 2.55 < qr_N < 4.5 \\ j_0^2(qr_N) & 4.5 < qr_N \end{cases}, \quad (6.34)$$

where $r_N \approx 1 \text{ fm} \times A^{1/3}$.

Because there are two model dependent parameters, a_p and a_n , it is not generally possible to compare experimental results for spin interactions from different nuclei. Given a specific particle model, however, results can be normalized to the cross section on proton targets, for example.

Of course, the target nucleus must have *some* nuclear spin, or there is no interaction ($\langle S_p \rangle = \langle S_n \rangle = 0$). Natural germanium is composed of five isotopes with the following abundances: ^{70}Ge (20.5%), ^{72}Ge (27.4%), ^{73}Ge (7.8%), ^{74}Ge (36.5%), and ^{76}Ge (7.8%); only the odd- A , odd- n isotope ^{73}Ge has nuclear spin.

6.5.2 Scalar Interactions

In minimal supersymmetry the axial vector interactions are quite small, so second order interactions (due to Higgs and squark exchange between the neutralinos and quarks as well as one-loop diagrams coupling neutralinos to gluons) are no longer negligible. The details of a particular model (supersymmetric or any generic effective scalar current-current interaction, $d_q^{(S)} \bar{\chi} \chi \bar{q} q$) can again be buried in the nucleon couplings f_n and f_p , the scalar analogs of a_n and a_p above. The resulting fiducial cross section is

$$\sigma_{0,scalar} = \frac{4\mu^2}{\pi} \left(Zf_p + (A-Z)f_n \right)^2. \quad (6.35)$$

The nucleon operators just count the number of each type, leading to the simple form of Eq. (6.35). For most neutralinos, $f_p \approx f_n$, so $\sigma_0 \propto A^2$, hence the attention given to scalar limits. (The A^2 enhancement of the cross section implies significantly higher event rates

for a scalar interaction than for an axial vector interaction with the same coupling strength.)

The form factor becomes just the Fourier transform of the nucleon density. A simple form that has been widely used,^{43, 45-50, 52, 163} corresponding to a Gaussian nuclear density with *r.m.s.* radius R_0 is

$$F^2(E) = \exp\left(-\frac{E}{E_{coh}}\right), \quad (6.36)$$

where the recoil energy is $E = q^2/(2M)$, the coherence energy is $E_{coh}^{-1} = 2MR_0^2/3$, and the nuclear radius is $R_0 = (0.3 + 0.89A^{1/3}) \text{ fm} \approx 1.2 A^{1/3}$. For natural germanium $E_{coh} = 50 \text{ keV}$. A more accurate form is^{163, 165, 167}

$$F^2(qR) = \left[\frac{3j_1(qR)}{qR}\right]^2 \exp[-(qs)^2], \quad (6.37)$$

where $s = 2.30 \text{ fm}$, $a = 0.52 \text{ fm}$,¹⁶⁸ and R is¹⁶³

$$R^2 = (1.23A^{1/3} - 0.60)^2 \text{ fm}^2 + \frac{7}{3}\pi^2 a^2 - 5s^2. \quad (6.38)$$

The last two terms amount to $-(4.5 \text{ fm})^2$.

The form factor expresses the loss of coherence as the momentum transfer increases. When the scattering is coherent for only a single nucleon the incoherent sum of individual nucleon amplitudes will give $\sigma_0 \propto A$, so form factor suppression beyond A^{-1} is unrealistic. This occurs for Eq. (6.36) at $E = E_{coh} \ln A$. At still higher momentum transfers the formulation in terms of proton and neutron amplitudes, f_p and f_n , breaks down (the scattering is incoherent even for a single nucleon) and we should add the quark and gluon amplitudes incoherently to obtain the form factor.

There are models where one f is much smaller than the other, so the coherence factor can be Z^2 or N^2 instead of A^2 . Therefore we can not generally compare cross section limits from different nuclei. Given a specific model, however, we can

normalize the cross section limits to the cross section on protons (or neutrons), for example.

Dirac particles can have vector interactions with nuclei. For a generic effective current-current vector interaction ($d_q^{(V)} \bar{\chi} \gamma^\mu \chi \bar{q} \gamma_\mu q$) the proton and neutron couplings are simply $b_p = 2d_u + d_d$ and $b_n = d_u + 2d_d$. The WIMP-nucleus coupling is $b_N = Zb_p + (A - Z)b_n$, and the fiducial cross section is

$$\sigma_0 = \frac{\mu^2}{64\pi} b_N^2. \quad (6.39)$$

For example, a heavy Dirac neutrino with standard electroweak coupling to the Z^0 has $b_n = 4G_F/\sqrt{2}$ and $b_p = b_n (1 - 4 \sin^2 \theta_w) = 0.07 b_n$. This is a case where the coherence factor is not A^2 but $\simeq N^2$.

Finally, Lewin and Smith¹⁶³ note that the fiducial cross sections in Eqs. (6.31), (6.35), and (6.39) are all proportional to μ^2 , so the more fundamental quantity proportional to the underlying interaction strength is σ_0/μ^2 . They advocate reporting limits in this unit (or the equivalent $R_{\sigma} M/(4\mu^2)$) as a first step to comparing results from different nuclei in a model independent way. For example, Caldwell, *et al.*⁵⁰ used this rescaling (along with A^2) to compare their silicon results to the cross section required for cosmion models.

6.5.3 Predictions of Minimal Supersymmetry

Within the context of a specific model, the relic abundance and elastic scattering cross section can be computed exactly. If we assume that the local dark halo density is made entirely of the specific particle, we can predict the event rate. This has been done for the LSP in minimal supersymmetry models by a number of authors.^{42-44, 169-174}

Generally scalar interactions dominate over axial vector interactions, so the coherence factor gives reasonably high cross sections on natural germanium. Figure 6.1 shows the

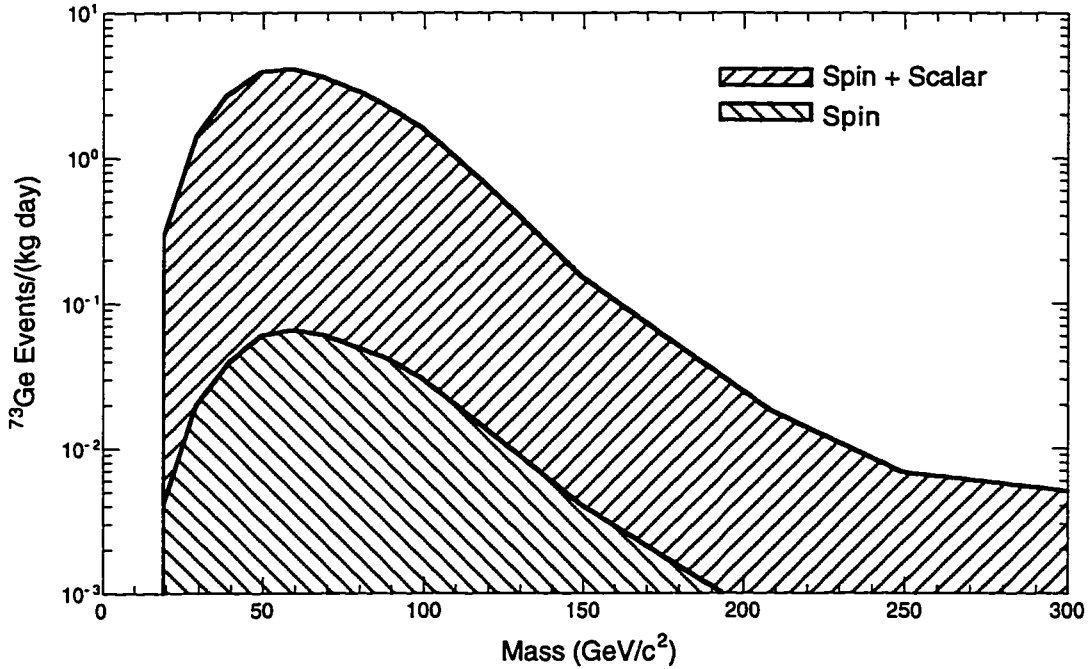


Figure 6.1. Event Rates for Cosmologically Interesting LSPs.

Region of event rate vs. LSP mass populated by cosmologically interesting LSPs for models that meet the accelerator constraints.⁴³ The smaller region encompasses the predicted event rates for the suite of models if only axial vector interactions are assumed; the large region includes the predicted event rates if both scalar and axial vector interactions are included.

range of event rates predicted for cosmologically interesting ($0.025 < \Omega_\chi h^2 < 1$) LSPs for models that meet all particle physics constraints.⁴³ The shaded regions encompass the event rates predicted by the suite of models. The Spin region is the range of event rates if only the axial vector interactions are included. The Spin + Scalar region includes both scalar and spin interactions of the neutralino. The rate is quoted per kilogram of ^{73}Ge , so the isotopic abundance has already been accounted for. The Dirac neutrino event rate is $\sim 250/(\text{kg day})$ and roughly independent of energy (see Figure 2.3 or Figure 6.3). Comparing to Figure 2.3, we see that current experiments are a factor of four higher than the largest predicted SUSY rate at $m \approx 50$ GeV.

6.6 Expected WIMP Spectrum

Given $d\sigma/d|\mathbf{q}|^2$, the cross section for scattering with energy deposition $E = |\mathbf{q}|^2/(2M)$ from relative velocity v , shown in Eq. (6.30), we can compute the total event rate at energy E per target mass, dR/dE , from

$$dR = \frac{1}{M} \frac{\rho_0}{m} \left(\frac{d\sigma}{d|\mathbf{q}|^2} d|\mathbf{q}|^2 \right) v f(\mathbf{v}) d^3v. \quad (6.40)$$

Now we are elaborating on Eq. (6.1) and Eq. (6.2) by including the momentum dependence of the cross section and the relative velocity distribution of the WIMPs, $f(\mathbf{v})$, and (implicitly) integrating over all velocities that can give recoil energy E .

The WIMP halo is assumed to be a non-rotating isothermal sphere with a Maxwellian velocity distribution in Galactic coordinates:

$$f(\mathbf{V}) d^3\mathbf{V} = \frac{1}{(\pi v_0^2)^{3/2}} \exp\left(-\frac{|\mathbf{V}|^2}{v_0^2}\right). \quad (6.41)$$

Here v_0 is the most probable WIMP velocity, taken as $v_0 = (220 \pm 20)$ km/s ($\bar{v} = \langle v \rangle = (2/\sqrt{\pi})v_0$, $v_{rms} = \langle v^2 \rangle^{1/2} = \sqrt{3/2}v_0$). Given that the detector on Earth moves through the Galaxy with a time dependent velocity \mathbf{v}_\oplus , the WIMP-detector relative velocity is $\mathbf{v} = \mathbf{V} - \mathbf{v}_\oplus$. In addition, assuming that the Galaxy (or local group) is finite in mass, there is a local escape velocity, v_{esc} , that truncates the distribution in Eq. (6.41). Local objects that acquire velocities greater than v_{esc} have become unbound from the Galaxy. Most authors use $v_{esc} = (600 \pm 25)$ km/s (but some authors allow significantly lower values¹⁷⁵). This also introduces a normalization correction, k' (divide Eq. (6.41) by k'):

$$k' = \operatorname{erf}\left(\frac{v_{esc}}{v_0}\right) - \frac{2}{\sqrt{\pi}} \frac{v_{esc}}{v_0} \exp\left(-\left(\frac{v_{esc}}{v_0}\right)^2\right) = 0.998. \quad (6.42)$$

(In principle the truncated velocity distribution and the density distribution should be found self-consistently. Since the normalization correction is so small, however, this approximation is negligible.)

The Earth's velocity in Galactic coordinates is dominated by the circular velocity of the local standard of rest about the Galactic center (~ 230 km/s), with an additional time independent piece from the Sun's peculiar velocity relative to the local standard of rest (16.5 km/s), and a time dependent piece from the Earth's motion about the Sun (32.4 km/s $\times \sin(d/365)$, where d is the number of days since 2 June). The orbit of the Earth about the Sun leads to an annual modulation of the relative velocity distribution, which could be useful in extracting a WIMP signal if an experiment runs for a number of years with a significant event rate. Typical experiments have run for weeks at a time (the longest being 60 days live time⁴⁷), so the annual modulation has not been used so far. However, the analysis usually has used the average Earth velocity for the period covered by the experiment, not the annual average.

Making these changes and integrating over the angle between \mathbf{V} and \mathbf{v}_\oplus and the polar angle, the relative speed distribution becomes

$$f(v)dv|_{v < v_\oplus + v_{esc}} = \frac{v dv}{v_\oplus v_0 \sqrt{\pi}} \left\{ \exp\left[-\left(\frac{v - v_\oplus}{v_0}\right)^2\right] - \exp\left[-\left(\frac{v + v_\oplus}{v_0}\right)^2\right] \right\}. \quad (6.43)$$

The momentum transferred is $|\mathbf{q}|^2 = 2\mu v^2(1 - \cos\theta) = 2ME$, where θ is the center of momentum scattering angle. To obtain a given energy deposition E the relative velocity must be at least $v_{min} = \sqrt{EM/(2\mu^2)} = v_0\sqrt{E/E_0}$ where $E_0 = 2(\mu^2/M)v_0^2$ is a characteristic energy ($1 \text{ keV} \leq E_0 \leq 80 \text{ keV}$ for $10 \text{ GeV} \leq m \leq \infty$ in germanium). Making the appropriate substitutions in Eq. (6.40) and integrating over the relative velocity from v_{min} to $v_\oplus + v_{esc}$, we have

$$\begin{aligned} \frac{dR}{dE} &= \frac{1}{M} \frac{\rho_0}{m} \sigma_0 \frac{2}{\sqrt{\pi}} v_0 \frac{1}{E_0} \frac{1}{k'} F^2(E) \\ &\times \left\{ \frac{\sqrt{\pi}}{4} \frac{v_0}{v_\oplus} \left[\operatorname{erf}\left(\frac{v_{\min} + v_\oplus}{v_0}\right) - \operatorname{erf}\left(\frac{v_{\min} - v_\oplus}{v_0}\right) \right] - \exp\left(-\left(\frac{v_{\text{esc}}}{v_0}\right)^2\right) \right\} \end{aligned} \quad (6.44)$$

The first set of factors amount to $R_0/(E_0 k')$, with R_0 defined in Eq. (6.2). The first term inside the $\{ \}$ is the dimensionless spectrum before imposing the escape velocity cutoff in the integral; the last exponential removes the contribution to the spectrum from Galactic velocities above v_{esc} . The argument to this exponential is 7.44, so the last term is 5.89×10^{-4} ; only if we are way out in the tail of the spectrum is it important. We can approximate the difference of error functions, $\operatorname{erf}(x + \delta x) - \operatorname{erf}(x - \delta x)$, by $(2/\sqrt{\pi})2\delta x \exp(-x^2)$ to obtain an adequate approximate spectrum:

$$\frac{dR}{dE} = \frac{R_0}{E_0} F^2(E) \exp\left(-\frac{E}{E_0}\right), \quad (6.45)$$

with

$$R_0 = \frac{1}{M} \frac{\rho_0}{m} \sigma_0 \bar{v} \quad (6.46)$$

and $E_0 = 2(\mu^2/M)v_0^2 = \frac{1}{2}(\pi \mu^2/M)\bar{v}^2$.

This is the long-awaited WIMP-nucleus exponential spectrum. We have dropped the escape velocity corrections since this form is only accurate to $\sim 5\%$ for $E < 2E_0$. From the form of Eq. (6.45) we see that, in the absence of form factors, E_0 is the mean energy deposition, and from Eq. (6.46) we see that the flux is given by the mean WIMP speed through the Galaxy.

The exponential spectrum of Eq. (6.45) is one of the reasons the exponential form factor given in Eq. (6.36) is so popular for scalar interactions: it amounts to an energy rescaling in Eq. (6.45), $E_0^{-1} \rightarrow E_F^{-1} = E_0^{-1} + E_{\text{coh}}^{-1}$. In germanium $1 \text{ keV} \leq E_F \leq 31 \text{ keV}$ for $10 \text{ GeV} \leq m \leq \infty$.

A more accurate form for the spectrum is¹⁶³

$$\frac{dR}{dE} = \frac{R_0}{E_0} F^2(E) c_1 \exp\left(-\frac{c_2 E}{E_0}\right), \quad (6.47)$$

where c_1 depends on the energy threshold and time of year, and c_2 is related to c_1 . Good average values are $c_1 = 0.751$ and $c_2 = 0.561$.

6.7 Determining Sensitivity Limits

Having done our best to obtain the lowest possible spectrum, $(dR/dE)|_{Observed}$, using the techniques in §6.1–§6.4, chosen the form factor from Eq. (6.33), (6.34), (6.36), or (6.37), chosen the spectral shape from Eq. (6.44), (6.45), or (6.46), and chosen values for the halo parameters, ρ_0 and v_0 (and possibly v_{esc}), we now are faced with the task of connecting the two sides of Eq. (6.1) and using some statistical test to make statements about Galactic WIMPs as dark matter.

6.7.1 Including the Detector Response

As we discussed earlier, the first step is to convolve the theoretical spectrum with the response function of the detector to obtain the "expected" spectrum. If the response is Gaussian with *r.m.s.* width σ (independent of or only weakly dependent on the energy) and we use the exponential spectrum of Eqs. (6.45) or (6.46), then the effect of the convolution (obtained by completing the square in the exponent) is to shift the spectrum up by $\sigma^2/(2E_F)$: $E \rightarrow E_{obs} - \sigma^2/(2E_F)$. Including the form factor rescaling (which should be done before the convolution):

$$\frac{dR}{dE_{obs}} = \frac{R_0}{E_0} \exp\left(\frac{\sigma^2}{2E_F^2}\right) \exp\left(-\frac{E_{obs}}{E_F}\right). \quad (6.48)$$

Labeling the exponential factor in σ by f_σ we finally obtain the expected spectrum:

$$\frac{dR}{dE_{obs}} = \frac{R_0}{E_0} f_\sigma \exp\left(-\frac{E_{obs}}{E_F}\right). \quad (6.49)$$

This is the signal spectrum used in Eq. (6.14). This means that the counting rate measured at E_{obs} is essentially the larger theoretical counting rate from a nuclear recoil energy lower by $\sigma^2/(2E_F)$. In typical germanium detectors with $\sigma \approx 1$ keV, the shift is -500 eV to -16 eV for $10 \text{ GeV} \leq m \leq \infty$, compared to E_F of 1 - 31 keV; the corresponding rate increase is 50% - 0.1%.

Here E_{obs} is the experimentally measured value of the recoil energy, which we obtain directly from the (Luke gain corrected) phonon pulse amplitude. If the actual recoil energy is not measured directly, as in ionization detectors, there is one more adjustment to make to account for the drastically different ionization energies, ϵ_e and ϵ_n , for electron recoils and nuclear recoils, respectively. With these detectors it has been the custom to present measured spectra of the collected charge, N_{eh} , in *electron equivalent energy*, $E_{ee} = N_{eh}\epsilon_e$. For electron recoils $N_{eh} = E/\epsilon_e$, so photo-peaks are labeled by the known photon energy ($E_{ee} = E$), while for nuclear recoils $N_{eh} = E/\epsilon_n$ and $E_{ee} = (\epsilon_e/\epsilon_n)E$. In these detectors the conservative assumption is that all of the measured spectrum might possibly be nuclear recoils, so E_{obs} in Eq. (6.48) and Eq. (6.49) is understood to mean the nuclear recoil energy, E , corresponding to E_{ee} : $E_{obs} = (\epsilon_n/\epsilon_e) \times E_{ee}$. Alternatively, we can use the energy scale $E_{F_{ee}} = (\epsilon_n/\epsilon_e)E_F$ and use E_{ee} directly in the exponential, taking care to multiply the right hand side by the Jacobian factor $(dE_{obs}/dE_{ee}) = \epsilon_n/\epsilon_e$.

6.7.2 Statistical Tests

Now we come to the statistical tests. The basic idea is to ask if the "expected" spectrum from a given WIMP, identified by its mass and cross section (or total event rate), plus an arbitrary non-negative background, is incompatible with the measured spectrum at some confidence level, CL (e.g., $CL = \text{"90% confidence level,"} = 1.28 \sigma$ single sided). The fact that the background is allowed to be arbitrary (but non-negative)

means that no fixed background model is subtracted from the measured data. In any given bin, as long as the expected count rate is less than the measured rate, the excess can be ascribed to background, *independent of what is happening in neighboring bins*. If the expected count rate exceeds the measured rate then there is an incompatibility with some statistical weight. With some of the methods to be described, several modestly incompatible bins can combine to exceed CL , but there is no subtraction in that, for example, a well resolved peak above a flat background does not force a few background counts in neighboring bins to be ascribed to background because of the tail of the response function.

Single Bin Method

The simplest method, used in the first published analysis⁴⁶ and two subsequent ones,^{48,52} increases the cross section until it is incompatible in any single energy bin ("single bin method"). This effectively allows for an arbitrary non-negative background since the expected counting rate is not required to be as large as the measured one everywhere; the excess measured rate is ascribed to background. This is implemented by determining for a given cross section what minimum counting rate in each bin is acceptable at CL by subtracting the appropriate number of standard deviations from the mean counting rate predicted by the expected spectrum. Then we increase the cross section until this CL minimum expected spectrum exceeds the data in one bin. An alternative, though theoretically less desirable, implementation is to create the CL upper limit measured spectrum by adding the appropriate multiple of the measured error in each bin to the contents of each bin, then increasing the cross section until the expected spectrum exceeds the CL upper limit measured spectrum in any bin.

Three Bin Method

The second method takes advantage of small incompatibilities in adjacent bins, none of which alone exceeds the CL , but which collectively are significant, to set tighter

bounds on the cross section or total event rate. It looks for three consecutive bins in the expected spectrum that each exceed the corresponding measured count rate by 1.2 standard deviations ("3 bin method"). By Monte Carlo, one can show that this is a 90% confidence limit test for the ionization experiments.^{47, 49, 52}

All Bins Method

The ultimate extension is to consider any bins, not a limited number, where the expected spectrum exceeds the measured spectrum ("all bins method").⁵² Using only these bins one can compute an analog to a χ^2 , call it κ^2 . This will be zero if the expected spectrum is everywhere less than the measured one. One fluctuates the expected spectrum to obtain the distribution in κ^2 for each cross section; the *CL* cross section is the one that gives *CL* of the $\kappa^2 > 0$. This has been used for one analysis.⁵²

Because the expected spectrum is exponential, whereas the measured spectra are more nearly flat, generally only a few bins are responsible for setting the limit for low mass WIMPs. This is the justification for the 3 consecutive bins method. As one might expect, the limits get stronger as one uses more of the data in moving from the single bin to three consecutive bins to all bins methods.⁵² Finally, note that in these methods the limits are ultimately determined by the measured counting rate, so there is little improvement after obtaining ~10 counts in each bin. In comparing the expected number of counts, minus a small multiple of the standard deviation, to the measured number of counts, if the standard deviation is small then we are really just using the expected number of counts. As a result, there is little improvement to be made even with infinite counting time and infinite mass detectors with the same background. This is why it is crucial to have some method to measure the background.

Subtracting Assumed Backgrounds

The final method that has been applied to the ionization experiments involves a background subtraction and generally results in lower cross section limits.^{48, 52} Since the

background is unmeasured, the first step is to find a background model that gives a reasonable χ^2 . Typically this has included a Gaussian or exponential noise tail, Gaussians for any obvious peaks, and flat or linear components to fit the background at high energy. Second, one adds the expected spectrum to the background model and minimizes the χ^2 again with respect to the background model parameters. The χ^2 increase establishes the confidence level, so by increasing the cross section we can find the value that meets the CL . This amounts to a background subtraction since the components of the background model are fixed. In particular, the forms used have included a flat component to fit the background at high energy. The flat component does not allow the background model to go to zero at zero energy. When we add in a light WIMP, the flat background component is essentially unchanged since none of the counts at high energy can be due to the WIMP (it's spectrum is falling exponentially). This effectively subtracts the flat level determined at high energy from the spectrum at low energy that we might ascribe to the WIMP. What is needed, at a minimum, is a background model that can go to zero at zero energy, allowing the WIMPs to account for all the rate at threshold. The same model must still give a reasonable fit to the measured spectrum by itself. Similar criticisms can be made by a determined skeptic about the tails of the Gaussians used to fit any peaks (which is not measured at low energy with the actual background[†]) or the noise tail (which we cannot know without reducing the counting rate at threshold, which we have already done to the limit of our abilities). The essential problem is that we have to assume a functional form for a background that we haven't independently measured. Therefore this method has been generally considered to be too optimistic for the ionization experiments since it was introduced.⁴⁵

[†]A determined skeptic can argue that the response is a truncated Gaussian, for example, due to the finite energy gap. This response could contribute essentially no counts below the observed peak.

6.7.3 Subtracting Measured Backgrounds

But what about CDMS? The electron/nuclear background discrimination allows us to measure the presumed dominant background of the ionization experiments. Having measured the background and the detector response independently, we can now legitimately subtract the background from each bin. How should we use all the bins together to constrain the WIMP event rate?

Suppose we actually have managed to subtract all of the backgrounds. Then, instead of being limited by the raw event rate, we become limited by the fluctuations in the background, *i.e.*, the precision with which we have measured the background. Eqs. (6.16) and (6.17) gave the best estimate and the variance of the total event rate using the data in the bin $[E, E + \delta E]$:

$$\hat{R}_0 = \frac{(1 - \beta)N_S - \beta N_B}{(\alpha - \beta)MTf_\sigma(E_F/E_0)} \frac{e^{E/E_F}}{1 - e^{-\delta E/E_F}}, \quad (6.50)$$

$$\sigma_{\hat{R}_0}^2 = \frac{QB}{MT\delta E(f_\sigma(E_F/E_0))^2} \left(\frac{\delta E e^{E/E_F}}{1 - e^{-\delta E/E_F}} \right)^2. \quad (6.51)$$

Of course, for a background limited experiment we expect $\hat{R}_0 \approx 0$.

But what about the other bins? Since we are assuming that all backgrounds have been removed, each bin gives us an independent measurement of R_0 . Taking the weighted average of the individual bin estimates given by Eq. (6.50) using the $\sigma_{\hat{R}_0}^2$ as the weights we expect to obtain $\langle \hat{R}_0 \rangle \approx 0$ with variance

$$\begin{aligned} \sigma_{\langle \hat{R}_0 \rangle}^{-2} &= \sum_i \sigma_{\hat{R}_0}^{-2} \\ &= \sum_i \frac{MT\delta E}{Q(E_i, \delta E)B(E_i, \delta E)} \left(\frac{f_\sigma E_F}{E_0} \frac{1 - e^{-\delta E/E_F}}{\delta E e^{E_i/E_F}} \right)^2 \end{aligned} \quad (6.52)$$

where $E_{i+1} - E_i = \delta E$.

If we start the analysis at threshold E_n , so $E_i = E_t + i\delta E$, we can extract the values at threshold from the sum:

$$\sigma_{(\hat{R}_0)} = \sqrt{\frac{Q(E_t)b(E_t) \times 2f_{\delta E}E_F}{MTf_{\sigma}^2(E_F/E_0)^2}} e^{E_t/E_F} \quad (6.53)$$

and bury the details in the correction $f_{\delta E}$,

$$f_{\delta E}^{-1} = \sum_i \frac{Q(E_i)b(E_i)}{Q(E_i, \delta E)B(E_i, \delta E)} e^{2E_i/E_F} \frac{2E_F}{\delta E} \left(\frac{1 - e^{-\delta E/E_F}}{e^{E_i/E_F}} \right)^2 \quad (6.54)$$

For Q and b independent of energy, $f_{\delta E} = 1$. Eq. (6.53) gives the 1-sigma sensitivity limit on R_0 for a background limited background subtracted experiment.

Comparing Eq. (6.53) to Eqs. (6.12) and (6.17), we see that the final result comes from the background counting rate at threshold integrated in an effective bin $2f_{\delta E}E_F$ and reduced by the background rejection factor Q . The effects of finite bin size and energy dependence in Q and b are buried in $f_{\delta E}$, and the energy resolution and form factor are expressed in f_{σ} and E_F , respectively.

One can show that the continuum limit is the optimal choice for $f_{\delta E}$.¹⁵⁹ We let δE go to dE , $B(E, \delta E)$ become $b(E)$ and

$$f_{\delta E}^{-1} = e^{2E_t/E_F} \int_{E_t}^{\infty} \frac{Q(E_t)b(E_t)}{Q(E)b(E)} e^{-2E/E_F} \frac{2dE}{E_F}. \quad (6.55)$$

Eq. (6.55) is the starting place to consider energy dependent quality factors and backgrounds. For example, consider power law forms for the product Qb :

$$Q(E)b(E) = Q(E_t)b(E_t) \left(\frac{E_t}{E} \right)^a. \quad (6.56)$$

One can put $f_{\delta E}$ in the form¹⁵⁹

$$f_{\delta E}^{-1} = \frac{e^{(E_t/E_F)}}{(E_t/E_F)^a} \Gamma(a+1) Q_z \left(2 \frac{E_t}{E_F} \middle| 2(a+1) \right), \quad (6.57)$$

where $Q_x(\chi^2|\nu)$ is the probability of obtaining a result greater than χ^2 from ν degrees of freedom.

6.8 Expected Sensitivity of CDMS at Stanford

Let us apply the machinery of Eq. (6.53) to a particular model using estimates for our backgrounds. We will first get a rough estimate for a particular WIMP mass, then consider the full range of WIMP masses and several energy thresholds. We will take $v_0 = 220$ km/s and consider natural germanium, $M = 73$ GeV/c², running for $MT = 100$ kg days.

6.8.1 Rough Sensitivity Estimate for $m = 20$ GeV/c²

First consider a rough estimate with $m = 20$ GeV/c² resulting in $E_F = 3.4$ keV. We will assume a threshold E_t of 2 keV, which is ~ 6 times the baseline energy resolution presented in §3.4; for energy resolutions $\sigma \ll 1$ keV the resolution correction is generally negligible. Since we have good background rejection and signal acceptance, though not necessarily at threshold, we'll take $Q = \beta$ as a rough estimate. The resulting 90% confidence level (single sided: 1.28σ) expected sensitivity, assuming $f_{\text{AE}} = 1$, is

$$R_0^{(90\% \text{ CL})} = 0.64 \frac{\text{events}}{\text{kg day}} \times \sqrt{\beta b_t}. \quad (6.58)$$

Now consider the background models from §4.4. We estimated 8 photons/(kg keV day) roughly independent of energy after applying the muon veto. Let us take $Q(E_t) \sim \beta_{en} \sim 0.02$ for the electron-nuclear recoil discrimination at threshold, which is a strong assumption. This alone gives a 90% confidence limit of 0.26 events/(kg day).

From the neutron Monte Carlo we estimated $5 \text{ events}/(\text{kg day}) \times E^{-1}$, and we assume the muon veto efficiency is $\beta_{\mu\text{-veto}} \sim 0.02$. The 90% confidence level sensitivity limit from this source is $0.14 \text{ events}/(\text{kg day})$.

Adding these in quadrature, which is equivalent to adding the backgrounds directly, we might expect a 90% confidence level limit of $0.29 \text{ events}/(\text{kg day})$.

6.8.2 Detailed Sensitivity Estimate

In fact, since $Q(E_i) = 0.26$, not 0.02 as assumed above, and $f_{\mathcal{E}} = 0.12$, not 1, the mean effective rejection factor $Qf_{\mathcal{E}} = 0.03$ for electron recoils, not 0.02 as assumed above. Including the neutron background we find a limit of $0.32 \text{ events}/(\text{kg day})$.

More generally, we can compute the 90% confidence sensitivity limit as a function of WIMP mass for a variety of energy thresholds using the same background model. We don't expect the muon veto efficiency for neutrons to be a strong function of the recoil energy. We will also include the threshold energy dependence of the rejection factor, Q , derived in §3.4, in computing $f_{\mathcal{E}}$. The resulting energy dependence of *background* \times *rejection factor* is

$$(Q(E)b(E))|_{Net} = \left(8 \times Q(E) + \frac{0.1 \text{ keV}}{E} \right) \times \frac{\text{events}}{\text{kg keV day}} \quad (5.59)$$

Figure 6.2 shows the resulting 90% confidence level sensitivity limits (from top to bottom) for $E_i = 5, 2, 1,$ and 0.5 keV (with $\sigma_E = E/6$). The effect of the threshold (and baseline resolution) is readily apparent for low WIMP masses. Since we have a recoil energy resolution of 330 eV , we should achieve a threshold of 2 keV . For high WIMP masses, the average energy saturates at 31 keV , so the result is largely independent of the WIMP mass until the threshold is a large fraction of the mean energy. The best sensitivity comes for moderate WIMP masses because the mean energy is larger than

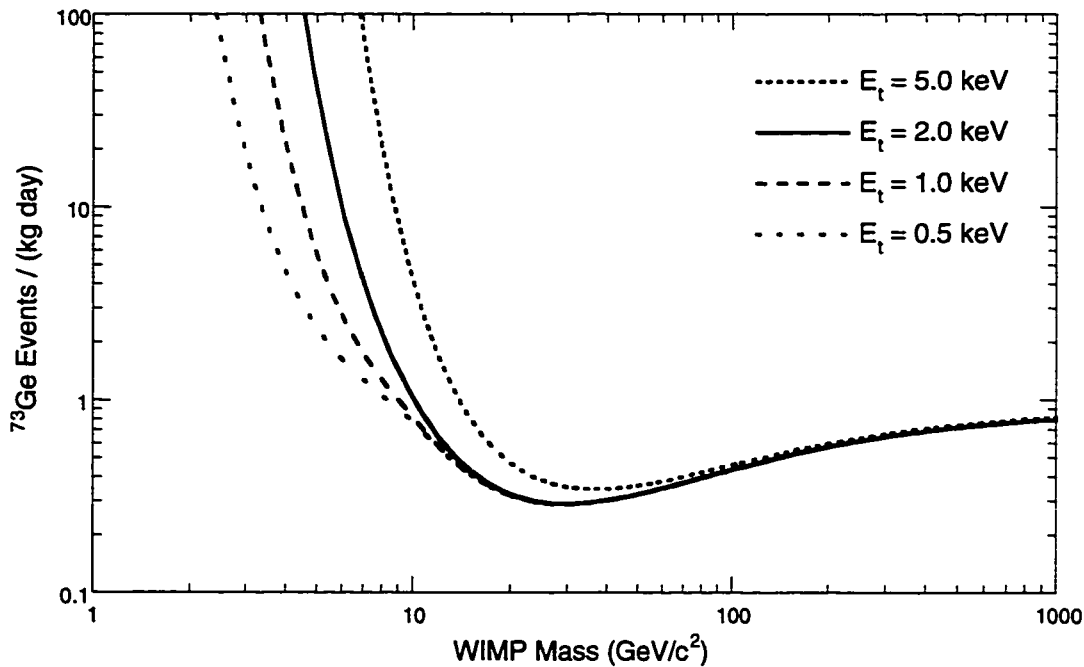


Figure 6.2. Sensitivity Limits vs. WIMP mass and Energy Threshold. Predicted 90% confidence level event rate sensitivity limits as a function of WIMP mass and threshold. The thresholds are (top to bottom) 5, 2, 1, and 0.5 keV.

the threshold, so we measure the bulk of the spectrum, but not so large that we have to integrate much of the background.

This background model is almost certainly dominated by the internal activity of the HPGe detector used to measure the photon spectrum in the shield and the bremsstrahlung from ^{210}Pb contamination in the lead shield (see §4.4). We expect to be able to make our cryogenic detectors significantly cleaner than the HPGe detector and to absorb the ^{210}Pb activity with a clean lead liner, reducing the raw electron recoil background rate to ~ 1 events/(kg keV day). Based on the measurements in the shield with the NaI and HPGe detector, we expect that the muon veto efficiency for neutrons is $\sim 99.5\%$, not the 98% assumed above. With these improvements we may be able to achieve a sensitivity for heavy WIMPs as low as 0.3 events/(kg day), a limit we have often quoted.

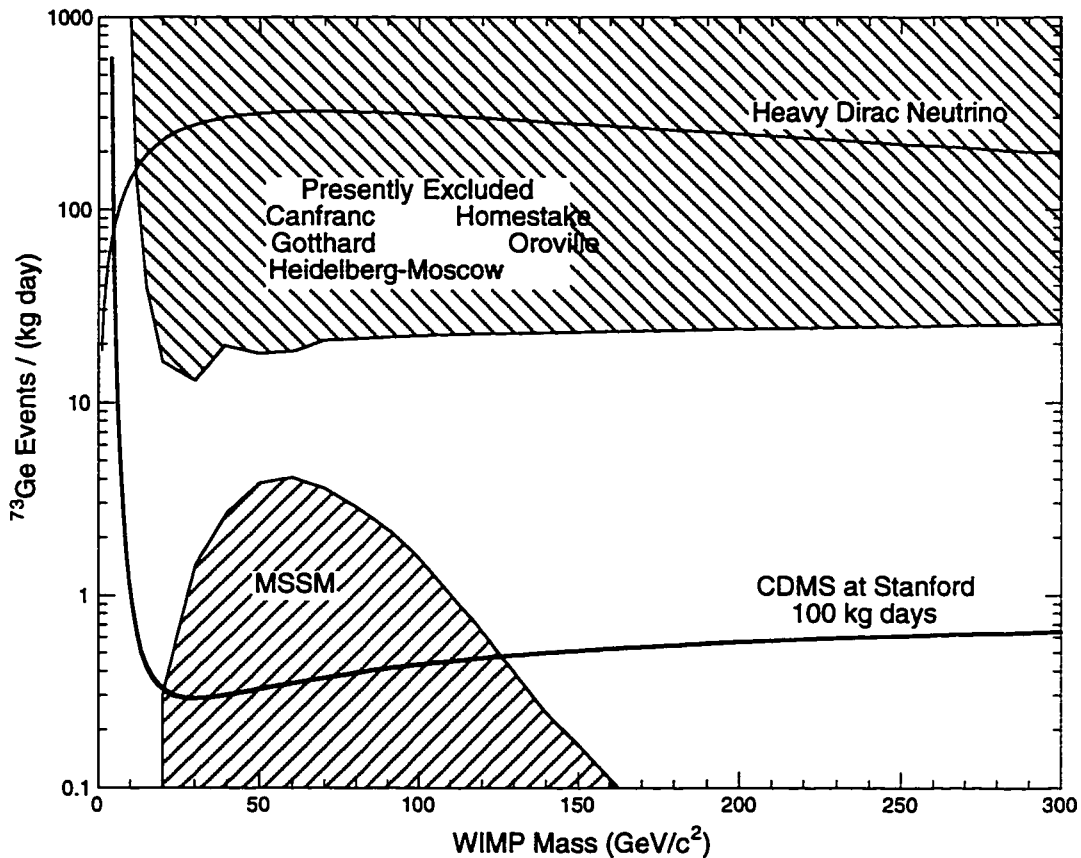


Figure 6.3. Current Limits, MSSM, and CDMS. Current WIMP event rate limits achieved with HPGe detectors (Homestake,⁴⁶ Oroville,⁴⁵ Gotthard,⁴⁹ Heidelberg-Moscow,⁴⁷ and Canfranc⁴⁸), predictions of minimal supersymmetric models (MSSM),⁴³ and the estimated 90% confidence level sensitivity limit for CDMS.

Figure 6.3 shows the current exclusion limits (see Figure 2.3), the region populated by supersymmetric models (see Figure 6.1), and the expected 90% confidence limit for CDMS with a 2 keV threshold. The CDMS sensitivity will be lower than the current limits by ~ 40 , made possible by the electron/nuclear recoil discrimination. At Stanford we will begin to test neutralinos as dark matter and constrain supersymmetric particle models.

6.9 The Future

In the longer term, we will have to operate these detectors at a deeper site to reduce the cosmic ray muon related backgrounds and cosmogenics in the detectors. We have received funding to construct a duplicate cryostat and are making plans to prepare a deep site, possibly the Soudan mine in collaboration with Fermilab. At a deep site, we can make a number of changes to the shielding system to take advantage of the reduced muon related neutron background. The only significant neutron source will be (α,n) reactions and fission from contamination in the laboratory, so we won't need the moderator inside the cryostat and the lead (though we will need moderator *outside* the lead). That lets us shrink the lead layer making it feasible to use higher quality lower activity lead. Without the internal moderator we can operate seven towers (*vs.* three at Stanford). With larger diameter and slightly thicker detectors, the total detector mass becomes 15 kg (*vs.* 1 kg). Because the muon flux, much reduced compared to Stanford, will be essentially vertical, a muon veto probably only has to cover the top of the apparatus. Finally, at a deep site we expect the photon backgrounds to be reduced, since there will be much less cosmogenic activity in all materials. We should be able to reach the electron recoil background levels achieved in the ionization experiments, ~ 1 event/(kg keV day). Taking all these factors together, a rough estimate of the deep site sensitivity is 0.01 events/(kg keV day), which will probe an even more significant piece of the MSSM predictions.

Appendix A. Thermal Conductivity Functions

To construct the thermal model we found it convenient to approximate the measured thermal conductivities of materials by a single analytic form:

$$\kappa(T) = \begin{cases} k_1 T^\alpha & T < \tau_1 \\ k_2 T^\beta & \tau_1 < T < \tau_2 \\ k_3 & \tau_2 < T \end{cases} \quad (\text{A.1})$$

where the temperature is in Kelvin and the conductivity is in W/(m K). Of course, not all the constants k_i , α , β , τ_1 , τ_2 , (seven altogether) are independent, since κ should be continuous, which gives two constraints ($k_1 \tau_1^\alpha = k_2 \tau_1^\beta$, $k_2 \tau_2^\beta = k_3$). This form has the virtue that, with the appropriate parameters, it gives rough agreement with experimental measurements for metals and insulators. (For insulators we typically set $\tau_2 = \infty$, making k_3 irrelevant.) It can also be integrated analytically to give the function $K(T)$ used extensively in Chapter 5:

$$K(T) = \begin{cases} \frac{k_1}{1+\alpha} T^{1+\alpha} & T < \tau_1 \\ \frac{k_1}{1+\alpha} \tau_1^{1+\alpha} + \frac{k_2}{1+\beta} (T^{1+\beta} - \tau_1^{1+\beta}) & \tau_1 < T < \tau_2 \\ \frac{k_1}{1+\alpha} \tau_1^{1+\alpha} + \frac{k_2}{1+\beta} (\tau_2^{1+\beta} - \tau_1^{1+\beta}) + k_3 (T - \tau_2) & \tau_2 < T \end{cases} \quad (\text{A.2})$$

Defining the new constants K_i as

$$\begin{aligned} K_1 &= \frac{k_1}{1+\alpha} \tau_1^{1+\alpha} \\ K_2 &= \frac{k_2}{1+\beta} \tau_1^{1+\beta}, \\ K_3 &= \frac{k_2}{1+\beta} \tau_2^{1+\beta}, \\ K_4 &= K_1 - K_2 + K_3, \end{aligned} \quad (\text{A.3})$$

we can rewrite the integrated conductivity in Eq. (A.2) as

$$K(T) = \begin{cases} \frac{k_1}{1+\alpha} T^{1+\alpha} & T < \tau_1 \\ K_1 - K_2 + \frac{k_2}{1+\beta} T^{1+\beta} & \tau_1 < T < \tau_2 \\ K_4 + k_3(T - \tau_2) & \tau_2 < T \end{cases} \quad (\text{A.4})$$

This function is invertible:

$$T(K) = \begin{cases} \left[\frac{1+\alpha}{k_1} K \right]^{\frac{1}{1+\alpha}} & K < K_1 \\ \left[\frac{1+\beta}{k_2} (K - K_1 + K_2) \right]^{\frac{1}{1+\beta}} & K_1 < K < K_4 \\ \tau_2 + \frac{K - K_4}{k_3} & K_4 < K \end{cases} \quad (\text{A.5})$$

This allows us to use Eq. (5.10) to compute the temperatures once we have computed the integrated power density, J , using Eq. (5.7).

Table A.1 shows the values we adopted for the seven constants. We did not always accept the "recommended" values for the pure material, but instead tried to use values that reflect what we felt we could achieve with actual materials. Measurements on the purest samples generally give higher conductivities, but we did not intend to build the cryostat out of the purest single crystal copper ever measured. To determine the constants, we graphed data from several samples of the material, then adjusted the parameters until the computed κ matched the measurements in form and value. (For example, most samples of copper give the same low temperature slope and high temperature value. What differs is the low temperature value and peak value. To obtain the parameters for a RRR value other than those of the measured samples, we adjusted the parameters until we had the right low temperature slope, high temperature value, and had the desired RRR.)

Table A.1. Thermal Conductivity Values Used in the Thermal Model.

Values of the constants defined in Eq. A.1 for the thermal conductivity function used in the thermal model for the cryostat. The k_i are in W/(m K); τ_i in K, and α and β are dimensionless. We obtained these values by examining the conductivities reported in Lounasmaa⁹⁵ and White,⁹⁷ and for individual materials the specific sources referenced below.

Material	k_1	α	τ_1	k_2	β	τ_2	k_3
Cu, RRR = 50 ¹³¹	50	1	20	3320	-0.4	200	400
Cu, RRR = 1000 ¹³¹	1000	1	6	33664	-0.963	100	400
Kevlar ¹²⁹	0.0021	1.6	40	0.4742	0.1308	∞	-
Manganin	0.10286	1.2964	20	0.68906	0.6616	∞	-
Nylon	0.00182	1.39	20	0.0348	0.4046	∞	-
Stainless Steel	0.12	1	80	1.7649	0.3865	∞	-
Titanium, alloy ¹²³⁻¹²⁵	0.11	1	23	0.6163	0.45	∞	-
Titanium, pure ¹²³⁻¹²⁵	0.6	1	33	-	-	33	20
Vespel ¹²⁸	0.0018	1.21	40	0.01856	0.5774	∞	-

Appendix B. Where to Find Further Information about the Monitoring System

Here are some hints for finding information about the Icebox and its Monitoring System. If you are trying to understand how to operate the fridge, go to the **Icebox Procedures** binder. If you want to understand the monitoring hardware, start with the **Multiplexing** note. For more detail about the overall circuit layout, including cabling and grounding, refer to the **Monitoring System Diagram**. The location of further documentation of every item shown in the diagram is given in the **Monitoring System Item List**.

The remainder of this document is an annotated table of contents for the **Icebox Procedures** binder and the **Icebox Monitoring System** binder. After the description of each document, the file path for any on-line version is given in square brackets. Unless otherwise noted, all paths assume [*UCB CfPA AppleTalk Zone: Godzilla: DKM DOCS: DIRECT DETECTION DOCS: 400 FRIDGE / ICEBOX*], represented by the symbol "@".

B.1 Icebox Procedures and General Information

B.1.1 Procedures

Operating the Oxford 400 mW Dilution Fridge: Post-assembly/Tails-only describes the cool-down and warm-up procedures for the fridge when running by itself, without the Icebox. At the end it describes how to clean the cold traps. [*@ Procedures: Post-assembly Tails-only*]

Single Shot Procedure is a fax from Oxford Instruments describing how to perform and interpret a single shot test of a dilution refrigerator.

Single Shot Record is a form for recording the single shot data. [CfPA: Godzilla: DKM DOCS: DIRECT DETECTION DOCS: 0 Fridge General: Single Shot Record]

Plumbing Schematics, highlighted to show the gas locations and flow paths during various modes of operation. John Taylor has this drawing on-line somewhere at LBL.

EH1200 Booster Pump Oil Change Procedure is copied from the Edwards manual.

B.1.2 Data Forms

Fridge Running Deed is the standard run sheet used in the Berkeley 75 mW fridge runs. [CfPA: Godzilla: DKM DOCS: DIRECT DETECTION DOCS: 0 Fridge General: Fridge Running Deed]

NOT Data Sheet is useful for recording the results of measurements made with the NaI of the ^{60}Co thermometer. [CfPA: Godzilla: DKM DOCS: DIRECT DETECTION DOCS: 0 Fridge General: NOT: NOT Data Sheet]

W Calculator takes the warm, background, and cold counts and computes the background-subtracted ratio W , with errors. [CfPA: Godzilla: DKM DOCS: DIRECT DETECTION DOCS: 0 Fridge General: NOT: W Calculator]

Co-60 Calculator is the same as **W Calculator**, except that it also looks up W in a table and interpolates the corresponding temperature.

B.1.3 General Calibrations

Fridge Nominal Values lists the values of the Oxford resistors and the throughputs at each stage of previous runs, along with the averages. This is useful during cooldown to check the current situation against historical performance. [@ Oxford 400 Fridge :Calibrations :Fridge Nominal Values]

Oxford R Values 3-wire shows the same type of information as **Fridge Nominal Values**, but measured in the early days with the 3-wire bridge. [@ Oxford 400 Fridge :Calibrations :Oxford R Values 3-wire]

Convectron plots the response of the Convectron gauge tubes to helium, as shown in the Convectron gauge manual. Also shown is the relation between the indicated pressure between the pumps and the actual circulation rate, obtained by multiplying the actual pressure for a given indicated pressure by the actual pumping speed from the Alcatel pump manual. [@ Plumbing: Gauges: Convectron]

Helium Press/Temp plots the ^4He and ^3He vapor pressures versus temperature. [@ Misc Calibrations: Helium Press/Temp]

Keg Pressure shows the keg pressure as a function of temperature. The keg pressure gauges are more than sensitive enough to see this effect, so be sure to check against the plot before panicking about lost mix. [@ Plumbing: Keg Pressure]

RT2 is a demountable RuO_2 thermometer. There are graphs of its calibration from 300 K down to 50 mK, and an extrapolation to 10 mK in **RuO #2**. [@ Sensors: Thermometers: Calibrations: RuO #2]

W at 0 degrees in Icebox is a table of the ratio of cold counts to warm counts from the ^{60}Co source for the Icebox can geometry. [CfPA: Godzilla: DKM DOCS: DIRECT DETECTION DOCS: 0 Fridge General: NOT: W at 0 degrees in Icebox]

Oxford Cooling Power Data summarizes the Oxford test results for heating the mixing chamber and/or the cold plate.

Some useful properties of helium and nitrogen, and gas flow conversions, are listed in **He and N2**. [@ Misc Calibrations: He and N2]

Oxford Instruments Germanium Resistance Calibration lists the calibration for a germanium RTD, which we believe is the Oxford supplied MC2 in the fridge.

B.2 Monitoring System

B.2.1 General

Multiplexing or A Multiplexing Scheme for Monitoring the Icebox gives a general overview of the monitoring system. It shows simplified schematics for the sensor readouts, as well as block diagrams for the multiplexed measurements. It also lists the steps to make a measurement and the parameters needed by the software. Finally, it shows how to organize the multiplexer hardware banks into the conceptual multiplexers used in the system. [@ Notes: Multiplexing Note: Multiplexing]

Monitoring System Diagram shows the entire warm electronics setup, including the cabling and grounding. Each item is numbered and listed in the **Monitoring System Item List**, along with a pointer to the documentation. [@ Electronics: Monitoring System Diagrams: Monitoring System Diagram] [@ Electronics: Monitoring System Diagrams: Monitoring System Item List]

Device Names describes the seeming illogic behind the names for sensors, heat sinks, and connectors. [@ Electronics: Monitoring System Diagrams: Device Names]

Sensor Locations and Flange Labels is a drawing of the Icebox showing where all the sensors are and the letter designations for all the flange locations.

B.3 Cryogenic Wiring

Fridge Oxford Wiring,

Fridge IVC Wiring,

Fridge OVC Wiring,

Cans IVC Wiring, and

Cans OVC Wiring are block diagrams for the cryogenic wiring and sensor locations. The legend is on **Fridge Oxford Wiring** only. All five documents are in [[@ Cryogenic Wiring: Wiring Block Diagrams](#)]

Wiring Table: Harness is the cryogenic piece of the **Wiring Table**, sorted in harness order, *i.e.*, in block diagram order. It starts with the sensor name and shows all connections through to the vacuum feedthrough. [[@ Cryogenic Wiring: Wiring Table](#)], sorted by Harness.

Ribbon Cable Connectors is a sketch that shows the location and numbering of the pins on the Oxford ribbon cable connectors between the Pot and the Still.

B.3.1 Wiring to MUX

Wiring Table: Connection is the warm piece of the **Wiring Table**, sorted by feedthrough and function. It lists the sensor name and pin, the cables the signal goes through, and finally the MUX slot and channel. [[@ Cryogenic Wiring: Wiring Table](#)], sorted by Feedthrough and Function.

B.3.2 MUX I/O Panels

DIRTY MUX I/O CABLE connects the Dirty MUX Card to the patch card in the Dirty MUX I/O Panel. [[@ Electronics: MUX I/O Panel: Dirty MUX I/O Cable](#)]

MUX BOARD CABLES connect the clean MUX cards to the patch cards in the MUX I/O Panel. [@ Electronics: MUX I/O Panel: MUX BOARD CABLES]

B.3.3 MUX

MUX Block Diagrams summarizes the readout path for each type of sensor. [@ Notes: Multiplexing Note: MUX Block Diagrams]

MUX Channel Assignments summarizes **Wiring Table: Connection**. It lists the sensor using each channel, as well as indicating the backplane and card buss jumpers required to configure the logical multiplexers. [@ Electronics: Monitoring System Diagrams: MUX Channel Assignments]

MUX Backplane Jumpers sketches the jumper locations for the card buss and the backplane busses, as copied from the manual.

GPIB Addresses lists the GPIB addresses used by the monitoring hardware. [@ Electronics: GPIB Addresses]

B.4 Schematics

B.4.1 Miscellaneous Schematics

Monitoring Supplies Box is the quad power supply for the monitoring system. [@ Electronics: Monitoring Power Supplies: Monitoring Supplies Box]

Fridge Skirt Positions is a sketch of the vertical and horizontal positions of the fridge skirts at the "C" flange.

Estimate of the LHe Bath Volume is a sketch estimating the LHe Bath volume.

B.4.2 Fridge Control

The **Heater and Thermometer Control Box** has two sections. The heater section powers the mixing chamber and still heaters. The thermometer section selects which thermometer should be connected to the front panel jack. All the thermometers are accessible to the monitoring system through the back panel. Graphs of the power versus current reading are from **Heater Powers**. [@ Electronics: Heater/Therm Box: Schematic] [@ Electronics: Heater Powers]

Circuit Diagram for the Oxford 400 Control Panel documents the pump and interlock control panel. [@ Electronics: Pump/Interlock Control]

B.4.3 MUX Interface

MUX Interface Box starts with a block diagram of the buffering and MUXed IV circuit, followed by the detailed diagrams and cable schematics. [@ Electronics: MUX INTERFACE BOX: MUX INTERFACE BOX]

B.4.4 MUX IV Boxes

Fridge Mixing Chamber IV Box details the dedicated IV circuits for the 10 mK sensors on the fridge side. These are all accessed through FT5. There is no on-line documentation for this box.

Icebox Mixing Chamber IV Box contains the dedicated IV circuits for the two 10 mK sensors on the can side, accessed through FT12. [@ Electronics: ICEBOX MC IV BOX: icebox MCIV box rev B]

B.4.5 Cables

Level Sensor Cables shows the construction of the 18 wire level sensor cable and the breakouts at each end.

MUX INT'F BOX CABLE ASSEMBLY details the octopus cable that connects the MUX Interface Box to the MUX I/O Panel (patch panel). [@ Electronics: MUX INTERFACE BOX: MUX INT'F BOX CABLE]

MONITOR CABLES details all the long cables from the feedthroughs to the DB37 connectors at the patch panel. [@ Electronics: MONITORING CABLES: MONITOR CABLES revC]

B.4.6 LN Autofill

LN FILL SWITCHBOX is the control box for the LN Autofill/Vent system. A cleaner version is **LN Autofill after AHS**. [@ Electronics: LN Autofill: LN Fill Switchbox], [@ Electronics: LN Autofill: LN Autofill after AHS]

LN Fill/Vent Plumbing diagrams the valve locations for the LN Autofill system. [@ Plumbing: LN Fill/Vent Plumbing]

DC Power Supply is the DC power supply for the quiescent heaters. [@ Electronics: LN Autofill: DC Power Supply]

B.5 Sensor Information

B.5.1 Devices: Miscellaneous

Pot Level Sensor Pinout is a copy of the diagram from Oxford for the Pot level sensor pinout, along with some diagnostic measurements. We have not been able to make this sensor read anything reasonable.

B.5.2 RuO₂ Sensors

B.5.3 Diode Sensors

Sunil's note explains how the data were fit, followed by graphs for each device.

The data should be in [[@ Sensors: Thermometers: Calibrations](#)]

B.5.4 Position Sensor Calibrations

Graphs of resistance versus length for the linear potentiometers used for the position sensors. [[@ Sensors: Position Sensors: Calibrations](#)]

References

1. E. W. Kolb and M. S. Turner, *The Early Universe* (Addison-Wesley, Redwood City, CA, 1990).
2. S. van den Bergh, *Science* **258**, 5081, 421-4 (1992).
3. G. Efstathiou, R. S. Ellis, and B. A. Peterson, *Mon. Not. Roy. Astr. Soc.* **232**, 2, 431-61 (1988).
4. J. Loveday, *et al.*, *Astroph. J.* **390**, 1, 338-44 (1992).
5. S. Tremaine, *Physics Today* **45**, 2, 28-36 (1992).
6. K. Kuijken, *Astroph. J.* **372**, 1, 125-31 (1991).
7. J. N. Bahcall, C. Flynn, and A. Gould, *Astroph. J.* **389**, 1, 234-50 (1992).
8. J. N. Bahcall, *Neutrino Astrophysics* (Cambridge University Press, New York, 1989).
9. M. R. Merrifield, *Astron. J.* **103**, 5, 1552-63 (1992).
10. G. Gilmore, *et al.*, *The Milky Way as a Galaxy* (University Science Books, Mill Valley, CA, 1990).
11. K. K. Kwee, C. A. Muller, and G. Westerhout, *Bull. As. Ins Neth.* **12**, 211 (1954).
12. D. Mihalas and J. Binney, *Galactic Astronomy: structure and kinematics* (W.H. Freeman, San Francisco, 1981).
13. R. A. Flores, *Phys. Lett. B* **215**, 1, 73-80 (1988).
14. D. Zaritsky, *et al.*, *Astroph. J.* **345**, 1, 759-69 (1989).
15. C. S. Kochanek, *Astroph. J.* **457**, 1, 228-43 (1996).
16. M. Fich and S. Tremaine, *Ann. Rev. Astr. Astrophy.* **29**, 409 (1991).
17. J. Binney, *Ann. Rev. Astr. Astrophy.* **20**, 399 (1982).
18. V. Trimble, *Ann. Rev. Astr. Astrophy.* **25**, 245 (1987).
19. C. J. Copi, D. N. Schramm, and M. S. Turner, *Science* **267**, 5195, 192-9 (1995).

20. D. Merritt, *Astroph. J.* **313**, 1, 121-35 (1987).
21. J. P. Hughes, *Astroph. J.* **337**, 1, 21-33 (1989).
22. C. L. Sarazin, *Rev. Mod. Phys.* **58**, 1, 1-115 (1986).
23. A. Dekel, *Ann. Rev. Astr. Astrophys.* **32**, 371 (1994).
24. L. L. Cowie, *Phys. Scr.* **36**, 102 (1991).
25. E. D. Loh and E. J. Spillar, *Astroph. J. Lett.* **307**, 2, L1-4 (1986).
26. S. R. Bahcall and S. Tremaine, *Astroph. J. Lett.* **326**, 2, L1-4 (1988).
27. D. Caditz and V. Petrosian, *Astrophysical Journal, Letters* **337**, 2, 65-8 (1989).
28. M. Omote and H. Yoshida, *Astroph. J.* **361**, 1, 27-31 (1990).
29. B. Paczynski, *Astroph. J.* **304**, 1, 1-5 (1986).
30. D. P. Bennett, *et al.*, in proceedings of 5th Annual Astrophysics Conference. Dark Matter, College Park, MD, USA, 1995, AIP Conference Proceedings #336 (American Institute of Physics, New York), 77-90.
31. L. Moscoso, in proceedings of 16th International Conference on Neutrino Physics and Astrophysics, Eilat, Israel, 29 May - 3 June 1994, edited by A. Dar, G. Eilam and M. Gronau, *Nuclear physics B38*, (Proceedings Supplements), 387-93 (1995).
32. A. Udalski, *et al.*, *Acta Astronomica* **45**, 1, 237-57 (1995).
33. C. Stubbs, personal communication, 1994.
34. E. I. Gates, G. Gyuk, and M. S. Turner, *Astrophysical Journal, Letters* **449**, 2, L123-6 (1995).
35. E. I. Gates, G. Gyuk, and M. S. Turner, *Phys. Rev. Lett.* **74**, 19, 3724-7 (1995).
36. E. Gates and M. S. Turner, *Phys. Rev. Lett.* **72**, 16, 2520-3 (1994).
37. M. I. Vysotskii, A. D. Dolgov, and Y. B. Zel'dovich, *JETP Lett.* **26**, 188 (1977).
38. K. Sato and H. Kobayashi, *Prog. Theor. Phys.* **58**, 1775 (1977).
39. B. W. Lee and S. Weinberg, *Phys. Rev. Lett.* **39**, 165 (1977).
40. P. Hut, *Phys. Lett.* **69B**, 85 (1977).

41. H. E. Haber and G. L. Kane, *Phys. Rep.* **117**, 2-4, 75-263 (1985).
42. T. Falk, K. A. Olive, and M. Srednicki, *Phys. Lett. B* **339**, 3, 248-51 (1994).
43. G. Jungman, M. Kamionkowski, and K. Griest, *Phys. Rep.* **267**, 5-6, 195-373 (1996).
44. M. Kamionkowski, *et al.*, *Phys. Rev. Lett.* **74**, 26, 5174-7 (1995).
45. D. O. Caldwell, *et al.*, *Phys. Rev. Lett.* **61**, 61, 510-13 (1988).
46. S. P. Ahlen, *et al.*, *Phys. Lett.* **B195**, 4, 603-8 (1987).
47. M. Beck, *et al.*, *Phys. Lett.* **B336**, 2, 141-6 (1994).
48. E. Garcia, *et al.*, *Phys. Rev.* **D51**, 4, 1458-64 (1995).
49. D. Reusser, *et al.*, *Phys. Lett.* **B235**, 1, 143-5 (1991).
50. D. O. Caldwell, *et al.*, *Phys. Rev. Lett.* **65**, 11, 1305-8 (1990).
51. J. Ellis, *et al.*, *Phys. Lett. B* **245**, 2, 251-7 (1990).
52. M. Gray, *A Search for Neutrino Oscillations in the Muon Neutrino to Electron Neutrino Appearance Channel at LSND*, Ph.D. thesis (University of California, Santa Barbara, 1995).
53. N. J. C. Spooner and P. F. Smith, *Phys. Lett. B* **314**, 3-4, 430-5 (1993).
54. T. Dombeck, A. Finch, and D. L. Grisham, *Nucl. Instr. Meth. Phys. Res. A* **272**, 3, 650-9 (1988).
55. G. F. Knoll, *Radiation Detection and Measurement* (Wiley, New York, 1989).
56. Z. H. Levine and D. C. Allan, *Phys. Rev. B* **44**, 23, 12781-93 (1991).
57. Z. H. Levine and D. C. Allan, *Phys. Rev. Lett.* **66**, 1, 41-4 (1991).
58. J. C. Mather, *Appl. Opt.* **23**, 4, 584-8 (1984).
59. R. Gaitskell, in proceedings of the Sixth International Workshop on Low Temperature Detectors, Interlaken, Switzerland, to appear in *Nuclear Instruments and Methods in Physics Research A* (1996).
60. P. F. Smith and J. D. Lewin, *Phys. Rep.* **187**, 5, 203-80 (1990).

61. J. R. Primack, D. Seckel, and B. Sadoulet, *Ann. Rev. Nucl. Part. Sci.* **38**, 751-807 (1988).
62. T. Shutt, *et al.*, *Phys. Rev. Lett.* **69**, 3531 (1992).
63. T. Shutt, *et al.*, *Phys. Rev. Lett.* **69**, 3452 (1992).
64. T. Shutt, *A Dark Matter Detector Based on the Simultaneous Measurement of Phonons and Ionization at 20 mK*, Ph.D. thesis (University of California, Berkeley, 1993).
65. I. S. Park, *Characterization and applications of neutron transmutation doped germanium*, Ph.D. thesis (University of California, Berkeley, 1988).
66. N. Wang, *A Cryogenic Phonon Detector to Search for Dark Matter Particles*, Ph.D. thesis (University of California, Berkeley, 1991).
67. A. L. Efros and B. I. Shkolovskii, *Electronic Properties of Doped Semiconductors* (Springer-Verlag, New York, 1984).
68. A. C. Cummings, Ph.D. thesis (University of California, Berkeley, in preparation).
69. S. H. Moseley, J. C. Mather, and D. McCammon, *J. Appl. Phys.* **56**, 5, 1257-62 (1984).
70. H. J. Maris and S. Tamura, *Phys. Rev. B* **47**, 2, 727-39 (1993).
71. T. More and H. J. Maris, in proceedings of Fifth International Workshop on Low-Temperature Detectors, Berkeley, CA, USA, 29 July-3 Aug. 1993, edited by S. Labov and B. Young, *Journal of Low Temperature Physics* **93**, 3-4, 387-92 (1993).
72. P. N. Luke, *J. Appl. Phys.* **64**, 6858 (1988).
73. K. D. Irwin, *et al.*, *Rev. Sci. Instr.* **66**, 11, 5322-6 (1995).
74. R. P. Welty and J. M. Martinis, in proceedings of 1990 Applied Superconductivity Conference, Snowmass, CO, USA, March 1991, *IEEE Transactions on Magnetics* **27**, 4, 2924-6 (1991).

75. K. D. Irwin, *Appl. Phys. Lett.* **66**, 15, 1998-2000 (1995).
76. C. A. Klein, *IEEE Trans. Nucl. Sci.* **NS-15**, 3, 214 (1968).
77. J. Lindhard, *et al.*, *Matematisk-fysiske Meddelelser udgivet af Det Kongelige Danske Videnskabernes Selskab* **33**, 10 (1963).
78. D. Yvon, personal communication, 1995.
79. A. Da Silva, *Development of a Low Background Environment for the Cryogenic Dark Matter Search*, Ph.D. thesis (University of British Columbia, 1996).
80. M. S. Longair, *High energy astrophysics* (Cambridge University Press, Cambridge, England, 1994).
81. D. Lal and B. Peters, *Hand. Phys.* **46**, 2, 551-612 (1967).
82. R. L. Brodzinski, *et al.*, *Nucl. Instr. Meth. Phys. Res. A* **292**, 2, 337-42 (1990).
83. D. O. Caldwell, *et al.*, *Phys. Rev. Lett.* **59**, 4, 419-22 (1987).
84. *Nuclides and Isotopes*, edited by F. W. Walker, J. R. Parrington, and F. Feiner (General Electric Company, Nuclear Energy Operations, 175 Curtner Avenue, M/C 397, San Jose, California, 1989).
85. N. E. Holden, *Isotopic Abundances*, February 23, 1989, report, BNL-NCS-42224 (Brookhaven National Laboratory, 1989).
86. M. Ivanovich and R. S. Harmon, *Uranium-series disequilibrium : applications to earth, marine, and environmental sciences* (Oxford University Press, Oxford, 1992).
87. T. Florkowski, L. Morawska, and K. Rozanski, *Nucl. Phys.* **2**, 1, 1-14 (1988).
88. Y. Feige, B. G. Oltman, and J. Kastner, *J. Geophys. Res.* **73**, 10, 3135-3142 (1968).
89. F. T. Avignone, *et al.*, *Phys. Rev. C* **34**, 2, 666-77 (1986).
90. G. Heusser, *Ann. Rev. Nucl. Part. Sci.* **45**, 45, 543-590 (1995).
91. R. L. Brodzinski, *et al.*, *J. Rad. Nucl. Chem.* **124**, 513 (1988).

92. A. Alessandrello, *et al.*, in proceedings of Low Temperature Detectors for Neutrinos and Dark Matter III, Gran Sasso, L'Aquila, Italy, September 20-23, 1989, edited by L. Brogiato, C. V. Camin and E. Fiorini, (Editions Frontières, Gif-sur-Yvette, France, 1990).
93. M. Chapellier, in proceedings of the Sixth International Workshop on Low Temperature Detectors, Interlakken, Switzerland, to appear in Nuclear Instruments and Methods in Physics Research A (1996).
94. L. Zerle, *et al.*, in proceedings of the Sixth International Workshop on Low Temperature Detectors, Interlakken, Switzerland, to appear in Nuclear Instruments and Methods in Physics Research A (1996).
95. O. V. Lounasmaa, *Experimental Principles and Methods Below 1 K* (Academic Press, London, 1971).
96. F. Pobell, *Matter and Methods at Low Temperatures* (Springer-Verlag, Berlin, 1992).
97. G. K. White, *Experimental Techniques in Low-Temperature Physics* (Clarendon Press, Oxford, 1978, revised 1987).
98. R. C. Richardson and E. N. Smith, *Experimental Techniques in Condensed Matter Physics at Low Temperatures* (Addison-Wesley, Redwood City, CA, 1988).
99. Oxford Instruments Ltd., Eynsham, OXON OX8 1TL, England, Model 400S Dilution Refrigerator.
100. C. Kittel, *Introduction to Solid State Physics* (John Wiley and Sons, New York, 1986, revised 1991), p. 115.
101. C. Kittel, *Introduction to Solid State Physics* (John Wiley and Sons, New York, 1986, revised 1991), p. 106.
102. J. M. Ziman, *Principles of the Theory of Solids* (Cambridge University Press, Cambridge, 1972), p. 231ff.

103. C. Kittel, *Introduction to Solid State Physics* (John Wiley and Sons, New York, 1986, revised 1991), p. 152.
104. F. R. Fickett, *J. Phys. F* **12**, 1753-69 (1982).
105. G. K. White, *Experimental Techniques in Low-Temperature Physics* (Clarendon Press, Oxford, 1978, revised 1987), p. 134ff.
106. E. M. W. Leung, *et al.*, in proceedings of Cryogenic Engineering Conference, Madison, Wisconsin, edited by K. D. Timmerhaus and H. A. Snyder, *Advances in Cryogenic Engineering* **25**, 489.
107. A. S. Shu, R. W. Fast, and H. L. Hart, in proceedings of Cryogenic Engineering Conference, edited by R. W. Fast, *Advances in Cryogenic Engineering* **31**, 455.
108. T. Ohmori, *et al.*, in proceedings of Cryogenic Engineering Conference, St. Charles, Illinois, edited by R. W. Fast, *Advances in Cryogenic Engineering* **33**, 323.
109. R. G. Scurlock and B. Saull, in proceedings of the Sixth International Cryogenic Engineering Conference, Grenoble, France, *Advances in Cryogenic Engineering*, 249.
110. Q. S. Shu, R. W. Fast, and H. L. Hart, *Cryo.* **26**, December, 671 (1986).
111. Q. S. Shu, R. W. Fast, and H. L. Hart, *Cryo.* **27**, June, 298 (1987).
112. M. Taneda, *et al.*, in proceedings of Cryogenic Engineering Conference, St. Charles, Illinois, edited by R. W. Fast, *Advances in Cryogenic Engineering* **33**, 305.
113. H. Burmeister, *et al.*, in proceedings of Cryogenic Engineering Conference, St. Charles, Illinois, edited by R. W. Fast, *Advances in Cryogenic Engineering* **33**, 313.

114. J. D. Gonczy, W. N. Boroski, and R. C. Niemann, in proceedings of Cryogenic Engineering Conference, UCLA, edited by R. W. Fast, *Advances in Cryogenic Engineering* **35 A**, 497.
115. *Metals Handbook*, edited by T. Lyman (The American Society for Metals, Cleveland, OH, 1948), p. 917.
116. *Metals Handbook*, edited by T. Lyman (The American Society for Metals, Cleveland, OH, 1948), p. 926.
117. R. C. Richardson and E. N. Smith, *Experimental Techniques in Condensed Matter Physics at Low Temperatures* (Addison-Wesley, Redwood City, CA, 1988), p. 121.
118. ASTM, *Standard specification for titanium and titanium alloy strip, sheet, and plate*, B 265 - 90 (ASTM, 1990).
119. *Metals Handbook*, edited by T. Lyman (The American Society for Metals, Cleveland, OH, 1948), p. 1143.
120. *Metals Handbook*, edited by T. Lyman (The American Society for Metals, Cleveland, OH, 1948), p. 555.
121. Dupont, *Vespel territory . . . performance plus*, product literature (Dupont, 1993).
122. Dupont, *Kapton*, product literature (Dupont, undated).
123. B. I. Ermolaev, *Metallovedenie i Termicheskaya Obrabotka Metallov* **12**, 46 (1974).
124. B. M. Zlobintsev and others, *Sov. J. Low Temp. Phys.* **5**, 7, 388 (1979).
125. B. M. Zlobintsev and others, *Fiz. Metal. Metalloved.* **47**, 6, 1310 (1979).
126. Y. S. Touloukian, *et al.*, *Thermal Conductivity: Metallic Elements and Alloys* (IFI/Plenum, New York, 1970).

127. Battelle Memorial Institute, Metals and Ceramics Information Center, *Handbook of Superconducting Machinery* (Metals and Ceramics Information Center, Battelle Columbus Laboratories, Columbus, Ohio, 1977).
128. M. Locatelli, *et al.*, *Cryo.* **16**, 374 (1976).
129. L. Duband, L. Hui, and A. Lange, *Cryo.* **33**, 6, 643-7 (1993).
130. Courtland Cable Company, Kevlar fiber strand No. B29/8X04.
131. R. A. Matula, *J. Phys. Chem. Ref. Data* **8**, 4, 1161-2, 1209-10 (1979).
132. C. Y. Ho, *et al.*, *J. Phys. Chem. Ref. Data* **3**, Supplement 1 (1974).
133. W. M. Blood, Jr., *MECL System Design Handbook* (Motorola Semiconductor Products Handbook, 1988).
134. G. Q. Jiang, *et al.*, *Rev. Sci. Instr.* **64**, 6, 1614-21 (1993).
135. Keithley Instruments, Test Instrumentation Group, Keithley Instruments, Inc., 28775 Aurora Road, Cleveland, OH 44139.
136. Analog Devices, INA110.
137. W. A. Bosch, *et al.*, *Cryo.* **26**, 1, 3 (1986).
138. M. W. Meisel, G. R. Stewart, and E. D. Adams, *Cryo.* **29**, 12, 1168 (1989).
139. Q. Li, *et al.*, *Cryo.* **26**, 8, 467 (1986).
140. J. Soudée, *et al.*, in proceedings of the Fifth International Workshop on Low Temperature Detectors, Berkeley, CA, edited by S. Labov and B. A. Young, *Journal of Low Temperature Physics* **93**, 3-4, 319 (1993).
141. R. W. Willekers, *et al.*, *Cryo.* **30**, April, 351 (1990).
142. Dale Electronics, 2300 Riverside Boulevard, Norfolk, NB 68701, 1% thick film 1 kohm surface mount resistors, part #RLWP-575-102-F.
143. J. W. Pierce, D. W. Kutty, and J. R. Larry, *Solid State Technology* **25**, 10, 85-92 (1982).

144. Lake Shore Cryotronics, 64 East Walnut Avenue, Westerville, OH 43081, Temperature Measurement and Control Catalog.
145. Bourns Instruments, linear potentiometer, P/N LCP12S-12, 5 kohm $\pm 20\%$.
146. American Magnetics, P. O. Box 2509, 112 Flint Road, Oak Ridge, TN 37831, Model 134 Liquid Helium Level Meter.
147. Varian Vacuum, 121 Hartwell Avenue, Lexington, MA 02173, Model 126 Ionization Gauge Tube.
148. Varian Vacuum, 121 Hartwell Avenue, Lexington, MA 02173, Model 843 Ratiomatic Ionization Gauge Controller.
149. MKS Baratron, 3350 Scott Boulevard, Building 4, Santa Clara, CA 95054, Model 622A 11TBE.
150. Granville Phillips, 3333 Bowers Avenue, Suite 130, Santa Clara, CA 95054, Convectron Gauge P/N: 275185.
151. Dynisco, Four Commercial Street, Sharon, MA 02067, Model G860-100-15 Strain Gauge Pressure Transducer.
152. Proteus Industries, 340 Pioneer Way, Mountain View, CA 94041, Model 100C-110 Fluid Flow Switch.
153. Lake Shore Cryotronics, 64 East Walnut Avenue, Westerville, OH 43081, QL36 phosphor-bronze cryogenic wire.
154. Samtec Inc., P. O. Box 1147, New Albany, IN 47151, 800-SAMTEC9, .050" micro strips, #TMS-150-01-S-S-RA.
155. Mill-Max Mfg. Corp., P. O. Box 300, 190 Pine Hollow Road, Oyster Bay, NY 11771., (516) 922-9253, pin receptacle #0461-0-15-21-11-35-04-0.
156. D. Seitz, personal communication, 1995.
157. National Instruments, 6504 Bridge Point Parkway, Austin, TX 78730.
158. Apple Computer, 20525 Mariani Avenue, Cupertino, CA 95014.

159. P. D. Barnes, Jr., *Estimating the Sensitivity of CDMS*, 21 February 1996, CDMS Technical Note (Center for Particle Astrophysics and U. C. Berkeley, 1996).
160. D. O. Caldwell, *et al.*, in proceedings of TAUP 89. Workshop on Theoretical and Phenomenological Aspects of Underground Physics, L'Aquila, Italy, September 20-23, 1989, edited by A. Bottino and P. Monacelli, (Editions Frontières, Gif-sur-Yvette, France, 1990), 353-8.
161. C. Athanassopoulos, *et al.*, Phys. Rev. Lett. **75**, 14, 2650-3 (1995).
162. J. E. Hill, Phys. Rev. Lett. **75**, 14, 2654-7 (1995).
163. J. D. Lewin and P. F. Smith, *Review of mathematics, numerical factors, and corrections for Dark Matter experiments based on elastic nuclear recoil*, 1 February 1996, RAL-TR 95 024 (Particle Physics Department, Rutherford Appleton Laboratory, 1996).
164. E. D. Commins and P. H. Bucksbaum, *Weak interactions of leptons and quarks* (Cambridge University Press, New York, 1983).
165. J. Engel, Phys. Lett. B **264**, 1-2, 114-19 (1991).
166. J. Engel, S. Pittel, and P. Vogel, International Journal of Modern Physics E **1**, 1, 1-37 (1992).
167. R. H. Helm, Phys. Rev. **104**, 1466 (1956).
168. G. Fricke, *et al.*, Atomic Data and Nuclear Data Tables **60**, 2, 177-285 (1995).
169. E. Diehl, *et al.*, Phys. Rev. D **52**, 7, 4223-39 (1995).
170. W. Xu, J. L. Lopez, and D. V. Nanopoulos, Phys. Lett. B **348**, 1-2, 105-10 (1995).
171. V. A. Bednyakov, H. V. Klapdor-Kleingrothaus, and S. G. Kovalenko, Phys. Rev. D **50**, 12, 7128-43 (1994).
172. A. Bottino, *et al.*, Astropart. Phys. **2**, 1, 67-75 (1994).
173. A. Bottino, *et al.*, Astropart. Phys. **2**, 1, 77-90 (1994).
174. A. Bottino, *et al.*, Astropart. Phys. **1**, 1, 61-76 (1992).

175. P. J. T. Leonard and S. Tremaine, *Astroph. J.* **353**, 1, 486-93 (1990).